# Engineering-Based Finite Element Approach to Appraise Massive Structures Affected by Alkali-Aggregate Reaction

By

RODRIGO VILELA GORGA

Under the supervision of

Dr. Leandro F. M. Sanchez

Co-supervisors

Dr. Beatriz Martín-Pérez

Dr. Martin Noël

A thesis submitted to the University of Ottawa in partial fulfilment of the requirements for the degree of

**Doctor of Philosophy**

uOttawa

Department of Civil Engineering
University of Ottawa
Ottawa, Ontario, Canada

January 2026

## Abstract

Alkali-aggregate reaction (AAR) is one of the most harmful distress mechanisms affecting the performance of aging concrete structures worldwide. In massive structures (e.g., dams), AAR has led to economic losses and negatively impacted structural safety. Some of the observed detrimental structural implications include loss of equipment alignment, excessive cracking leading to leakage, map cracking, concrete mechanical properties deterioration, introduction of excessive stresses on pre-stressing strands, inability to operate gates, and closure of expansion joints.

Traditional structural design standards and hand-calculations are not able to accurately represent the effects of AAR on the performance of affected concrete structures due to its overall complexity and anisotropic induced expansion. Therefore, finite element (FE) modelling is one of the most reliable alternatives to evaluate AAR's structural implications. Several prediction models have been developed to assess the macroscopic consequences of AAR, ranging from simplified approaches that do not consider the implications of essential parameters to very complex micro-meso models that require extensive fitting. However, a thorough and comprehensive approach able to assess the current damage state (diagnosis) and to predict potential of further damage (prognosis), while (1) accounting for the most important parameters affecting the reaction, (2) accounting for the mechanical properties of deteriorated materials, and (3) not requiring fitting of parameters, is still lacking. In this context, Gorga (2018) proposed a practical, yet accurate engineering-based FE modelling framework for assessing AAR damage and predicting the future behaviour of affected slender structures, such as bridges. It is currently one of the most comprehensive approaches to assess AAR-affected slender structures, as it does not require fitting parameters.

Even so, there is currently no macro-model capable of assessing AAR-affected massive structures (such as dams) that is able to achieve all the previously listed features. Dams are more complex systems for many reasons, including geometry and structural behaviour, unusual rehabilitation techniques (i.e., slot cutting), unique AAR kinetics, and thermal effects. Moreover, the economic impact and safety risks associated with the operation of massive structures are also much larger than those for slender structures, as they are often critical structures. Regarding rehabilitation of AAR-affected massive structures, often the only alternative is slot cutting, which consists of cutting vertical slots on the dam body to release the built-up compressive stresses and reduce permanent displacements. Even though there are several reports in the literature describing successful implementation of this rehabilitation technique, its efficacy remains the subject of ongoing debate among researchers.

In this context, the main goals of the current thesis are: (1) to develop an updated all-encompassing modeling approach to assess AAR-affected concrete structures (with focus on massive structures) based on what had been proposed by Gorga (2018) and (2) to simulate and verify the effectiveness of slot cutting as a rehabilitation technique for AAR-affected massive strcutures.

The first goal intends to ensure that all relevant phenomena are accounted for while keeping the same overall characteristics of the original approach (engineering-based assessment without the need for fitting). The commercially available software package Abaqus is used as the FE modelling platform. Key features in dam behaviour that are necessary to implement include: (i) updating the simulation to make it a fully integrated thermo-structural-AAR model, (ii) developing a new stress history-dependent creep subroutine, (iii) validating the thermal behaviour of mass concrete, (iv) validating the analysis in prestressed concrete structures, and (v) adopting an updated semi-empirical AAR model that considers the effect of leaching and alkali release from aggregates. All these steps are validated through data from laboratory tests or AAR-affected dams (Paulo Afonso IV and Bemposta dams). The second goal intends to settle the discussion within the engineering community regarding the effectiveness of slot cutting as a rehabilitation technique, clearly defining the mechanisms involved, their effect on the progression of the reaction, the influence of the most important variables on the slot cuts, and identifying in which situations the rehabilitation technique can be beneficial to the serviceability of the structure.

**Keywords**: Alkali-aggregate reaction, concrete, finite element, prognosis, diagnosis, dam, slot cutting.

# Table of Contents

## List of Figures

## List of Tables

## Important Definitions and Acronyms

The following abbreviations and acronyms will be consistently used throughout this thesis to avoid confusion:

- AAR = alkali-aggregate reaction
- ACR = alkali-carbonate reaction
- ASR = alkali-silica reaction
- CDP = concrete damaged plasticity (material model)
- CPT = concrete prism test
- CSA = Canadian Standard Association
- DRI = damage rating index
- FE = finite element
- FT = freeze-thaw (cycles)
- E = exposed
- NE = non-exposed
- PAIV = Paulo Afonso IV dam
- RBC = Robert-Bourassa/Charest Overpass
- RH = relative humidity
- SDT = stiffness damage test
- USDFLD and UEXPAN = specific types of Abaqus user subroutine

# 1. INTRODUCTION

## 1.1 General

Alkali-aggregate reaction (AAR) represents a critical deterioration mechanism impacting and significantly reducing the service life of concrete infrastructure globally (Chulliat et al., 2017; Nomura et al., 2013; Shayan et al., 2009). In massive structures, AAR is known to cause damage that can lead to economic losses and negatively impact their structural safety (Veilleux, 1995).

AAR is broadly classified into two primary categories: alkali-carbonate reaction (ACR) and alkali-silica reaction (ASR), with the latter being the predominant form observed in practice. ASR is usually described as a chemical reaction between the alkalis from the concrete pore solution and the reactive silica from the aggregates, which forms an expansive gel (Fournier & Bérubé, 2000). Subsequently, this gel absorbs water from the surrounding environment, resulting in volumetric expansion that induces internal expansive pressures and tensile stresses within both the reactive aggregates and the adjacent cement paste. In contrast, ACR is a less prevalent phenomenon, and its underlying mechanisms remain incompletely understood. Some studies suggest that ACR may constitute a specific variant of ASR (Katayama, 2010; Katayama & Grattan-Bellew, 2012), while others defend that it is a totally different distress mechanism (CSA A864, 2000; Fecteau et al., 2012).

AAR-induced expansion within concrete is anisotropic and is influenced by several parameters, such as temperature, alkali loading, type and nature/minerology of aggregates, presence of moisture, stress-state, etc. (Gautam et al., 2017; Goshayeshi, 2019). Depending on the expansion level attained, damage resulting from the distress mechanism can compromise the operation of the structure and even negatively affect the capacity of the system. Therefore, adequate condition assessment of AAR-affected structures is essential to ensure safety and serviceability. Due to the complexity of the phenomena involved in the development of AAR and its macroscopic implications, traditional structural design standards and hand-calculations are not able to accurately represent the effects of the distress mechanism. Therefore, FE modeling is one of the most reliable alternatives to (1) assess the current deterioration degree (i.e., diagnosis), (2) understand the impact of the deterioration on the different members or in the entire structure, (3) predict the potential of further damage due to AAR (i.e., prognosis), and (4) confidently appraise the safety and integrity of the structure at different points in time. Figure 1-1 illustrates the extent of AAR-induced damage in the reinforced concrete piers of the Robert-Bourassa Charest Overpass, located in Québec City, Canada.

a b

**Figure 1-1. AAR damage extent on Robert-Bourassa Charest Overpass: a. Close up of the cracks on the side of the pier, b. Overview of the pier distress. Source: Sanchez et al. (2016).**

Several finite element (FE) models have been developed over the years to describe the implications of AAR at several scales for both slender and massive structures, ranging from microscopic models describing the diffusion of ions and formation of secondary products such as ASR gel (Multon et al., 2009; Poyet et al., 2007) to macroscopic approaches assessing the overall structural implications (Charlwood, 1994; Grimal et al., 2008; Saouma et al., 2015; Ulm et al., 2000). Considerable progress has been achieved recently in the area, especially due to a better understanding of the reaction parameters and behaviour. However, there is still a need for an approach that intuitively describes the reaction without oversimplifying the physicochemical aspects involved nor overcomplicating them by requiring extensive fitting of parameters for each case based on the literature, laboratory data, or even engineering assumptions. In this context, the model by Gorga (2018) was proposed.

The novel approach was able to assess slender structures and predict their future behaviour by adequately accounting for the most important parameters affecting the reaction. The most important characteristics of the model are:

1- Estimation of the free AAR expansion curve through a time-dependent semi-empirical approach based on the most important parameters affecting AAR development, i.e., alkali content, humidity, type and reactivity of the aggregate, temperature, and (indirectly) exposure conditions.
2- Representation of the anisotropic stress-state dependent AAR expansion as a function of time.
3- Inclusion of concrete mechanical properties deterioration (compressive strength, tensile strength and modulus of elasticity) as a function of the induced expansion.

4- Simulation of concrete damage in both compression and tension, allowing for an accurate representation of damage propagation and accumulation.

5- No necessity of fitting parameters.

The model was validated based on data from both laboratory tests and an AAR-affected bridge that was in service for almost 50 years. A very good match between calculated and measured values was observed, proving the accuracy and validity of the approach for slender structures.

Regarding rehabilitation of AAR-affected massive structures, very few alternatives are available and often the only viable option is to perform slot cutting. This rehabilitation technique consists of cutting vertical slots on the dam body to release the built-up compressive stresses, reduce permanent displacements, restoring operational clearances, and extending the structure's service life (Caron et al., 2001). Several reports are available in the literature describing successful implementation and computer simulations of this technique (Charlwood, 1994 in Amberg et al., 2009, Grimal et al., 2008, Chulliat et al., 2017, Curtis et al., 2005, Curtis et al., 2016, Li & Coussy, 2002, 2004, Metalssi et al., 2014); however, its efficacy remains the subject of ongoing debate among researchers (Caron et al., 2001; Gocevski & Yildiz, 2017; Veilleux, 1995).

## 1.2 Research Significance

Dams represent critical infrastructure assets worldwide, serving essential functions in water supply, flood control, hydroelectric power generation, and irrigation. Unlike slender concrete structures — such as bridges or high-rise buildings, which are characterized by high aspect ratios, flexibility, and reliance on the combined effect of tensile strength from steel reinforcement and compressive strength from concrete—concrete dams are typically massive, rigid structures designed to withstand immense hydrostatic pressures through compressive resistance and gravitational stability. This fundamental structural difference amplifies the consequences of any degradation in dams, as failures can lead to catastrophic flooding, loss of life, and widespread economic disruption, far exceeding the localized impacts often associated with slender structure failures.

One of the most insidious threats to dam integrity is the alkali-aggregate reaction, a distress mechanism that induces expansive swelling in concrete, leading to cracking, undesired deformation, and even reduced load-bearing capacity (Chulliat et al., 2017; Nomura et al., 2013; Shayan et al., 2009). AAR can profoundly compromise the operational reliability and service life of dams, necessitating costly monitoring, repairs, or even decommissioning, as evidenced by numerous historical cases where affected structures have required extensive interventions to maintain safety and functionality (Abraham & Sloan, 1978; Chulliat et al., 2017; Droz et al., 2013; Horswill et al., 1994; Veilleux, 1995).

Massive structures affected by distress mechanisms such as AAR must also take into consideration additional scenarios that are usually deemed secondary for slender structures. For example, AAR-affected dams must consider local and global stability as potential critical failure modes, evaluate the consequences of size effect on AAR kinetics (e.g., alkali release from aggregates, source of silica from large aggregates, lack of leaching, etc.), consider watertightness as a critical serviceability condition – as water leakage can significantly affect the operation of the system, and carefully address the effect of thermal gradients, which may significantly influence structural behaviour and the kinetics of AAR. The significant differences listed preclude the use of identical evaluation methods for both structure types, as doing so would yield inaccurate results. In summary, AAR in dams presents a unique design and engineering challenge, necessitating specialized modeling and mitigation strategies to address the amplified risks and broader implications for safety and serviceability.

Furthermore, in the realm of rehabilitating AAR-affected dams, slot cutting stands out as one of the most frequently employed—and often the sole feasible—remediation approaches to mitigate the high compressive stresses and undesired deformations generated by the reaction. Although slot cutting has been successfully modeled and implemented across multiple real-world projects, the engineering community has yet to achieve a unified consensus on critical aspects such as optimal slot geometry, sequencing, and long-term performance outcomes.

Despite the significant developments in the field of diagnosis and prognosis of AAR-affected structures in recent years, the existing literature lacks a comprehensive model capable of accurately simulating the behaviour of AAR in dams under realistic conditions without oversimplifying or overcomplicating the most important aspects affecting reaction and without the need for fitting parameters. In this context, the proposed finite element modeling framework intends to validate a novel all-encompassing approach able to accurately simulate AAR in massive structures. By addressing this gap, the proposed model not only enhances the precision of dam health evaluations, but also informs more sustainable design and maintenance practices, ultimately contributing to the resilience of critical water infrastructure in the face of aging assets and climate-induced stressors. Similarly, the ongoing debate within the engineering community regarding the impact of critical aspects and the overall effectiveness of slot cutting as a rehabilitation technique reinforces the importance of a thorough assessment of the procedure and the critical variables involved. By completing this assessment and addressing this gap, the engineering-based proposed frameworks aims to: i) enhance the comprehension regarding slot cutting as a rehabilitation strategy and its overall effectiveness, and ii) advance the field of predictive reliability for these vital infrastructures by clearly describing the mechanisms involved in slot cutting, as well as the effects and contributions of the most important parameters (i.e., number of cuts, cut width, cut depth, contribution of creep, effect and proximity of discontinuities such as gates and turbine opening, effect of temperature gradients, and determination of when to perform the cuts).

## 1.3 Objectives and scope of the work

Traditional structural design standards and hand-calculations are not able to accurately represent the macro effects of AAR on the performance of structures due to its non-linear and anisotropic nature. For example, there is no standard design calculation procedure able to account for effects such as varying mechanical properties as a function of expansion level or AAR-induced expansion redistribution as a function of the stress state. In order to be able to properly represent those phenomena and the effect of all the releveant parameters, more powerful and sofisticated calculation approaches are necessary. In this context, finite element (FE) modelling is one of the most reliable alternatives to evaluate the structural implications of AAR.

The current thesis has two main goals. The first is to develop an all-encompassing FE modeling approach within the well established FE software Abaqus (Standard), by Simulia, to assess AAR-affected structures, with focus on massive structures. The proposed framework is based on the work developed by Gorga (2018) for slender structures, ensuring that all additional relevant phenomena affecting massive structures are accounted for while keeping the same overall characteristics of the original approach, i.e., (1) accounting for the most important parameters affecting the reaction, (2) accounting for the mechanical properties of deteriorated materials as a function of the expansion, and (3) not requiring fitting of parameters. The most important steps necessary to achieve the main goal are to:

1- Develop modeling approaches and validate them against laboratory experiments – ensuring measured results closely match FEA results for all cases – to assess:
    a. Thermal behaviour of concrete – including accounting for the effect of concrete heat of hydration, and convection, conduction and radiation (along with solar radiation) interactions.
    b. Prestressed concrete – including incorporating the effects of prestressed strands/tendons and prestressing losses.
    c. Slot cutting rehabilitation technique – including the pre- and post-cut behaviour through adequate contact interaction.
2- Implement (into the FEA subroutine) an updated semi-empirical AAR free expansion model capable of considering the effect of leaching, alkali release, alkali content, temperature, and relative humidity. The previous analytical model implemented was the best available alternative at the time of its development. However, new research has indicated that a better approach is now available, being validated against specimens that have been exposed to the environment and monitored for decades.
3- Develop and implement a new expansion subroutine capable of representing both thermal and AAR expansion to have a fully integrated thermo-structural model. For massive structures, thermal gradients also lead to differential AAR-induced expansion strains. The only way to accurately capture this behaviour, which is one of the critical factors leading to macroscopic damage, is for the thermal and mechanical analyses to be fully integrated.
4- Implement a new stress history and time-dependent creep model. AAR expansion can lead to high compressive and tensile stresses, both of which lead to creep strain. Moreover, when slot cutting is performed, the local stress state changes, significantly affecting creep

strain in that vicinity. In order to capture all these behaviours accurately, a new subroutine is necessary as there are no built-in models within Abaqus software able to do so for elasto-plastic analyses.

5- Verify the overall accuracy and applicability of the proposed approach by simulating and assessing in-service AAR-affected massive structures (Bemposta dam in Portugal and Paulo Afonso IV dam in Brazil).

The second main goal of the thesis is to study and evaluate slot cutting as a rehabilitation technique. There is no consensus within the engineering community regarding the effectiveness of slot cutting, with conflicting reports both supporting and opposing its use. Therefore, developing a better understanding of the mechanisms involved, their effects on the reaction, and the influence of the most important parameters affecting the rehabilitation technique, is an essential step to determine the effectiveness of slot cutting and in which situation it is recommended.

A summary of the goals and steps required is presented in Figure 1-2.

The framework proposed consists exclusively of numerical simulations using FE modelling, which is validated using data from both laboratory tests and in-service AAR-affected dams. Through partnerships, data from two dams has been obtained: Paulo Afonso IV dam (from CHESF, Brazil) and Bemposta dam (from LNEC, Portugal). All the data obtained from the analyses helps to better understand the effects of AAR on massive structures, as well as to provide the engineering community with a new validated and engineering-based tool to assess the current and predict the future condition of all types of AAR-affected concrete structures.

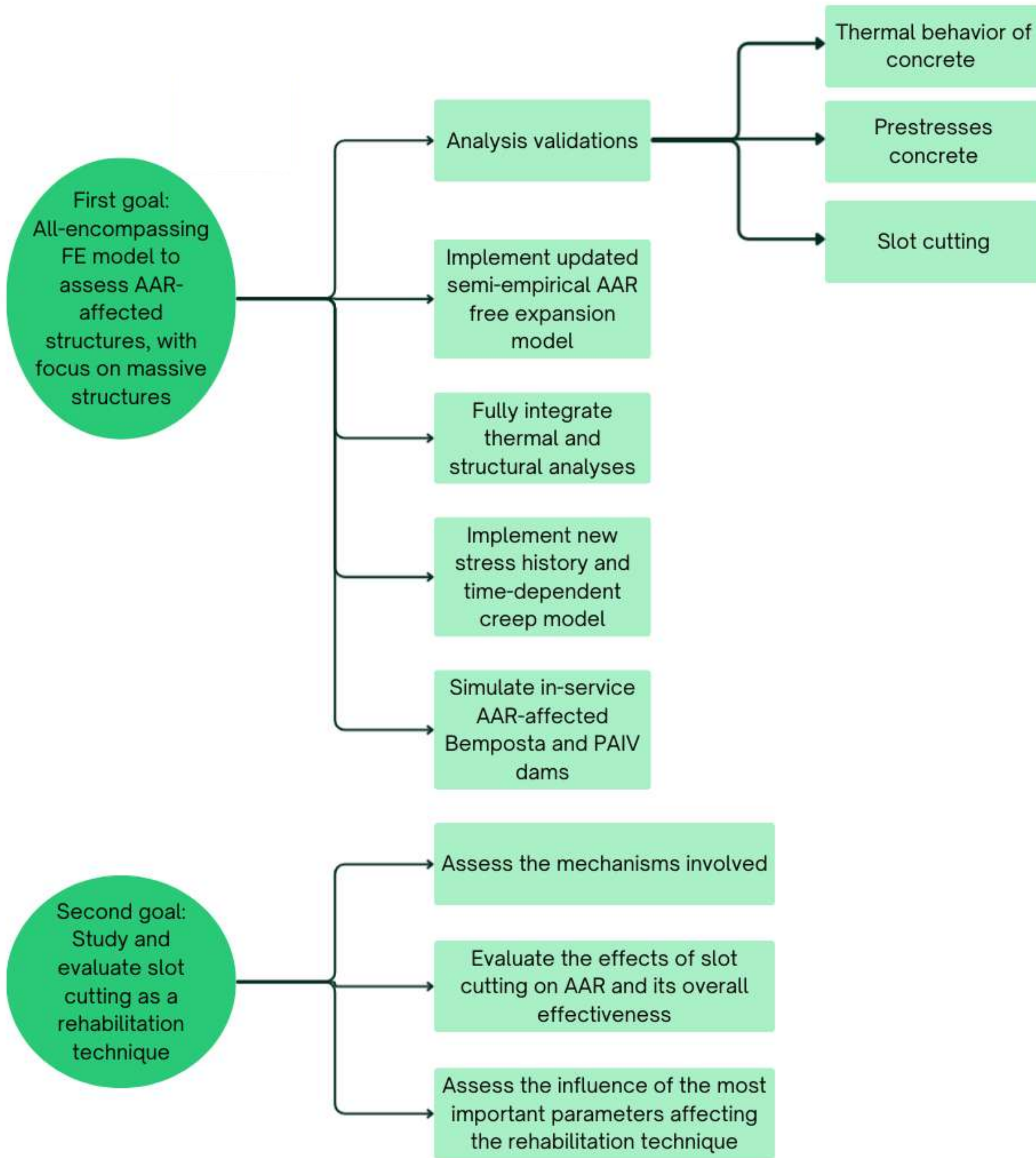


**Figure 1-2. Diagram of thesis goals and main steps**

## 1.4 Research methodology

In order to achieve the objectives previously listed, the methology presented below is required. The simulations proposed can be divided in two categories: (1) validation analyses based on laboratory experiments and model improvements, and (2) assessment of in-service dams.

The first validation analysis is related to performing the simulation of mass concrete thermal behaviour, including heat of hydration. As previously stated, temperature plays a very important role on the development of AAR on massive structures, as it is the main cause of expansion gradients between different parts of the dam. Therefore, properly simulating conduction, convection and radiation is essential to properly assess AAR. Moreover, the effect of heat of hydration on the overall structure needs to be studied, as it significantly increases the temperature of the concrete at early ages (possibly affecting AAR expansion rates) and can lead to thermal cracking. Therefore, the laboratory experiment performed by Lawrence (2009) was simulated to validate the modeling approach proposed. The author cast large concrete blocks and measured the temperature variation at different depths. The blocks were exposed on the top surface, while being insulated on all other sides. This allows the thermo-mechanical modeling proposed approach to be validated, as well as the adopted thermal parameters (which were obtained from the literature). Heat of hydration was modeled as a time-dependent body heat flux boundary condition for a specific concrete mix. Convection between the different materials was modeled as surface film condition interaction, based on provided temperature amplitudes and convection coefficients. Conduction within a body (comprising one or more materials) was modeled through material properties definitions (specific heat and conductivity). Sun radiation was simulated as a (periodic) time-dependent surface heat flux boundary condition, which is calculated based on several parameters, including latitude, surface orientation, surface angle with horizontal plane, etc.

Radiation thermal losses to the environment were simulated through surface radiation interactions, which are based on emissivity constant, Stefan-Boltzmann constant and varying ambient temperature. This validation is reported in Chapter 4.

The second validation analysis covers the simulation of prestressed concrete structures. Some dams use prestressing as a way to counteract high tensile stresses in specific concrete components, like spillways. Therefore, it is important to be able to accurately simulate the effect of prestressing on both the tendon/strand and concrete, as well as structural failure. In order to achieve this goal, the laboratory experiment performed by Cheng et al. (2009) was adopted as a validation analysis. The authors prestressed concrete beams and tested them up to failure (i.e., member collapse due to excessive cracking and/or reinforcement/prestressed strand yielding), with the entire force-deflection behaviour being recorded. As the prestressing approach needs to be consistent with the AAR expansion approach, the solution adopted was to create prestressing through an equivalent thermal strain on the reinforcement. The value of the reinforcement coefficient of expansion can vary over time, meaning that once AAR expansion begins to develop based on a concrete temperature curve, the prestressing in the reinforcement can be kept constant. This validation is reported in Chapter 5.

The third validation analysis is intended to tackle both creep and slot cutting at the same time. Creep plays an important role in slot cutting as the rehabilitation technique changes the internal stresses, meaning that a constant global variation of the modulus of elasticity (like what had been done before) is likely not representative. Therefore, the laboratory experiment proposed by Caron et al. (2001) will be simulated. The authors performed slot cutting on concrete beams under compression and measured the response (closure and strains) over time, meaning that the short and long-term responses recorded can be used to validate both slot cutting simulation and creep approach. It was observed that none of the approaches from the literature were suitable for simulating slot cutting. Therefore, the rehabilitation technique was modeled with a novel approach, including contact activation and deactivation, along with a “dummy” concrete part. Creep was coded directly into the Abaqus subroutine according to the Dirichlet series in order to take into consideration the entire stress history of each element without having to store all the data (see Chapter 6).

In order to complete both dam assessments, the proposed modeling approach had to be further developed. First, recent work on the semi-empirical free AAR expansion equation (De Grazia et al., 2021; Nguyen et al., 2022) is implemented directly into the Abaqus subroutine, allowing the calculation to be made a function of the expansion level instead of time. Moreover, the effect of leaching and alkali release can now be directly accounted for within the calculation, as well as new findings regarding the effects of temperature, relative humidity and alkali content, making it more suitable to be applied to massive structures. The equation has already been succesfully used to simulate the expansion on field exposed blocks tested by Fournier et al. (2009), with the next clear step being to use it for larger (dam) structures. Second, the Abaqus subroutine is also updated to fully integrate thermal and non-linear AAR-mechanical analyses (as of Chapter 5, as in Chapter 4 isothermal regions were manually subdivided). This allows for the seasonal thermal effect to be incorporated along with AAR, as well as the exact influence of temperature on the kinetics of the reaction on each individual element.

Paulo Afonso IV Dam is used as a first iteration of the proposed approach, including application of uncoupled thermal modeling (including heat of hydration), prestressing and indirectly accounting for the size effect on AAR kinetics. Data for validation from this dam is limited, as monitoring was not done extensively. Therefore, a model of the spillway (the region with the most amount of data available) is used as a first attemp to include the new parameters and start to understand their effects. Parameters that are used for validation of the simulation include recorded expansion rate and cracking extent/location from field investigations. Regarding structural prognosis, the most important aspects assessed are the expansion values along the gate axis – as it can affect the gate operation; the stresses on the prestressing tendons – as they can be increased by AAR expansion and cracking; and cracking extent at critical regions. This validation is reported in Chapter 5.

Bemposta Dam is the second and complete iteration of the model, including all developments previously described. The dam has an extensive amount of recorded data that is be used for the validation, including vertical, radial and tangential displacments (from plumb lines and surveys), as well as in-situ free and restrained expansion. Moreover, new data from laboratory experiments (damage rating index) of concrete cores is also used to further verify the proposed approach. The goal of this simulation is to prove the proposed approach is able to accurately perform the diagnosis and prognosis of massive structures, accounting for all the most important parameters affecting the reaction, while requiring no (or a minimal amount of) fitting. Complimentarily, the results obtained are compared to the already existing model developed by LNEC (Portugal), highlighting their similarities, differences and predictions.

### 1.5 Thesis Organization

The thesis consists of seven chapters. The overall description of each chapter is presented below.

- Chapter 1 introduces the research needs, objectives and scope of the work, and research methodology.

- Chapter 2 reviews the current AAR-modeling state-of-the-art, by first discussing the main topics related to modeling AAR and dams, and then comparing existing AAR macro-models, highlighting their similarities, differences and basic concepts. The chapter concludes highlighting the existing knowledge gaps to justify the need for the development of the proposed approach.

- Chapter 3 presents a summary description of the approach proposed by Gorga (2018) for modeling AAR-affected slender structures.

- Chapter 4 presents the first technical paper on the assessment of the AAR-affected Paulo Afonso IV dam. This paper includes prestressed concrete validation, thermal behaviour of concrete validation and a first attempt at incorporating the effects of massive structures on AAR. This paper has been published in the ASCE Journal of Performance of Constructed Facilities:

  Gorga, R.V., Sanchez, L.F., Martín-Pérez, B., Fecteau, P.L., Cavalcanti, A., & Silva, P.N. (2020). Finite Element Assessment of the ASR-Affected Paulo Afonso IV Dam. Journal of Performance of Constructed Facilities, 34.

- Chapter 5 presents the second technical paper on the complete assessment of the AAR-affected Bemposta dam. This paper includes slot cutting and creep validation analyses, as well as developments on the model regarding fully integrating thermal and mechanical analyses, updated AAR kinetics semi-empirical equation and creep modeling implementation.

- Chapter 6 presents the third technical paper on the assessment of slot cutting as a rehabilitation technique on a generic AAR-affected dam, as well as the mechanisms involved and the effect of the most important parameters.

- Chapter 7 concludes the thesis by presenting conclusions and recommendations for future work.

## 1.6 References

Abraham, T. J., & Sloan, R. C. (1978). TVA cuts deep slot in dam, ends cracking problem. Civil Engineering—ASCE, 48(1), 66–70.

Amberg, F., Bremen, R., & Brizzo, N. (2009). Rehabilitation of the Pian Telessio dam (IT) affected by AAR-reaction. Commission Internationale Des Grands Barrages.

Caron, P., Tinawi, R., & Léger, P. (2001). Slot cutting response of compressed concrete structures. 4th International Conference on Fracture Mechanics in Concrete and Concrete Structures, 879–886.

Charlwood, R. (1994). A review of alkali aggregate in hydro-electric plants and dams. International Journal on Hydropower Dams, 73–80.

Cheng, H. T., Mohammed, B. S., & Mustapha, K. N. (2009). Experimental and analytical analysis of pretensioned inverted T-beam with circular web openings. International Journal of Mechanics and Materials in Design, 5(2), 203–215.

Chulliat, O., Grimal, E., & Bourdarot, E. (2017). Chambom Dam - A Struggle Against AAR. Dam Swelling Concrete (DSC 2017).

CSA A864. (2000). Guide to the Evaluation and Management of Concrete Structures Affected by Alkali-Aggregate Reaction.

Curtis, D. D., Davis, B. J., Rahman, S., & Powell, R. C. (2005). Updated Assessment of Concrete Growth Effects on Hiwassee Dam. 25th Annual USSD Conference.

Curtis, D. D., Feng, L., Sooch, G. S., Zheng, J., & Fletcher, J. (2016). Practical Analysis and Assessment of AAR Affected Dams and Hydroelectric Plants. United States Society of Dams, 36th Annual USSD Conference.

De Grazia, M. T., Goshayeshi, N., Gorga, R., Sanchez, L. F. M., Santos, A. C., & Souza, D. J. (2021). Comprehensive semi-empirical approach to describe alkali aggregate reaction (AAR) induced expansion in the laboratory. Journal of Building Engineering, 40.

Droz, P., Menouillard, T., Vallotton, O., & Leroy, R. (2013). Slot cutting an AAR-affected dam: case study of the Salanfe dam. International Journal on Hydropower and Dams, 20(5).

Fecteau, P. L., Fournier, B., Choquette, M., & Duchesne, J. (2012). Contribution to the understanding of the so-called alkali–carbonate reaction (ACR). 14th International Conference on Alkali-Aggregate Reaction - ICAAR.

Fournier, B., & Bérubé, M.-A. (2000). Alkali-aggregate reaction in concrete: a review of basic concepts and engineering implications. Canadian Journal of Civil Engineering, 27(2), 167–191.

Fournier, B., Ideker, J. H., Folliard, K. J., Thomas, M. D. A., Nkinamubanzi, P. C., & Chevrier, R. (2009). Effect of environmental conditions on expansion in concrete due to alkali–silica reaction (ASR). Materials Characterization, 60(7), 669–679.

Gautam, B. P., Panesar, D. K., Sheikh, S. A., & Vecchio, F. J. (2017). Multiaxial expansion-stress relationship for alkali silica reaction-affected concrete. ACI Materials Journal, 114(1), 171–184.

Gocevski, V., & Yildiz, E. (2017). Macro-modelling of AAR-affected hydraulic structures. Dam Swelling Concrete (DSC 2017).

Gorga, R. V. (2018). Engineering-Based FE Approach to Appraise Slender Structures Affected by Alkali-Aggregate Reaction (AAR) [M.A.Sc. Thesis]. University of Ottawa.

Goshayeshi, N. (2019). Contribution to the Development of Analytical Models to Forecast Alkali-Aggregate Reaction (AAR) Kinetics and Induced Expansion [M.A.Sc. Thesis, University of Ottawa].

Grimal, E., Sellier, A., Le Pape, Y., & Bourdarot, E. (2008). Creep, shrinkage, and anisotropic damage in alkali-aggregate reaction swelling Mechanism-Part I: A constitutive model. ACI Materials Journal, 105(3), 227–235.

Horswill, P., Snowden, H. N., & Weeks, R. C. (1994). Val de la Mare Dam, Jersey: Instrumentation, monitoring and stability analysis of an ASR damaged dam. 8th Conference of the British Dam Society, 119–133.

Katayama, T. (2010). The so-called alkali-carbonate reaction (ACR) — Its mineralogical and geochemical details, with special reference to ASR. Cement and Concrete Research, 40(4), 643–675.

Katayama, T., & Grattan-Bellew, P. E. (2012). Petrography of Kingston experimental sidewalk at age 22 years - ASR as the cause of deleteriously expansive, so-called alkali-carbonate reaction. 14th International Conference on Alkali-Aggregate Reaction - ICAAR.

Lawrence, A. M. (2009). A finite element model for the prediction of thermal stresses in mass concrete [PhD Thesis]. University of Florida.

Li, K., & Coussy, O. (2002). Concrete ASR degradation: from material modeling to structure assessment. Concrete Science and Engineering, 4(13), 35–46.

Li, K., & Coussy, O. (2004). Numerical assessment and prediction method for the chemico-mechanical deterioration of ASR-affected concrete structures. Canadian Journal of Civil Engineering, 31(3), 432–439.

Metalssi, O. O., Seignol, J. F., Rigobert, S., & Toutlemonde, F. (2014). Modeling the cracks opening-closing and possible remedial sawing operation of AAR-affected dams. Engineering Failure Analysis, 36, 199–214.

Multon, S., Sellier, A., & Cyr, M. (2009). Chemo–mechanical modeling for prediction of alkali silica reaction (ASR) expansion. Cement and Concrete Research, 39(6), 490–500.

Nguyen, T. N., Sanchez, L. F. M., Li, J., Fournier, B., & Sirivivatnanon, V. (2022). Correlating alkali-silica reaction (ASR) induced expansion from short-term laboratory testings to long-term field performance: A semi-empirical model. Cement and Concrete Composites, 134(2).

Nomura, M., Komastubara, A., Fujimoto, K., & Torii, K. (2013). Evaluation of maintenance methods for ASR-damaged structures in Hokuriku district, Japan. 3rd International Conference on Sustainable Construction Materials and Technologies.

Poyet, S., Sellier, A., Capra, B., Foray, G., Torrenti, J. M., Cognon, H., & Bourdarot, E. (2007). Chemical modelling of Alkali Silica reaction: Influence of the reactive aggregate size distribution. Materials and Structures/Materiaux et Constructions, 40(2), 229–239.

Sanchez, L. F. M., Fournier, B., Bastien, J., Mitchell, D., & Noël, M. (2016). Overall assessment of an ASR affected overpass “Robert-Bourassa/Charest” after nearly 50 years in service. 8th International Conference on Bridge Maintenance, Safety and Management - IABMAS.

Saouma, V. E., Martin, R. A., Hariri-Ardebili, M. A., & Katayama, T. (2015). A mathematical model for the kinetics of the alkali–silica chemical reaction. Cement and Concrete Research, 68, 184–195.

Shayan, A., Xu, A., & Salamy, R. (2009). Effectiveness of CFRP wrapping in confining the expansion of AAR-affected concrete. 7th Austroads Bridge Conference.

Ulm, F.J., Coussy, O., Kefei, L., & Larive, C. (2000). Thermo-Chemo-Mechanics of ASR Expansion in Concrete Structures. Journal of Engineering Mechanics, 126(3), 233–242.

Veilleux, M. (1995). Hyrdo-Quebec`s experience using deep slot cutting to rehabilitate concrete gravity dams affected by alkali-aggregate reaction. 2nd International Conference on Alkali-Aggregate Reactions in Hydroelectric Plants and Dams.

# 2. LITERATURE REVIEW

## 2.1 Alkali-aggregate reaction (AAR)

The alkali-aggregate reaction (AAR) represents a critical deterioration mechanism impacting concrete infrastructure globally (Fournier & Bérubé, 2000). AAR is broadly classified into two primary categories: alkali-carbonate reaction (ACR) and alkali-silica reaction (ASR), with the latter being the predominant form observed in practice. The mechanistic progression of ASR is relatively well elucidated, encompassing several key stages. Initially, a chemical reaction between the "unstable" silica mineral forms, which are found within fine and/or coarse reactive aggregate materials, and the alkali hydroxides (Na, K – OH) dissolved in the concrete pore solution takes place and generates a secondary product, the so-called alkali-silica gel. Subsequently, this gel absorbs water from the surrounding environment, resulting in volumetric expansion that induces internal expansive pressures and tensile stresses within both the reactive aggregates and the adjacent cement paste. Then these stresses exceed the material's tensile strength, extensive microcracking ensues, often compromising the mechanical integrity, durability, and, in some instances, the functionality of the affected structure (Fournier & Bérubé, 2000; Giaccio et al., 2008). In contrast, ACR is a less prevalent phenomenon, and its underlying mechanisms remain incompletely understood. Some studies suggest that ACR may constitute a specific variant of ASR (Katayama, 2012; Katayama & Grattan-Bellew, 2012), while others attribute to ACR a distinct mechanism (CSA A864, 2000; Fecteau et al., 2012).

From a chemical perspective at the microscale, the ASR process can be described as follows (Bazant & Steffens, 2000; Glasser & Kataoka, 1981; Kurtis & Monteiro, 2003). First, the $OH^-$ ions from the concrete pore solution react with the silanol groups ($Si - O$), leading to the cleavage of siloxane bonds (Si-O-Si) and the formation of additional chemical bonds. Then, on the surface of the aggregate, the silanol groups react with the $OH^{-}$ ions, liberating water molecules. Subsequently, cations of the concrete pore solution such as $Na^{+}, K^{+}$ and $Ca^{2+}$ are electrostatically attracted to the alkali-silicate ($Si-O^{-}$), diffusing into the gel to neutralize the charge imbalance. Upon reaching saturation, an expansive alkali-silicate gel is formed, comprising silica, alkalis, water, and other ions. This alkali-silicate gel is hydrophilic (swells in the presence of water), and it has a specific volume greater than that of the reactant materials. Moreover, the chemical composition of the gel is highly variable, which means that its physicochemical properties can be quite diverse, therefore making the prediction of its behaviour difficult.

From a deterioration perspective, Sanchez et al. (2015) proposed a qualitative damage model (Figure 2-1) that describes ASR distress generation and development at the meso-scale, based on petrographic analysis performed at 16x magnification. This model delineates the progression of ASR-induced distress across varying levels of expansion, as summarized below:

<u>Low expansion levels (around 0.05%)</u>: At this stage, two distinct crack morphologies, designated as Type A and Type B, are observed within aggregate particles, while cracking in the cement paste remains infrequent, and alkali-silica gel is rarely detected. Type A are sharp cracks that correspond to opened cracks cutting the aggregates particles, predominantly forming in previously fractured or more porous zones within the particles. In general, these zones facilitate the alkali ions penetration, accelerating the reaction process relative to other areas of the bulk aggregate particle. Conversely, Type B cracks, often described as “onion skin” or “en-echelon” fractures, develop in aggregate particles lacking pre-existing fractures or porosity. These cracks exhibit a near-homogeneous alkali ion penetration, manifesting features almost parallel (peripheral) to the aggregate’s boundaries.

Moderate expansion levels (from 0.10% to 0.12%): As expansion progresses, the aforementioned crack types continue to propagate, and alkali-silica gel becomes discernible, particularly within open cracks in the aggregate particles. Some type A cracks reach and extend into the cement paste, though their propagation remains limited. Type B cracks, however, continue to develop within the confines of the aggregate boundaries, without significant extension into the cement paste.

High expansion levels (approximately 0.20%): At this stage, ASR gel is observed both within the aggregate particles and in the surrounding cement paste. Type A cracks fully extend into the cement paste on both sides of the aggregate particles, establishing connectivity with the matrix. Meanwhile, Type B cracks typically envelop more than half of the aggregate particle.

Very high expansion levels (0.30% and beyond): At these advanced stages, the quantity of alkali-silica gel increases significantly compared to lower expansion levels. Type A cracks interconnect with other Type A and/or Type B cracks originating from different reactive aggregate particles, forming an extensive cracking network throughout the concrete matrix. Additionally, Type B cracks may extend into the interfacial transition zone (ITZ), potentially causing debonding of the aggregate particles, or into the bulk cement paste, thereby integrating with the broader cracking network. It is noteworthy that the presence of Type A and Type B cracks is not universal across all reactive aggregates, and that particular crack types may form preferentially in certain types of aggregates, depending on their nature.

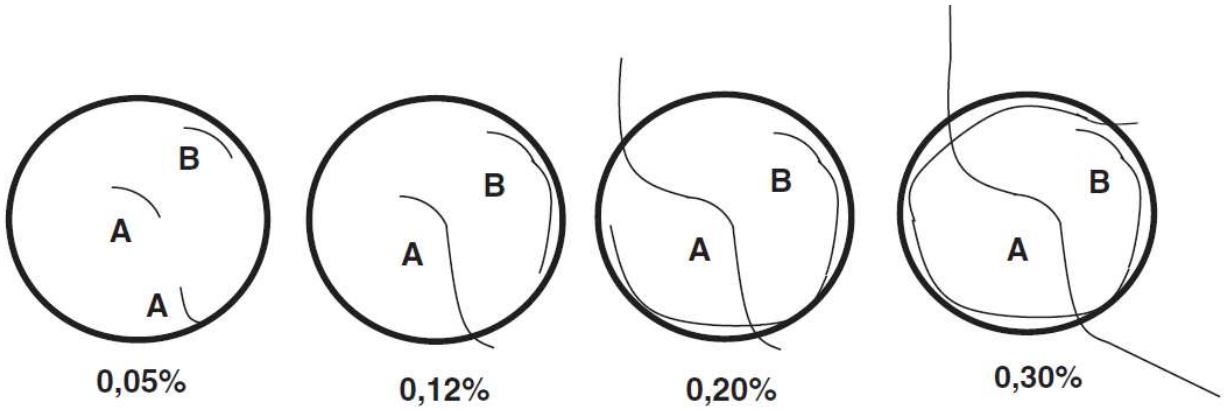


**Figure 2-1. Qualitative ASR damage model for expansions varying from 0.05% to 0.30%. Source: Sanchez et al. (2015)**

According to Fournier & Bérubé (2000), the alkali-carbonate reaction (ACR) constitutes a distinct mechanism from the alkali-silica reaction (ASR). ACR occurs when dolomite crystals from the aggregates are exposed to the alkali hydroxides present in the concrete pore solution, initiating a dedolomitization process. This reaction yields secondary products, including brucite, calcite, and alkali carbonates. The formation of these products generates micro-cracks, which serve as conduits for deeper penetration of ions from the pore solution into the reactive aggregate particles. Furthermore, the alkali carbonates produced may react with portlandite in the concrete matrix, regenerating alkali hydroxides in the pore solution. This regenerative process suggests that ACR could potentially persist indefinitely under conducive conditions. According to Rogers et al. (2000), ACR induces very fast and extensive expansion in concrete prism specimens, as well as severe damage within the first few years in the field when the conditions are favorable.

It is important to emphasize that the approach outlined in subsequent chapters were developed for alkali-aggregate reaction (AAR) in general, although the validations presented are derived exclusively from ASR-affected specimens and structural members. Similarly, several of the authors cited in the following sections worked with AAR while others worked only with ASR.

Consequently, references to “ASR” indicate research focused solely on that reaction, whereas “AAR” denotes broader statements/conclusions applicable to both ASR and ACR.

## 2.2 Factors affecting AAR expansion

### 2.2.1 Temperature

Temperature plays a major role on both the kinetics and ultimate expansion of alkali-aggregate reaction (AAR), as extensively documented in the literature (Fournier & Bérubé, 2000; Hobbs, 1988; Larive, 1997). Ulm et al. (2000) characterize AAR as a thermo-activated process, wherein elevated temperatures accelerate reaction rates. This acceleration is attributed to the thermal enhancement of two critical processes: the dissolution of reactive silica and the formation of reaction products. Experimental findings by Larive (1997) shows a faster reaction at a higher temperature and also a slightly greater final expansion value (Figure 2-2). This increased expansion is hypothesized to result from the higher amount of leaching and lower gel viscosity triggered under higher temperatures.

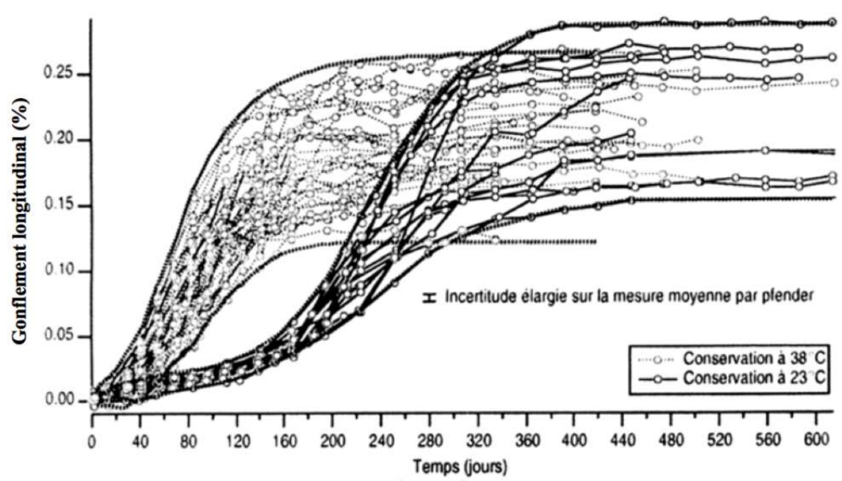


**Figure 2-2. Expansion over time for specimens at different temperatures (38ºC and 23ºC). Source: Larive (1997).**

Research has identified a "pessimum" temperature range (38–40°C) associated with maximum alkali-silica reaction (ASR) expansion under fixed alkali content (Olafsson, 1986). Urhan (1987), supported by subsequent studies (Chatterji & Christensen, 1990; Nishibayashi et al., 1991), proposed that elevated temperatures enhance both the kinetics of silica dissolution and the formation of calcium-silicate-hydrate (C-S-H). However, beyond a certain threshold, the rate of C-S-H formation exceeds the silica dissolution and the expansion due to ASR deaccelerates. Additionally, Comi & Pignatelli (2012) suggest that higher temperatures not only accelerate the reaction but also reduce the viscosity of the alkali-silica gel, enabling it to penetrate concrete pores more readily, thereby diminishing the overall expansive potential of the reaction.

In contrast, recent studies comparing results from the Accelerated Brazilian Concrete Prism Test (ABCPT), the Accelerated Mortar Bar Test (AMBT), and the Accelerated Concrete Prism Test (ACPT) indicate that temperature influences both the kinetics and the maximum expansion of AAR, with no observable "pessimum" temperature (Goshayeshi, 2019). Moreover, higher temperatures (up to 80ºC) display an increase in both the reaction rate and final expansion, without a "pessimum" temperature being observed.

Larive (1997) proposed that the temperature-dependent rate of AAR expansion can be modeled using the Arrhenius equation. Pesavento et al. (2012) elaborate that this equation, rooted in Classical Irreversible Thermodynamics, describes the temperature dependence of a parameter — such as the characteristic ($\tau_c$) or latency time ($\tau_L$) defined by Larive (1997) — through an exponential relationship. This new parameter value is based on the original parameter value for a known temperature ($\tau(\theta_0)$) and the activation energy of that parameter (U), which represents the minimum energy required for the reaction to proceed. The specific formulation, as proposed by

Ulm et al. (2000), is based on the Arrhenius equation (Equation 2-1), and is presented in Equation 2-2:

$$k = Ae^{\frac{U}{R\theta}} \tag{2-1}$$

$$\tau(\theta) = \tau(\theta_0)e^{U\left(\frac{1}{\theta}-\frac{1}{\theta_0}\right)} \tag{2-2}$$

where k is the reaction rate, A and R are constants, U is the activation energy and θ is the temperature. Moreover, the authors stated the following values of $U_c = 5400 \pm 500K$ and $U_L = 9400 \pm 500K$ for $\tau_c$ and $\tau_L$, respectively.

### 2.2.2 Humidity

Water is a critical factor in the progression of AAR due to its multifaceted role in the reaction process (Bazant & Steffens, 2000). Firstly, water serves as the transport medium, facilitating the diffusion of hydroxyl and alkali ions through the concrete pore solution. Secondly, it is chemically essential for the formation of the expansive alkali-silica gel, enabling the dissolution of siloxane bonds. Thirdly, the gel's expansion is directly contingent upon its absorption of water from the surrounding porous medium.

The influence of water on ASR development was initially observed by Vivian (1981), who demonstrated that sufficiently low water content (relative humidity) could halt the ASR-induced mechanism. This finding was subsequently corroborated by other researchers (Kurihara & Katawaki, 1989; Olafsson, 1986). Larive (1997) further elucidated water's dual role as both a reagent and a reaction medium. As a reagent, water governs the magnitude of gel swelling, which is proportional to the availability of water during the reaction. However, only water not consumed by cement hydration may react and lead to AAR development. As a reaction medium, water must be present in sufficient quantities to enable the transport of reactive species, supporting the existence of a critical humidity threshold below which both the chemical reaction and gel swelling cease. Larive (1997) also explains that the migration of water within the concrete (i.e., shrinkage) is not affected by AAR, which means both phenomena can be assumed to happen independently of each other.

Poyet et al. (2006) conducted an extensive experimental investigation into the effects of water on ASR. Their tests revealed that a relative humidity as low as 59% still provided sufficient water to sustain ASR, albeit at a reduced reaction rate and with lower maximum expansion, as illustrated in Figure 2-3a. Additionally, the authors examined the impact of cyclic wetting and drying, comparing short (14-day) and long (28-day) cycles, as shown in Figure 2-3b. Their findings indicated that the expansion of both short and long cycle cases was always bound by those corresponding to 59% RH and 96% RH.

a b

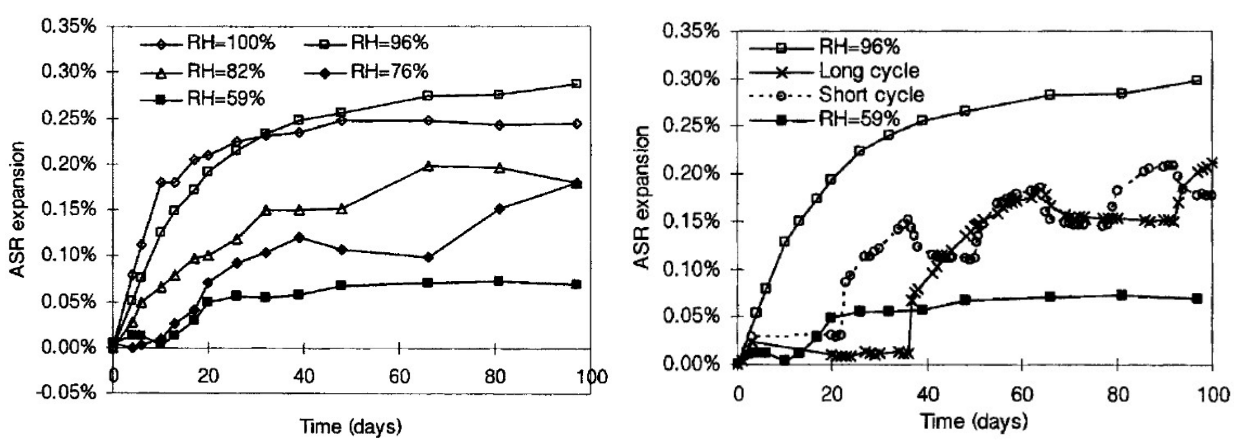


**Figure 2-3. Effect of constant and varying relative humidity conditions on ASR expansion. Source: Poyet et al. (2006).**

Several models incorporate the relationship proposed by Capra & Bournazel (1998) to account for the influence of relative humidity (h) on alkali-silica reaction (ASR) behaviour. The general approach proposed is presented in Equations 2-3 and 2-4, where the ASR-induced expansion ($\varepsilon_{\mathrm{ASR}}$) is modeled as a function of time (t), relative humidity (h), temperature ($\theta$) and stress-state ($\sigma$). In this formulation, $\varepsilon^{100\%}$ is the swelling observed at 100% relative humidity, $\mathrm{g}(\mathrm{T}, \sigma)$ is a function to take temperature and stress-state into consideration, f(h) is a function that incorporates the influence of relative humidity and m is an empirical constant (usually taken equal to 8).

$$\varepsilon_{\mathrm{ASR}}(\mathrm{t}, \mathrm{h}, \theta, \sigma) = \varepsilon^{100\%}(\mathrm{t})\mathrm{f}(\mathrm{h})\mathrm{g}(\theta, \sigma) \tag{2-3}$$

$$\mathrm{f}(h) = \left(\frac{h}{100}\right)^{m} \tag{2-4}$$

Alternatively, two other models, one proposed by Bazant & Steffens (2000) and the other by both Li et al. (2000) and Li & Coussy (2002), assume that the initial dry ASR expansive gel needs to absorb/imbibe water in order to create a fluid and expand. The model developed by Bazant & Steffens (2000) assumes that this water absorption/imbibition only occurs above a relative humidity threshold of 85%. The second model assumes that the gel continuously incorporates water based on its availability, without specifying a distinct humidity threshold.

A more sophisticated model evaluating the influence of water on ASR was proposed by Poyet et al. (2006). This model describes the rate of ASR-induced expansion ($\dot{\varepsilon}^{ASR}$) through Equations 2-5 to 2-9. A dimensionless parameter ($A$) is introduced to quantify ASR progression as a function of time ($t$) and the saturation ratio ($Sr$), which is a function of the mass of water per unit volume of concrete ($C$) and the saturated mass of water per unit volume of concrete ($C_{sat}$). The parameter $A$ is formulated based on the value of a constant characterizing the kinetics of ASR ($\alpha_0$), on the minimal ASR advancement needed to initiate swelling ($A_0$, representing the gel volume needed to fill the porous space surrounding the aggregate), on a function ($\beta$) that accounts for the fact that the involved chemical phenomena are limited around residual saturated zones of concrete, and on a function ($\alpha$) that alters ASR kinetics based on $Sr$. Additionally, the model incorporates a parameter $K$ that correlates expansion with reaction advancement, where $\langle X \rangle^+$ represents the positive part of $X$, $Sr_0^\alpha$ and $Sr_0^\beta$ define the thresholds below which $\alpha$ and $\beta$ are zero, respectively, and $m_\alpha$ and $m_\beta$ stand for potential non-linearities in the reaction kinetics.

$$\dot{A}(Sr,t) = \frac{\partial A}{\partial t}(Sr,t) = \alpha_0 \alpha(Sr)[\beta(Sr) - A(Sr,t)] \tag{2-5}$$

$$if \begin{cases} A(Sr,t) < A_0 \rightarrow \dot{\varepsilon}^{ASR}(Sr,t) = \dfrac{\partial \varepsilon^{ASR}}{\partial t}(Sr,t) = 0 \\ A(Sr,t) \geq A_0 \rightarrow \dot{\varepsilon}^{ASR}(Sr,t) = \dfrac{\partial \varepsilon}{\partial t}(Sr,t) = K\dot{A}(Sr,t) \end{cases} \tag{2-6}$$

$$\alpha(Sr) = \left( \frac{\langle Sr - Sr_0^\alpha \rangle^+}{1 - Sr_0^\alpha} \right)^{m_\alpha} \rightarrow 0 \leq \alpha(Sr) \leq 1 \tag{2-7}$$

$$\beta(Sr) = \left( \frac{\langle Sr - Sr_0^\beta \rangle^+}{1 - Sr_0^\beta} \right)^{m_\beta} \rightarrow 0 \leq \beta(Sr) \leq 1 \tag{2-8}$$

$$Sr = \frac{C}{C_{sat}} \tag{2-9}$$

The parameters $\alpha_0$, $A_0$, $K$ in the model proposed by Poyet et al. (2006) must be specifically determined for each case, while the saturation ratio ($Sr$) can be estimated from experimental mass variation recorded data. A parametric study conducted by Poyet et al. (2006) identified optimal values for the parameters as follows $Sr_0^\alpha = 0$, $Sr_0^\beta = 0$, $m_\alpha = 1$ and $m_\beta = 1$. Additionally, Equations 2-5 to 2-9 cannot be solved analytically when $Sr$ changes over time, which means that

Equations 2-5 to 2-9 should be based on the mean value of $Sr$ (represented by $\overline{Sr}$) between two times $t$ and $t + \partial t$, with $t_1$ being a time included in that interval, as presented in Equation 2-10.

$$A(\overline{Sr}, t) = \beta(\overline{Sr}) - [\beta(\overline{Sr}) - A(\overline{Sr})]e^{-\alpha_0 \alpha(\overline{Sr})(t_1 - t)} \quad (2\text{-}10)$$

Recent research by Goshayeshi (2019), building on the framework of Poyet et al. (2006), indicates that humidity influences both AAR kinetics and the final expansion, which can be correlated to the original AAR kinetics equation proposed by Larive (1997). Moreover, the author supports the hypothesis of a minimum humidity threshold that halts AAR development entirely, estimated at 50% relative humidity.

### 2.2.3 Alkali Content

As previously discussed, alkali hydroxides (i.e., $Na^+$, $K^+$ and $OH^-$) present in the concrete pore solution are critical constituents for the initiation and progression of alkali-aggregate reaction (AAR), as established by Fournier & Bérubé (2000). Generally, an increase in the alkali content of the mix leads to an increase in the final AAR expansion, as illustrated in Figure 2-4.

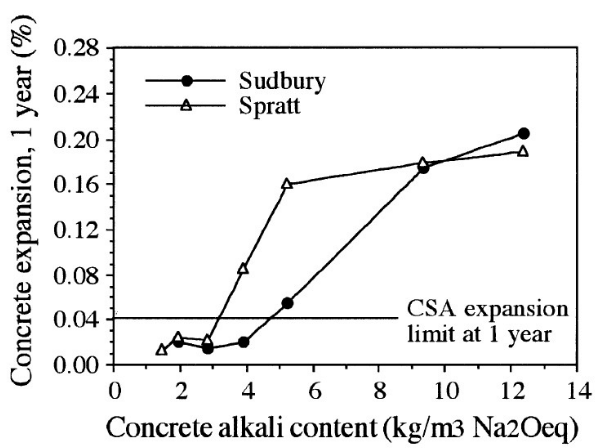


**Figure 2-4. One-year expansions of concrete prisms made with highly reactive Spratt limestone and moderately reactive Sudbury gravel and different concrete alkali contents. Source: Fournier & Bérubé (2000).**

It is noteworthy that, while Portland cement constitutes the primary source of alkalis in concrete, other constituents such as aggregates, water, supplementary cementitious materials (SCM's), special admixtures, seawater, and even de-icing salts can also elevate the alkali content in the concrete pore solution, thereby heightening the risk of AAR-induced distress (Diamond, 1989; Fournier & Bérubé, 2000).

Furthermore, the migration of alkalis through processes such as localized surface evaporation, electric/magnetic fields and currents, or cathodic protection systems can locally increase the alkali concentration in the pore solution. These phenomena contribute to anisotropic expansion in AAR-affected concrete and exacerbate the overall distress of the structure (Fournier & Bérubé, 2000; Moore, 1978; Ozol, 1990; Shayan & Song, 2000).

The semi-empirical model by Goshayeshi (2019) is able to indirectly account for the effect of leaching by increasing the initial value of alkali content, as performed by Gorga et al. (2020). More recently, Nguyen et al. (2022) developed an approach to account for the effect of alkali content and leaching directly. The authors proposed modifying parameters to Larive's equation, introducing the concepts of a "no-leaching" expansion curve that is calculated based on expansion and leaching data obtained from laboratory tests, as shown in Equations 2-11 through 2-17.

$$A = \frac{A_0}{1 - LA} \tag{2-11}$$

$$A_0 = A(1 - LA) \tag{2-12}$$

$$\varepsilon^{\infty}_{no\ leaching} = \varepsilon^{\infty}_{leaching} \frac{k_{\varepsilon,A}}{k_{\varepsilon,A0}} \tag{2-13}$$

$$k_{C,LA} = -1.05LA + 1 \tag{2-14}$$

$$k_{L,LA} = -0.7LA + 1 \tag{2-15}$$

$$\tau_{c,no\ leaching} = \frac{\tau_{c,leaching}}{k_{c,LA}} \tag{2-16}$$

$$\tau_{L,no\ leaching} = \frac{\tau_{L,leaching}}{k_{L,LA}} \tag{2-17}$$

where $A$ is the new calculated alkali content required to compensate for the leaching and to simulate the ideal "no leaching" scenario, $A_0$ is the initial alkali content, $LA$ (%) is the leaching amount measured in one year, $k_{\varepsilon,A}$ is the expansion at infinity parameter for $A$, $k_{\varepsilon,A0}$ is the expansion at infinity parameter for $A_0$, $\varepsilon_{leachin}^{\infty}$ is the original expansion at infinity, $\varepsilon_{no\ leaching}^{\infty}$ is the modified expansion at infinity for the "no-leaching" scenario, $k_{C,LA}$ is the $\tau_c$ modifying parameter for LA, $k_{L,LA}$ is the $\tau_L$ modifying parameter for LA, $\tau_{c,leaching}$ and $\tau_{L,leaching}$ are the original values for $\tau_c$ and $\tau_L$, and $\tau_{c,no\ leaching}$ and $\tau_{L,no\ leaching}$ are the modified parameters $\tau_c$ and $\tau_L$ for the "no-leaching" scenario. Note that the equations for $k_{C,LA}$ and $k_{L,LA}$ were determined through laboratory tests.

### 2.3 AAR-induced expansion development

Several mathematical models have been developed in the past to represent the AAR-induced expansion mechanism. Among those, the model proposed by Larive (1997) is the most widely adopted. This model, represented by an exponential equation shown in Figure 2-5 and Equation 2-18, is able to simulate the primary meso-to-macro-scale stages of AAR expansion ($\varepsilon_{AAR}$). The formulation relies on time ($t$) and three mathematical key variables: characteristic time $\tau_c$, latency time $\tau_l$ , and AAR expansion at infinity $\varepsilon_{AAR}^{\infty}$.

$$\varepsilon_{AAR}(t) = \frac{1 - e^{-\frac{t}{\tau_c}}}{1 + e^{-\frac{(t-\tau_l)}{\tau_c}}} \times \varepsilon_{AAR}^{\infty} \quad (2\text{-}18)$$

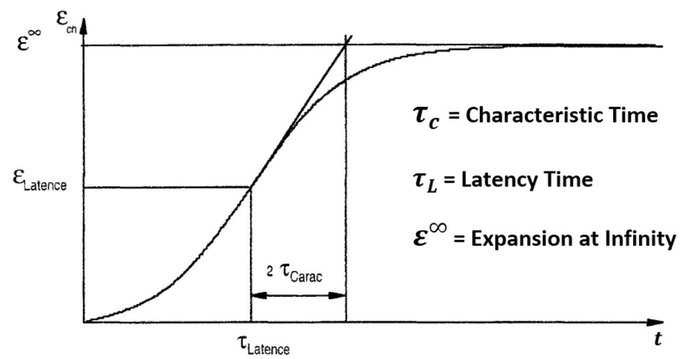


**Figure 2-5. Larive's Equation. Source: Adapted from Larive (1997).**

Even though contemporary models frequently incorporate the equation proposed by Larive (1997) to describe the kinetics of the reaction or its variants with considerable success (Comi & Pignatelli, 2012; Pan et al., 2013; Saouma & Perotti, 2006), Equation 2-18 has one major limitation: the lack of clear physical meaning for its mathematical parameters. In this context, it is very hard to develop an intuitive understanding of the parameter value ranges and their significance.

As an alternative, some researchers have selected a different approach to describe the reaction (Bangert et al., 2004; Capra & Sellier, 2003; Grimal et al., 2008a; Grimal et al., 2008b). Rather than relying on mathematical equations to simulate AAR-induced expansion, they have developed chemical equations based on the consumption of AAR's compounds (i.e., alkalis, silica, water, ions, etc.) to represent the reaction mechanism.

A third, less common approach assumes that AAR-induced expansion progresses linearly over time. Gocevski & Yildiz (2017) applied this assumption in their model of an AAR-affected dam, assuming that the expansion rate remains constant, as variations in the expansion rate over the service life of a massive structure would be negligible

As previously discussed, the most important macroscopic consequence of ASR in concrete is the induced expansion and subsequent development of tensile stresses in the concrete due to gel swelling. Early models treated this expansion as equivalent to a thermal isotropic expansion (Charlwood, 1994). However, recent studies have demonstrated that ASR expansion is anisotropic and closely tied to the local stress state in the affected region (Gautam et al., 2017; Multon & Toutlemonde, 2006; Saouma & Perotti, 2006). Note that the approaches presented below consider only the expansion due to ASR, isolated by deducting the strain generated by the applied mechanical loads (Poisson effect), creep, and shrinkage.

Although Larive (1997) observed stress-state dependency and expansion redistribution in specimens unrestrained in one direction, Saouma & Perotti (2006) proposed one of the first simplified macroscopic models to account for the influence of local stress-state on ASR expansion based on the work of Multon (2003). Their model assumes that when expansion is constrained by compressive stresses, it is redistributed to less-restrained directions according to predefined weights along each principal stress direction. Figure 2-6 illustrates these weights for uniaxial, biaxial, or triaxial stress-state conditions (Saouma & Perotti, 2006), where $\sigma_u$ represents the ultimate stress and $f'_c$ is the concrete's compressive strength. Notably, the model posits that a triaxial compressive stress state reduces, but does not entirely eliminate, the expansion.

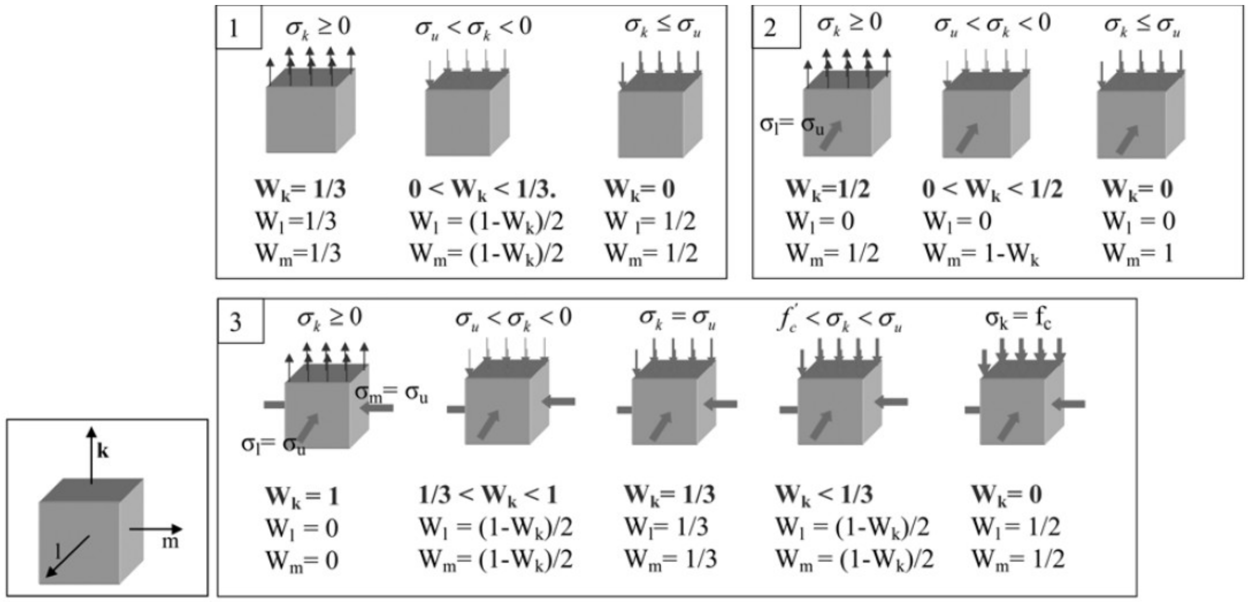


**Figure 2-6. Redistribution weights for uniaxial (1), biaxial (2), and triaxial (3) stress-states. Source: Saouma & Perotti (2006).**

Multon & Toutlemonde (2006) advanced the understanding of the anisotropic nature of ASR-induced expansion by investigating the behaviour of ASR-affected concrete cores under three distinct confinement conditions. The specimens were either unconfined or passively confined by steel rings of two different thicknesses (3 mm or 5 mm) placed radially along the length of the specimen. The applied stresses for each of the 3 confinement cases were either 0 $MPa$, 10 $MPa$, or 20 $MPa$. Based on the experimental data, the authors proposed a relationship as depicted in Figure 2-7, where $\alpha_{ASR}$ represents the ASR anisotropy (ratio between the longitudinal expansion/strain $\varepsilon_{zz}^{imp}$ and the radial expansion/strain $\varepsilon_{rr}^{imp}$), $\sigma_{zz} - \sigma_{mean}$ is the axial stress deviator defined by the axial stress $\sigma_{zz}$ and the mean stress $\sigma_{mean}$, $\sigma_{res}$ is the restraining stress generated by the steel rings, $R_i$ is the internal radius (core radius), and $R_e$ is the external radius (core plus steel ring radius).

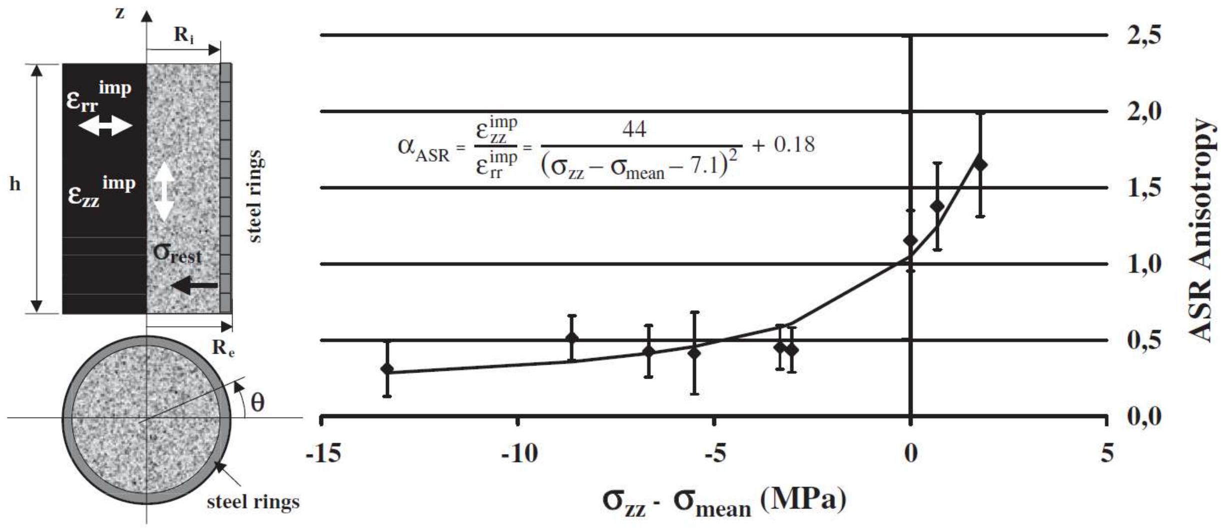


**Figure 2-7. Specimen's set up on the left and proposed ASR anisotropy vs axial stress deviator relationship on the right. Source: Multon & Toutlemonde (2006).**

The results indicate that when the axial stress deviator is negative (i.e., the axial direction is more compressed than the radial direction), axial expansion is reduced while radial expansion is increased. This effect stabilizes at an ASR anisotropy equal to 0.3, suggesting that, regardless of the confining pressure in a given direction, a residual expansion persists along that axis. Likewise, when the axial stress deviator is positive (i.e., the radial stress is larger than the axial stress), the axial expansion is increased while the radial stress is reduced. Multon & Toutlemonde (2006) propose a maximum value of 5 for the ASR anisotropy based on the inverse of the asymptotical coefficient for the negative axial stress deviator. However, it is critical to note that this hypothesis remains unverified under tensile stress conditions, as no such stresses were applied during the experiments.

It is noteworthy that Multon & Toutlemonde (2006) successfully evaluated uniaxial, biaxial, and triaxial stress-state conditions by utilizing the confinement provided by steel rings. However, their study did not encompass biaxial or triaxial stress states with differing stresses along the x and y directions.

A significant advancement was made by Gautam et al. (2017), who conducted experiments at the University of Toronto on 254-mm square concrete cubes, both reactive and non-reactive, as depicted in Figure 2-8a. These specimens were subjected to uniaxial, biaxial, and triaxial stress-state conditions to establish a comprehensive stress-state dependency relationship for ASR expansion. The results, illustrated in Figure 2-8b, demonstrate that varying stress states exert a substantial influence on the magnitude of ASR-induced expansion.

a b

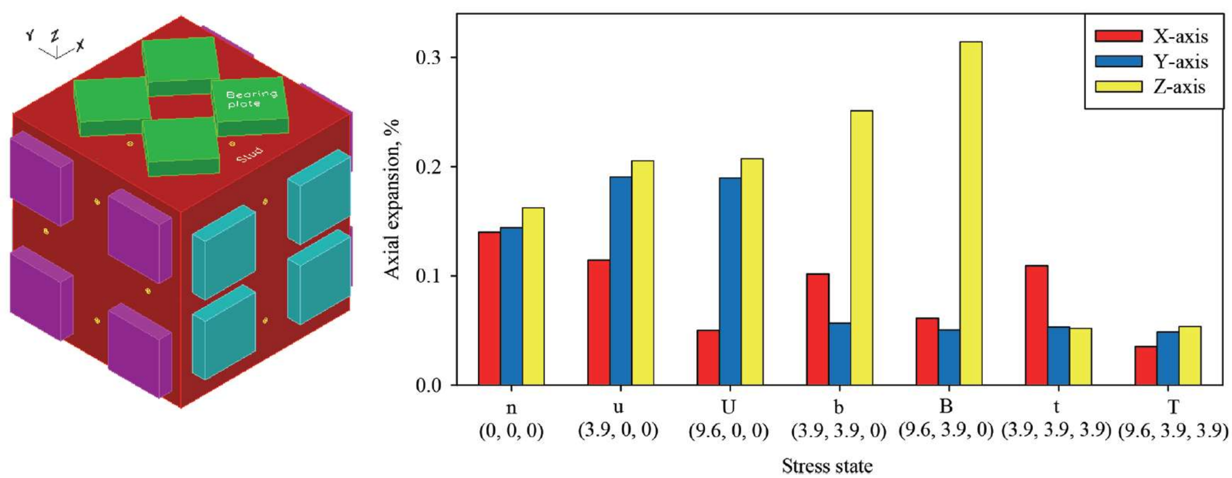


**Figure 2-8. Concrete cube specimen on the left and ASR axial expansion (%) vs stress-state (MPa) on the right. Source: Gautam et al. (2017).**

The authors proposed an S-shaped exponential equation to describe the independent behaviour of the reaction in each direction ($i$) based on the stress ($f$) and on the initial free volumetric expansion ($pe_{free\,vol}$) - equal to 100%, with 33.3% free expansion ($pe_{free\,i}$) in each direction, as shown in Figure 2-9. According to Equations 2-19 to 2-21, their approach suggests that there is an uncoupled strain (independent of the strain in the other directions) and a maximum possible axial strain in each direction, $pe_{un}$ and $pe_{max}$, respectively. If the sum of the $pe_{max}$ across the three principal directions is less than 100%, the expansion in each direction ($pe_i$) is equal to its respective $pe_{max}$. However, if this sum exceeds 100%, the difference between the free volumetric expansion (100%) and the sum of $pe_{un}$ is distributed among the principal directions according to specific weights. These weights are calculated as the ratio between the difference between $pe_{max} - pe_{un}$ in each direction and the sum of $pe_{max} - pe_{un}$. Then, the $pe_i$ equals the sum of $pe_{un\,i}$ and the weighted value of $w_i pe_{max\,i}$.

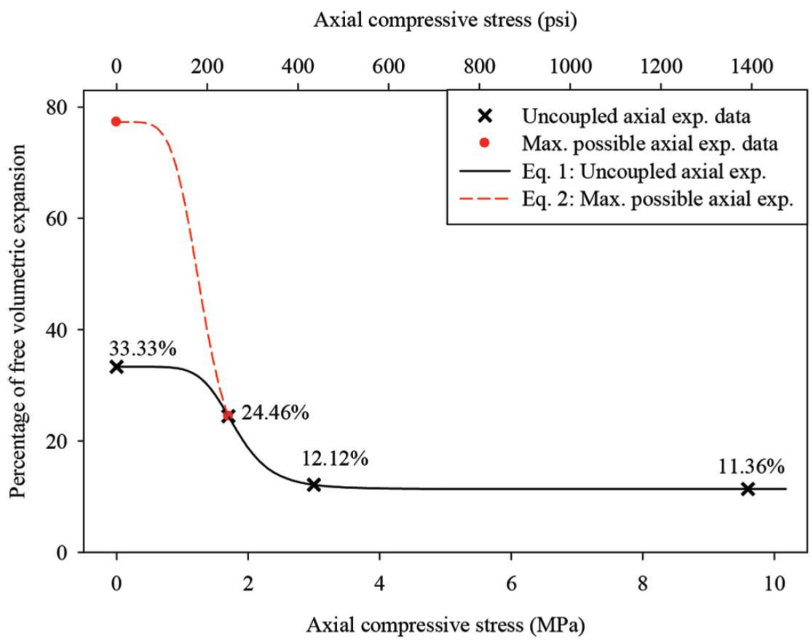


**Figure 2-9. Percentage of free ASR volumetric expansion vs axial compressive stress. Source: Gautam et al. (2017).**

$$pe_{un} = 11.4 + \frac{33.3 - 11.4}{1 + \left(\frac{f}{1.8}\right)^{6.5}} \; for\; f \leq 0 \tag{2-19}$$

$$pe_{max} = 11.4 + \frac{77.2 - 11.4}{1 + \left(\frac{f}{1.3}\right)^{5.4}} \; for\; f \leq 0 \tag{2-20}$$

$$
if \begin{cases} \sum_{i=1}^{3} pe_{max\,i} \leq 100\% \rightarrow pe_i = pe_{max\,i} \\ \sum_{i=1}^{3} pe_{max\,i} > 100\% \rightarrow w_i = \dfrac{pe_{max\,i} - pe_{un\,i}}{\sum_{i=1}^{3}(pe_{max\,i} - pe_{un\,i})} \rightarrow pe_i = pe_{un\,i} + w_i pe_{max} \end{cases} \tag{2-21}
$$

Other researchers have proposed alternative models to describe the stress-state dependency of AAR expansion, ranging in complexity. For instance, Gocevski & Yildiz (2017) assume that the redistribution is a function of the stress at which the confinement starts affecting the expansion and the stress at which it totally prevents the reaction from happening, with a linear variation between the two values. In contrast, Grimal et al. (2008a) and Grimal et al. (2008b) propose a more intricate model, attributing the stress-state dependency of AAR to the swelling anisotropy induced by oriented cracking and the interaction between gel pressure and long-term strain (creep). Despite their differences, all these models consistently demonstrate the highly anisotropic nature of AAR expansion, underscoring that it cannot be accurately represented by an isotropic expansion framework.

## 2.4 Influence of AAR on the affected material's mechanical properties

Crouch & Wood (1990) observed that sound concrete exhibits high compressive strength and modulus of elasticity, but relatively low tensile strength and brittle failure under uniaxial compressive and tensile loads. However, both its ductility and strength in compression and tension are increased when concrete is confined (triaxially loaded), as can happen due to AAR. Furthermore, the material's sensitivity to confinement can be tied to the presence of small defects or microcracks in the composite material. This confinement effect becomes increasingly complex in damaged materials (Crouch & Wood, 1990), underscoring the importance of accurately characterizing the deterioration of mechanical properties due to AAR expansion for the reliable assessment of affected structures (Kubo & Nakata, 2012).

Multiple studies have reported that AAR causes a significant and rapid reduction in the tensile strength and modulus of elasticity of affected concrete, whereas compressive strength is less impacted, exhibiting notable reductions only at high expansion levels (Sanchez, 2014; Smaoui et al., 2004). The Institute of Structural Engineers (IStructE, 1992) notes that the in-service compressive strength of concrete structures typically exceeds the 28-day design value, suggesting that AAR-induced deterioration is generally insufficient to reduce compressive strength below the original design specifications. However, research by Wood & Johnson (1993) and Wood et al. (1989) indicates that this holds true only for low to moderate expansion levels (up to 0.10%). Therefore, concrete subjected to higher expansions has to be carefully assessed as the deterioration of its mechanical properties may pose significant concerns.

Giaccio et al. (2008) identified two key aspects of mechanical property deterioration due to AAR. First, compressive strength is affected across all stages of the reaction, including crack initiation, stable crack propagation, and unstable crack growth, which can be correlated with the microscopic distress features characteristic of AAR damage. Second, the reaction rate, cracking patterns, and resultant deterioration of mechanical properties vary depending on the type and nature of the aggregates used in the concrete mix.

Sanchez et al. (2017) advanced this understanding by investigating the influence of the type/nature of aggregates, along with the compressive strength of the specimen, on the mechanical properties of AAR-affected concrete. The authors found that the modulus of elasticity (Figure 2-10) and tensile strength (Figure 2-11) are more severely impacted than compressive strength, though the latter can still experience significant reductions at higher expansion levels (up to 30%, as shown in Figure 2-12). This reduction in compressive strength was linked to ASR-induced microscopic distress features, which typically originate within the aggregate particles and propagate into the cement paste only at moderate to high expansion levels.

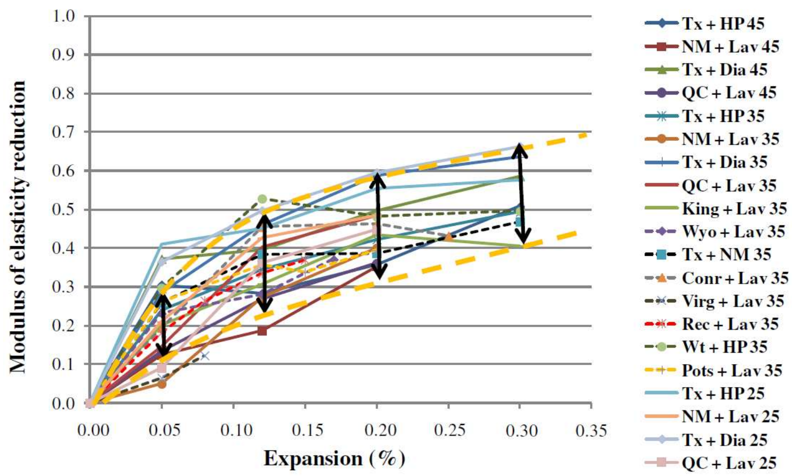


**Figure 2-10. Decrease in modulus of elasticity as a function of AAR expansion. Source: Sanchez et al. (2017).**

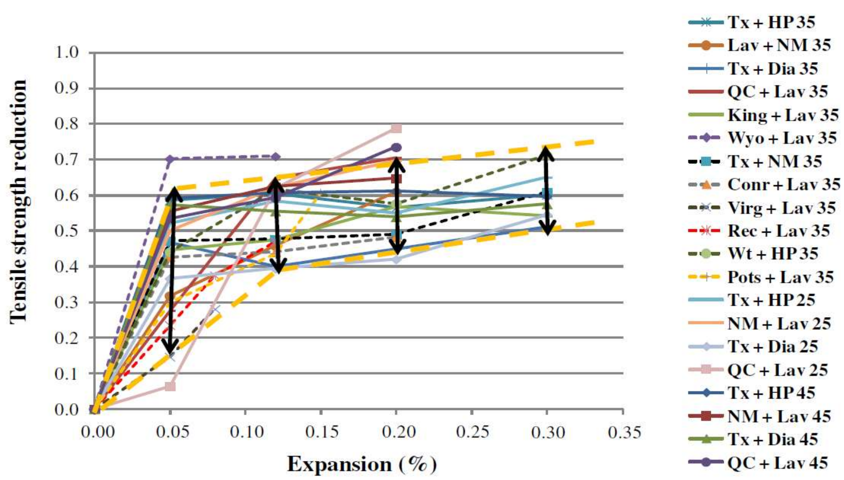


**Figure 2-11. Decrease in tensile strength as a function of AAR expansion. Source: Sanchez et al. (2017).**

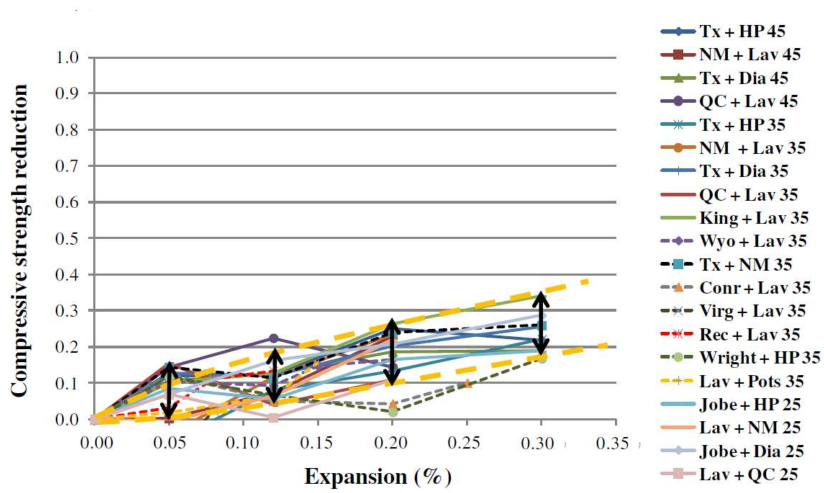


**Figure 2-12. Decrease in compressive strength as a function of AAR expansion. Source: Sanchez et al. (2017).**

The deterioration of concrete's mechanical properties is a critical phenomenon intricately linked to the level of AAR expansion, the type and nature of the aggregate, and the material's compressive strength. While most AAR expansion models account for this deterioration to varying degrees, certain models adopt simplified assumptions, utilizing either the undamaged (design) mechanical properties or the deteriorated (field-tested) properties throughout the entire service life of the structure. Based on the evidence presented, such assumptions are inadequate for accurately predicting the structural performance of AAR-affected systems over time. Specifically, using undamaged properties overestimates performance at later stages, while relying on deteriorated properties underestimates performance at earlier stages.

## 2.5 FE modeling of AAR-affected structures

### 2.5.1 Damage propagation (cracking)

To model structural damage (material nonlinearity) in the finite element (FE) analysis of reinforced concrete structures, a damage propagation approach for the concrete must be defined. These approaches are broadly categorized as either discrete or continuum, as illustrated in Figure 2-13.

Among the continuum approaches, three widely adopted methods are smeared cracking (either fixed or rotated), brittle cracking, and damaged plasticity (Malm, 2016). While the mathematical formulations of these methods vary across different authors, the fundamental principles underlying each approach are outlined below.

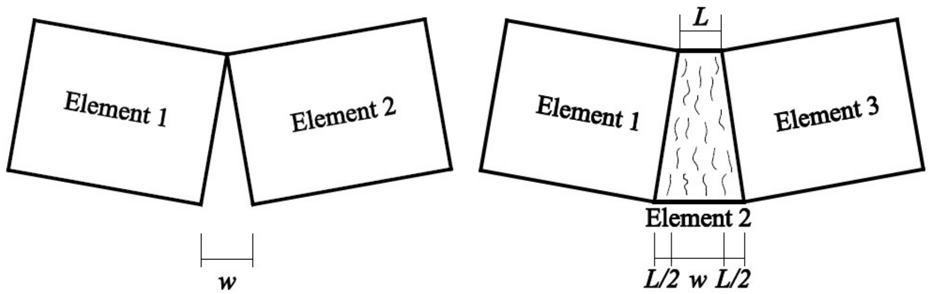


**Figure 2-13. Discrete crack on the left and continuum crack on the right. Source: Malm (2016).**

The discrete crack approach typically initiates at the interface between two adjacent finite elements, where a physical separation representing an actual crack is generated (Malm, 2016). However, due to the diffuse and extensive cracking patterns characteristic of AAR, this method is generally deemed unsuitable for realistically simulating AAR-induced damage.

The smeared cracking approach is the most widely utilized approach, wherein the cracks are not tracked independently, but rather assumed to be a component of the total strain of the element (Malm, 2016). The total strain comprises the elastic strain of uncracked concrete and the plastic strain, which accounts for the nonlinear behaviour of the crack(s). The plastic strain is defined as the crack opening displacement divided by the crack band length. Notably, when the finite element size exceeds the characteristic crack spacing, the cracking strain within that element may represent multiple cracks. However, if the elements are sufficiently small, uncracked elements may exist between cracks, allowing the model to capture the actual crack spacing. Consequently, the accuracy of this approach is highly dependent on the specified mesh size.

In the smeared cracking approach, cracks are assumed to initiate when the principal tensile stress reaches a threshold defined by the “crack detection surface,” which may lie within the biaxial tension region or a combined tension-compression region (Chaudhari & Chakrabarti, 2012). A representative failure surface in the two-dimensional principal stress planes is presented in Figure 2-14. According to Johnson (2006), the formulation usually forces the constitutive calculations (stress and strain) to be performed independently at each integration point, enabling localized reductions in stress and stiffness in the presence of cracks. Furthermore, Chaudhari & Chakrabarti (2012) and Johnson (2006) state that the model is usually capable of accounting for tension stiffening, concrete crushing, tension softening, compression hardening and (in the fixed approach) shear retention. The latter is generally defined using reduction coefficients or predefined nonlinear curves that describe the material’s behaviour, such as stress-strain relationships, stress-displacement responses, or fracture energy-crack opening displacement curves.

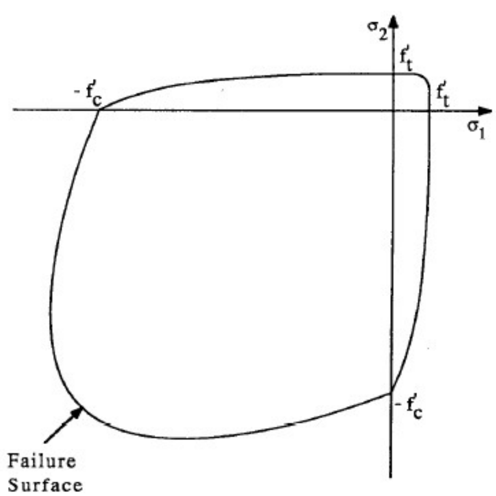


**Figure 2-14. Two-dimensional idealized failure surface. Source: Chaudhari & Chakrabarti (2012).**

The brittle cracking model, as described by Johnson (2006), assumes that concrete behaviour is primarily governed by tensile cracking. Similar to the smeared cracking approach, cracks are modeled in a smeared manner, with post-cracking tension softening defined as a function of either a stress-strain relationship or a fracture energy criterion. However, this model incorporates a brittle failure criterion, whereby an element fails when a predefined number of cracks form, resulting in the complete loss of tensile stiffness for that element. Crack initiation is determined by a specific criterion, such as the Rankine criterion, where cracks form when the maximum principal tensile stress exceeds the concrete's specified tensile strength.

The damaged plasticity approach, sometimes referred to as equivalent plastic strain, models cracks as the plastic component of the total strain within each independent finite element, with mechanical properties reduced according to a defined failure criterion. As illustrated in Figure 2-15 and explained by Wahalathantri et al. (2011), concrete exhibits linear-elastic behaviour until the elastic limit (yield) surface is reached. Beyond this point, nonlinear inelastic behaviour in tension or compression dominates, enabling the model to fully describe the damage characteristics of the material by developing plastic strain locally until global equilibrium is reached. Malm (2016) notes that the reduction in mechanical properties is governed by tensile and compressive damage parameters, which can be conceptually understood as the evolution of damage based on the ratio of the remaining concrete area in tension, as depicted in Figure 2-16. As the load increases, the plastic zone also increases, therefore simulating damage accumulation. Furthermore, the size and orientation of cracks can be qualitatively estimated by analyzing the plastic strain in each element (Malm, 2016). The model also accommodates phenomena such as tension stiffening, concrete crushing, tension softening and compression hardening by specifying a stress-strain relationship, stress-displacement relationship or by applying a fracture energy criterion (Johnson, 2006).

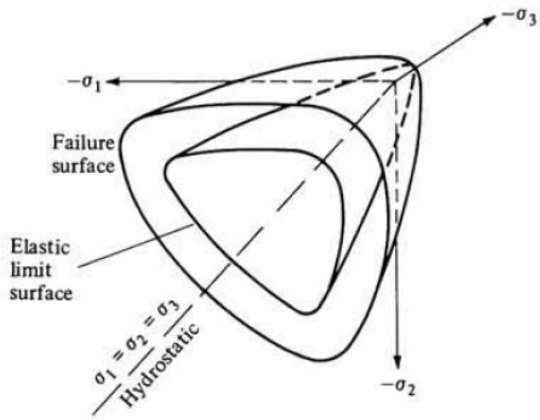


**Figure 2-15. Schematic Failure Surface of Concrete in Three-Dimensional Stress Space. Source: Chen (2007).**

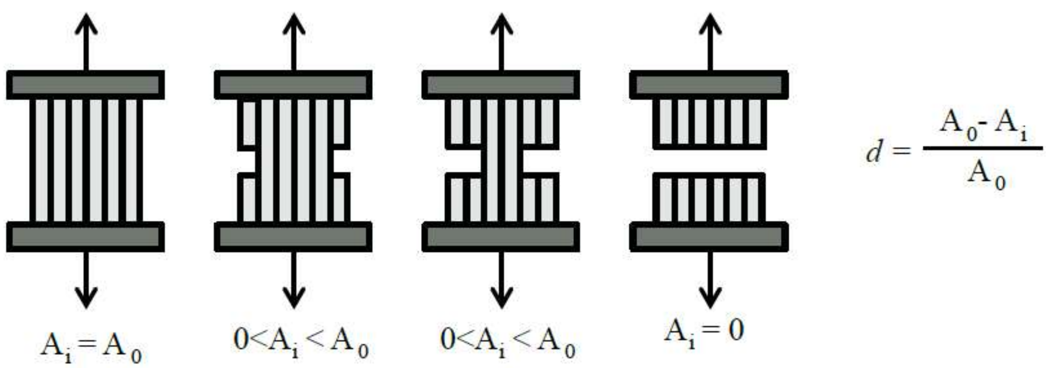


**Figure 2-16. Damage parameter simplified concept. Source: Jirasek (2014).**

A critical feature of the damaged plasticity approach is the viscosity coefficient (rate effect), which is especially important in FE analysis, because it tends to reduce pathological mesh size dependencies. The concrete damaged plasticity model is a local continuum damage model (i.e., strain softening model), which means that the constitutive behaviour at a point is independent of the actions/variables at a distance (neighbouring points). Therefore, when an element undergoes softening, deformation is locally concentrated, leading to the damage to growing only in that point and resulting in further softening. Viscosity counteracts this by increasing the stiffness of the element as the deformation rate increases in the softer (damaged) element, thereby preventing the deformation from accumulating in only one element and facilitating the propagation of damage to adjacent elements (Niazi et al., 2012).

Malm (2016) highlights that a key advantage of material models grounded in fracture mechanics, such as smeared cracking and damaged plasticity approaches, is their reliance on a limited number of parameters. Most of these parameters can be directly correlated to the tangible physical and mechanical properties of the material, thereby enhancing the models' practical applicability.

### 2.5.2 Concrete Material Model

In FE analysis of AAR-affected concrete, macro-models typically discretize concrete as either a porous medium (Grimal et al., 2008a) or a continuous medium (Saouma & Perotti, 2006), each with distinct advantages and limitations depending on their computational implementation.

Porous medium models, as described by Bear & Bachmat (1990), conceptualize concrete as a composite of a solid matrix (also referred to as the solid phase or the skeleton) and void spaces, which may contain single-phase or multiphase fluids (e.g., water, air). In multiphase scenarios, each fluid occupies a distinct portion of the void space, forming a loosely connected matrix of solid material interspersed with pores. The material can be either a connected porous medium, where all pore spaces are connected (Bear & Bachmat, 1990), or a disconnected porous material, where some pore spaces are separated from the remaining regions (Luikov, 1980). However, the microscopic nature of the void's configuration, which influences the fluid flow, heat transfer, chemical reactions, etc., is extremely complex and random according to Bear & Bachmat (1990). Therefore, a continuous porous medium material model is usually implemented in order to allow for an analytical solution (based on differentiable quantities) for the transport phenomena. This means that the material is basically a quasi-homogeneous medium that behaves as a continuum that fills up the entire domain, with each phase occupying its own continuum. This approach sacrifices detailed information about the microscopic configuration of the interface boundary conditions and the actual variation of quantities within each phase, but the macroscopic effect of these factors is still maintained through coefficients, whose structure and relationship to the statistical properties of the different phases configuration can still be evaluated (Amhalhel & Furmański, 1997).

In contrast, continuous medium models assume that concrete completely fills its occupied space without pores or voids, as outlined by Malvern (1969). These models employ continuous functions, ensuring that all derivatives are continuous, allowing classical theories of elasticity, plasticity, fluid mechanics, and thermodynamics to predict behaviour that closely aligns with real-world observations across a wide range of conditions. However, this approach simplifies the material's microscopic structure, rendering it less suitable for certain analyses.

The choice between these two modeling approaches for representing the concrete medium of AAR models remains a subject of ongoing debate within the AAR engineering community. Modeling concrete as a continuous medium simplifies computational implementation and reduces the number of required parameters, but it addresses chemical aspects of AAR (such as gel formation, water absorption, and consumption of alkalis and silica) only indirectly. Conversely, treating concrete as a continuous porous medium allows direct consideration of these chemical processes, but it necessitates the definition of additional parameters, which must be derived from complex experiments, literature, curve fitting, or, in some cases, non-technical assumptions.

### 2.5.3 Creep

Concrete is a visco-elasto-plastic material, meaning that its stress-strain response depends on the rate of loading and on the loading time-history (Collins & Mitchell, 1997; Mehta & Monteiro, 2014). In this context, creep can be understood as an increase in strain when concrete is subjected to a constant stress, which may be generated from mechanical loading, thermal loading, chemical expansion, etc. This strain can be positive or negative, depending on the stress history applied to the member. For example, if a load is sustained for an extended period of time and then removed, the section will experience creep followed by partial creep recovery, as shown in Figure 2-17. Note that part of the creep strain is recoverable, while the other part is irreversible.

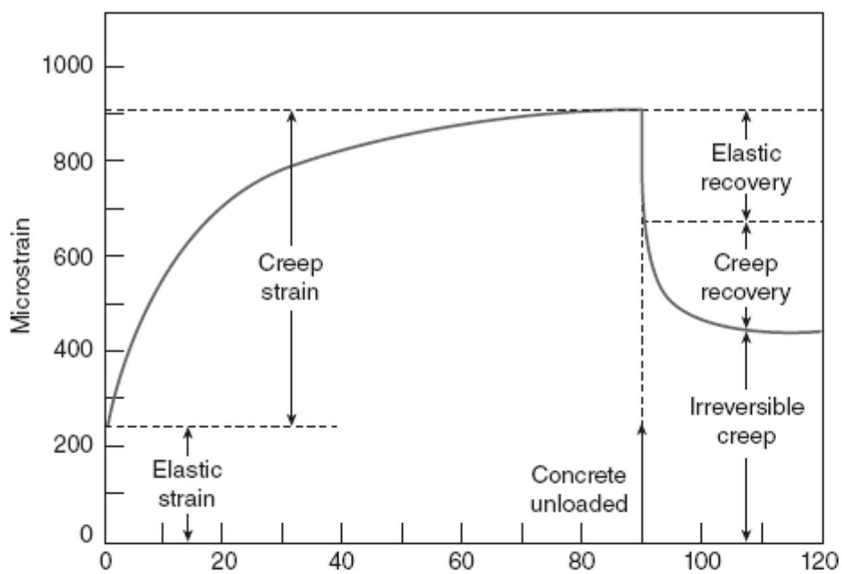


**Figure 2-17. Reversibility of creep – loading and unloading in uniaxial compression. Source: Mehta & Monteiro (2014).**

Creep is a complex phenomenon and is considered to be a function of several parameters, including stress state, temperature, relative humidity, curing conditions, volume-to-surface ratio, concrete strength, strain-softening, concrete mix parameters (aggregate fraction, elastic modulus of the aggregate, cement content, water-cement ratio, and maximum aggregate size), time of loading, and age of concrete (Bazant, 1988; Collins & Mitchell, 1997).

Creep can be divided into two different types: basic creep strain (without drying) and drying creep. However, it is common practice to ignore this distinction and assume that creep is simply the deformation under load in excess of the sum of the elastic strain (and drying shrinkage strain) (Mehta & Monteiro, 2014).

Moreover, the typical creep behaviour can be divided into three stages: primary, secondary and tertiary creep (Figure 2-18) (Yu et al., 2021). In the primary stage, creep strain notably increases while the strain rate remains mostly stable. In the secondary stage, also known as the stable stage, the strain rate is basically constant. Lastly, in the tertiary or accelerated stage, the creep strain increases exponentially with time, ultimately leading to creep failure. In general, creep behaviour is closely linked to the loading level. Below 40% of the concrete strength (linear creep threshold), the relationship between creep strain and stress is linear and satisfies the superposition principle. Between 40 and 70%, non-linear creep characteristics can be observed. Above 70%, creep reaches the tertiary stage.

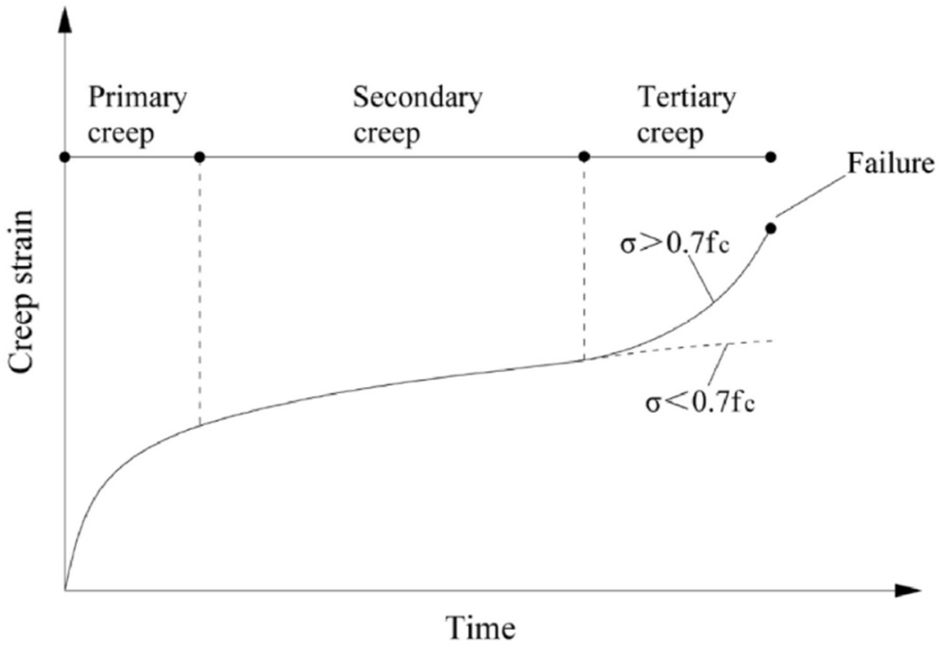


**Figure 2-18. Typical creep evolution curve of concrete under sustained loading. Source: Yu et al. (2021).**

Applying the superposition principle, uniaxial creep can be mathematically represented as a generic function if a stress history is assumed as a succession of infinitesimal stresses ($d\sigma$) applied at time $t'$ (Batista, 1998). This function is often called the creep compliance function $J(t, t')$, and it represents the strain at time $t$ caused by a constant unit stress acting since the loading time $t'$. If the strain is assumed to be composed only of the elastic and creep components, this function can be determined as shown in Equations 2-22 and 2-23.

$$\varepsilon(t) = \int_{t'}^{t} J(t, t')d\sigma(t') \tag{2-22}$$

$$J(t, t') = \frac{1 + \phi(t, t')}{E(t)} \tag{2-23}$$

where $t$ is the total time, $t'$ is the time at loading, and $\phi(t,t')$ is the creep coefficient. Note that, in general, superposition is valid within the service stress range of structures, as strains produced in the concrete body at any time $t$ by a stress increment at any time $t'$ are independent of the effects of any stress applied either earlier or later than $t'$ as long as the stress-strain behaviour is linear (Bazant, 1988; Mehta & Monteiro, 2014). The creep compliance function is often represented as shown in Figure 2-19.

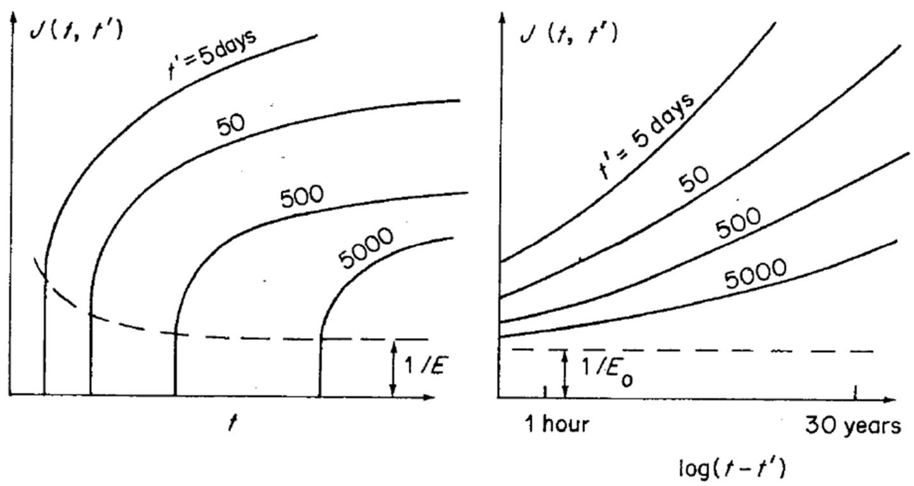


**Figure 2-19. Creep compliance curves for concrete of various ages $t'$ at loading. Source: Bazant (1988).**

The creep coefficient can be obtained directly from laboratory tests, or it can be predicted based on empirical, semi-empirical or analytical equations that try to account for several of the parameters previously described. For example, Collins & Mitchell (1997) state that Equation 2-24 can provide a good approximation of creep strain.

$$\phi(t,t') = 3.5K_cK_f\left(1.58 - \frac{H}{120}\right)t'^{(-0.118)}\left(\frac{(t-t')^{0.6}}{10+(t-t')^{0.6}}\right) \tag{2-24}$$

where $t$ is the number of days after casting, $t'$ is the number of days after casting when concrete is loaded, $H$ represents the relative humidity level, $K_f$ is a factor accounting for concrete strength, and $K_c$ is a factor that accounts for the influence of volume-to-surface ratio of the member.

Note that the inverse of the creep compliance function $[1/J(t,t')]$ is also known as the relaxation function $[E_R(t,t')]$, and it represents the stress at time $t$ caused by a constant strain introduced at time $t'$ (Bazant & Wu, 1974).

Classically, creep has been modeled as a reduction in the modulus of elasticity over time. If the stress is constant (as well as all other parameters affecting the reaction), this approach is relatively simple to implement as it only depends on the analysis time. This has been adopted in Gorga (2018) as a simplified approach to simulate creep according to Equation 2-25.

$$\sigma = \varepsilon E_{eff}(t) = \frac{\varepsilon E_0}{1 + \phi(t,t')} \tag{2-25}$$

where $E_{eff}(t)$ is the effective modulus of elasticity at time $t$, and $E_0$ is the initial modulus of elasticity.

However, properly implementing creep as a strain that takes into consideration the effect of the entire stress-history applied is significantly more complex. In this case, the stress-history can be approximated as a sum of stress increments (Figure 2-20), leading to Equation 2-26 (Batista, 1998).

$$\varepsilon(t) = \sum_{k=1}^{n} J(t,t'_k)\Delta\sigma(t'_k) \tag{2-26}$$

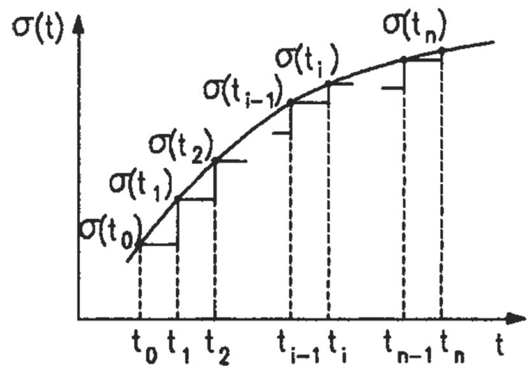


**Figure 2-20. Stress-history as sum of stress increments. Source: Batista (1998).**

Equation 2-26 can accurately predict creep strain, but it requires the entire stress-history to be computationally stored to properly calculate the effect of all the stress increments (Batista, 1998). As the analysis time progresses, the amount of stored data continues to increase, which is not feasible for large-scale simulations.

An alternative to storing all this data is to approximate the calculation of uniaxial creep strain through a series of exponential equations known as Dirichlet series (Batista, 1998; Bazant & Wu, 1973, 1974; Póvoas, 1991). These series make use of Kelvin or Maxwell chain rheological models to represent the visco-elastic behaviour of concrete (Mehta & Monteiro, 2014). In essence, both models comprise several dashpot-spring assemblies in order to capture the variation of strain over time. The spring has an immediate response, whereas the dashpot has a delayed response, leading to the behaviour shown in Figure 2-21. Note that in Figure 2-21 "creep" reffers to constant stress and "relaxation" to constant strain.

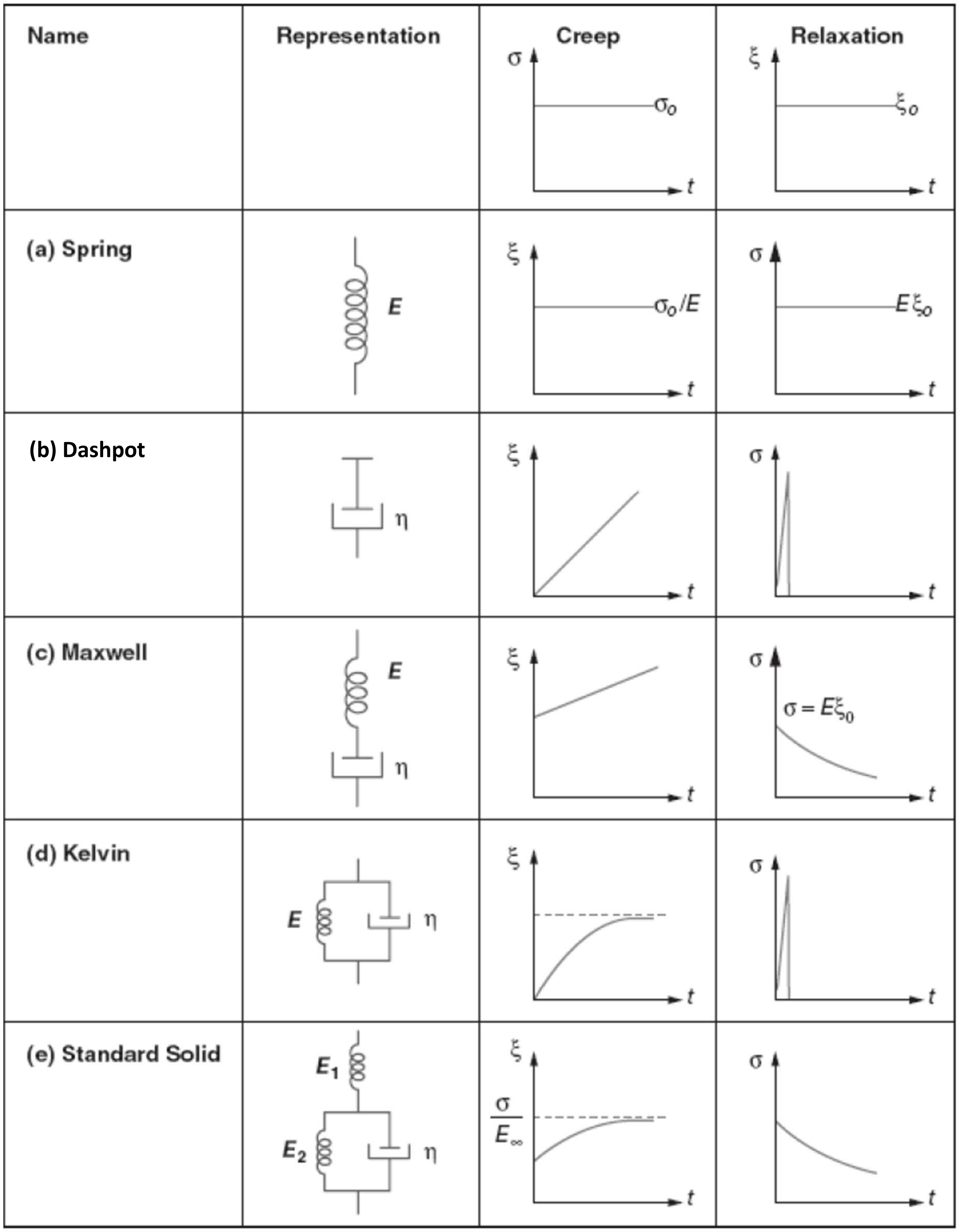


**Figure 2-21. Rheological models and their creep and relaxation responses. Source: Mehta & Monteiro (2014).**

In general, the dashpot can be understood as a piston displacing viscous fluid in a cylinder with a perforated bottom. Then, from Newton's law of viscosity (Equation 2-27):

$$\frac{d\varepsilon}{dt} = \frac{\sigma(t)}{\eta} \tag{2-27}$$

where $d\varepsilon/dt$ is the strain rate, and $\eta$ is the viscosity coefficient (of the dashpot).

From equilibrium, compatibility equations and constitutive relationships, it can be shown that the Kelvin and Maxwell models result in Equations 2-28 and 2-29, respectively. A complete description of the mathematical proof can be found in Mehta & Monteiro (2014).

$$\varepsilon(t) = \frac{\sigma}{E}\left(1 - e^{-E\times t/\eta}\right) \tag{2-28}$$

$$\varepsilon(t) = \frac{\sigma}{E} + \frac{t \times \sigma}{\eta} \tag{2-29}$$

Two important concepts can then be defined. For the Kelvin model, the ratio $\tau = \eta/E$ is known as retardation time, and for the Maxwell model, the ratio $T = \eta/E$ is known as relaxation time. Both characterize how quickly the creep process will be, with small values being related to faster response.

Alone, both rheological models are not able to accurately capture the visco-elastic behaviour of real concrete structures. However, a common strategy to improve their performance is to chain several Kelvin or Maxwell models in series or parallel and also include additional spring components (like the "standard solid" in Figure 2-21).

As shown in Figure 2-22, chaining Maxwell models in series or Kelvin models in parallel does not accomplish anything, as the final equation is the same as that for a single model with $E_i$ and $\eta_i$ values equal to the sum of all individual models. However, chaining Maxwell models in parallel or Kelvin models in series allows the representation of more complex behaviours, as springs and dashpots with different values can be specified at the same time (Figure 2-23). This is especially true if the adopted $E_i$ and $\eta_i$ cover a large range of values.

a b

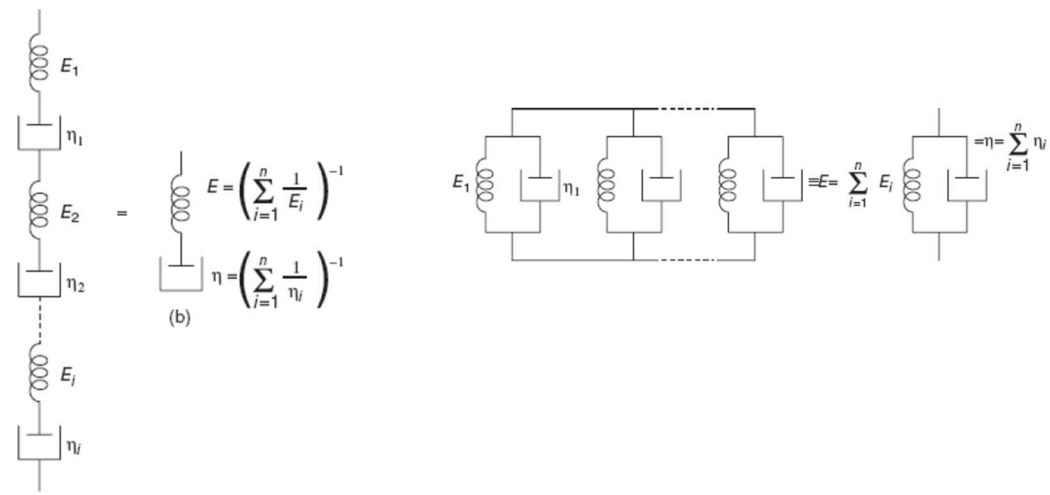


**Figure 2-22. Chain of rheological Maxwell in series on the left and Kelvin in parallel on the right. Source: Mehta & Monteiro (2014).**

a b

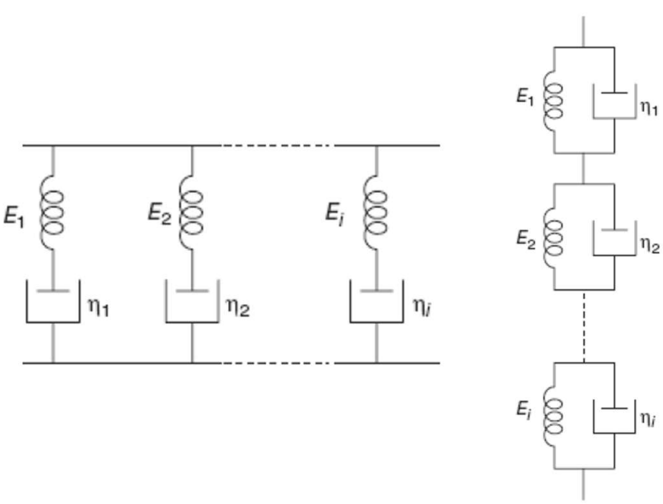


**Figure 2-23. Chain of rheological Maxwell in parallel on the left and Kelvin in series on the right. Source: Mehta & Monteiro (2014).**

When a number N of Kelvin models are assembled in a chain in order to represent a creep compliance curve, the equation for the Dirichlet series (Equation 2-30) is obtained (Póvoas, 1991). Moreover, Figure 2-24 illustrates the physical meaning of this equation, where the gradual contribution of each Kelvin series adds up to a total approximated creep compliance curve. Note that creep compliance curves represent the value for a given value of stress, meaning that the strain calculated through Equation 2-30 is per stress value used to generate the creep compliance curve.

$$\varepsilon(t,t') = C(t,t') = \sum_{i=1}^{N} \frac{1}{E_i(t')} \times \left(1 - \mathrm{e}^{-\frac{(t-t\prime)}{\tau_i}}\right) \tag{2-30}$$

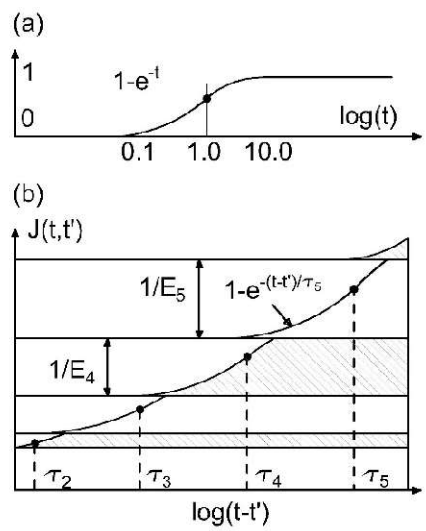


**Figure 2-24. Dirichlet series graphical representation of creep compliance function: a) Curve for a single term and b) Complete curve. Source: Póvoas (1991).**

Even though not described in this document, a similar approach can be performed for chained Maxwell models (Bazant & Wu, 1974). Both have advantages and disadvantages, and both are able to capture the behaviour of concrete creep (Bazant & Wu, 1973, 1974).

Once one (or more) creep compliance curve(s) is (are) known, it is imperative that adequate values of $E_i$ and $\tau_i$ be selected. Batista (1998), Bazant (1988) and Póvoas (1991) describe a simple approach to accurately determine the coefficients for any creep compliance curve(s):

1. Determine the number of time intervals ($n$), time of loading ($t'$) and total analysis time ($t_f$).
2. Define the number ($N$) of Kelvin models that will be in the chain (usually $5 \leq N \leq 8$).
3. Determine the retardation times ($\tau_i$) of the Kelvin chain, keeping in mind that the entire curve must be able to be approximated by the equation. Times logarithmically spaced as shown in Equation 2-31 often produce good results.

$$\tau_i = \begin{cases} \tau_1 = 0.1 & \\ \tau_i = \tau_1 \times 10^{(i-1)} & for\ i = 2, N \end{cases} \tag{2-31}$$

4. Determine the loading ages ($t'_j$), i.e., time since loading has been applied, for the specified values of $n$, $t'$ and $t_f$. Again, times logarithmically spaced are suggested as presented in Equations 2-32 and 2-33.

$$t'_j = \begin{cases} t'_1 = t' & \\ t'_j = t' + 10^{\alpha(j-1)} & for\ 1 < j < n \\ t'_n = t_f & \end{cases} \tag{2-32}$$

$$\alpha = \frac{\log_{10}(t_f - t')}{n - 1} \tag{2-33}$$

5. For each loading age $t'_j$ (for $j = 1, n$), determine the value of $1/E_i(t'_j)$ (for $i = 1, N$) using Equation 2-34.

$$C(t_n, t'_j) = \sum_{i=1}^{N} \frac{1}{E_i(t'_j)} \times \left(1 - \mathrm{e}^{-(t_n - t'_j)/\tau_i}\right) \tag{2-34}$$

6. Ensure that all values of $E_i(t'_j) > 0$ and use the least square method to obtain an approximation of the creep compliance curve to the desired accuracy level.

Results from the previously described procedure can be represented graphically as shown in Figure 2-25.

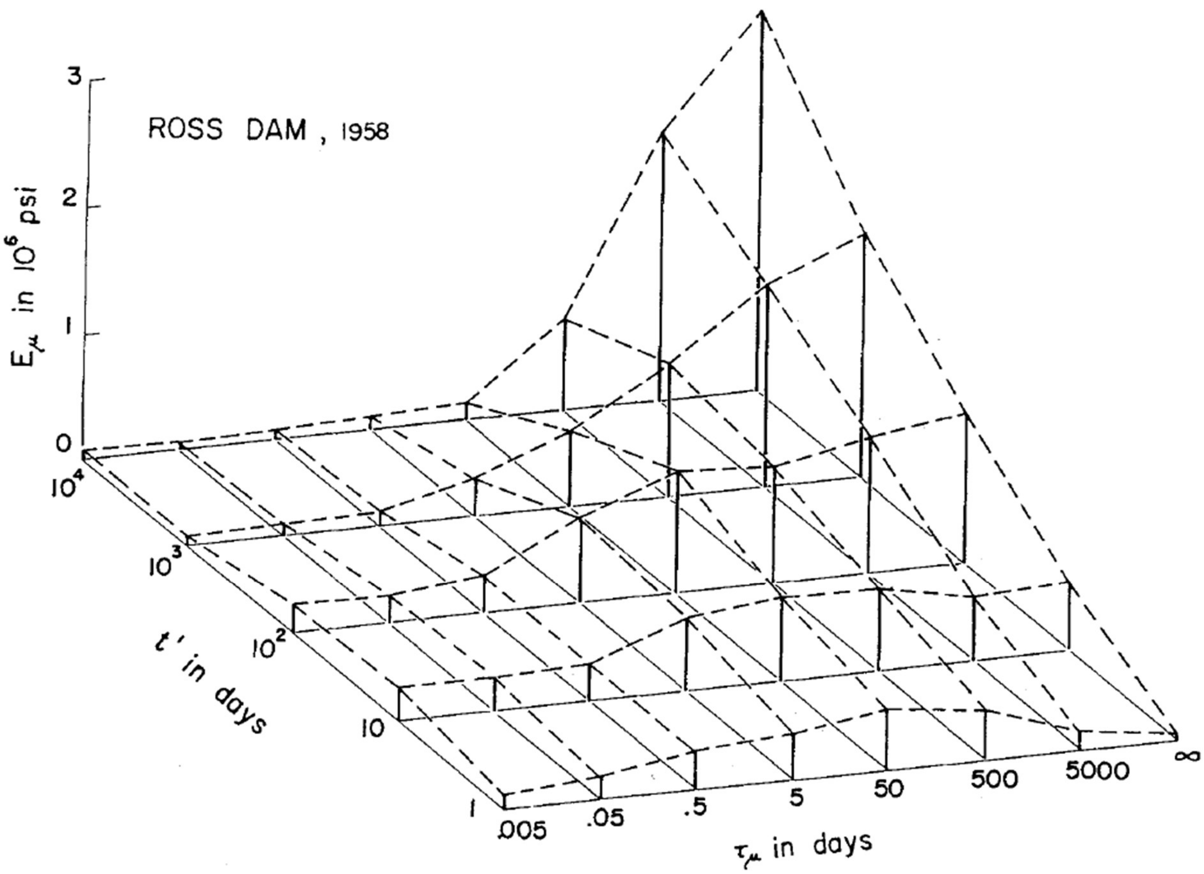


**Figure 2-25. Example of coefficients of $E_i$ and $\tau_i$ calculated for Ross Dam. Source: Bazant & Wu (1974).**

Once the coefficients $E_i$ and $\tau_i$ have been defined and based on the (integral) rectangular approximation of stress increments shown in Figure 2-20, the creep strain at a given time $t_n$ can be given by Equation 2-35 (Batista, 1998; Bazant & Wu, 1973; Póvoas, 1991).

$$\varepsilon_{creep}(t_n) = \int_{t'}^{t_n} C(t_n, t')d\sigma(t') \tag{2-35}$$

Integrating between two time steps ($t_{n-1}$ and $t_n$) and subtracting the two results in Equation 2-36:

$$\Delta\varepsilon_{creep} = \varepsilon_{creep}(t_n) - \varepsilon_{creep}(t_{n-1}) \tag{2-36}$$

As long as the material properties are maintained constant between time increments and the stress variation over the stress-history is constant (i.e., without jumps, which is common for non-cracked concrete), Equations 2-26 and 2-35 can be used to approximate the uniaxial creep strain at time $t_n$ (Equation 2-37) and at time $t_{n-1}$ (Equation 2-38). Note that the distinction between $t$ and $t'$ is neglected in the calculations below for simplicity.

$$\begin{aligned} \varepsilon_{creep}(t_n) &= \sum_{k=1}^{n} C(t_n, t_k)\Delta\sigma(t_k) \\ &= C(t_n, t_1)\Delta\sigma(t_1) + \cdots + C(t_n, t_{n-1})\Delta\sigma(t_{n-1}) + C(t_n, t_n)\Delta\sigma(t_n) \end{aligned} \tag{2-37}$$

$$\begin{aligned} \varepsilon_{creep}(t_{n-1}) &= \sum_{k=1}^{n} C(t_{n-1}, t_k)\Delta\sigma(t_k) \\ &= C(t_{n-1}, t_1)\Delta\sigma(t_1) + \cdots + C(t_{n-1}, t_{n-1})\Delta\sigma(t_{n-1}) \end{aligned} \tag{2-38}$$

By subtracting both equations, it is possible to obtain Equation 2-39, which represents the incremental uniaxial creep strain $\Delta\varepsilon_{creep}(t_n)$ for the time increment $\Delta t_n = t_n - t_{n-1}$. Note that, by definition, $C(t_k, t_k) = 0$.

$$\begin{aligned} \Delta\varepsilon_{creep}(t_n) = {} & [C(t_n, t_1) - C(t_{n-1}, t_1)]\Delta\sigma(t_1) + \cdots \\ & + [C(t_n, t_{n-2}) - C(t_{n-1}, t_{n-2})]\Delta\sigma(t_{n-2}) + C(t_n, t_{n-1})\Delta\sigma(t_{n-1}) \end{aligned} \tag{2-39}$$

Using the Dirichlet series approximation (Equation 2-30) based on the previous time step and making use of the generic mathematic relation presented in Equation 2-40, it is then possible to obtain the equation for uniaxial creep strain increment as shown in Equation 2-41.

$$[C(t_n, t_k) - C(t_{n-1}, t_k)]\Delta\sigma(t_k) = \Delta\sigma(t_k)\sum_{i=1}^{N}\frac{1}{E_i(t_k)} \times \left(\mathrm{e}^{-(t_{n-1}-t_k)/\tau_i}\right) \times \left(1 - \mathrm{e}^{-\Delta t_n/\tau_i}\right) \tag{2-40}$$

$$\begin{aligned}\Delta\varepsilon_{creep}(t_n) = {} & \Delta\sigma(t_1)\sum_{i=1}^{N}\frac{1}{E_i(t_1)} \times \left(\mathrm{e}^{-(t_{n-1}-t_1)/\tau_i}\right) \times \left(1 - \mathrm{e}^{-\Delta t_n/\tau_i}\right) + \cdots \\ & + \Delta\sigma(t_{n-2})\sum_{i=1}^{N}\frac{1}{E_i(t_{n-2})} \times \left(\mathrm{e}^{-(t_{n-1}-t_{n-2})/\tau_i}\right) \times \left(1 - \mathrm{e}^{-\Delta t_n/\tau_i}\right) \\ & + \Delta\sigma(t_{n-1})\sum_{i=1}^{N}\frac{1}{E_i(t_{n-1})} \times \left(1 - \mathrm{e}^{-\Delta t_n/\tau_i}\right)\end{aligned} \tag{2-41}$$

Equation 2-41 can be re-writen in a more concise manner as shown in Equations 2-42, 2-43 and 2-44. When calculating the creep strain increment at time $t_n$ (i.e., $\Delta\varepsilon_{creep}(t_n)$), variable $\varepsilon_i^*(t_{n-1})$ represents the group of interval variables describing the influence of the entire stress history up to the time increment $t_{n-1}$ that will influence the subsequent time increment.

$$\Delta\varepsilon_{creep}(t_n) = \sum_{i=1}^{N}\varepsilon_i^*(t_{n-1}) \times \left(1 - \mathrm{e}^{-\Delta t_n/\tau_i}\right) \tag{2-42}$$

$$\varepsilon_i^*(t_{n-1}) = \varepsilon_i^*(t_{n-2}) \times (\mathrm{e}^{-\Delta t_{n-1}/\tau_i}) + \Delta\sigma(t_{n-1})/E_i(t_{n-1}) \tag{2-43}$$

$$\varepsilon_i^*(t_1) = \Delta\sigma(t_1)/E_i(t_1) \tag{2-44}$$

With this approach, it is then possible to calculate the uniaxial creep strain taking into consideration the entire stress history by only storing the $\varepsilon_i^*(t_n)$ variable. Obviously, this is significantly more computationally efficient than storing the entire stress history, allowing for much more optimized simulations.

In AAR-affected structures, creep is a phenomenon that happens in parallel with AAR-induced expansion. Even though stresses and the consequential anisotropic (stress-state dependent) AAR expansion are not directly related to creep, creep affects the overall behaviour of the structure – mostly displacement and strain. Therefore, from a macroscopic point of view, accounting for creep is important to fully describe the structural response of the system over time.

### 2.5.4 Shrinkage

According to Collins & Mitchell (1997), concrete undergoes a natural process of moisture loss to the surrounding environment over time, resulting in a volumetric reduction unless maintained at 100% relative humidity or submerged in water. This phenomenon, known as drying shrinkage, is influenced by factors such as environmental relative humidity, time, the surface area exposed to drying, the volume of concrete, and the composition of the concrete, especially the amount of water and the type of aggregate (low or high absorptivity). In most standards, drying shrinkage is represented as a negative strain, reflecting the decrease in volume imposed on the structure.

Drying shrinkage can impact AAR development in several ways. Firstly, if differential shrinkage induces sufficient surface cracking, the ingress and accumulation of water from environmental sources such as rain, snow, or splashing may locally accelerate the AAR reaction rate. Secondly, even in the absence of cracking, shrinkage alters the moisture content at the concrete surface, potentially modifying the reaction kinetics in that region. However, since shrinkage is typically more pronounced during the early stages of concrete curing, while AAR often requires several years to generate significant internal stresses, the combined macro-scale effect of these two phenomena appears less critical compared to other mechanisms, such as creep and the deterioration of mechanical properties. This observation is supported by experimental findings from Larive (1997).

## 2.6 Types of AAR models

Esposito (2016) categorizes AAR models into four primary scales: micro, micro-meso, meso, and macro. While various researchers employ different classification criteria, Esposito's (2016) framework is adopted here due to its intuitive and straightforward approach. The following review outlines these categories.

Macro-scale models focus on simulating concrete expansion at the structural level, typically by imposing strains that represent the expansive effects of the AAR gel over time. Early models assumed this strain to be equivalent to isotropic thermal expansion; however, recent studies (Section 2.3) have demonstrated that AAR expansion is anisotropic, with reaction kinetics playing a critical role in its development. These models prioritize the macroscopic impacts of AAR on structural members or systems, such as failure load, reinforcement yielding, cracking, deformation, and effects on serviceability, rather than delving deeply into the chemical processes involved.

Meso-scale models address AAR-induced internal pressure at the material level, treating concrete as a heterogeneous composite comprising aggregates (coarse and fine) and a matrix phase. The matrix is usually assumed to consist of cement paste, occasionally including an interfacial transition zone (ITZ) bonding the aggregates to the paste. In general, expansion is modeled as a direct consequence of the swelling gel, necessitating precise definition of the concrete's microstructure (e.g., volume fraction and shape of aggregates) within a representative elementary volume (REV) and the mechanical properties of each phase. Due to the complex microstructure and physicochemical interactions, meso-scale models exhibit greater variability than macro-scale models.

Micro-meso-scale models describe AAR at the aggregate level as a function of the gel production. These models couple the physicochemical aspects of AAR based on mass or volume change of the gel with the mechanical behaviour of concrete, which is represented as strain or pressure at the aggregate level.

Micro-scale models focus on ion diffusion-reaction mechanisms at the level of chemical reaction products, offering the most detailed approach to modeling AAR chemistry, including silica consumption, alkali consumption, and alkali leaching. While their primary aim is to elucidate the chemical processes leading to reaction product formation, these models have also been applied to analyze the mechanical consequences of AAR at the concrete material level.

## 2.7 AAR macro-models

This section reviews macro-scale models proposed for simulating AAR-induced expansion and damage, with a focus on their overall characteristics. A subsequent section in this chapter addresses models specifically applied to dam structures. A comprehensive summary of the reviewed models is presented in Table 2-1. Only publications post-2000 are considered, as earlier AAR models, such as those by Charlwood (1994), Léger et al. (1996), Huang M. & Pietruszczak S. (1996), Capra & Bournazel (1998) and Malla & Wieland (1999), are deemed outdated due to significant advancements in understanding AAR mechanisms. The model by Grimal et al. (2008a) and Grimal et al. (2008b) discussed in the following section, warrants particular attention. Although classified by Esposito (2016) as a micro-meso model due to its focus on gel production at the aggregate level, it is included here as a potential macro-model, given its successful application to both concrete members and massive concrete structures.

Ulm et al. (2000) were the first to implement Larive's (1997) findings into their model, enabling a more accurate representation of ASR than previously achieved. Despite its advancements, their approach has limitations, including assumptions of isotropic expansion, neglect of creep, constant humidity, and reliance on outdated sources. Nevertheless, it marked a significant milestone in accurately simulating AAR.

The original model developed by Li & Coussy (2002) and Li & Coussy (2004) was able to simulate AAR in three dimensions, but shared similar shortcomings with Ulm et al. (2000). Despite its demonstrated applicability, the failure to account for reaction anisotropy, creep, and variable humidity renders the model outdated for contemporary analysis, particularly in light of current understanding of AAR's physicochemical mechanisms.

Several poromechanical models, proposed by Capra & Sellier (2003), Bangert et al. (2004) and both Fairbairn et al. (2004) and Farage et al. (2004), adopted a different approach by emphasizing detailed physicochemical aspects of AAR, incorporating additional variables. These models employ sophisticated mathematical frameworks but are inherently complex, requiring fitting of multiple parameters to represent micro-scale phenomena at the macro scale. This complexity reduces their user-friendliness and limits their appeal for widespread adoption within the engineering community.

| | | Ulm et al. (2000) | Li & Coussy (2002, 2004) | Capra & Sellier (2003) | Bangert et al. (2004) | Fairbairn et al. (2004) & Farage et al. (2004) | Saouma & Perotti (2006) | Grimal et al. (2008 a, b) | Esposito & Hendrix (2012) | Comi et al. (2012) | Pesavento et al. (2012) | Pan et al. (2013a, b) | Winnicki et al. (2014) | Ben Ftima et al. (2017) | Gocevski & Yildiz (2017) | Gorga et al. (2018) |
|---|---|---|---|---|---|---|---|---|---|---|---|---|---|---|---|---|
| Kinetics | based on Larive | X | X | | | X | X | | X | X | X | X | X | X | | X |
| | based on chemical equations | | | X | X | | | X | | | | | | | | |
| | linear | | | | | | | | | | | | | | X | |
| ASR expansion | Ortho or Anisotropic (stress-state dependent) | | | X | | | X | X | X | | | X | | X | X | X |
| | Isotropic (stress-state independent) | X | X | | X | X | | | | X | X | | X | | | |
| ASR temperature dependency | varying temp over time | X | X | | | X | X | | X | X | X | X | X | X | X | X |
| | constant temp | | | X | X | | | X | | | | | | | | |
| ASR humidity dependency | varying humidity over time | | | | X | X | | | | X | X | | X | X | X | X |
| | constant humidity | X | X | X | | | X | X | X | | | X | | | | |
| mechanical properties | yes - function of ASR expansion or other | | | X | X | | X | X | X | X | X | X | X | | | X |
| | no - undamaged values or field measurements only | X | X | | | X | | | | | | | | X | X | |
| damage propagation (cracking) | smeared cracking approach | X | X | X | | X | X | X | X | X | ? | | X | X | | |
| | damaged plasticity cracking approach | | | | | | | | | | ? | X | | | X | X |
| | brittle model | | | | X | | | | | | ? | | | X | | |
| Concrete material type | Porous media | | | X | X | X | | X | X | X | X | | | | | |
| | Continuous (isotropic or anisotropic) | X | X | | | | X | | | | | X | X | X | X | X |
| Creep | yes | | | | | | | X | | | X | X | | X | | X |
| | no | X | X | X | X | X | X | | X | X | | | X | | X | |
| Shrinkage | yes | | | | | | | X | | | X | | | X | | |
| | no | X | X | X | X | X | X | | X | X | | X | X | | X | X |
| Application | Massive structures | | | | | | | | | | | X | | ? | ? | |
| | Slender structures | | | | | | | X | | X | | | | ? | ? | X |
| | Cores or Specimens | | | X | | X | X | X | X | X | X | X | X | ? | ? | |
| Validation | Massive structures | X | X | | | X | X | X | | X | | X | X | X | X | X[1] |
| | Slender structures | X | X | X | X | | | | | | | | | | | X |
| | Cores or Specimens | | | | X | | | | | | | | | | | X |
| Number of dimensions of the | 3D | | X | | | X | | X | | X | | X | | X | X | X |
| | 2D | X | X | X | X | | X | | X | X | X | | X | | | |

**Table 2-1 – Comparison of existing AAR models**

Saouma & Perotti (2006) developed a macro-scale model for AAR that is widely regarded as one of the most significant contributions to date due to its balance of simplicity, accuracy, and intuitiveness. This model has served as a robust foundation for many subsequent models post-2006. However, it has three primary limitations: it is restricted to two-dimensional simulations, has been applied only to concrete cores, and does not account for creep. Despite these constraints, its importance in the current state-of-the-art remains indisputable.

Grimal et al. (2008a) and Grimal et al. (2008b) advanced the poromechanical approach by comprehensively modeling both the chemical and physical aspects of AAR in detail. Their model accounts for an extensive range of parameters, ranging from the gel volume required to fill porosity associated with reactive aggregates to capillarity effects, but it comes at the cost of defining 32 variables. While this approach has demonstrated its applicability to macro-scale structures, the large number of parameters renders it complex, limiting its widespread validation.

Similarly, the poromechanical models proposed by Esposito & Hendriks (2012) and Pesavento et al. (2012) address numerous critical factors influencing AAR. Both were able to account for a number of important aspects affecting the reaction; however, their primary limitation lies in the lack of extensive validation and practical applications. Both models have been applied only to concrete cores, which is insufficient to fully demonstrate their capability to capture the structural implications of ASR.

Comi et al. (2012) introduced a poromechanical model that is comparatively simpler and more intuitive than other previously discussed models. It incorporates several critical parameters influencing alkali-aggregate reaction (AAR); however, it assumes isotropic reaction behaviour and neglects the effect of creep. These assumptions limit the model's ability to fully capture the distress mechanisms associated with AAR, despite its promising framework.

A highly promising model was proposed by Pan et al. (2013a) and Pan et al. (2013b) , which accounts for nearly all significant aspects of the AAR reaction, except for the influence of time-varying humidity on reaction kinetics and the deterioration of compressive strength. The authors demonstrated the model's applicability, particularly in Pan et al. (2013b). Nevertheless, the model's intuitiveness could be enhanced by assigning physical significance to certain coefficients and incorporating updates based on recent literature, such as advancements in understanding the deterioration of mechanical properties.

The continuous model developed by Winnicki et al. (2014) is also noteworthy but shares limitations with Comi et al. (2012), including the assumption of isotropic reaction behaviour and the omission of creep effects. Furthermore, the model's controversial assertion that ASR may improve the structural response of dam structures contradicts the majority of findings in the literature. Consequently, it can be inferred that this model does not fully capture the structural implications of ASR.

The model developed by Ben Ftima et al. (2017) incorporates all parameters deemed critical for AAR modeling, with the notable exception of mechanical property deterioration as a function of expansion level. However, the model appears tailored specifically to dam structures rather than serving as a general AAR model. Additionally, the authors provide limited details on how these parameters are integrated into the model, making it challenging to fully assess its methodology and the precise manner in which the variables are accounted for in the simulation.

Similarly, the model proposed by Gocevski & Yildiz (2017) is a notable recent contribution. Its assumption of linear expansion is considered valid only for massive structures, which restricts its applicability to other structural types. Moreover, it does not account for creep, and it has its own approach to simulate the anisotropic behaviour of the expansion, which does not exactly follow what has been proposed by other authors when stating, for example, that there is a confining stress capable of completely stopping AAR expansion. Consequently, this model is not regarded as an optimal representation of AAR behaviour across diverse contexts.

A more detailed description of each individual model was presented in Gorga (2018), where the characteristics of each model related to (i) kinetics, (ii) stress-state dependency, (iii) temperature, (iv) humidity, (v) mechanical properties deterioration, (vi) cracking, (vii) concrete material medium (i.e., porous or continuum medium), (viii) creep, (ix) shrinkage, (x) application, and (xi) validation are presented. Note that application refers to analyses that were used to compare the results of the model to measured data (displacements, stresses, strains, etc.) or observed patterns (cracking, failure mechanism, etc.) without the need for fitting parameters to each specific situation. Conversely, validation refers to analyses where results were fitted to match the desired data (for example, several displacements points measured were used to define the kinetics of the reaction and estimate the future behaviour), where results were evaluated through parametric studies of specific coefficients or where results were not compared to any recorded or observed data.

## 2.8 Dam modeling – General assessment

### 2.8.1 Types of dam analyses

According to Malm (2016), there are basically three types of FE analyses conducted on dams: mechanical, transport, and fluid mechanics.

Mechanical analyses examine the structural implications of the dam, i.e., deformations, stresses, strains, etc. Transport analyses approach the variation of temperature, moisture content, and the transportation of compounds or chemicals in dams. Lastly, fluid mechanics study the behaviour of water.

In this literature review, only the mechanical and thermal transport analyses are covered. Moisture transport analyses are not described because they are not the focus of the document and also because they are, up to a certain extent, analogous to thermal transport analyses. Of course, the coefficients have different physical meanings, but computationally speaking, both are transport analyses and can be approached in a very similar fashion. Moreover, the transportation of chemicals and fluid mechanics analyses are out of the scope of this study.

Additionally, Leger et al. (1993) describe two overall approaches for computer simulation of dams, one more complex and one simpler. The complex approach consists of using a (coupled) thermo-inelastic model to simulate the variation of temperature, stresses, strains, and displacements over time. This approach is more precise, but it is also numerically more intensive and it requires a greater amount of detailed historical information about the dam and its material properties, which might not be available.

The simpler approach consists of uncoupled thermal and mechanical analyses. First, a heat transfer analysis is conducted, either as a steady-state or transient analysis, based on the material's thermal properties and on historic environmental conditions. This is used to understand the thermal behaviour of the dam and to obtain values such as the average annual concrete temperature (also known as "stress-free" reference temperature, according to the authors), temperature envelopes (areas with the same approximate behaviour), frost penetration, etc. Next, a structural analysis is performed. Loads (self-weight, hydrostatic, seismic, etc.) and selected temperature fields are applied in order to assess the stress distribution of the dam and the effects of the critical temperature fields. Finally, structural safety evaluation procedures are conducted for the critical cases based on the results obtained.

### 2.8.2 Geometrical model

According to Malm (2016), the FE dam model can be conducted in either two or three dimensions. In 3D, the model can either use solid or shell elements, which allow the structure and its surroundings to be modeled in greater detail. Shell elements are capable of modeling slender dams (buttress dams, for example), and their main advantages are that the analysis is faster and sectional forces can be obtained directly. However, shell elements have the disadvantage of being less precise regarding cracking propagation, and constraining corners can be difficult. Alternatively, solid elements are more numerically costly, but they are capable of modeling any structure, can assess cracking propagation accurately, and are easily constrained.

Another important aspect for 3D dam models is defining the size of the region being analyzed. Malm (2016) states that, as long as the mechanical mode of action or failure mechanism is being captured, symmetry can be used and only part of the dam has to be modeled, which tends to reduce the computational effort. Otherwise, in more complex cases such as arch dams, the entire structure usually must be modeled.

The other viable option is to model the dam in two dimensions and assume plane-strain state. Malm (2016) explains that this simplification should only be adopted if the geometry of the dam is uniform (gravity dams, for example), and discontinuities such as expansion joints are equally spaced and are placed sufficiently far from each other.

It is also important to emphasize the difference between plane stress and plane strain. According to Logan (2011), plane-strain is a state of strain in which the strain normal to the plane considered and the shear strains along the plane are assumed to be zero. For example, in a x-y plane, $\varepsilon_z = \gamma_{xz} = \gamma_{yz} = 0$. This approach is realistic for long bodies with constant cross-sectional areas subjected to load applied only on the x-y plane without variations along z. Conversely, plane stress is a stress state at which the normal and the shear stresses directed perpendicular to the plane are assumed to be zero. It is usually used to model thin elements with loads acting only on the x-y plane.

In some cases, as presented by Malkawi et al. (2003), both 2D and 3D models may provide satisfactory results for the same dam. However, when the geometry is more complex, like the arch dam modeled by Hjalmarsson & Pettersson (2017), a 3D model is usually assumed to be the best alternative.

### 2.8.3 Modeling dam surroundings

Another important aspect is how to model the dam's surroundings, i.e., water, air and rock mass (which can also be understood as the soil or the foundation). As presented by Leger et al. (1993), water and air are usually taken into consideration through boundary conditions, which are capable of representing their thermal and structural implications without having to actually be discretized as elements. However, the same approach is usually not the best alternative for the rock mass.

According to Malm (2016), the rock mass can be modeled in 3 different ways: defined as a boundary condition, using spring elements (or equivalent special-purpose elements) to represent the stiffness of the rock mass, or including a large part of the surrounding rock mass with solid elements.

Malm (2016) states that the use of boundary conditions directly on the dam is usually not adopted because it does not realistically represent most real cases. The only exception is for when the rock surface is irregular (blasted), and it is free of loose particles/dust. It is indeed the least computationally demanding option; however, it usually leads to unrealistic stresses due to the model being stiffer than reality, and it is incapable of assessing the effect of uplift pressure in the base of the dam.

The second alternative is the use of spring elements (or equivalent elements) in order to simulate the stiffness of the foundation, as described by Malm (2016). The author explains that it is relatively simple to define nonlinear properties for the springs and, additionally, this approach allows the analysis to assess both sliding failures (by evaluating the friction in the horizontal direction as a function of the load in the vertical direction) and overturning failures (by defining springs with zero stiffness for tensile loads).

According to Malm (2016), modeling the rock mass with solid elements is a very precise approach, but it is the most computationally demanding alternative. So, a common option that tries to reduce the computational effort and still maintain continuity between the elements of the dam and the rock mass is to discretize the elements close to the dam with a relatively finer mesh and coarser elements further away from the structure. This can be done because the main goal of the analysis is the behaviour of the dam itself, not the foundation far away from it. Also, the author suggests, as good practice, to model the depth of the rock mass with at least the same value as the height of the dam and the length of the rock mass (perpendicular to the stream direction) with at least the same length as the dam. Figure 2-26 illustrates a dam FE model where the rock mass is modeled.

It is also important to emphasize that the necessary boundary conditions should be applied to the edges of the rock mass and that, if sliding stability has to be analyzed when solid elements are being used, friction has to be accounted for. This approach is further described by Malm (2016) and performed by Goldgruber (2015). Note that, in most FE models, friction is taken into account through contact analyses, which are usually very computationally demanding.

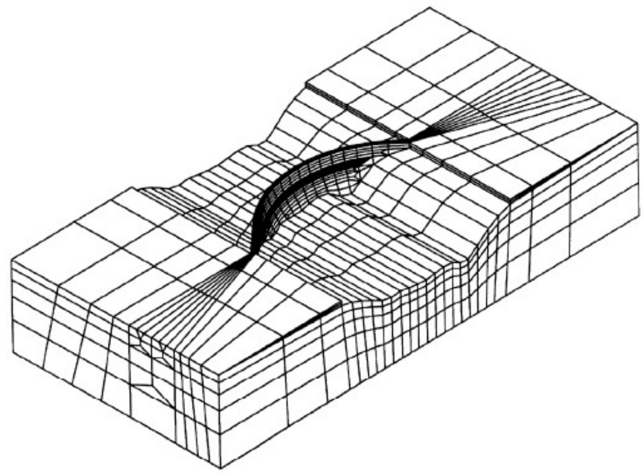

**Figure 2-26. Dam modeled with its surroundings. Source: Malla & Wieland (1999).**

### 2.8.4 Modeling dam joints

According to Malm (2016), the behaviour of joints and the interactions between joint and their surroundings may influence the response of the dam. The five most common types of joints are foundation contact, contraction joints, construction (or lift) joints, existing cracks on deteriorated dams, and rock fractures. Figure 2-27 illustrates three failure modes due to problems related to joints: contraction joint openings, construction (or lift) joints sliding relative to each other, and cracks due to the inexistence (or erroneous design) of contraction joints due to thermal effects.

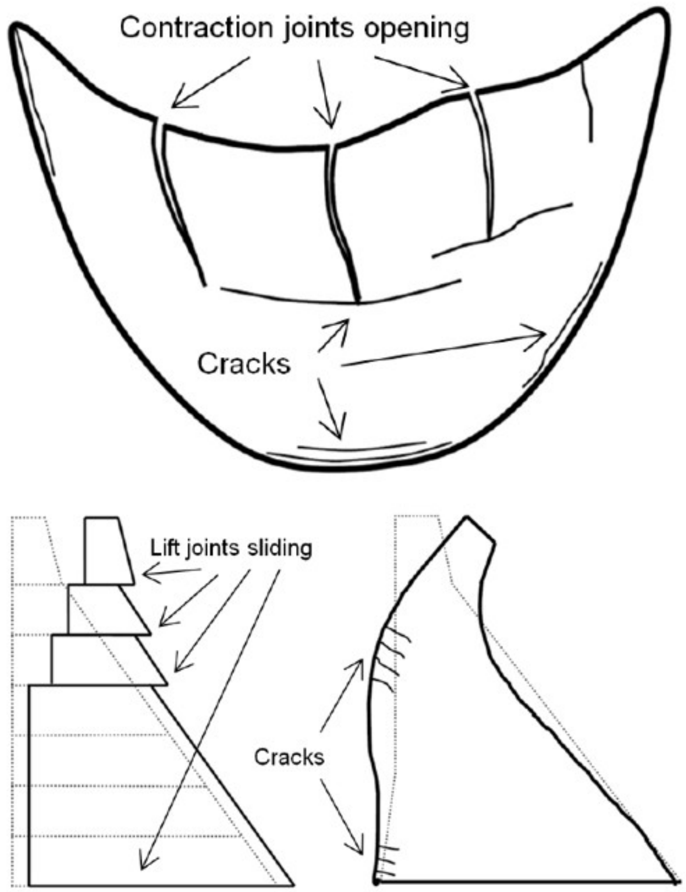


**Figure 2-27. Failure modes due to problems related to joints. Source: ICOLD Technical Committee A (2022).**

Malm (2016) states that foundation contact refers to the interface between concrete and the irregular shaped rock mass, which usually contains a significant amount of rock bolts. The possible approaches to model this type of joint have already been discussed.

According to the author, contraction joints are designed to allow relative movement between different monoliths due to shrinkage, thermal expansion, ASR, etc. Since these joints are not designed to transmit any forces, they are usually chosen as the location of the boundary conditions. However, special attention should be taken in arch dams because these joints are usually modeled as shear keys, which results in high shear resistance in the stream direction but no (or almost no) tensile forces and low shear resistance in the vertical direction.

Goldgruber (2015) performed a study that illustrates the influence that different methods of assessing contraction joints have on the stress field of an arch dam. He compared 4 cases: (a) no contraction joints (isotropic and monolithic structure), (b) indirectly accounting for contraction joints (orthotropic material with different properties in the tangential, radial and vertical directions), (c) contraction joints modeled as separate columns without interaction between them, and (d) contraction joints modeled as separate columns with interaction describing friction and hard contact that allows for separation in the normal direction. Figure 2-28 illustrates the vertical stress fields (in MPa) calculated for all cases.

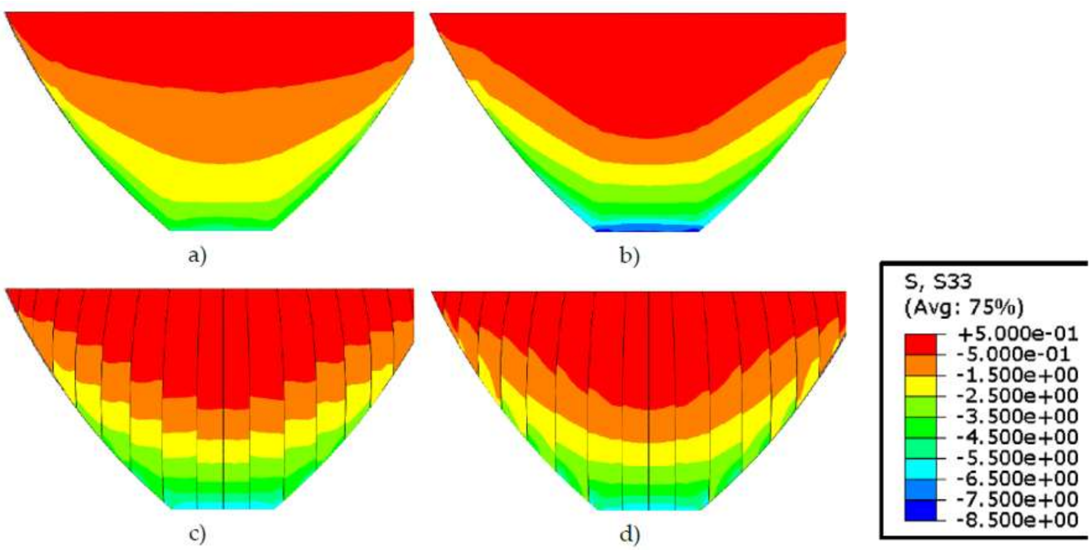


**Figure 2-28. Modeling contraction joints (vertical stresses in MPa) – a) isotropic material (no contraction joints), b) orthotropic material (indirect approach), c) separate columns without interaction between them and d) separate columns with interaction between them. Source: Goldgruber (2015).**

Case (a) is the most common approach in the literature, but the final results are not precise because stresses between columns are fully transferred.

Case (b) yields overall good results, but it tends to overestimate the stresses near the upstream toe. The basic concept is to only attribute values to the material properties in the relevant directions and a residual (1% of original) value on the others. For example, the modulus of elasticity is equal to 1% in the tangential direction and takes the original value in both the vertical and radial directions. Also, Poisson's ratio is equal to the original value in the tangential direction and residual in the other directions. Lastly, the shear modulus is assumed equal to its original value in the tangential direction and reduced in the other directions.

Case (c) is also widely used and yields good results even though it displays some discontinuities between columns. However, it is usually limited to linear analyses because of the superposition technique used in the model, where the results of even and odd numbered columns are calculated in different time steps and then added together, which is not valid for non-linear analyses.

Case (d) is the most accurate because it describes the model in greater detail, and it is the most realistic approach. Therefore, the author recommends this alternative even though it is the most computationally demanding.

Construction joints are usually designed to be load carrying (i.e., reinforcement bars crossing the joints), and the structure can usually be assumed to be monolithic if this is the case (Malm, 2016). However, if the construction joints are expected to weaken the dam and act as possible failure planes, their structural effect can be assessed by either reducing the material properties values close to the interface or by defining discrete cracks at the region of the lift joints and using a contact formulation to describe cohesion and friction.

The author also states that existing cracks can form potential failure planes or propagate through the structure due to external loads, which increases the likelihood of the development of a failure plane. Cracks can be modeled using a discrete approach for the crack itself, similar to what was described for construction joints, and the appropriate formulation for the uncracked region.

Rock fractures can potentially form sliding surfaces. According to Gustafsson et al. (2008), there are three types of failure modes used to categorize failure in the rock: failure in the contact between concrete and rock, failure along a fracture plane or other source of weakness within the foundation, and failure in the rock mass. As per Malm (2016), rock fractures can be modeled in a similar manner as contraction joints or existing cracks, with the addition of a coefficient of friction.

### 2.8.5 Dam loads

There are numerous loads acting on dams under service conditions. According to USACE (1995), the most important loads are self-weight, water pressure, uplift pressure, silt pressure, wave pressure, ice pressure, thermal loads, and seismic loads. Figure 2-29 illustrates the distribution and orientation of the loads.

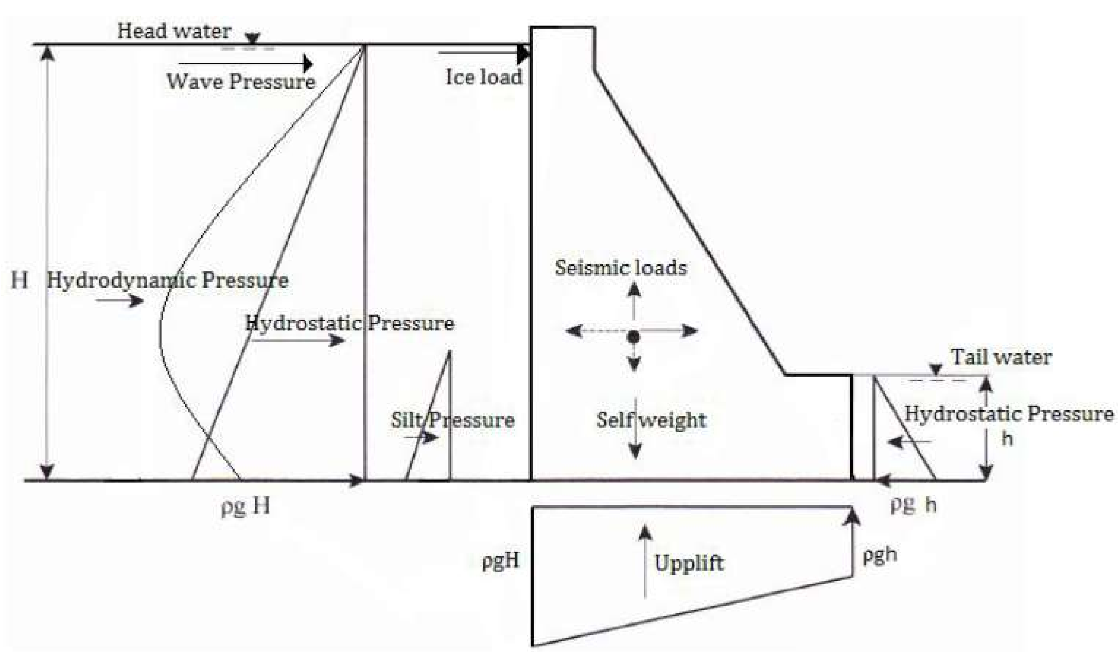


**Figure 2-29. Loads acting on dams. Source: Alsuleimanagha & Liang (2012).**

Self-weight load, also known as dead load, is simply the weight of the structure acting on its center of gravity (USACE, 1995). It is usually one of the major resisting forces on dams.

Water pressure may act only on the upstream or on both the upstream and the downstream of the dam (USACE, 1995). Considered to be the major overturning load, it is a consequence of the weight of the water acting on the structure (hydrostatic pressure). According to Malm (2016), the load should be applied to the dam and the rock mass based on the highest elevation that the water is normally stored at. Also, it can be applied to the model as either a pressure load (simpler alternative) or based on a pore pressure distribution through a transport analysis. The second approach is more complex because it requires a totally different analysis to calculate the necessary values, but it is more accurate and it provides the uplift pressure automatically.

Uplift pressure, also known as internal hydrostatic pressure, is the upward pressure caused by the water that seeps through the dam body or its foundation (USACE, 1995). Malm (2016) states that the load is usually applied to the model as pressure load. However, this approach means that the uplift pressure is not dependent on joint openings (cracked based analysis) between the concrete and the foundation, which might lead to an underestimation of the uplift pressure and incorrectly maintain the resultant force far away from the downstream. Therefore, in certain cases, more detailed analyses like those proposed by FERC (2002), USBR (2006) or McKay & Lopez (2013) may be necessary.

Silt pressure or earth pressure is the load on the upstream face resulting from the weight of settled sediments (USACE, 1995). The measurement of suspended sediments usually indicates the probability of accumulation of settled sediments, which can be defined either as active, passive or at rest depending on the lateral deformation of the structure (Malm, 2016).

Wave pressure is mainly a function of the wind velocity and extent of the reservoir (USACE, 1995). It acts at the top of the upstream face, and the most important aspect related to this type of load is to determine the height of the waves in order to prevent over topping caused by wave splashing.

Ice pressure is the load resulting from the volumetric expansion of the ice caused by temperature variations (USACE, 1995). It acts at the top of the upstream face (global effect) or in localized areas (i.e., between dam pillars, at gates, etc.), and it only happens in cold climate regions (Malm, 2016).

Thermal load is the result of differential or restrained volumetric expansions in the dam due to temperature variations (USACE, 1995). During construction, the main source of heat is the concrete itself (concrete hydration is an exothermic phenomenon). However, during the service life, the main source is the reservoir on the upstream face and the sun radiation on the downstream face.

Seismic load is a result of the vertical, horizontal, or vertical and horizontal ground acceleration (USACE, 1995). When the acceleration is horizontal, the seismic load can be decomposed in two components acting on the opposite direction of the acceleration: the dynamic force acting on the dam structure due to its inertia, and the hydrodynamic load acting on the upstream face due to the acceleration of the water of the reservoir. When the acceleration is vertical, the main consequence is a variation (increase or decrease) in the unit weight of the water of the reservoir and the dam`s body.

Additionally, Malm (2016) states that there are less common loads that might have to be taken in consideration in specific cases. Examples are wind load, traffic load, loads due to explosions and impacts, concentrated forces due to gates or generator in the powerhouse, prestressed tendons, effects of the construction process, etc.

Depending on the goal of the analysis, not all the loads described must be considered. Therefore, a careful assessment of the local conditions in extreme and regular load conditions, as well as an understanding of the goal of the model, are required to decide what loads should be included.

### 2.8.6 Dam thermal assessment – Steady state vs transient analyses

If thermal analyses are to be conducted, the model has to be calculated as either steady-state or transient. According to Karwa (2017), heat flows by conduction from the higher temperature to the lower temperature point. If the equation governing the variation of temperature is only a function of the space coordinates, the analysis is referred to as steady-state. Otherwise, if it is a function of both the space coordinates and time, the analysis is transient.

As demonstrated by Malkawi et al. (2003), a coupled transient thermal-structural analysis requires additional parameters compared to simple structural analyses. The most important are the convection coefficient for both air (based on the wind speed), the water and rock mass, the coefficient of thermal expansion, the initial temperature of all components, the specific heat, and the thermal conductivity. Additional parameters that might be required are the solar energy absorption coefficient, the solar absorptivity of the surface, the total amount of solar energy reaching the surface, the thermal radiation coefficient, and the emissivity (Leger et al., 1993).

### 2.8.7 Dam thermal assessment – Influence of temperature

Different types of dams present different thermal behaviours. A more massive type of dam, as concrete gravity dams (which are usually built using rolled compacted concrete - RCC), generates a large amount of heat due to cement hydration and may take a long period of time to stabilize the internal temperature, as shown by Malkawi et al. (2003). Figure 2-30 illustrates that the effect of the environmental conditions is greater in regions closer to the external surface of the dam (i.e., 7 m deep from the surface) compared to regions further away from the surface (i.e., 14 m deep from the surface).

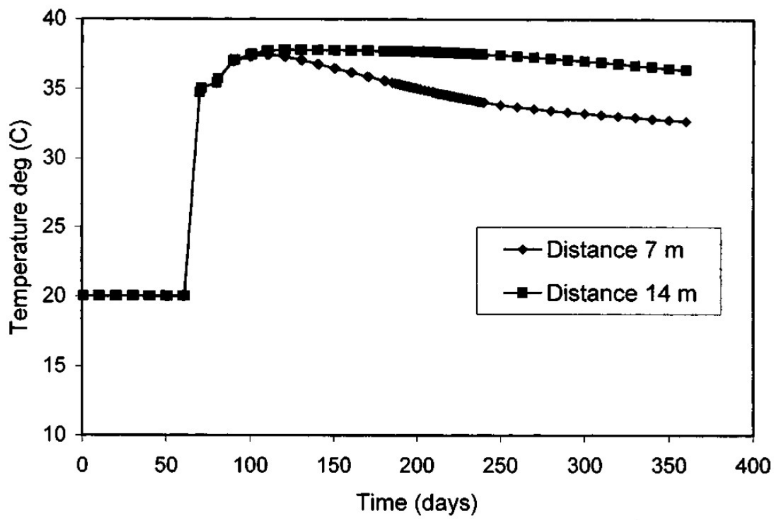


**Figure 2-30. Temperature variation over time in a gravity dam at points close (7 m deep) and further away (14 m deep) from the surface. Source: Malkawi et al. (2003).**

Conversely, the internal and external temperatures of slenderer dams, like arch dams or buttress dams, are very dependent on the external conditions, as presented by Hjalmarsson & Pettersson (2017).

According to Malkawi et al. (2003), in gravity RCC dams, the reduction of temperature over time is associated with two types of cracking: surface gradient and mass gradient cracking.

Surface gradient cracking is usually observed when the reservoir is first filled. The water in contact with the dam body cools the surface, which generates a thermal gradient between the lower temperature of the surface and the warm core. The thermal gradient builds up non-uniform surface thermal tensile stresses, therefore leading to localized cracking. In general, this type of damage is not considered a structural problem unless the cracks extend through to the drainage gallery.

Mass gradient cracking tends to happen well after the building stage is over. The cooling of the central mass of the dam reduces its volume, which might lead to cracking through the body of the dam if the volume variation is restrained (as it usually is because of the rock foundation).

Cracking is a serious problem in dams because it doesn't only reduce the leak-tightness of the structure and increase the hydraulic pressure within the dam, but it also reduces the modulus of elasticity and it might compromise the dam's stability (Malm, 2016).

Malkawi et al. (2003) state that, in general, the temperature distribution through the dam and its evolution with time are a function of the concrete material properties (thermal conductivity, specific heat, etc), climatic factors, construction procedure, thickness of lifts, initial temperature of lifts, and interval between successive placements. Moreover, for the specific case of RCC, the most influential parameter is the temperature of the concrete aggregates, especially because low volumes of water are used in this construction method.

According to Cotoi (2015), the seasonal changes in temperature of the air and of the water in the reservoir propagate only 5 to 6 meters from the face of the dam. Moreover, the daily variation of temperature affects only the first 20 to 30 centimeters of the dam body. Therefore, the author concluded that both seasonal and daily variations are either too small to induce significant volumetric changes in the dam or are absorbed by the contraction joint, which means that the horizontal movement is negligible. However, they are large enough to induce secondary (tensile) stresses, which may lead to the development of progressive deterioration (cracking). Additionally, Leger et al. (1993) state that seasonal thermal stresses have been linked to long-term degradation of mechanical properties (compressive strength and modulus of elasticity) in dams located in northern regions.

Hjalmarsson & Pettersson (2017) also emphasize that non-linear analyses are always history-dependent, which means that the structural implications of a cold year followed by a warm year might not be the same as of a warm year followed by a cold year, for example. Therefore, available data should be gathered and carefully analyzed prior to the development of the model in order to properly assess the dam.

Lastly, depending on the accuracy level required for the analysis, minor factors influencing the thermal analysis can be included. For example, Hjalmarsson & Pettersson (2017) state that snow might act as an insulating layer over the soil or the dam during the winter months and that the temperature of the water of the dam can be assumed to vary with depth. Leger et al. (1993) mention that the latent heat of fusion of water in the soil (energy gain/release to change from solid to liquid or liquid to solid state) affects the depth of frost penetration.

### 2.8.8 Dam thermal assessment – Boundary conditions

As presented by Hjalmarsson & Pettersson (2017), all external faces of the FE model have to be either in contact with air, in contact with water, in contact with the rock mass or insulated. If the soil around the dam is being modeled, it is important to notice that the convective heat coefficient values between either water or air and the soil/rock are likely not the same as the values between water or air and concrete.

According to Leger et al. (1993), the concrete-air heat transfer is defined by three parameters: the heat flow from the sun, convection (gain or loss of heat to surroundings) and radiation (electromagnetic heat loss or gain). The values of these parameters are mostly influenced by the air and concrete temperatures, wind speed and solar radiation intensity. Note that due to the sun's radiation, the concrete surface is usually warmer than the air.

The authors state that the amount of non-reflected solar energy $q_s$ $[W/m^2]$ absorbed by the dam is given by:

$$q_s = aI_t \tag{2-45}$$

where $a$ is the solar absorptivity of the surface, and $I_t$ is the total amount of solar energy reaching the surface.

Also, Leger et al. (1993) affirm that Newton's law of cooling is capable of describing convection ($q_c$), which can be understood as the heat gain or loss to the surroundings as a result of temperature differences between the dam and the surroundings.

$$q_c = -h_c(T_a - T) \tag{2-46}$$

where $h_c$ is the convection coefficient $[W/m^2K]$, $T$ is the temperature of the surface [K], and $T_a$ is the surroundings temperature [K].

Moreover, the surface of the dam releases electromagnetic radiation (thermal radiation, referred to as $q_r$) if the dam and the surroundings are not at the same temperature. According to the authors, this phenomenon can be calculated by the Stefan-Boltzmann law:

$$q_r = -eC_s(T_a^4 - T^4) \tag{2-47}$$

where $e$ is the emissivity of the surface, and $C_s$ is the Stefan-Boltzmann constant $(5.669 \times 10^{-8} W/m^2)$.

Alternatively, assuming that within the range of temperature differences between the air and the concrete surface, heat loss by radiation is small, the equation can be expressed in the quasi-linear form presented below, according to Mirambell & Aguado (1990) and Elbadry & Ghali (1983):

$$q_r = -h_t(T_a - T) \tag{2-48}$$

where $h_t$ is given by:

$$h_t = eC_s(T_a^2 + T^2)(T_a + T) \tag{2-49}$$

According to Leger et al. (1993), the presented equations can be assumed to apply at all interfaces (i.e. concrete-air, concrete-water and concrete-foundation), or concrete may be assumed to be at the same temperature as the air, water or foundation rock in each interface. However, it is important to emphasize that the second approach implies that thermal radiation and convection would not occur, which is only a valid assumption if the thermal gradient is assumed to be very small.

Malm (2016) states that, if nodal temperatures are defined instead of convective boundary conditions, the interface between two prescribed temperatures would display unrealistic sharp variations in temperature and, probably, result in unrealistic stress concentration. Therefore, applying convective boundary conditions is usually recommended.

Additionally, Leger et al. (1993) emphasize that after the heat of hydration has dissipated, the temperature is governed by the cyclical boundary conditions. Therefore, the initial temperature of the body should be realistic and as close to the final reference temperature as possible to speed up the convergence of the solution. If the conditions of the material during the construction are not available, the reference final temperature can be estimated as the weighted average of the temperature of the elements as a function of their volume for a thermal steady-state analysis, where the boundary conditions are the mean values of air, water and foundation temperature applied as nodal temperatures.

Complimentarily to what was presented so far, Leger et al. (1993) provide approaches to assess the convection coefficient as a function of the wind speed, the reservoir's temperature variation as a function of the depth, the air temperature variation when data is not available, the solar radiation and, the foundation temperature variation.

## 2.9 AAR structural implications on dams

According to Charlwood et al. (2012) and Charlwood & Sims (2017), the following performance parameters are affected by ASR in all types of dams:

1- Loss of equipment clearances and alignment;
2- Progressive development of map cracking on downstream face;
3- Significant leaching of concrete at joints;
4- Excessive concrete deterioration (including freeze-thaw damage);
5- Development of new systematic cracking patterns at structural discontinuity areas;
6- Continuous upstream/downstream and vertical deformations at crest;
7- Differential movements (or offsets) at horizontal or vertical joints opening and/or leakage at horizontal lift joints;
8- Tightness of vertical construction and/or expansion joints;
9- Closure of expansion joints (or slots cuts);
10- Spalling of crest, parapet walls and bridge decks at vertical joints;
11- Separation of embedded parts and
12- Changes in leakage at abutments.

Additionally, the authors also present the performance parameters affected by ASR specifically for each type of dam and three of the most important subsections: the powerhouse, the intake and the spillway. First, the following is expected in ASR-affected gravity dams:

1- Separation or slip of horizontal joints;
2- Upstream crest movements (usually upstream but not always);
3- Cracks at structural discontinuities;
4- Changes in geometry;
5- Excessive leakage affecting uplift pressure and leaching of joints.

In arch dams, the structural implications presented below are likely to happen:

1- Upstream movement in an “m” shape at crest;
2- Signs of separation or slip on horizontal lift joints;
3- Formation of structural cracks in galleries;
4- Diagonal cracks on downstream face parallel to dam/abutment contact;
5- Excessive leakage affecting uplift pressure and leaching of joints;
6- Changes to abutment thrusts, possibly affecting stability.

Moreover, in buttress dams the following might be observed:

1- Cracking at structural connections of slabs affecting water tightness;
2- Cracking and deterioration of buttresses with possible impacts on reinforcing steel.

Also, localized damage due to ASR in powerhouses likely present the following consequences:

1- Signs of “ovalling” of units affecting runner and generator air gap clearances;
2- Loss of shaft alignment, head cover bolts misalignment;
3- Stress buildup in penstocks due to compression or shear effects;
4- Distortion or cracking of stay ring, wicket gates, liners, etc;
5- Diagonal cracking of draft tube piers;
6- Interference with draft tube gate clearances;
7- Distortion, separation or overstressing of embedded parts;
8- Leakage;
9- Misalignment of crane rails;
10- Distortion of superstructure frames.

At intakes, the following is expected:

1- Gate clearances and distortion of hoists;
2- Diagonal cracking in water passage piers;
3- Lateral movement of end piers into the openings.

Finally, at spillways:

1- Loss of gate clearances and binding of gates;
2- Lateral movement of end piers into the openings;
3- Cracking of piers.

## 2.10 AAR macro-models applied to dam structures

### 2.10.1 General

As discussed previously, only papers published after 2000 were considered in this review. AAR models from before that year were assumed to be outdated because recent studies have dramatically changed the way the reaction is understood.

### 2.10.2 Ulm et al. (2000)

Ulm et al. (2000) validated their coupled thermo-chemo-mechanical model based on a 2D gravity dam analysis (Figure 2-31). Nodal temperature boundary conditions on the upstream and downstream faces were defined based on average temperatures and on the heat characteristic length. Even though results were not compared to measured data, the authors observed the formation of an ASR front propagation in the zone described by the heat characteristic length due to the effect of the reaction's chemical kinetics (temperature dependency). Moreover, it was reported that the damage starts at the interface between the core and the ASR front due to the differential expansions, chronologically leading to irreversible localized cracking, crack propagation to the surface and delamination.

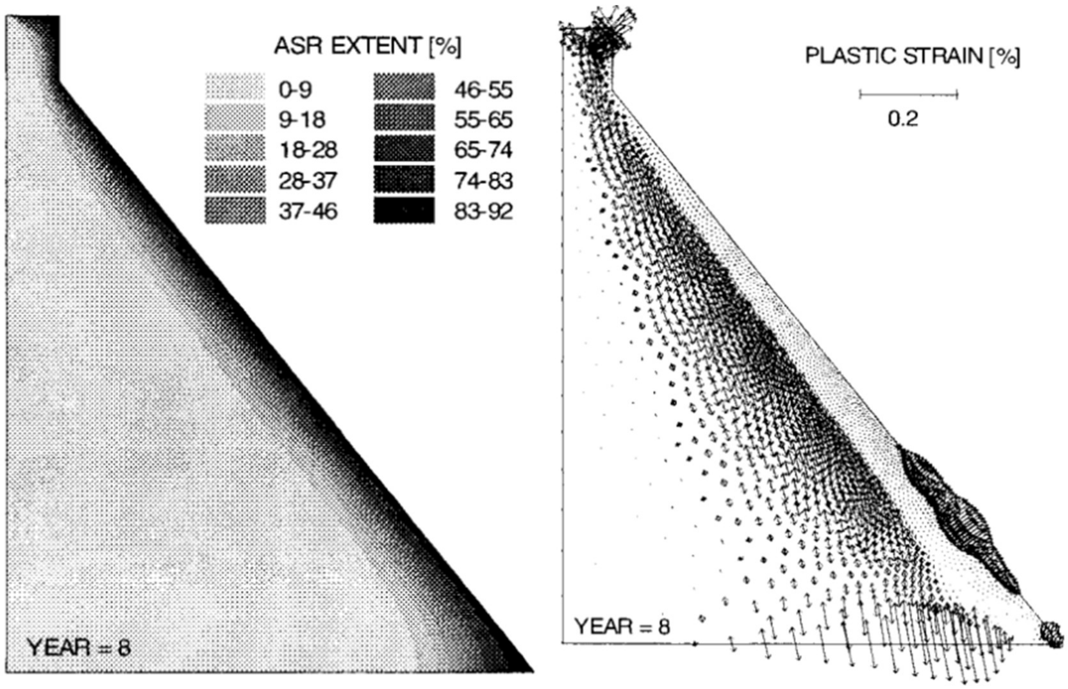


**Figure 2-31. "Pop-outs" at dam surface after 8 years - ASR extent (left) and principal plastic strain (right). Source: Ulm et al. (2000).**

### 2.10.3 Li & Coussy (2002) and Li & Coussy (2004)

Seignol et al. (2016) analyzed the Veytaux power plant, which is an ASR-affected hydraulic facility in Switzerland consisting of 4 blocks measuring approximately 30 by 30 m placed side by side in a rock-cavern (Figure 2-32). The authors used the rheological chemo-plastic model developed by Li & Coussy (2002) and Li & Coussy (2004) to describe the reaction and enhanced it by implementing 3 complimentary aspects to the model: (i) the anisotropic stress-state dependent ASR expansion described by Multon & Toutlemonde (2006), (ii) the modification of the mechanical properties according to Seignol et al. (2012), and (iii) the influence of temperature and humidity on the reaction kinetics was assessed according to Seignol et al. (2009). The 3D analysis was performed in three steps: thermal analysis with nodal temperature boundary conditions (i.e., Dirichlet boundary condition), humidity transport analysis with nodal humidity values boundary condition, and mechanical analysis based on the temperature and humidity fields previously calculated. The FEM model's parameters were fitted based on measured data and sample tests. The whole concrete structure was analyzed first, and then the results of the global analysis were applied to the critical locations in order to assess their current and future state.

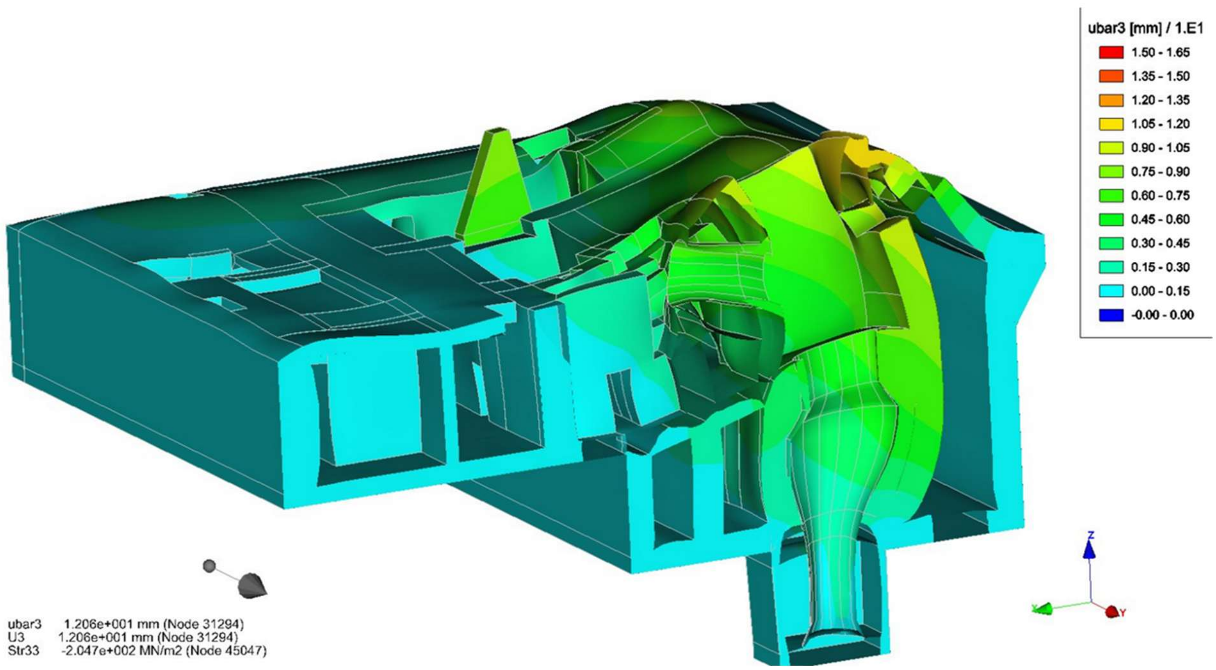


**Figure 2-32. Deformation in Veytaux power plant block 1 and color map for global displacement [mm] at present time in a cross-section through the pump pit. Source: Seignol et al. (2016).**

### 2.10.4 Fairbairn et al. (2004) and Farage et al. (2004)

Fairbairn et al. (2004) and Farage et al. (2004) validated their thermo-chemo-mechanical model by analyzing the Furnas concrete gravity dam (Figure 2-33). For the 3D validation analysis, parameters were first calibrated based on Larive (1997). Then, temperature and humidity fields were defined based on average values, which were applied as nodal temperature and nodal relative humidity boundary conditions. The level of the reservoir was assumed to be constant, and the temperature of the water varied with the depth. The FEM results for displacement at the top of the dam matched measured data from the real dam; however, this was the only data that was evaluated.

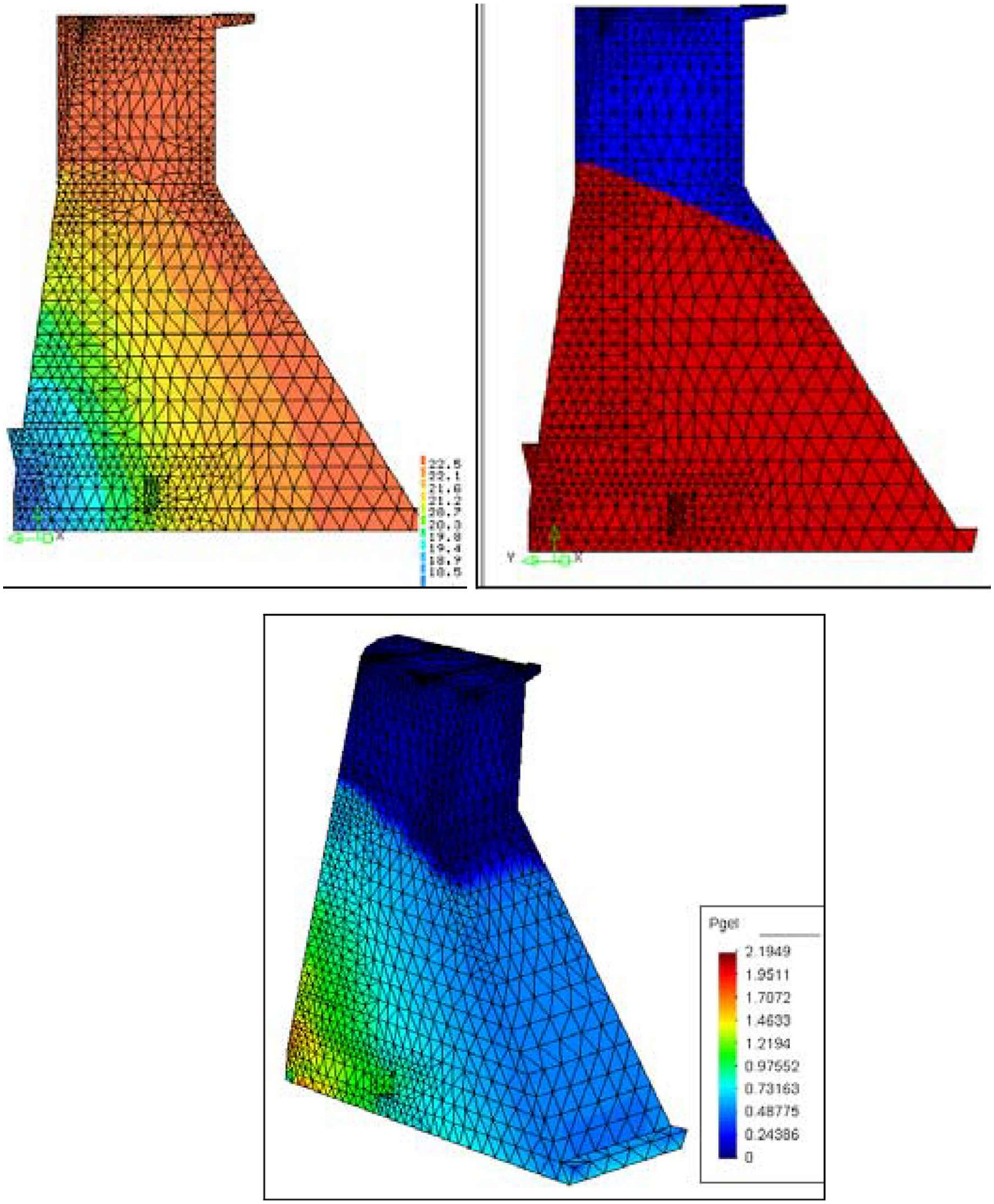


**Figure 2-33. Furnas dam: Top left – steady-state temperature fields; top right – steady-state humidity fields; bottom – gel pressure fields. Source: Fairbairn et al. (2004).**

### 2.10.5 Saouma & Perotti (2006)

Saouma & Perotti (2006) performed a validation study of an arch-gravity dam affected by ASR (Figure 2-34) based on their thermo-hygro-chemo model. According to the authors, the first step of the 2D analysis was to identify the stress-free temperature and to define the yearly variation of the hydrostatic level (pool elevation), water temperature and air temperature. Then, a transient thermal analysis was performed in order to define the temperature fields required due to the thermodynamic nature of the reaction. Heat was assumed to be transferred by conduction only, with convection and radiation being approximated through an additional temperature. They found that the analysis was harmonic after 4 years with a 1-year period. The humidity was assumed to be equal to 100% at all times for the entire dam.

The thermal fields obtained were then transferred to the mechanical model, in which all the loads were applied and the structural implications of both the temperature and the ASR reaction were accounted for.

Their results showed that the stress redistribution predicts the effects of ASR more accurately than if the reaction is assumed as isotropic. Moreover, they also observed a lift-off along the central portion of the dam-foundation interface and tensile stresses build up inside the dam body due to the thermal load. However, further evaluation of the model is limited because it is not correlated with any field measurements.

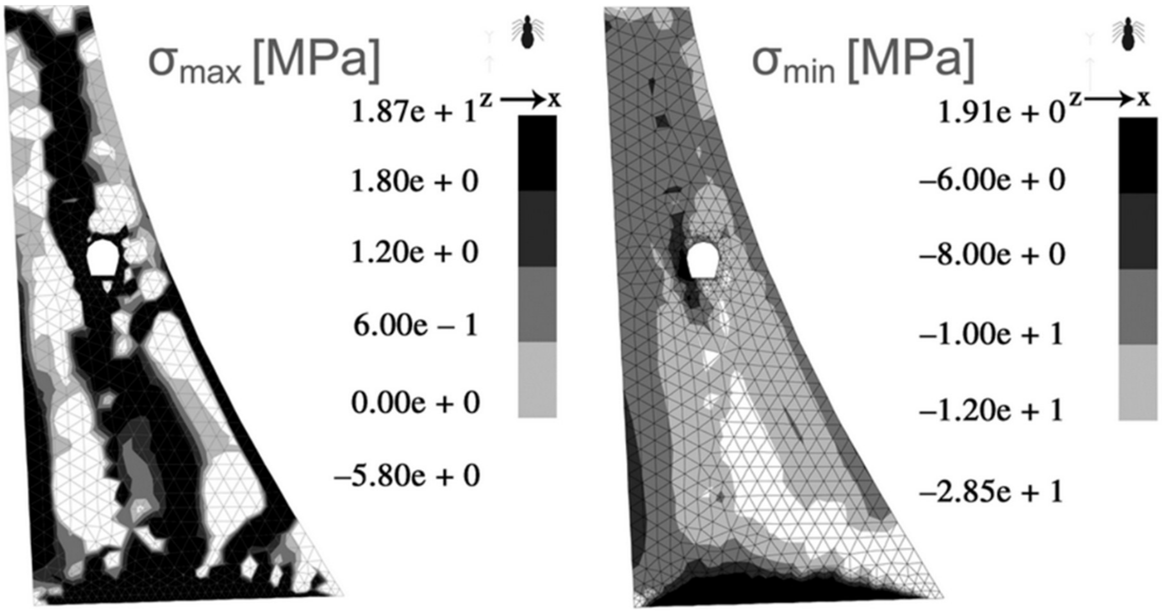


**Figure 2-34. Principal stress field: Left – maximum stress; Right – minimum stress. Source: Saouma & Perotti (2006).**

Additionally, Rodríguez et al. (2012) used the models developed by Ulm et al. (2000) and Saouma & Perotti (2006) to model a double-curvature arch dam (Figure 2-35 through Figure 2-37). Data gathered for almost 50 years regarding environmental conditions, dam temperatures and displacements was used to validate their approach. The authors first conducted a thermal analysis, and then a mechanical analysis was used to define the expansion progress, i.e. kinetics based on Larive (1997), as a function of the measured data. At the end, good agreement was found between FEM results and measured data for the entire structure, which allowed the authors to predict the future behaviour of the dam.

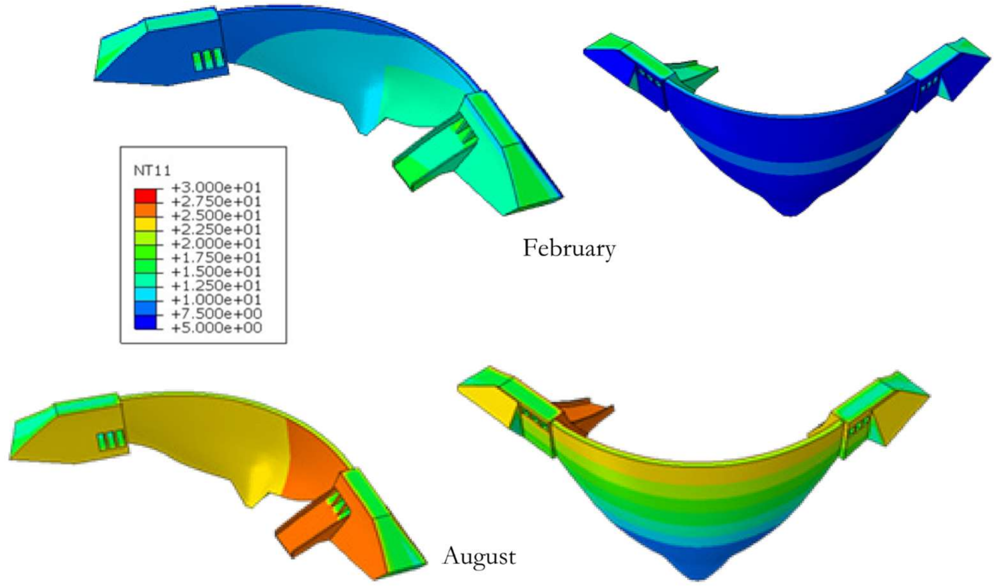


**Figure 2-35. Temperature field [ºC]. Source: Rodríguez et al. (2012).**

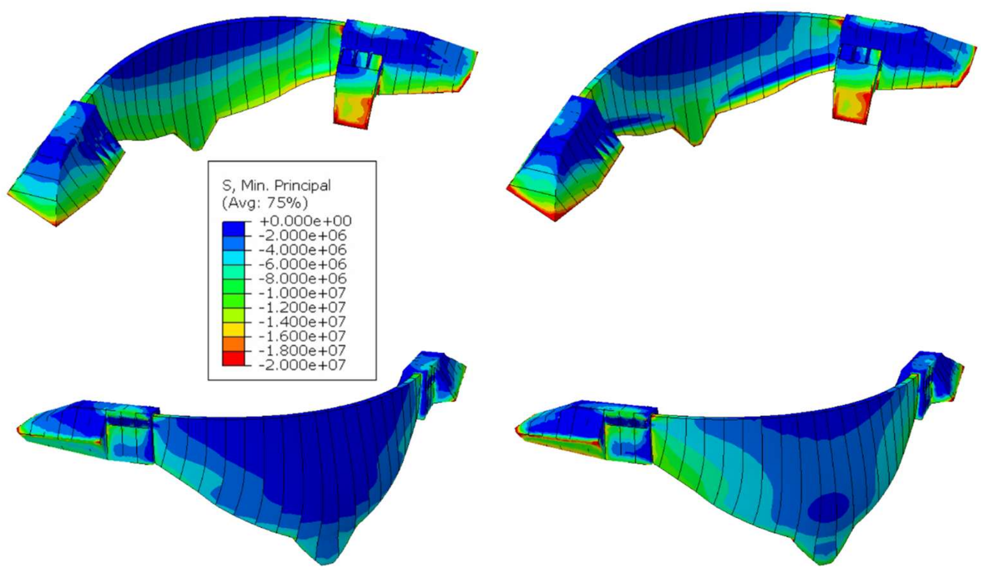


**Figure 2-36. Compressive stresses [Pa]. Source: Rodríguez et al. (2012).**

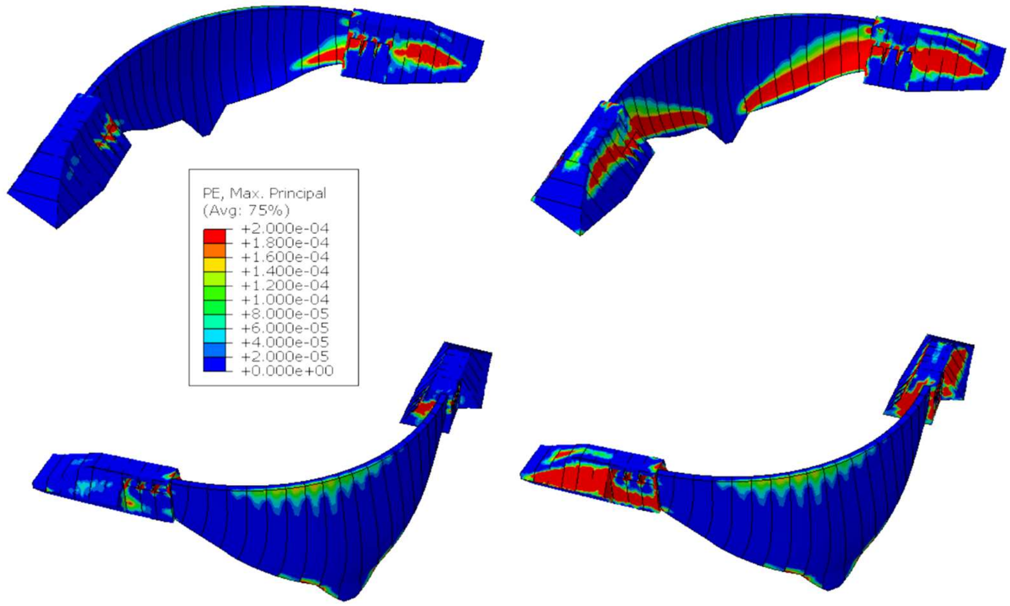


**Figure 2-37. Equivalent plastic strain (cracking). Source: Rodríguez et al. (2012).**

### 2.10.6 Grimal et al. (2008a) and Grimal et al. (2008b)

Chulliat et al. (2017) analyzed the Chambon gravity dam, located in the French Alps (Figure 2-38 and Figure 2-39), based on the approach proposed by Grimal et al. (2008a) and Grimal et al. (2008b) for ASR and delayed ettringite formation (DEF). The authors further enhanced the rheological model that accounts for the interaction between ASR, creep, shrinkage and damage based on Sellier et al. (2016).

The simulation accounted for the different types of concrete that compose the dam, the chemical reaction was assumed always possible due to high alkali content in the mix and silica content in the aggregate, and the dam temperature was assumed to be uniform and constant based on the overall average temperature of the structure over its lifespan. The model was calibrated (parameters were fitted) based on measured data, and laboratory tests were performed in order to define the concrete strength, modulus of elasticity, creep coefficients, ASR kinetics, chemical advancement, and damage. The results were in agreement with the measured data regarding stress orientation and intensity, cracking pattern and overall structural behaviour. The authors were confident in the results, which allowed them to predict the future behaviour of the dam and suggest remedial works to minimize the impact of ASR in the future.

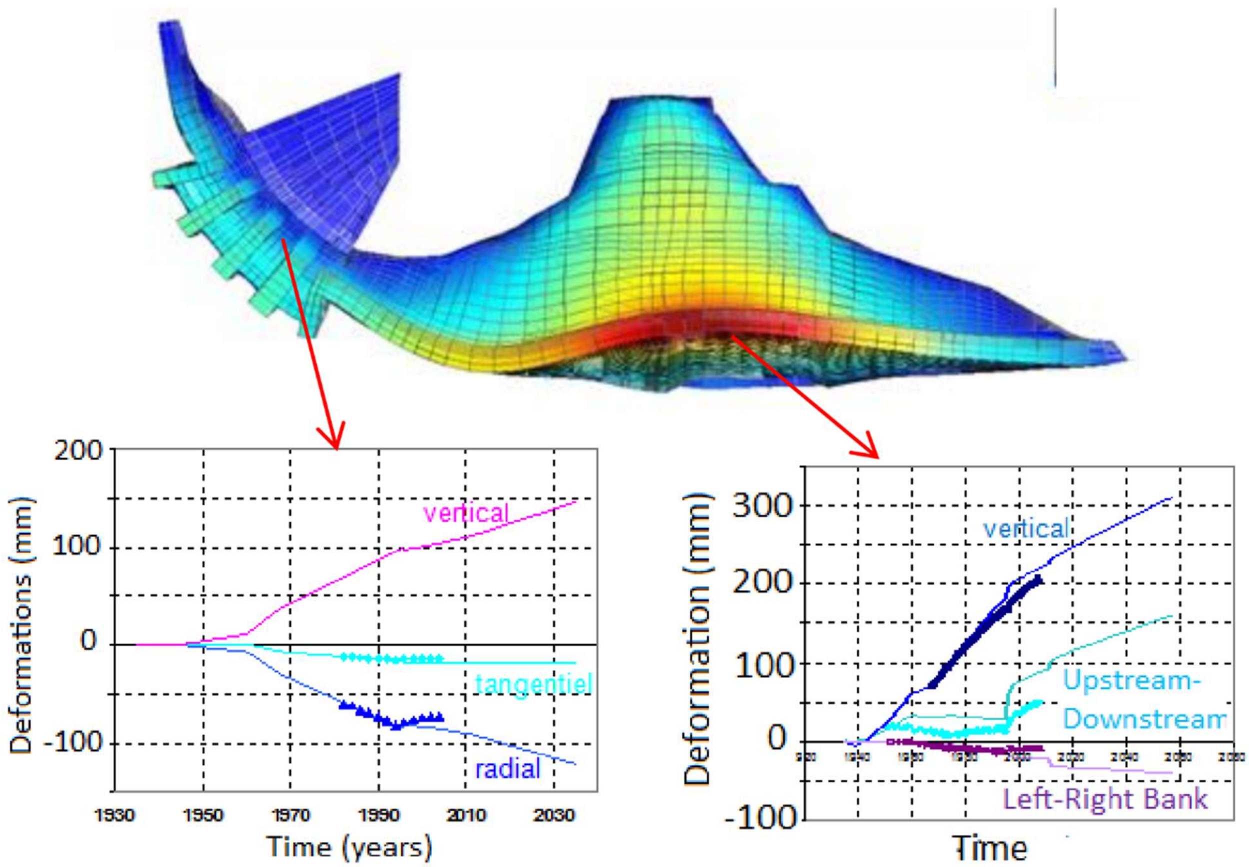


**Figure 2-38. Chambon dam - comparison of measured and computed deformations. Source: Chulliat et al. (2017).**

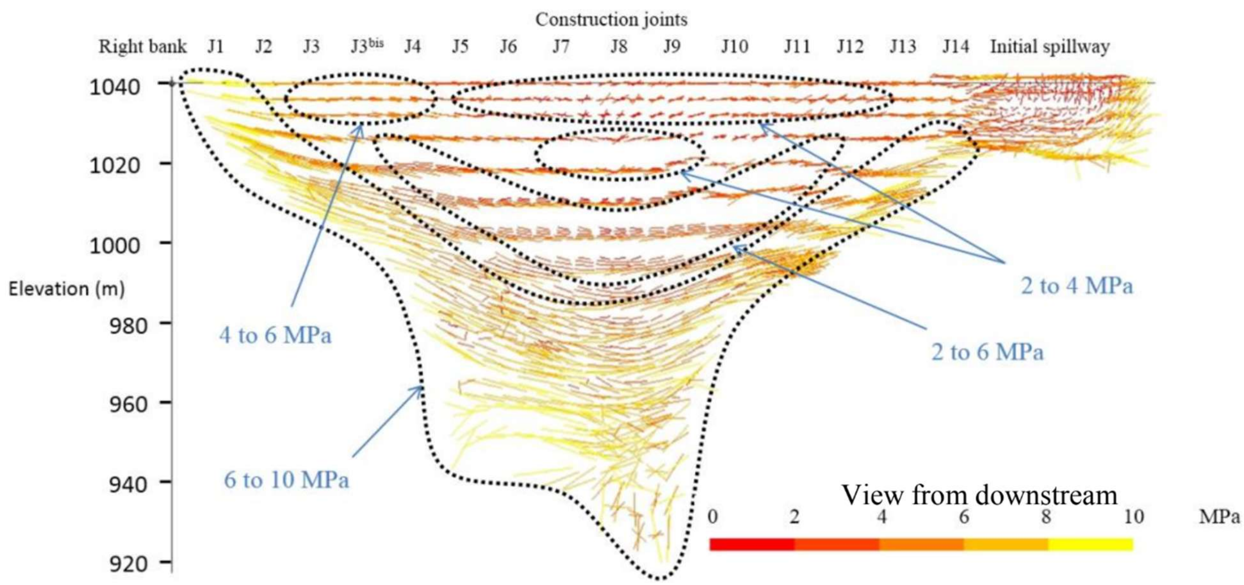


**Figure 2-39. Chambon dam – maximum principal compressive stresses. Source: Chulliat et al. (2017).**

### 2.10.7 Comi et al. (2012)

Comi et al. (2012) validated their model by analyzing the gravity dam of the Beauharnois power plant in Québec, Canada (Figure 2-40 and Figure 2-41). FE results were compared to values reported by Bérubé et al. (2000) and Kladek et al. (1995).

The authors first calibrated the proposed equations for the elastic parameters of concrete and gel (concrete was considered as a two-phase porous heterogeneous material), as well as parameters defining the expansion due to ASR and parameters governing the damaged response based on experiments reported in the literature. Kinetics parameters not reported in the literature were assumed based on engineering judgement.

The influence of humidity was accounted for through diffusion analyses of moisture based on relative humidity (instead of degree of saturation). The humidity history was imposed to the structure based on yearly variations, with initial humidity conditions having been previously estimated. The influence of temperature was assessed through heat diffusion analyses based on characteristic lengths. Values of the yearly variation of the temperature of air, water (based on the varying reservoir depth) and soil were applied to the structure; the type of boundary condition was not specified. Thermal parameters were assumed constant, and the relative humidity diffusion coefficient varied with the degree of saturation.

The temperature fields and humidity fields were then imported into the mechanical analysis after the two transport analyses were completed to consider their structural effects.

The results corroborated what was proposed by Ulm et al. (2000); in massive structures, the temperature gradient is the governing cause of structural damage, while the humidity gradient has almost no influence on the analysis due to the small value of the humidity characteristic length. The value of the heat characteristic length is usually in meters, while the humidity characteristic length is in centimeters; therefore, the overall behaviour of the dam is governed by the initial humidity. The authors even stated that the overall effect of the humidity gradient could have been neglected in this case, even though this might not be true for slenderer structures (like buttress dams). Moreover, the appearance of the first cracks and the displacement rate found matched what was recorded by Bérubé et al. (2000).

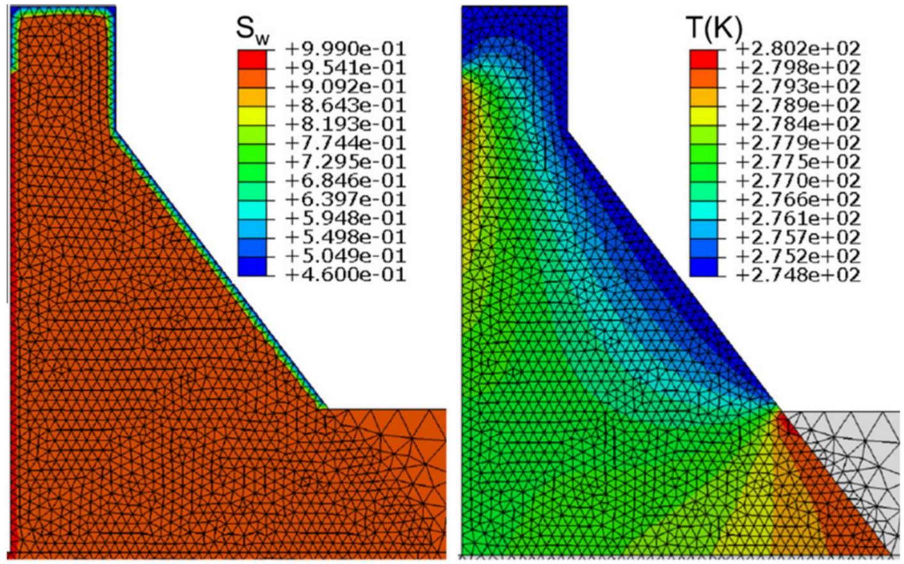


**Figure 2-40. Beauharnois gravity dam: left – degree of saturation; right – temperature. Source: Comi et al. (2012).**

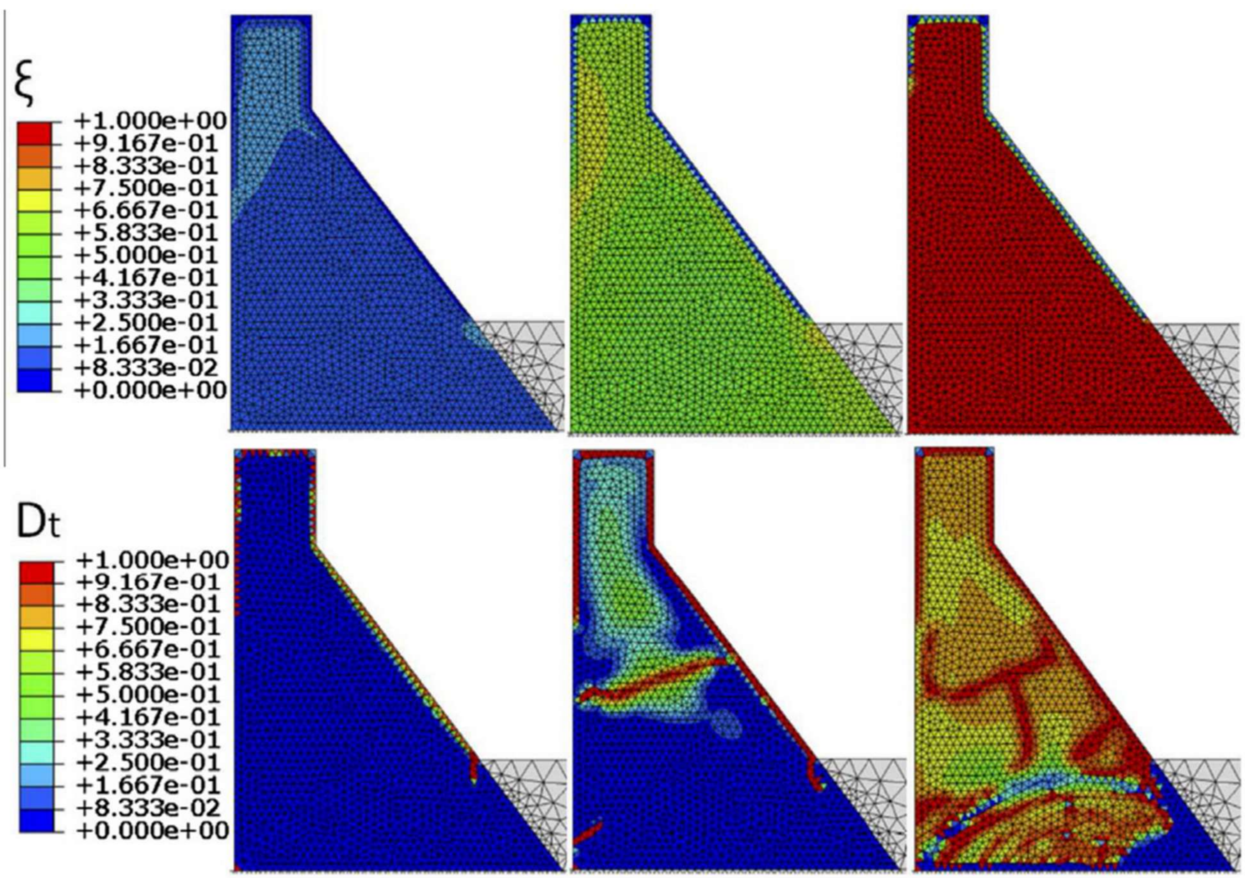


**Figure 2-41. Beauharnois gravity dam: top – reaction extent in relation to final expansion (at 3, 6 and 60 years); bottom –damage (plastic strain) extent (at 3, 6 and 60 years). Source: Comi et al. (2012).**

### 2.10.8 Pan et al. (2013a) and Pan et al. (2013b)

Pan et al. (2013a) validated their chemo-elasto-plastic model by analyzing the Fontana gravity dam (Figure 2-42 and Figure 2-43). The simulation of the gravity dam consisted of a thermal analysis followed by a mechanical analysis, which was based on the calculated temperature fields. In the thermal analysis, the authors neglected the heat of hydration of concrete, based on the assumption that it is not relevant for long-term analyses. Moreover, the initial temperature of the model was the yearly average temperature of the air; the yearly temperature variations of both air and water were imposed as nodal temperature boundary conditions, and the solar radiation was ignored. In the mechanical analysis, the hydrostatic load was assumed as a function of the reservoir's depth variation over time. The effect of humidity was neglected based on the assumption that its influence on dams is very small. Therefore, a constant value of 100% humidity was assumed for the entire model.

The resulting cracking pattern matched the field observations; however, that was the only parameter that was compared to the field measurements by the authors.

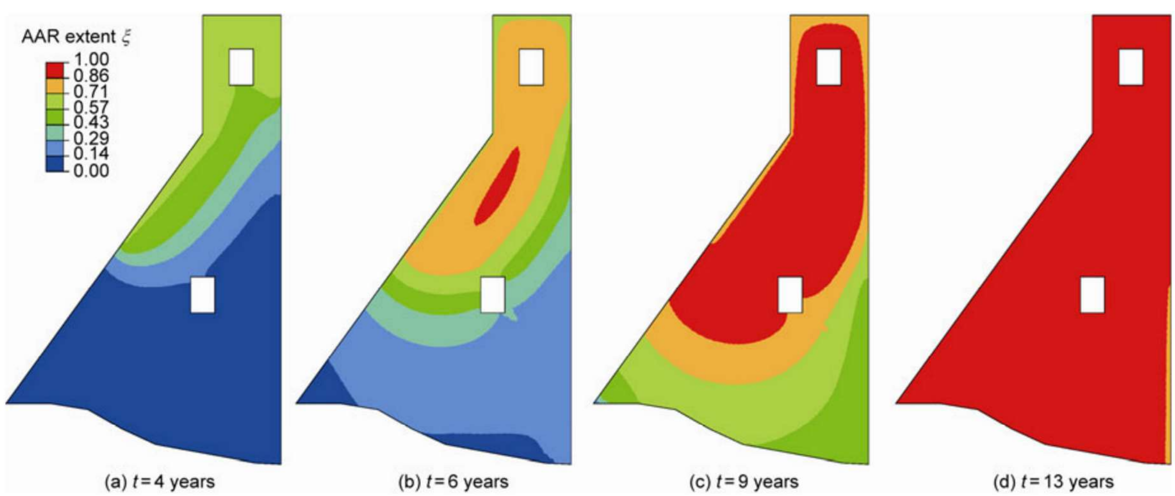


**Figure 2-42. Fontana gravity dam: reaction extent in relation to final expansion at 4, 6, 9 and 13 years. Source: Pan et al. (2013a).**

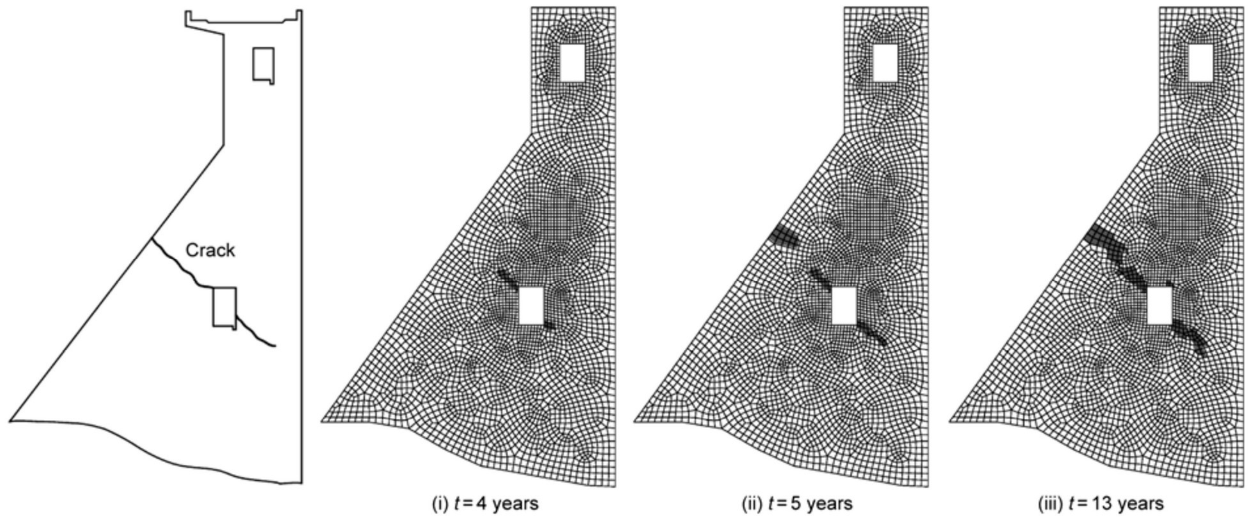


**Figure 2-43. Fontana gravity dam: cracking pattern (field inspection and calculated at 4, 5 and 13 years). Source: Pan et al. (2013a).**

Later, the enhanced model by Pan et al. (2013b) was validated by analyzing the Kariba arch dam (Figure 2-44 through Figure 2-46). A similar approach was adopted; however, no thermal analysis was conducted. The authors neglected the thermal analysis because the seasonal temperature variations were considered low; therefore, their effects over time could be ignored. The calculated radial displacements and most of the vertical displacements matched the measured data well, which was gathered for over 30 years. The same was found when comparing the cracking pattern predicted and the limited information about the actual cracking pattern of the dam. Lastly, it is important to emphasize that the authors noticed a close correlation between the radial displacements and the reservoir's depth variation.

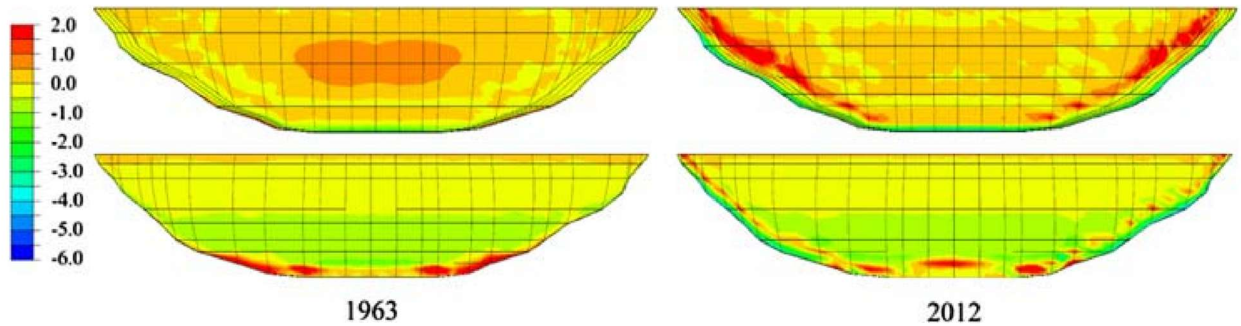


**Figure 2-44. Kariba arch dam: maximum principal stress in 1963 and 2012 (in MPa). Source: Pan et al. (2013b).**

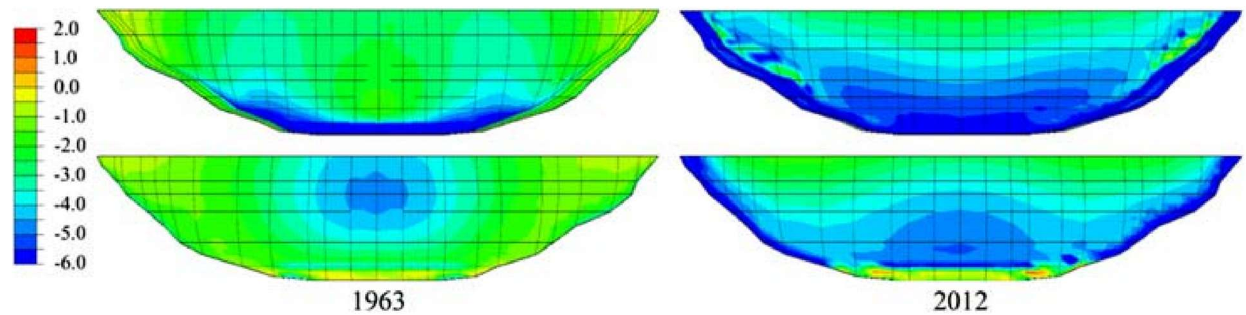


**Figure 2-45. Kariba arch dam: minimum principal stress in 1963 and 2012 (in MPa). Source: Pan et al. (2013b).**

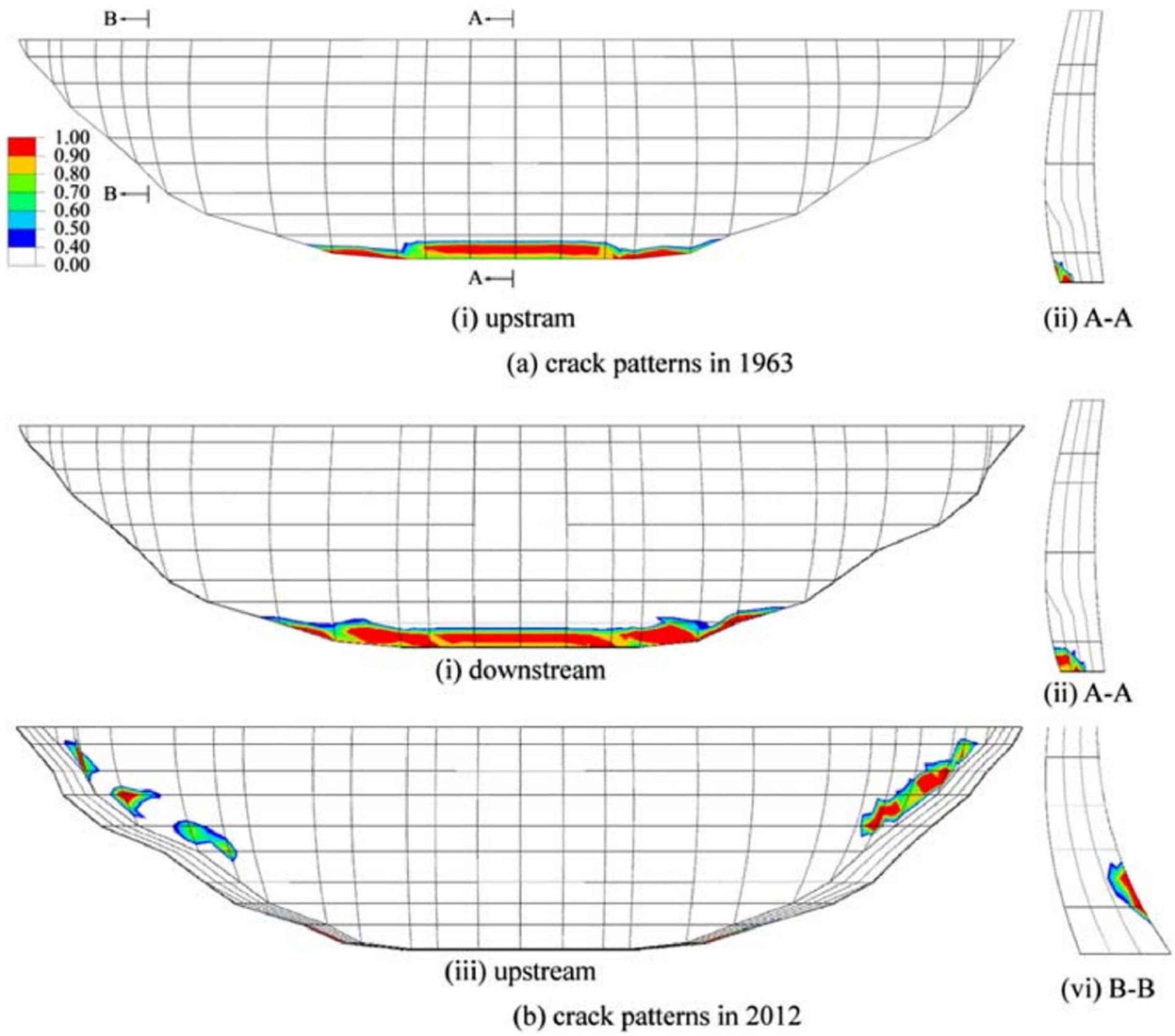


**Figure 2-46. Kariba arch dam: predicted crack pattern (in 1963 and 2012). Source: Pan et al. (2013b).**

### 2.10.9 Winnicki et al. (2014)

Winnicki et al. (2014) assessed the Fontana gravity dam to validate their thermo-hygro-chemo-plastic model (Figure 2-47). The authors first performed a thermal analysis and a humidity transfer analysis to determine the temperature and relative humidity fields. Constant thermal capacity and conductivity coefficients were assumed for the thermal analysis, while the moisture capacity and the diffusion coefficient were taken as a function of the relative humidity for the humidity transfer analysis. Boundary conditions were applied as nodal temperatures and relative humidity values changing based on yearly variations. After, the calculated values were used as input for the mechanical analysis, where all loads were accounted for. Note that the hydrostatic load was assumed to change over time based on water level variation.

The resulting cracking pattern obtained from the 2D analysis of the Fontana gravity dam matched relatively well the actual patterns observed in the dam. However, the authors reached a "controversial" conclusion by stating that the ASR-affected model had a global safety factor greater than that of the undamaged structure, which means that the structural effects of ASR made the dam safer. They explained that this probably occurred because the ASR expansion led to higher compressive stresses in the critical zone, thereby having this beneficial effect. No further comparison with measured data from the dam is mentioned in the paper.

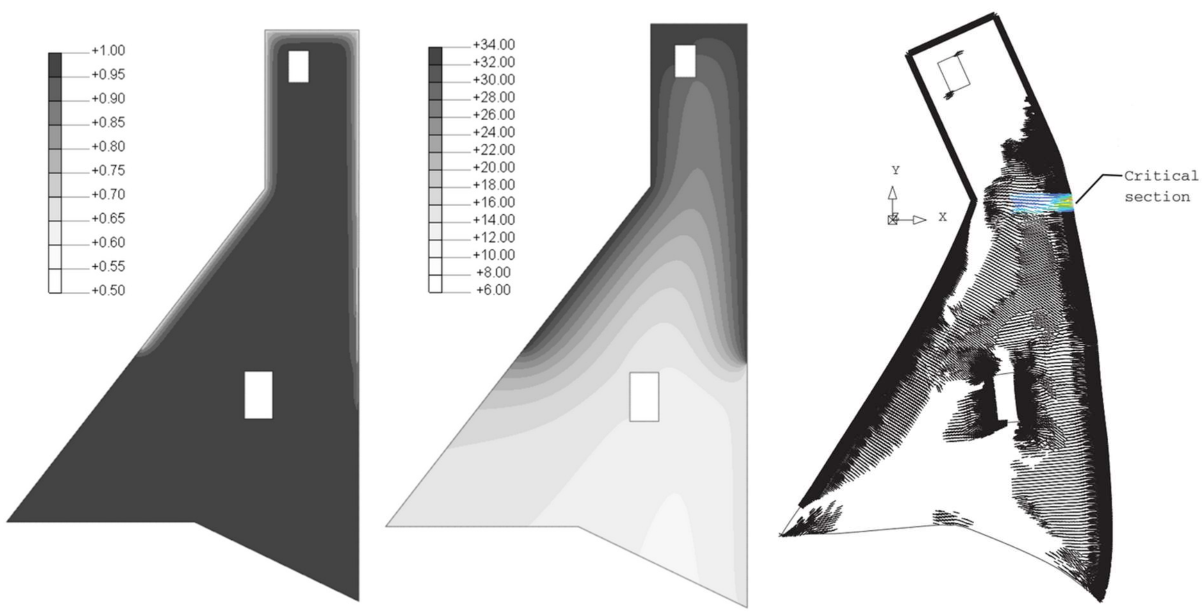


**Figure 2-47. Fontana gravity dam: left – relative humidity field; middle – temperature field [ºC]; right – crack pattern after 30 years of ASR action for maximum overtopping. Source: Winnicki et al. (2014).**

### 2.10.10 Ben Ftima et al. (2017)

Ben Ftima et al. (2017) developed two complementary models to assess the sliding safety factor (SSF) and structural safety margin of dams: a quasi-static explicit continuum nonlinear finite element smeared cracking model (QSE-FEM-S) and a quasi-static explicit continuum nonlinear finite element model using the strength reduction approach (QSE-FEM-D). The approach was validated by analyzing a gravity dam and its spillway (Figure 2-48).

The proposed approach is divided in two steps. First, the QSE-FEM-S is calibrated based on field measurements and used to identify the dominant crack patterns forming potential failure planes. It is a thermo-hygro-chemo-mechanical model that also accounts for creep, damage accumulation (cracking) and shrinkage. Note that the temperature and humidity fields are calculated through thermal analyses and humidity transport analyses. Then, the next step is to use the QSE-FEM-D to compute the initial condition to perform a “stability analysis”.

According to the authors, the discrete model is adopted for two reasons. First, it yields classical engineering scalar stability indicators for the SSF, which are easier to interpret than the results from the smeared cracking model. Second, QSE-FEM-S displays intrinsic uncertainty when estimating the fracture parameters and, consequently, the safety margin of the dam. Therefore, using the QSE-FEM-D is a more attractive alternative.

The QSE-FEM-S validation analysis results for the gravity dam matched well the cracking patterns observed in the real dam, after the model was calibrated based on field measurements. Furthermore, the results were conclusive enough to allow the identification of a potential 3D cracking surface in the spillway and part of the pier. These results were then transferred to the QSE-FEM-D, where the SSF was determined for the current state of the ASR-affected dam. Note that, in the QSE-FEM-D, the cracking surface interface was modeled with zero cohesion and a non-zero value for the friction coefficient.

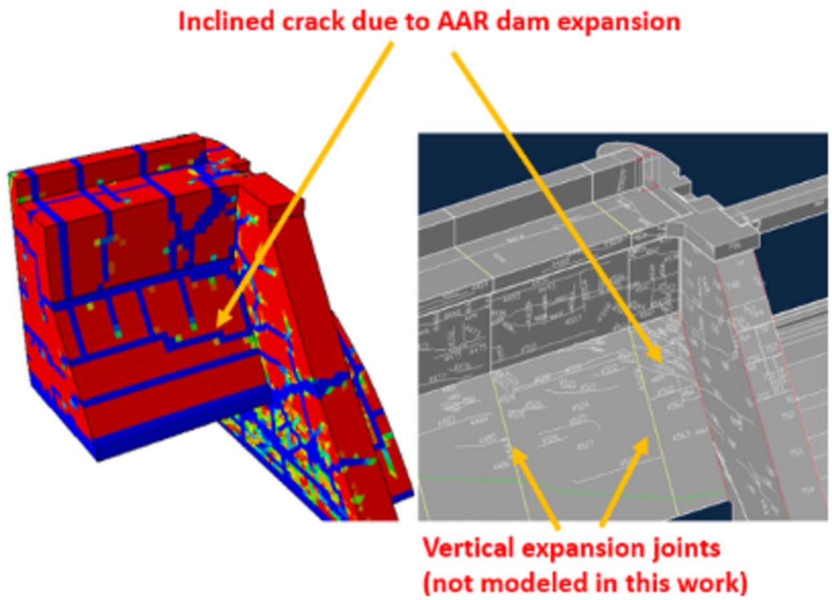


**Figure 2-48. Gravity dam: left – predicted damage pattern (damaged elements in blue); right – observed cracking pattern. Source: Ben Ftima et al. (2017).**

### 2.10.11 Gocevski & Yildiz (2017)

The model presented by Gocevski & Yildiz (2017), which is implemented in Abaqus Explicit – Simulia (2014), is validated by analyzing a hydroelectric power plant (Figure 2-49 and Figure 2-50). The approach assumes that the free AAR rate of expansion can be considered constant (linear) for structural evaluations because the change in rate over the lifespan of the structure is negligible, and it doesn't have to be represented by an exponential function. Moreover, the maximum free AAR expansion is assumed to be that for the specific concrete mix exposed to optimum humidity and temperature conditions.

Humidity transport analyses and thermal analyses were conducted before the mechanical analysis in order to determine the humidity and temperature fields. The results of displacements and cracking patterns matched the measured values well, which allowed the authors to evaluate the structural safety of the dam, the expected lifespan of uninterrupted production and when retrofitting would be required.

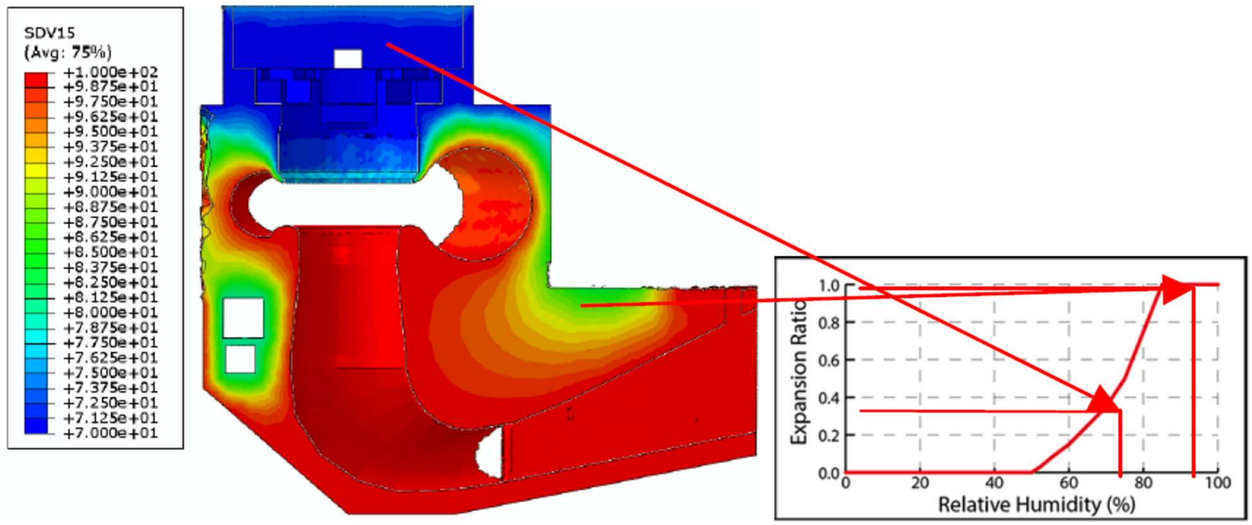


**Figure 2-49. Hydroelectric power plant: Effect of relative humidity on the AAR expansion. Source: Gocevski & Yildiz (2017).**

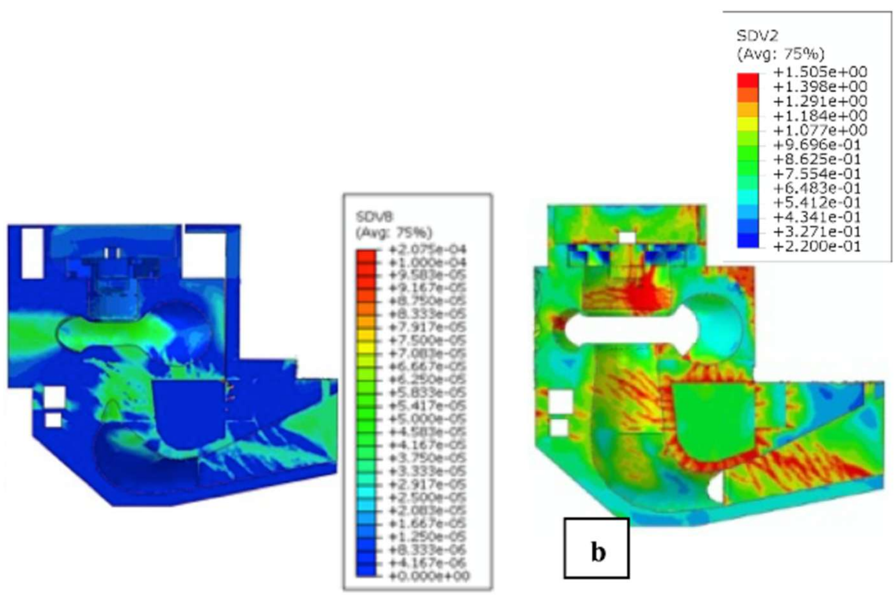


**Figure 2-50. Gravity dam: left – Variation of rate of expansion at 50 years after construction; right – cracking pattern. Source: Gocevski & Yildiz (2017).**

## 2.11 Slot cutting on AAR-affected dams

One of the few alternatives that has been demonstrated to have beneficial effects on AAR-affected dams is the slot cutting technique. It consists of cutting vertical slots on the dam with diamond wire saws, with the main goal of reducing permanent displacements that may be impairing gates and turbine functionality, and to release (some of) the built-up compressive stresses that have developed within the dam body as concrete expands due to AAR (Caron et al., 2001). Additionally, it can also reduce the detrimental effects of cyclic seasonal temperature loadings in cold climates, reduce leakage, and close cracks/joints.

This technique has successfully been applied to several dams, and beneficial effects have been observed. Some of these succesfull implementations include the Fontana gravity dam - USA (Abraham & Sloan, 1978), the Pian Telessio arch-gravity dam - Italy (Amberg et al., 2009), the Chambon gravity dam - France (Chulliat et al., 2017), the Hiwasse gravity dam - USA (Curtis et al., 2005), the Mactaquac gravity dam - Canada (Curtis et al., 2016), and the Salanfe gravity dam - Switzerland (Droz et al., 2013).

However, there are also cases where slot cutting has been reported to have led to further damage (increase in expansion rate and cracking) when compared to a “no intervention” scenario (Gocevski & Yildiz, 2017). The authors suggest that slot cuts on gravity dams and its components should not be performed if the expansion rate is categorized as mild (less than 15 micro-strain per year) or if the aggregate is moderately reactive according to CSA A23.2-14A (2014) (expansion between 0.040 and 0.120 % per year) with a concrete mix containing alkali content lower than 1.8 $kg/m^3$. Additionally, Caron et al. (2001) and Veilleux (1995) state that slot cutting may lead to detrimental effects, including the restart of high swelling rate due to release of beneficial restraints, the formation of high stress concentration zones near the slot tip, the potential occurrence of secondary deformations detrimental to the functionality of mechanical equipment, the introduction of new thermal boundary conditions by allowing penetration of cold/warm air, and the requirement of sealing/waterproofing, monitoring and maintenance.

The overall effect of slot cutting is highly dependent on the material, geometric, and structural properties of each dam structure. However, a brief review of the data available in the literature shows that slot cutting should favour several smaller cuts instead of fewer larger cuts to distribute the stress release more evenly and avoid cutting along existing vertical joints (Amberg et al., 2009; Caron et al., 2001; Chulliat et al., 2017; Curtis et al., 2005, 2016; Metalssi et al., 2014; Veilleux, 1995). This is in accordance with the slot cutting influence zone theory proposed by Caron et al. (2001), in which the authors state it is a function of the elastic slot closure ($\delta_e$), initial stress ($\sigma_0$), slot depth ($h_c$), elastic modulus of elasticity ($E_0$), and type of boundary condition (fixed or free - $\beta$), as shown in Figure 2-51. The relation between these parameters is given in Equation 2-50. Moreover, regarding geometry, slot widths are usually between 10 and 20 mm, depth is between 15 and 50% of the dam height (therefore not going all the way down to the base), and spacing is usually between 25 and 100 m.

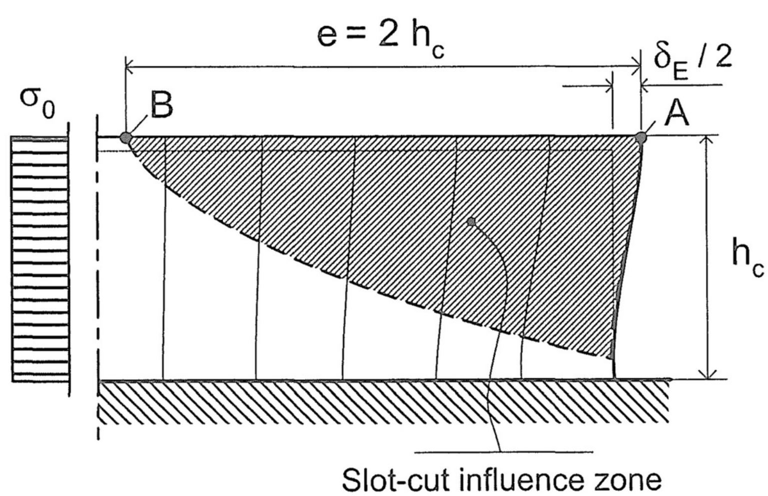


**Figure 2-51. Slot cutting influence zone. Source: Caron et al. (2001).**

$$\delta_e = \frac{\beta h_c \sigma_0}{E_0} \tag{2-50}$$

Regarding numerical simulations, slot cuts have been reported to have been modeled in three different ways: as contact without element removal (Droz et al., 2013; Metalssi et al., 2014), by simple element removal of one layer at a time (Saati & Mortazavi, 2009), or by implementing an artificial "slot cutting material", which has its stiffness reduced before it is deleted in an explicit (quasi-static) analysis (Gocevski & Yildiz, 2017). Most of the published literature that included a slot cutting simulation did not provide a description of how it was implemented (Amberg et al., 2009; Chulliat et al., 2017; Curtis et al., 2005, 2016; Veilleux, 1995).

Overall, slot cutting is a major (expensive) intervention technique. It creates new joints that must be assessed, monitored, and maintained (Veilleux, 1995). Therefore, adequate structural assessment and numerical modeling are essential to determine if the technique is recommended, how to perform it, and if/when future remedial works are required.

### 2.12 Gap in the state-of-the-art

Based on the review of existing models that have been used to simulate dam structures, there is still a need for a model capable of accurately describing the physicochemical nature of AAR on massive structures, without overcomplicating or oversimplifying the reaction or the parameters involved. In order to do so, a model must accomplish the following:

1- It should account for the most important parameters influencing the reaction:

   a. Anisotropic stress-state-dependent expansion,
   b. Kinetics and final expansion dependency on temperature, humidity, alkali content, aggregate type and aggregate reactivity,
   c. Mechanical properties deterioration as a function of the expansion,

d. Size effect (alkali release from large aggregates, source of silica from large aggregates and lack of leaching).

2- It needs to be able to simultaneously incorporate the effect AAR along with non-linear mechanical behaviour, thermal behaviour, steel reinforcement (regular and prestressed), and creep (including the entire stress history of each region).

3- It needs to be validated through comparisons with both experiments and real case scenarios.

4- It should be able to simulate the structural effects of the reaction without need for fitting or non-technical guesses based on the information available, to provide a more reliable interpretation of the prognosis and diagnosis of the structure.

5- Results should, whenever possible, be supported by supplementary multi-level assessment laboratory tests such as damage rating index (DRI) in order to validate the proposed free expansion curve, assumptions, and modeling approach.

6- It should be able to simulate rehabilitation techniques, like slot cutting.

Additionally, another critical aspect that is still highly debated within the engineering community is the efficiency of slot cutting as a rehabilitation technique for AAR-affected. The physical mechanisms involved and their influence on AAR development have never been properly addressed, complicating decisions regarding the timing, location, characteristics, and necessity of implementing this intervention. Therefore, a parametric analysis on a generic dam is proposed to evaluate the influence of key parameters affecting slot cutting. These parameters include cut width, depth, timing of the cut, number of cuts, and the presence of discontinuities. The analysis aims to identify scenarios in which slot cutting is likely to be a recommended rehabilitation strategy.

## 2.13 References


Abraham, T. J., & Sloan, R. C. (1978). TVA cuts deep slot in dam, ends cracking problem. *Civil Engineering—ASCE*, *48*(1), 66–70.

Alsuleimanagha, Z., & Liang, J. (2012). *Dynamic analysis of the Baozhusi dam using FEM* [M.A.Sc.]. KTH Royal Institute of Technology.

Amberg, F., Bremen, R., & Brizzo, N. (2009). Rehabilitation of the Pian Telessio dam (IT) affected by AAR-reaction. *Commission Internationale Des Grands Barrages*.

Amhalhel, G., & Furmański, P. (1997). Problems of modeling flow and heat transfer in porous media. In *Institute of Heat Engineering*. Institute of Heat Engineering.

Bangert, F., Kuhl, D., & Meschke, G. (2004). Chemo-hygro-mechanical modelling and numerical simulation of concrete deterioration caused by alkali-silica reaction. *International Journal for Numerical and Analytical Methods in Geomechanics*, *28*(7–8), 689–714.

Batista, A. L. (1998). *Análise do comportamento ao longo do tempo de barragens abóbada* [Ph.D. Thesis]. Universidade Técnica de Lisboa and Laboratório Nacional de Engenharia Civil (LNEC).

Bazant, Z. P. (1988). *Mathematical modeling of creep and shrinkage of concrete* (1st ed.). John Wiley and Sons.

Bazant, Z. P., & Steffens, A. (2000). Mathematical model for kinetics of alkali–silica reaction in concrete. *Cement and Concrete Research*, *30*(3), 419–428.

Bazant, Z. P., & Wu, S. T. (1973). Dirichlet Series Creep Function for Aging Concrete. *Journal of the Engineering Mechanics Division*, *99*(2), 367–387.

Bazant, Z. P., & Wu, S. T. (1974). Rate-type creep law of aging concrete based on maxwell chain. *Materials and Structures*, *7*, 45–60.

Bear, J., & Bachmat, Y. (1990). Introduction to modeling of transport phenomena in porous media. In *Introduction to modeling of transport phenomena in porous media* (4th ed.). Kluwer Academic Publishers.

Ben Ftima, M., Léger, P., & Boussaha, F. (2017). Structural Modeling. *Dam Swelling Concrete (DSC 2017)*, 176–187.

Bérubé, M.A., Durand, B., Vézina, D., & Fournier, B. (2000). Alkali-aggregate reactivity in Québec (Canada). *Canadian Journal of Civil Engineering*, *27*(2), 226–245.

Capra, B., & Bournazel, J. P. (1998). Modeling of Induced Mechanical Effects of Alkali-Aggregate Reactions. *Cement and Concrete Research*, *28*(2), 251–260.

Capra, B., & Sellier, A. (2003). Orthotropic modelling of alkali-aggregate reaction in concrete structures: numerical simulations. *Mechanics of Materials*, *35*(8), 817–830.

Caron, P., Tinawi, R., & Léger, P. (2001). Slot cutting response of compressed concrete structures. *4th International Conference on Fracture Mechanics in Concrete and Concrete Structures*, 879–886.

Charlwood, R. (1994). A review of alkali aggregate in hydro-electric plants and dams. *International Journal on Hydropower Dams*, 73–80.

Charlwood, R., Scrivener, K., & Sims, I. (2012). Recent developments in the management of chemical expansion of concrete in dams and hydro projects—Part 1: Existing structures. *Hydro 2012 - Innovative Approaches to Global Challenges*.

Charlwood, R., & Sims, I. (2017). A Review of the Effectiveness of Strategies to Manage Expansive Chemical Reactions in Dams and Hydro Projects. *Dam Swelling Concrete - DSC 2017*, 3–39.

Chatterji, S., & Christensen, P. (1990). Studies of alkali-silica reaction. Part 7. Modelling of expansion. *Cement and Concrete Research*, *20*(2), 285–290.

Chaudhari, S. V., & Chakrabarti, M. A. (2012). Modeling of Concrete for Nonlinear Analysis using Finite Element Code ABAQUS. *International Journal of Computer Applications*, *44*(7), 14–18.

Chen, W.F. (2007). *Plasticity in Reinforced Concrete*. J. Ross Publishing.

Chulliat, O., Grimal, E., & Bourdarot, E. (2017). Chambom Dam - A Struggle Against AAR. *Dam Swelling Concrete (DSC 2017)*.

Collins, M. P., & Mitchell, D. (1997). Stress-strain response of reinforcement. In *Prestressed concrete structures*. Reponse Publications.

Comi, C., Kirchmayr, B., & Pignatelli, R. (2012). Two-phase damage modeling of concrete affected by alkali–silica reaction under variable temperature and humidity conditions. *International Journal of Solids and Structures*, *49*(23–24), 3367–3380.

Comi, C., & Pignatelli, R. (2012). *Modeling of degradation induced by alkali-silica reaction in concrete structures*. Italy.

Cotoi T. (2015). *Dam engineering GRV BUTT.*

Crouch, R. S., & Wood, J. G. M. (1990). Damage evolution in AAR affected concretes. *Engineering Fracture Mechanics*, *35*(1–3), 211–218.

CSA A23.2-14A. (2014). *Potential Expansivity of Aggregates - Procedure for Length Change Due to Alkali-Aggregate Reaction in Concrete Prisms*.

CSA A864. (2000). *Guide to the Evaluation and Management of Concrete Structures Affected by Alkali-Aggregate Reaction*.

Curtis, D. D., Davis, B. J., Rahman, S., & Powell, R. C. (2005). Updated Assessment of Concrete Growth Effects on Hiwassee Dam. *25th Annual USSD Conference*.

Curtis, D. D., Feng, L., Sooch, G. S., Zheng, J., & Fletcher, J. (2016). Practical Analysis and Assessment of AAR Affected Dams and Hydroelectric Plants. *United States Society of Dams, 36th Annual USSD Conference*.

Diamond, S. (1989). ASR – Another look at mechanisms. *8th International Conference on Alkali-Aggregate Reaction in Concrete - ICAAR*.

Droz, P., Menouillard, T., Vallotton, O., & Leroy, R. (2013). Slot cutting an AAR-affected dam: case study of the Salanfe dam. *International Journal on Hydropower and Dams*, *20*(5).

Elbadry, M. M., & Ghali, A. (1983). Temperature Variations in Concrete Bridges. *Journal of Structural Engineering*, *109*(10), 2355–2374.

Esposito, R. (2016). *The Deteriorating Impact of Alkali-Silica Reaction on Concrete: Expansion and Mechanical Properties*. Ipskamp Drukkers.

Esposito, R., & Hendriks, M. A. N. (2012). Degradation of the mechanical properties in ASR-affected concrete: Overview and modeling. *Numerical Modeling Strategies for Sustainable Concrete Structures - SSCS 2012*.

Fairbairn, E., Ribero, F., Toledo-Filho, R., Lopes, L., & Silvoso, M. (2004). Smeared cracking FEM simulation of alkali silica expansion using a new macroscopic coupled model. *12th International Conference on Alkali-Aggregate Reaction - ICAAR*.

Farage, M. C. R., Alves, J. L. D., & Fairbairn, E. M. R. (2004). Macroscopic model of concrete subjected to alkali–aggregate reaction. *Cement and Concrete Research*, *34*(3), 495–505.

Fecteau, P. L., Fournier, B., Choquette, M., & Duchesne, J. (2012). Contribution to the understanding of the so-called alkali–carbonate reaction (ACR). *14th International Conference on Alkali-Aggregate Reaction - ICAAR*.

FERC. (2002). *Engineering Guidelines for the Evaluation of Hydroelectric Projects - Chapter 3. Gravity dams*.

Fournier, B., & Bérubé, M.-A. (2000). Alkali-aggregate reaction in concrete: a review of basic concepts and engineering implications. *Canadian Journal of Civil Engineering*, *27*(2), 167–191.

Gautam, B. P., Panesar, D. K., Sheikh, S. A., & Vecchio, F. J. (2017). Multiaxial expansion-stress relationship for alkali silica reaction-affected concrete. *ACI Materials Journal*, *114*(1), 171–184.

Giaccio, G., Zerbino, R., Ponce, J. M., & Batic, O. R. (2008). Mechanical behaviour of concretes damaged by alkali-silica reaction. *Cement and Concrete Research*, *38*(7), 993–1004.

Glasser, L. S. D., & Kataoka, N. (1981). The chemistry of 'alkali-aggregate' reaction. *Cement and Concrete Research*, *11*(1), 1–9.

Gocevski, V., & Yildiz, E. (2017). Macro-modelling of AAR-affected hydraulic structures. *Dam Swelling Concrete (DSC 2017)*.

Goldgruber, M. (2015). *Nonlinear Seismic Modelling of Concrete Dams* [PhD Thesis]. Graz Technical University.

Gorga, R. V. (2018). *Engineering-Based FE Approach to Appraise Slender Structures Affected by Alkali-Aggregate Reaction (AAR)* [M.A.Sc. Thesis]. University of Ottawa.

Gorga, R. V., Sanchez, L. F. M., Martín-Pérez, B., Fecteau, P. L., Cavalcanti, A. J. C. T., & Silva, P. N. (2020). Finite Element Assessment of the ASR-Affected Paulo Afonso IV Dam. *Journal of Performance of Constructed Facilities*, *34*(4).

Goshayeshi, N. (2019). *Contribution to the Development of Analytical Models to Forecast Alkali-Aggregate Reaction (AAR) Kinetics and Induced Expansion* [M.A.Sc. Thesis, University of Ottawa].

Grimal, E., Sellier, A., Le Pape, Y., & Bourdarot, E. (2008). Creep, shrinkage, and anisotropic damage in alkali-aggregate reaction swelling Mechanism-Part I: A constitutive model. *ACI Materials Journal*, *105*(3), 227–235.

Grimal, E., Sellier, A., Pape, Y. Le, & Bourdarot, E. (2008). Creep, Shrinkage, and Anisotropic Damage in Alkali-Aggregate Reaction Swelling Mechanism-Part II: Identification of Model Parameters and Application. *ACI Materials Journal*, *105*(3), 236–242.

Gustafsson, A., Johansson, F., Rytters, K., & Stille, H. (2008). *Betongdammars glidstabilitet - förslag på nya riktlinjer - Elforsk report 08:59*.

Hjalmarsson, F., & Pettersson, F. (2017). *Finite element analysis of cracking concrete-arch dam due to seasonal temperature variation* [M.A.Sc. Thesis]. Lund University.

Hobbs, D. W. (1988). *Alkali-silica reaction in concrete*. Thomas Telford Publishing.

Huang M., & Pietruszczak S. (1996). Numerical analysis of concrete structures subjected to alkali-aggregate reaction. *Mechanics of Cohesive-Frictional Materials*, *1*(4), 305–319.

ICOLD Technical Committee A. (2022). *Non-Linear Modelling of Concrete Dams - Bulletin*.

IStructE. (1992). *Structural effects of alkali-silica reaction : Technical guidance on the appraisal of existing structures*. Institution of Structural Engineers (IStructE) Ltd.

Jirasek, M. (2014). *Modeling of localized inelastic deformation*.

Johnson, S. (2006). *Comparison of Nonlinear Finite Element Modeling Tools for Structural Concrete*.

Karwa, R. (2017). Heat and mass transfer. In *Heat and Mass Transfer*. Springer Singapore.

Katayama, T. (2012). Late-expansive ASR in a 30-year old PC structure in eastern Japan. *14th International Conference on Alkali-Aggregate Reaction - ICAAR*.

Katayama, T., & Grattan-Bellew, P. E. (2012). Petrography of Kingston experimental sidewalk at age 22 years - ASR as the cause of deleteriously expansive, so-called alkali-carbonate reaction. *14th International Conference on Alkali-Aggregate Reaction - ICAAR*.

Kladek, I., Pietruszczak, S., & Gocevski, V. (1995). Modelling of mechanical effects of alkali–silica reaction in Beauharnois powerhouse. *5th International Symposium on Numerical Models in Geomechanics*, 639–645.

Kubo, Y., & Nakata, M. (2012). Effect of reactive aggregate on mechanical properties of concrete affected by alkali-silica reaction. *14th International Conference on Alkali-Aggregate Reaction - ICAAR*.

Kurihara, T., & Katawaki, K. (1989). Effects of moisture control and inhibition on alkali silica reaction. *8th International Conference on Alkali-Aggregate Reaction - ICAAR*, 629–634.

Kurtis, K. E., & Monteiro, P. J. M. (2003). Chemical additives to control expansion of alkali-silica reaction gel: Proposed mechanisms of control. *Journal of Materials Science*, *38*(9), 2027–2036.

Larive, C. (1997). *Apports combinés de l'expérimentation et de la modélisation à la compréhension de l'alcali-réaction et de ses effets mécaniques*.

Léger, P., Côté, P., & Tinawi, R. (1996). Finite element analysis of concrete swelling due to alkali-aggregate reactions in dams. *Computers & Structures*, *60*(4), 601–611.

Leger, P., Venturelli, J., & Bhattacharjee, S. S. (1993). Seasonal temperature and stress distributions in concrete gravity dams. Part 2: behaviour. *Canadian Journal of Civil Engineering*, *20*(6), 999–1017.

Li, K., & Coussy, O. (2002). Concrete ASR degradation: from material modeling to structure assessment. *Concrete Science and Engineering*, *4*(13), 35–46.

Li, K., & Coussy, O. (2004). Numerical assessment and prediction method for the chemico-mechanical deterioration of ASR-affected concrete structures. *Canadian Journal of Civil Engineering*, *31*(3), 432–439.

Li, K., Ulm, F. J., Coussy, O., Larive, C., & Fan, L. (2000). Chemoelastic modelling of alkali-silica reaction in concrete. *11th International Conference on Alkali-Aggregate Reaction in Concrete - ICAAR*.

Logan, D. L. (2011). *A First Course in the Finite Element Method* (5th ed., Issue Isbn 0495667919). CL Engineering.

Luikov, A. V. (1980). *Heat and mass transfer*. Mir Publishers.

Malkawi, A. I. H., Mutasher, S. A., & Qiu, T. J. (2003). Thermal-Structural Modeling and Temperature Control of Roller Compacted Concrete Gravity Dam. *Journal of Performance of Constructed Facilities*, *17*(4), 177–187.

Malla, S., & Wieland, M. (1999). Analysis of an arch–gravity dam with a horizontal crack. *Computers & Structures*, *72*(1–3), 267–278.

Malm, R. (2016). *Guideline for FE analyses of concrete dams*.

Malvern, L. E. (1969). *Introduction to the mechanics of continuous medium*. Prentice-Hall Inc.

McKay, M., & Lopez, F. (2013). *Practical methodology for inclusion of uplift and pore pressures in analysis of concrete dams*.

Mehta, P. K., & Monteiro, P. J. M. (2014). *Concrete: Microstructure, Properties, and Materials* (4th ed.). McGraw-Hill Education.

Metalssi, O. O., Seignol, J. F., Rigobert, S., & Toutlemonde, F. (2014). Modeling the cracks opening-closing and possible remedial sawing operation of AAR-affected dams. *Engineering Failure Analysis*, *36*, 199–214.

Mirambell, E., & Aguado, A. (1990). Temperature and Stress Distributions in Concrete Box Girder Bridges. *Journal of Structural Engineering*, *116*(9), 2388–2409.

Moore, A. E. (1978). Effect ofMoore, A.E. electric current on alkali–silica reaction. *4th International Conference on Alkali–Aggregate Reaction - ICAAR*.

Multon, S. (2003). *Evaluation Expérimentale et Théorique des Effets Mécaniques de l'Alcali Réaction sur des Structures Modéles* [PhD. Thesis]. Université de Marne la Vallée.

Multon, S., & Toutlemonde, F. (2006). Effect of applied stresses on alkali–silica reaction-induced expansions. *Cement and Concrete Research*, *36*(5), 912–920.

Nguyen, T. N., Sanchez, L. F. M., Li, J., Fournier, B., & Sirivivatnanon, V. (2022). Correlating alkali-silica reaction (ASR) induced expansion from short-term laboratory testings to long-term field performance: A semi-empirical model. *Cement and Concrete Composites*, *134*(2).

Niazi, M. S., Wisselink, H. H., & Meinders, T. (2012). Viscoplastic Regularization of Local Damage Models: A Latent Solution. *Key Engineering Materials*, *504–506*, 845–850.

Nishibayashi, S., Okada, K., Kawamura, M., Kobayashi, K., Kojima, T., Miyagawa, T., Nakano, K., & Ono, K. (1991). Alkali-silica reaction—Japanese experience. In *The Alkali-Silica Reaction in Concrete* (1st ed., pp. 270–306). CRC Press.

Olafsson, H. (1986). The effect of relative humidity and temperature on alkali expansion of mortar bars. *7th International Conference on Concrete Alkali-Aggregate Reactions - ICAAR*.

Ozol, M. A. (1990). *Alkali–silica reaction of concrete electrical substation piers accelerated by electrical currents - Petrography applied to concrete and concrete aggregates*.

Pan, J., Feng, Y. T., Jin, F., & Zhang, C. (2013). Numerical prediction of swelling in concrete arch dams affected by alkali-aggregate reaction. *European Journal of Environmental and Civil Engineering*, *17*(4), 231–247.

Pan, J., Feng, Y., Xu, Y., Jin, F., Zhang, C., & Zhang, B. (2013). Chemo-damage modeling and cracking analysis of AAR-affected concrete dams. *Science China Technological Sciences*, *56*(6), 1449–1457.

Pesavento, F., Gawin, D., Wyrzykowski, M., Schrefler, B. A., & Simoni, L. (2012). Modeling alkali–silica reaction in non-isothermal, partially saturated cement based materials. *Computer Methods in Applied Mechanics and Engineering*, *225–228*, 95–115.

Póvoas, R. H. C. F. (1991). *Modelos não-lineares de análise e dimensionamento de estruturas laminares de betão incluindo efeitos diferidos* [Ph.D. Thesis]. University of Porto.

Poyet, S., Sellier, A., Capra, B., Thèvenin-Foray, G., Torrenti, J.M., Tournier-Cognon, H., & Bourdarot, E. (2006). Influence of Water on Alkali-Silica Reaction: Experimental Study and Numerical Simulations. *Journal of Materials in Civil Engineering*, *18*(4), 588–596.

Rodríguez, J., González, P., Martinez, F., & Marti, J. (2012). Concrete Swelling in a Double Curvature Dam. *14th International Conference on Alkali-Aggregate Reaction in Concrete, May 20 – 25, 2012, Austin, Texas | 14th International Conference on Alkali-Aggregate Reaction - ICAAR*.

Rogers, C., Grattan-Bellew, P. E., Doug Hooton, R., Ryell, J., & Thomas, M. D. A. (2000). Alkali-aggregate reactions in Ontario. *Canadian Journal of Civil Engineering*, *27*(2), 246–260.

Saati, V., & Mortazavi, A. (2009, May 19). Numerical Modeling of In-situ Stress Calculation Using Borehole Slotter Test. *International Symposium on Rock Mechanics (ISRM) - SINOROCK 2009*.

Sanchez, L. F. M. (2014). *Contribution to the Assessment of Damage in Aging Concrete Infrastructures Affected by Alkali-Aggregate Reaction* [PhD. Thesis]. Université Laval.

Sanchez, L. F. M., Fournier, B., Jolin, M., & Duchesne, J. (2015). Reliable quantification of AAR damage through assessment of the Damage Rating Index (DRI). *Cement and Concrete Research*, *67*, 74–92.

Sanchez, L. F. M., Fournier, B., Jolin, M., Mitchell, D., & Bastien, J. (2017). Overall assessment of Alkali-Aggregate Reaction (AAR) in concretes presenting different strengths and incorporating a wide range of reactive aggregate types and natures. *Cement and Concrete Research*, *93*, 17–31.

Saouma, V., & Perotti, L. (2006). Constitutive Model for Alkali-Aggregate Reactions. *Materials Journal*, *103*(3), 194–202.

Seignol, J. F., Boldea, L., Leroy, R., & Godart, B. (2016). Numerical model applied to the reassessment of the serviceability and safety of AAR-affected power-plant. *15th International Conference on Alkali-Aggregate Reaction - ICAAR*.

Seignol, J. F., Boldea, L., Leroy, R., Godart, B., & Hammerschlag, J. G. (2009). Hydro-power structure affected by alkali-aggregate reaction: a case study involving numerical re-assessment. *International Conference on Computational Technologies in Concrete Structures*.

Seignol, J. F., Omikrine-Metalssi, O., Baghdadi, N., & Toutlemonde, F. (2012). From AAR to DEF: numerical modeling of structures affected by expansive reactions in concrete. *14th International Conference on Alkali-Aggregate Reaction - ICAAR*.

Sellier, A., Multon, S., Buffo-Lacarrière, L., Vidal, T., Bourbon, X., & Camps, G. (2016). Concrete creep modelling for structural applications: non-linearity, multi-axiality, hydration, temperature and drying effects. *Cement and Concrete Research*, *79*, 301–315.

Shayan, A., & Song, G. (2000). Electrochemical effects of combined AAR and cathodic protection in concrete. *11th International Conference on Alkali–Aggregate Reaction - ICAAR*.

Simulia. (2014). *Abaqus/CAE - Complete Abaqus Environment* (6.14). Dassault Systèmes Corporation.

Smaoui, N., Bérubé, M. A., Fournier, B., & Bissonnette, B. (2004). Influence of specimen geometry, orientation of casting plane, and mode of concrete consolidation on expansion due to ASR. *Cement, Concrete and Aggregates*, *26*(2), 58–70.

Ulm, F.-J., Coussy, O., Kefei, L., & Larive, C. (2000). Thermo-Chemo-Mechanics of ASR Expansion in Concrete Structures. *Journal of Engineering Mechanics*, *126*(3), 233–242.

Urhan, S. (1987). Alkali silica and pozzolanic reactions in concrete. Part 1: Interpretation of published results and an hypothesis concerning the mechanism. *Cement and Concrete Research*, *17*(1), 141–152.

USACE. (1995). *Gravity dam design - Report EM 1110-2-2200*.

USBR. (2006). *State-of-Practice for the Nonlinear Analysis of Concrete*.

Veilleux, M. (1995). Hyrdo-Quebec`s experience using deep slot cutting to rehabilitate concrete gravity dams affected by alkali-aggregate reaction. *2nd International Conference on Alkali-Aggregate Reactions in Hydroelectric Plants and Dams*.

Vivian, H. E. (1981). The effect of drying on reactive aggregate and mortar expansions. *5th International Conference on Alkali-Aggregate Reaction - ICAAR*.

Wahalathantri, B. L., Thambiratnam, D. P., Chan, T. H. T., & Fawzia, S. (2011). A material model for flexural cracks simulation in reinforced concrete elements using ABAQUS. *EddBE2011*.

Winnicki, A., Seręga, S., & Norys, F. (2014). Chemoplastic modelling of Alkali-Silica Reaction (ASR). *Computational Modelling of Concrete Structures - Proceedings of EURO-C 2014*, *2*, 765–774.

Wood, G. M., & Johnson, R. A. (1993). *The Appraisal and Maintenance of Structures with Alkali-Silica Reaction*.

Wood, G. M., Norris, P., & Leek, D. (1989). Physical behaviour of AAR damaged concrete in structures and in test conditions. *8th International Conference on Alkali-Aggregate Reaction in Concrete - ICAAR*.

Yu, P., Li, R. Q., Bie, D. P., Liu, X. C., Yao, X. M., & Duan, Y. H. (2021). A coupled creep and damage model of concrete considering rate effect. *Journal of Building Engineering*, *45*(15).

# 3. GORGA (2018) APPROACH FOR MODELING AAR-AFFECTED SLENDER STRUCTURES - SUMMARY

## 3.1 General model description and validation analyses

The model proposed by Gorga et al. (Gorga, 2018; Gorga et al., 2018, 2021) uses the concrete damaged plasticity (CDP) model, available in the commercial FE software Abaqus Standard (Simulia, 2014), to simulate concrete. This material model describes the elastic and inelastic hydrostatic pressure-dependent behaviour of concrete under both compression and tension (Bompa & Onet, 2010; Simulia, 2014; Wahalathantri et al., 2011). Moreover, concrete crushing or tensile cracking are assumed as the main failure mechanisms, with cracking intensity and orientation being evaluated through the development of plastic strain. In summary, if an element or region overcomes the elastic limit, it starts developing plastic strain locally until global equilibrium is reached. This means that, as the load increases, the plastic zone also increases, thus simulating damage accumulation. Creep is only modeled indirectly according to Equations 3-1 and 3-2 (Collins & Mitchell, 1997). These equations represent creep strain through an isotropic reduction of the modulus of elasticity as a function of time, relative humidity, concrete strength, and volume-to-surface ratio. This equation is not dependent on the stress level.

$$\phi(t) = 3.5K_cK_f\left(1.58 - \frac{H}{120}\right)t_i^{-0.118}\left(\frac{(t-t_i)^{0.6}}{10+(t-t_i)^{0.6}}\right) \quad (3\text{-}1)$$

$$E_{eff}(t) = \frac{E}{1+\phi(t)} \quad (3\text{-}2)$$

where $t$ is the number of days after casting, $t_i$ is the number of days after casting when concrete was loaded, $\phi(t)$ is the creep coefficient, $H$ represents the relative humidity level, $K_f$ is a factor accounting for the concrete strength, $K_c$ is a factor that accounts for the influence of volume-to-surface ratio of the member, $E$ is the original modulus of elasticity and $E_{eff}(t)$ is the effective modulus of elasticity at time $t$.

The mechanical properties deterioration (i.e., reduction of modulus of elasticity, compressive strength and tensile strength) is assumed to be a function of the AAR expansion level, according to Sanchez et al. (2017) (as shown in Section 2.4). Therefore, the actual local degradation of all mechanical properties and their implication on the global structural behaviour can be accurately estimated throughout the service life of the structure.

As shown by Figure 2-10 through Figure 2-12, the reduction of modulus of elasticity can reach up to 65%, tensile strength up to 75% and compressive strength up to 35% for an expansion level of 0.3%. This means that assuming a constant value for the mechanical properties will severely underestimate the mechanical behaviour of the structure if the undamaged values are assumed, or not capture the original development and underestimate the development of the reaction if (damaged) values from a single point in time are adopted. Therefore, the only correct approach is to model the variation of the properties, as was performed by Gorga (2018).

AAR expansion is modeled by an imposed anisotropic and stress-state dependent equivalent AAR strain, according to Gautam et al. (2017), as described in Section 2.3. This was implemented through an Abaqus user subroutine (USDFLD), programmed in Fortran and applied individually to each concrete element of the simulation.

The unrestrained reaction kinetics and expansion prediction over time (i.e., reference free expansion input curve) are calculated according to the physicochemical semi-empirical model developed by Goshayeshi (2019). The semi-empirical model is an adaptation of Larive's curve (Larive, 1997) with the addition of new parameters to account for the direct effect of temperature, aggregate type (coarse, fine or coarse and fine), aggregate reactivity (from negligible to very high damage degree), moisture (i.e., relative humidity), and alkali content in the mix. The parameters have a clear physical meaning and can vary over time, allowing for an accurate representation of the in-service condition of affected structures and indirectly representing phenomena like size effect and exposure conditions. The base equation is presented by Equation 3-3. Additionally, it was observed that the semi-empirical AAR model is able to roughly capture the in-service expansion potential based on long-term test results reported by Fournier et al. (2016) and Sanchez et al. (2016). This is the main assumption linking reaction kinetics obtained from accelerated laboratory tests and in-service structures.

$$\varepsilon_{ASR}(t) = \frac{1 - e^{-\frac{t}{\tau_c k_{C,T} k_{C,RH}}}}{1 + e^{-\frac{(t - \tau_l k_{L,T} k_{L,RH})}{\tau_c k_{C,T} k_{C,RH}}}} \times (k_{\infty,T} k_{\infty,RH} k_{\infty,A}) \varepsilon_{ASR}^{\infty} \tag{3-3}$$

where $\tau_c$ is the characteristic time, $\tau_l$ is the latency time, $\varepsilon_{AAR}^{\infty}$ is the expansion at infinity, $k_{C,T}$ is the temperature modification coefficient for $\tau_c$, $k_{C,RH}$ is the relative humidity modification coefficient for $\tau_c$, $k_{L,T}$ is the temperature modification coefficient for $\tau_l$, $k_{L,RH}$ is the relative humidity modification coefficient for $\tau_l$, $k_{\infty,T}$ is the temperature modification coefficient for $\varepsilon_{ASR}^{\infty}$, $k_{\infty,RH}$ is the relative humidity modification coefficient for $\varepsilon_{ASR}^{\infty}$, and $k_{\infty,A}$ is the alkali content modification coefficient for $\varepsilon_{ASR}^{\infty}$.

Steel rebars are modeled as an elasto-plastic material, following the true stress-strain curve of the material. Therefore, damage propagation at or close to structural failure can be correctly assessed. Perfect bond between rebars and concrete is assumed, as nodes are shared between both materials. The authors performed a total of two validations before using the proposed approach to simulate real structures, including simulating sound reinforced concrete and ASR-affected reinforced concrete. All data was based on experimental results obtained through laboratory tests.

As shown in Figure 3-1, modelling sound reinforced concrete proved that the material models and modeling approach was able to accurately represent the structural behaviour of the reinforced concrete members up to (shear or bending) failure. Experimental values were obtained from

Vecchio & Shim (2004), with a total of 6 beams being simulated in order to try to incorporate a reasonable range of spans (3.6 to 6.4 m) and failure modes (diagonal tension, shear compression and flexure compression). Note that this work was selected because it not only reports the force vs displacement curve of each beam, but also their cracking pattern and alternative FE modeling approach for comparison. The analysis was conducted in 2D, using truss elements (T2D2) to represent the reinforcement and plane-stress elements with reduced integration (CPS4R) to model concrete. The ultimate load prediction and the cracking pattern were accurately captured for all beams used in the validation. The predicted ultimate deflection at midspan for the sound concrete validation was satisfactory, even though a larger variability was observed. Additionally, parametric analyses were performed to determine the optimal values for the coefficients of the CDP model, which were used for all subsequent simulations.

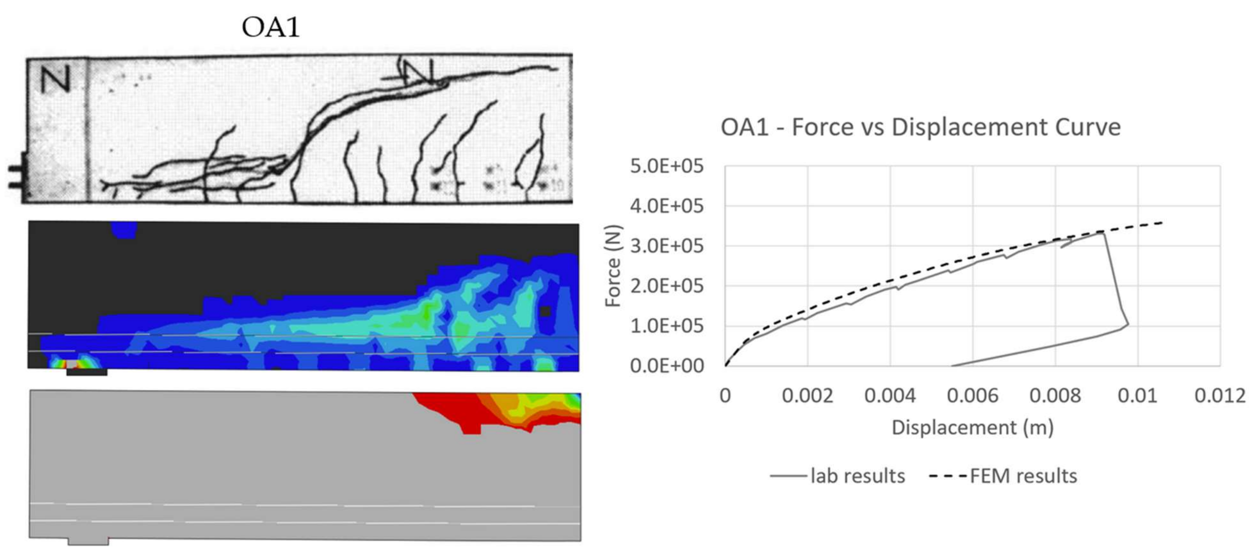


**Figure 3-1. Sound reinforced concrete validation results for Beam OA1 – Left (from top to bottom): reported damage, FE tensile damage and FE compressive damage (represented by plastic strain); Right: Force-displacement curve reported vs calculated (FE). Experimental values adapted from Vecchio & Shim (2004).**

Moreover, the anisotropic stress-state dependent ASR expansion behaviour (Gautam et al., 2017) was validated by simulating ASR-affected push-off specimens with different amounts of reinforcement confinement, i.e., containing zero, two or four 400R steel 10M stirrups (Sanchez et al., 2016) (Figure 3-2). The authors performed a series of tests with different reinforcement ratios, ASR-induced damage levels and confinement configurations to evaluate the effect of ASR damage on the shear capacity of reinforced concrete members, having recorded the AAR expansion over time along the critical shear plane. All specimens were 650-mm high, 450-mm wide and 200-mm thick. The aggregate used was a highly reactive gravel from New Mexico, USA (with a mineralogical composition comprised of mixed volcanic, quartzite and chert), combined with a non-reactive natural sand. The concrete presented a compressive strength of 35 MPa at 28 days and a total alkali loading of 4.63 $kg/m^3$. The push-off specimens were fabricated and stored according to the CPT test (i.e., 38°C at 100% RH) to accelerate ASR development. The FE model was built with three-dimensional coupled temperature-displacement 8-node elements with reduced integration (C3D8RT) representing the concrete and three-dimensional 2-node beam elements (B31) to model the reinforcement. Perfect bond was assumed. Results for the four stirrups specimen (4S) were slightly higher than the experimental values for a combination of the following reasons: 1) anisotropic model adopted not being able to fully describe the stress-state dependency of AAR considering that it doesn't account for the influence of tensile stresses on the expansion; 2) the mathematical implementation not being able to fully described the development of stresses due to AAR over time, especially in the early stages; 3) not modelling the variability of macro effects due to the complex and anisotropic nature of AAR-affected concrete micro-structure (pore distribution, aggregate size, shape, texture and mineralogy, gel formation, etc.); and 4) influence of confinement on chemical development of the reaction, which is still not fully understood. Nevertheless, results were found to be accurate overall.

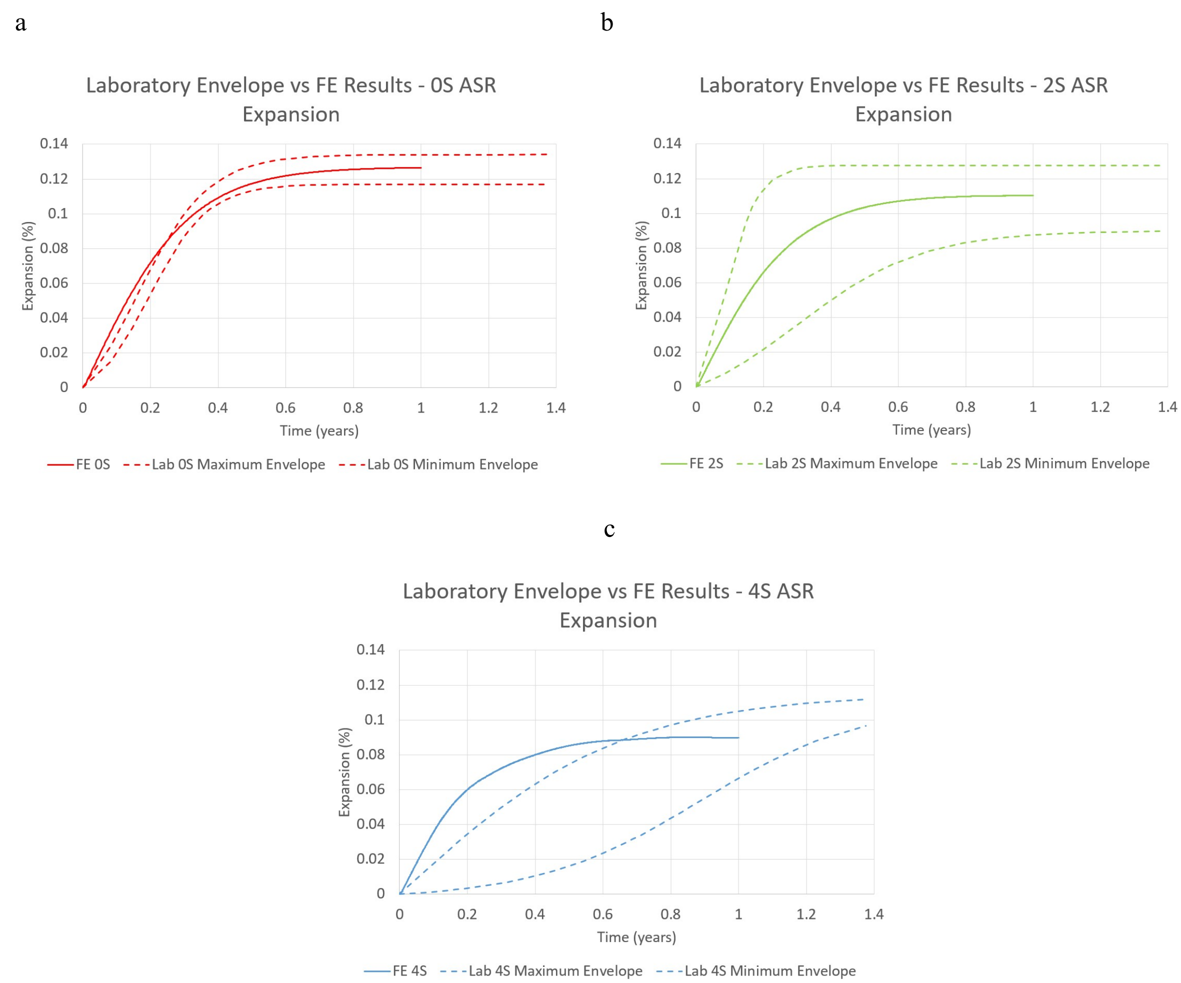


**Figure 3-2. Expansion vs time curve - FE results and lab envelopes: a. 0S (no stirrups), b. 2S (two stirrups), c. 4S (four stirrups). Source: Gorga et al. (2018).**

Note that a full description of the validation analyses previously described, including all the finite element implementation and assumptions adopted, can be found in Gorga et al. (Gorga, 2018; Gorga et al., 2018, 2021).

## 3.2 Robert Bourassa Charest (RBC) Overpass

The modelling approach summarized in Section 3.1 was applied to the Robert-Bourassa Charest (RBC) overpass, which was an ASR-affected highway bridge structure built in 1966 in Quebec City, Canada. The reinforced concrete structure comprised a deck of varying thickness, four rows of eight Y-shaped piers and massive concrete foundations. The piers were classified in 2 different categories: exposed (E) and non-exposed (NE) piers (Sanchez et al., 2018). Exposed piers were assumed to be highly subjected to solar radiation, weathering (rain, snow, freezing rain, etc.), pollution and splashing of both water and de-icing salts. Conversely, non-exposed piers were considered to be mostly protected from those factors because of their surroundings. The overall geometry of the RBC is shown in Figure 3-3.

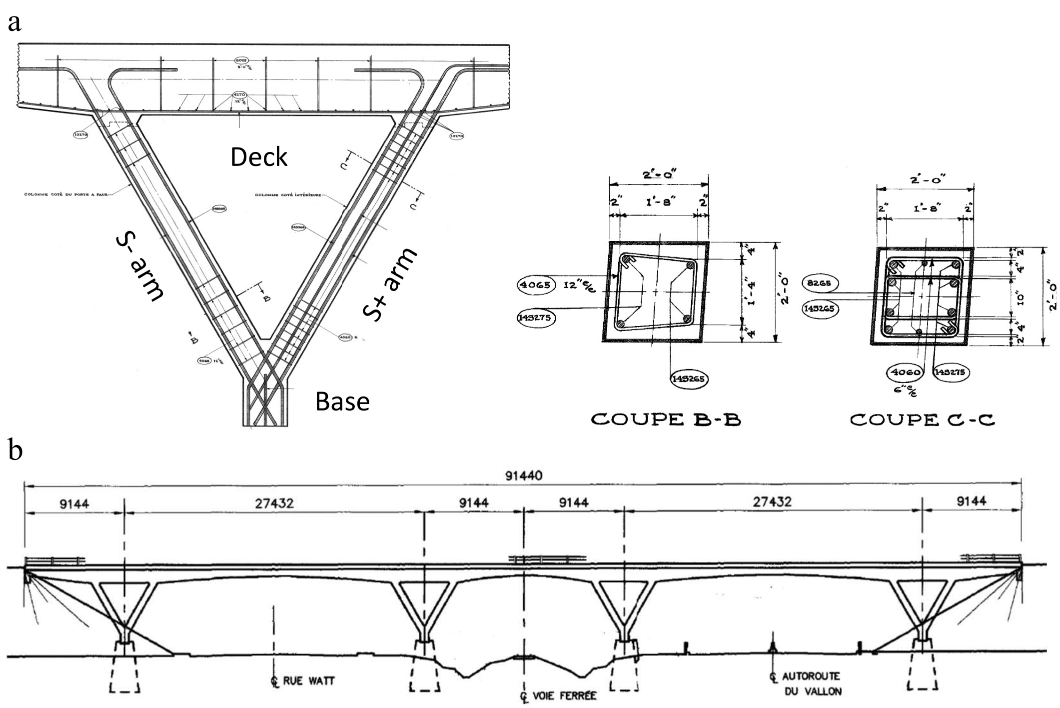


**Figure 3-3. Y-shaped pier original design: a. Reinforcement detail (dimensions in inches), b. Overpass longitudinal view (dimensions in mm). Source: Adapted from MTQ - Ministry of Transportation of Quebec (1964).**

Over the last three decades of the service life of the overpass, several distress signs were observed on various structural members (Bérubé et al., 2005). The deck presented steel corrosion and concrete delamination/spalling. The foundation showed signs of concrete map cracking, scaling, disaggregation, and pop-outs. The piers presented concrete spalling and steel corrosion. According to microscopic analyses, the prior distress signs were mainly triggered by ASR and freeze-thaw (FT) cycles. Due to the extent of damage and results from laboratory tests, the structure was considered unsafe and was demolished in 2010/2011. However, prior to the demolition, cores were extracted and some pier arms were taken to a laboratory for further microscopic and mechanical (macroscopic) analyses (Sanchez et al., 2016). The data from these tests enabled a thorough evaluation of the bridge's damage degree at the time of the demolition.

Amongst the analyses performed, interesting results were obtained through the Damage Rating Index (DRI), a microscopic tool often used to appraise damage and development of internal swelling reaction (ISR) mechanisms such as AAR (Sanchez et al., 2016). Results were able to determine an equivalent expansion level for each exposure class, which can be understood as the estimated ASR development (or expansion attained to date) needed to cause a damage degree similar to that observed in the DRI procedure. An average value of 0.05% for the NE piers and 0.09% for the E piers was determined, even though the aggregate was considered highly reactive and would present a free expansion potential of 0.20-0.25% in the concrete prism test according to CSA A23.2-14A (2014).

Moreover, strain relief tests were performed on the stirrups of both piers (Sanchez et al., 2016). The strain was measured using strain-gauges at the middle of stirrups of the S+ arm. Average values indicated that the average strain was equal to 569 µstrain for the NE piers and 1,290 µstrain for the E piers.

A model of the pier was created for each exposure condition, accounting for the local climatic data, reinforcement confinement (Saatcioglu & Razvi, 1992), concrete creep and mechanical properties deterioration as a function of the expansion level (Table 3-1) (Gorga et al., 2018). It was assumed that the temperature of the entire slender member is the same, but the relative humidity of the environment was assumed to only affect the concrete cover, with the core being saturated (based on the equations proposed by Ulm et al. (2000) and Comi et al. (2012)). The influence of all additional phenomena affecting the exposed pier (e.g., sun radiation and its consequent hourly variations of temperature or temperature gradients, exposure to rain and snow, exposure to de-icing salts, splashing due to traffic, pollution, etc.) was accounted for indirectly by changing the reference temperature and relative humidity. The temperature was increased by 13.5ºC according to the temperature differentials for exposure conditions of concrete structures (summer conditions) from CSA S6-14 (2014). Three approaches to alter the reference relative humidity were assessed: using the original values, assuming global increase and assuming local (cover only) increase. The new relative humidity was calculated by assuming 100% RH whenever it rained and the following day, based on the local daily values of precipitation.

**Table 3-1: Mechanical properties deterioration. Source: Sanchez et al. (2016).**

| Expansion [%] | 0.05% | 0.12% | 0.20% |
|---|---|---|---|
| $f'_c$ reduction [%] | 6.8 | 0.6 | 11.0 |
| E reduction [%] | 9.1 | 36.3 | 44.8 |
| $f'_t$ reduction [%] | 6.5 | 62.0 | 78.8 |

Analyses indicated that the best approach to simulate the effect of exposure is to increase the temperature and use the original relative humidity values, which is the only value discussed hereafter (Gorga et al., 2018).

The predicted equivalent damage, based on microscopic analyses, matched well with the reference expansion curves yielded by the semi-empirical ASR model when the climatic conditions were considered, as shown in Table 3-2.

Similarly, the stirrup strain obtained from the finite element model also matched the values measured in the laboratory (Gorga et al., 2018). An error of 3.2% was observed for the non-exposed case and -32.6% for the exposed case. This means that the proposed model is capable of accurately simulating the effects of the reaction when the climatic conditions are accounted for and the member is protected. Moreover, it was observed that the underestimation of the strain value for the exposed case is likely because the effect of other distress mechanisms (e.g., freeze-thaw (FT) cycles) was not simulated. Microscopic analyses estimated that approximately 25% of the damage observed on the exposed pier was due to FT, which corroborates the numerical results.

**Table 3-2: Equivalent (measured) vs reference (semi-empirical) expansions. Source: Gorga et al. (2018).**

| Case | Equivalent Expansion [%] | Reference Expansion [%] | |
|---|---|---|---|
| Non-Exposed | 0.05 | NE core | 0.06 |
| | | NE cover | 0.04 |
| Exposed | 0.09 | E core (RH original) | 0.11 |
| | | E cover (RH original) | 0.07 |

The cracking pattern obtained by the model matched the cracking orientation, cracking intensity and location of spalling/delamination observed in the field for both cases, as shown in Figure 3-4. Note that regions in blue are lightly damaged, regions in red are moderately damaged and regions in light grey are highly damaged (largest cracks and/or indication of possible spalling or delamination).

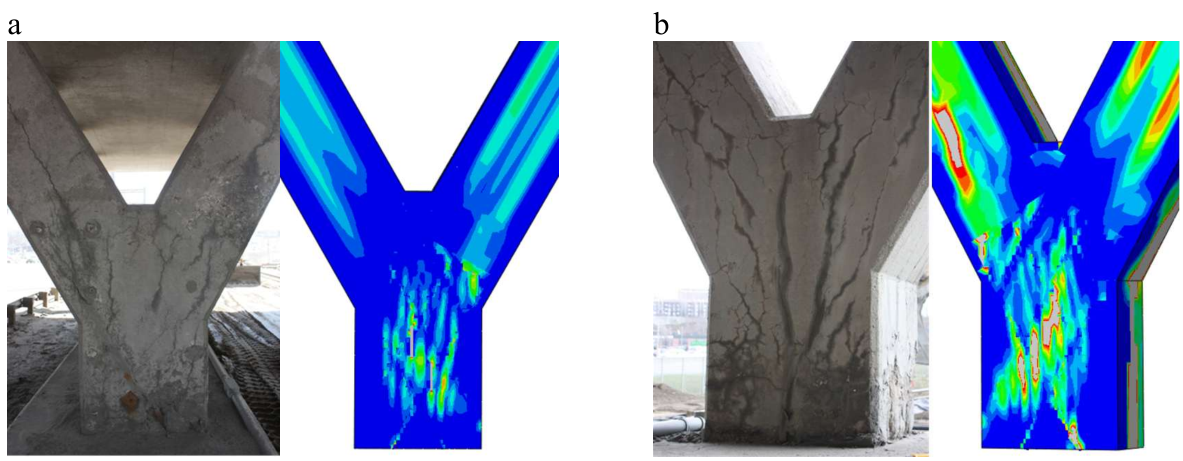


**Figure 3-4. Damage on the base of the pier (real and FE model plastic strain) at time of demolition: a. Non-exposed case, b. Exposed case. Source: Gorga et al. (2018).**

Lastly, it was observed that the structure was near global failure at the time of demolition, given that several stirrups in the exposed pier had already yielded due to ASR expansion. Therefore, the model results support the decision to demolish the overpass. The reinforcement stresses (in MPa) are shown in Figure 3-5.

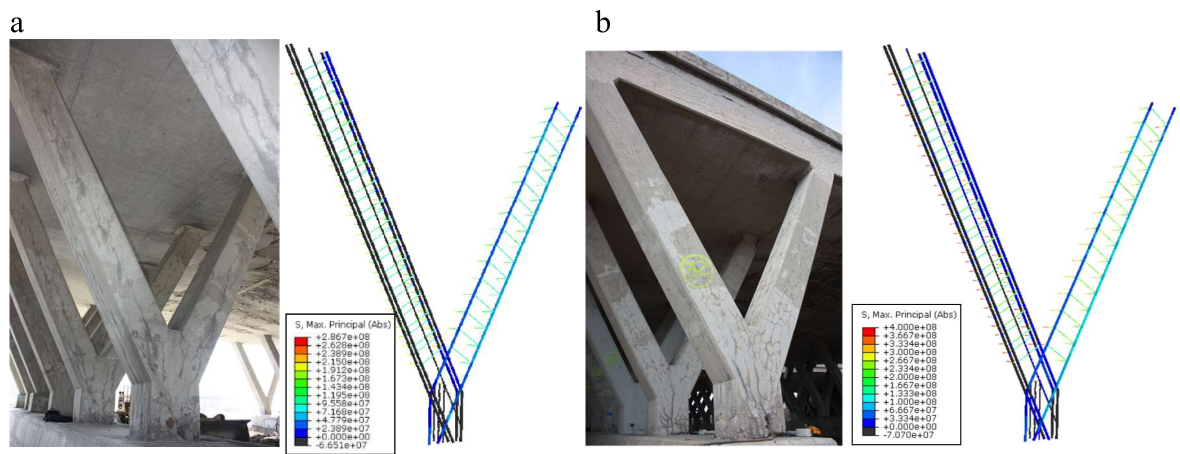


**Figure 3-5: Observed damage on the pier and FE model stress on reinforcement at time of demolition: a. Non-exposed case, b. Exposed case. Source: Gorga et al. (2018).**

### 3.3 References

Bérubé, M. A., Smaoui, N., Fournier, B., Bissonnette, B., & Durand, B. (2005). Evaluation of the expansion attained to date by concrete affected by alkali–silica reaction. Part III: Application to existing structures. *Canadian Journal of Civil Engineering*, *32*(3), 463–479.

Bompa, D. V., & Onet, T. (2010). Identification of concrete damaged plasticity constitutive parameters. *The National Technical-Scientific Conference- Modern Technologies for the 3rd Millenium*, 39–46.

Collins, M. P., & Mitchell, D. (1997). Stress-strain response of reinforcement. In *Prestressed concrete structures*. Reponse Publications.

Comi, C., Kirchmayr, B., & Pignatelli, R. (2012). Two-phase damage modeling of concrete affected by alkali–silica reaction under variable temperature and humidity conditions. *International Journal of Solids and Structures*, *49*(23–24), 3367–3380.

CSA A23.2-14A. (2014). *Potential Expansivity of Aggregates - Procedure for Length Change Due to Alkali-Aggregate Reaction in Concrete Prisms*.

CSA S6-14. (2014). *Canadian highway bridge design code*.

Fournier, B., Chevrier, R., Bilodeau, A., Nkinamubanzi, P.C., & Bouzoubaa, N. (2016). Comparative field and laboratory investigations on the use of supplementary cementing materials (SCMs) to control alkali-silica reaction (ASR) in concrete. *15th International Conference on Alkali-Aggregate Reaction - ICAAR*.

Gautam, B. P., Panesar, D. K., Sheikh, S. A., & Vecchio, F. J. (2017). Multiaxial expansion-stress relationship for alkali silica reaction-affected concrete. *ACI Materials Journal*, *114*(1), 171–184.

Gorga, R. V. (2018). *Engineering-Based FE Approach to Appraise Slender Structures Affected by Alkali-Aggregate Reaction (AAR)* [M.A.Sc. Thesis]. University of Ottawa.

Gorga, R. V., Sanchez, L. F. M., & Martín-Pérez, B. (2018). FE approach to perform the condition assessment of a concrete overpass damaged by ASR after 50 years in service. *Engineering Structures*, *177*, 133–146.

Gorga, R. V., Sanchez, L. F. M., Martín-Pérez, B., & Noël, M. (2021). Engineering-based finite-element approach to appraise reinforced concrete structures affected by alkali–aggregate reaction. *Magazine of Concrete Research*, *74*(8), 379–391.

Goshayeshi, N. (2019). *Contribution to the Development of Analytical Models to Forecast Alkali-Aggregate Reaction (AAR) Kinetics and Induced Expansion* [M.A.Sc. Thesis, University of Ottawa].

Larive, C. (1997). *Apports combinés de l'éxpérimentation et de la modélisation à la compréhension de l'alcali-réaction et de ses effets mécaniques*.

MTQ - Ministry of Transportation of Quebec. (1964). *Report on the Robert-Bourassa Charest overpass reinforcement and overall dimensions*.

Saatcioglu, M., & Razvi, S. R. (1992). Strength and Ductility of Confined Concrete. *Journal of Structural Engineering*, *118*(6), 1590–1607.

Sanchez, L. F. M., Fournier, B., Bastien, J., & Mitchell, D. (2016). *Assessment of structures subjected to concrete degradation*.

Sanchez, L. F. M., Fournier, B., Bastien, J., Mitchell, D., & Noël, M. (2016). Overall assessment of an ASR affected overpass "Robert-Bourassa/Charest" after nearly 50 years in service. *8th International Conference on Bridge Maintenance, Safety and Management - IABMAS*.

Sanchez, L. F. M., Fournier, B., Jolin, M., Mitchell, D., & Bastien, J. (2017). Overall assessment of Alkali-Aggregate Reaction (AAR) in concretes presenting different strengths and incorporating a wide range of reactive aggregate types and natures. *Cement and Concrete Research*, *93*, 17–31.

Sanchez, L. F. M., Noël, M., & Santos, V. A. A. (2018). Techniques to rehabilitate bridge columns affected by alkali-silica reaction (ASR). *9th International Conference on Bridge Maintenance, Safety and Management - IABMAS*, 1066–1073.

Simulia. (2014). *Abaqus/CAE - Complete Abaqus Environment* (6.14). Dassault Systèmes Corporation.

Ulm, F.-J., Coussy, O., Kefei, L., & Larive, C. (2000). Thermo-Chemo-Mechanics of ASR Expansion in Concrete Structures. *Journal of Engineering Mechanics*, *126*(3), 233–242.

Vecchio, F. J., & Shim, W. (2004). Experimental and Analytical Reexamination of Classic Concrete Beam Tests. *Journal of Structural Engineering*, *130*(3), 460–469.

Wahalathantri, B. L., Thambiratnam, D. P., Chan, T. H. T., & Fawzia, S. (2011). A material model for flexural cracks simulation in reinforced concrete elements using ABAQUS. *EddBE2011*.

# 4. TECHNICAL PAPER 01/03 – FINITE ELEMENT ASSESSMENT OF THE ASR-AFFECTED PAULO AFONSO IV DAM

Gorga, R.V.[a]; Sanchez, L. F. M. [a]; Martín-Pérez, B. [a]; Fecteau, P.L. [b]; Cavalcanti, A.J.C.T. [c]; Silva, P.N. [c]

(a) University of Ottawa, ON, Canada
(b) GHD, Quebec City, QC, Canada
(c) CHESF, Recife, PE, Brazil

## 4.1 Abstract

Various numerical models have been developed to appraise alkali-silica reaction (ASR) induced expansion and to predict its potential to generate further damage. Gorga et al. (2018) proposed a finite element approach that does not oversimplify nor overcomplicate the reaction analysis, while still being capable of representing the anisotropic expansion and its macroscopic consequences. Slender structures have already been successfully simulated using this approach, although it has never been applied to assess massive structures. This paper presents the validation analyses and the simulations performed on an ASR-affected dam in Brazil to appraise the accuracy of the previously proposed approach for massive structures. Results suggest that the numerical model is quite promising for appraising ASR development over time, based on both the damage observed in the field and on test specimens. Moreover, phenomena not directly accounted for in the model (such as alkali release from aggregates and the absence of important amount of leaching) were found to play an important role in ASR-affected massive structures.

*Keywords: alkali-silica reaction (ASR), concrete deterioration, expansion, finite element, dam, mass concrete*

## 4.2 Introduction

### 4.2.1 AAR Finite Element Modelling

Alkali-aggregate reaction (AAR) is one of the most harmful distress mechanisms affecting the durability and serviceability of critical infrastructure worldwide. AAR is generally divided into two main categories: alkali-carbonate reaction (ACR) and alkali-silica reaction (ASR), with the latter being by far the most common AAR type found around the world (Fournier & Bérubé, 2000). ASR is a chemical reaction between "unstable" silica mineral forms within the aggregates and alkali hydroxides (Na, K – OH) dissolved in the concrete pore solution (Fournier & Bérubé, 2000). This generates a secondary alkali-silica gel that induces expansive pressures within the reacting aggregate material(s) and the adjacent cement paste upon moisture uptake from its surrounding environment. This phenomenon eventually leads to microcracking, reduction of the material's properties (mechanical/durability) and, in some cases, structural implications capable of affecting the functionality of the structure (Fournier & Bérubé, 2000).

One of the most challenging aspects of assessing AAR-affected aging infrastructure is to correlate its distress features with the reduction in mechanical properties, physical integrity, durability, and performance of the material along with its structural implications (Sanchez et al., 2015). In this context, a number of finite element (FE) models were developed with the aim of appraising the current distress condition of AAR-affected infrastructure (i.e., Diagnosis) along with predicting the potential of the reaction to generate further damage (i.e., Prognosis). A very intuitive classification is presented by Esposito (2016), where the existing ASR models are divided into 4 different categories: micro-models (based on ion diffusion/reaction products), micro-meso-models (based on gel production), meso-models (based on internal pressure) and macro-models (based on concrete expansion). The present work focuses only on macro-models, which is likely the only type of model capable of describing the overall structural implications of ASR on large structures.

Various macro-models have been developed over the past three decades, ranging from simple models, where isotropic strain is implemented to represent ASR's expansion (Charlwood, 1994), to very complex approaches, i.e., poromechanical models (Grimal, et al., 2008). According to Goshayeshi (2019), some of the most important parameters affecting the reaction are temperature, moisture (i.e., relative humidity), aggregate reactivity, aggregate type, alkali content and exposure conditions. Moreover, according to Gautam et al. (2017) the expansion is anisotropic and stress-state dependent. In general, the aforementioned models developed recently address most of those parameters in some way (Comi et al., 2012; Grimal, et al., 2008; Pan, et al., 2013; Saouma & Perotti, 2006). However, the model proposed by Gorga (2018) and validated for ASR-affected slender structures by Gorga et al. (2018) accounts for all of those parameters in a simple yet reliable fashion, without overcomplicating nor oversimplifying the physico-chemical aspects of the reaction. The approach has been proven to be very useful to appraise ASR-affected slender structures, yet its applicability to massive structures still has to be verified, which is the main purpose of the current work.

The FE model proposed by Gorga et al. (2018) is based on the concrete damaged plasticity (CDP) model, which is available in the commercial FE software Abaqus (Simulia, 2014), and it is capable of representing the elastic and inelastic hydrostatic pressure-dependent behaviour of concrete under both compression and tension (Bompa & Onet, 2010; Wahalathantri et al., 2011). Moreover, its main failure mechanisms are assumed to be either concrete crushing or tensile cracking, and the model is capable of qualitatively estimating the cracking intensity and orientation by evaluating the plastic strain. In summary, if an element or region overcomes the elastic limit, it starts developing plastic strain locally until global equilibrium is reached. This means that, as the load increases, the plastic zone also increases, thus simulating damage accumulation. The mechanical properties deterioration (i.e., reduction of modulus of elasticity, compressive strength and tensile strength) is assumed to be a function of the AAR expansion level, according to Sanchez et al. (2017). The AAR expansion is assumed to be anisotropic and stress-state dependent, as proposed by Gautam et al. (2017), which is implemented through an Abaqus user subroutine (USDFLD). Lastly, the reaction kinetics and expansion prediction over time were described by the physicochemical analytical model developed by Goshayeshi (2019) (reference free expansion input curve; see Appendix for further details) and computationally implemented in the FE model by imposing an equivalent AAR strain.

### 4.2.2 Paulo Afonso IV Dam

Paulo Afonso IV (PAIV) dam (Figure 4-1) is located in the city of Paulo Afonso, PE, Brazil, and it is owned by the Companhia Hidro-Elétrica do São Francisco (CHESF), who provided the data presented in this paper. The dam was built between 1975-1981 and started to operate in 1979, with the first signs of ASR being observed in 1985. The dam is currently in operation and, even though distress signs such as map cracking, alkali-silica gel leaching and water leaking have been observed, the reaction has not yet compromised the overall performance of the dam. Numerous regions of the dam have displayed significant damage due to ASR; yet, since the spillway has had the most data available, only this region is modeled and validated in this research.

a

b

**Figure 4-1. Paulo Afonso IV dam - Spillway: a. Overview, b. Close-up of the ASR damage.**

Laboratory test procedures and in-situ stress measurements were performed in order to determine the material properties of the structure (Cavalcanti et al., 2006). Moreover, the original design specifies the following aspects: a) coarse aggregate (granitic gneiss) with nominal maximum particle size of 19 mm, b) portland cement (PC type GU, ASTM type I) with high alkali content

(1.0%), c) 28-day compressive strength of 36 MPa, d) 357 $kg/m^3$ of PC, which yields a 3.57 $kg/m^3$ total alkali content in the concrete mixture and, e) five prestressed 7-wire strands of 48.3 mm diameter with initial prestressing stress of 149 MPa, yielding stress of 158 MPa and ultimate stress of 186 MPa. Note that a normal alkali content for PC type GU lies between 0.8% and 1% and that the coarse aggregate used in the dam may be classified as moderately reactive, according to Sanchez et al. (2016). Therefore, based on the description of the massive structure, two extra validation analyses needed to be performed before modeling the spillway to ensure that the model is properly accounting for the materials properties: i.e., a prestressed concrete and a thermal analysis validation.

### 4.2.3 Research Significance

This paper presents the condition assessment of the spillway of the ASR-affected PAIV dam. The main objective of this work is to verify the applicability and accuracy of the FE approach proposed by Gorga et al. (2018) for massive structures, which has already been successfully used for slender structures. The results obtained through the computational model are compared to available data on the current state of the structure with the aim of predicting the future behaviour (i.e., Prognosis) of the dam. Based on the presented information, a more accurate decision-making process regarding future structural intervention and rehabilitation will be possible.

## 4.3 Prestressed Concrete Validation

### 4.3.1 Description

Cheng et al. (2009) tested several five-meter long inverted T prestressed concrete beams and the case without circular opening along the length was chosen for this validation. The beam was simply supported on both ends, the loading was monotonic center-point and force-controlled. The full force-deflection curves at midspan and a picture of the beam right after global failure are presented in the paper. The geometry is presented below (Figure 4-2).

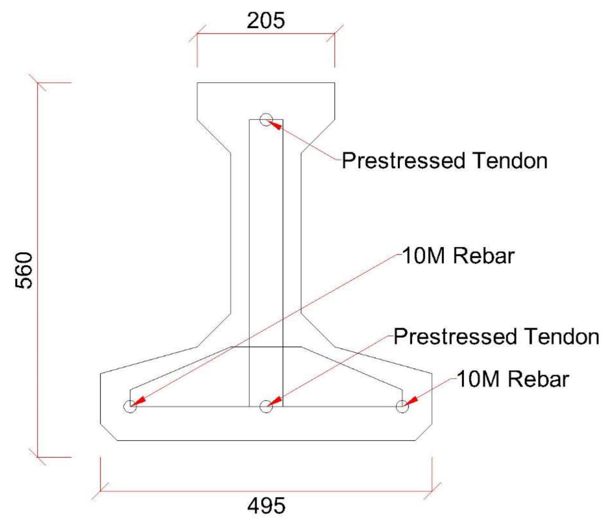


**Figure 4-2. Prestressed inverted T-beam (dimensions in mm). Source: Adapted from Cheng et al. (2009).**

The beam presented two 12.9 mm pretensioned prestressed strands with ultimate strength of 1860 MPa, one at the bottom and one at the top, as well as two 10M rebars with yielding stress of 350 MPa and 8M stirrups with yielding stress of 400 MPa. The strands were pretensioned with a force equal to 111.6 kN and then released once the concrete reached the desired compressive strength of 45 MPa.

The FE approach implemented was based on the sound concrete validation presented by Gorga et al. (2018). However, it is worth noting that there are two important differences here. First, an equivalent negative thermal gradient was imposed to the strands to simulate the prestressing prior to the load application. Second, the beam was assumed to fail whenever either the strands yielded (loss of prestressing) or the concrete reached the crushing strain (0. 35%).

### 4.3.2 Discussion of results

The force-deflection at midspan curves for both the laboratory test and the FE analysis are illustrated in Figure 4-3a, and a comparison of the cracking pattern for the ultimate load is presented in Figure 4-3b-c. Note that the only prestressing loss accounted for in the model was due to anchorage, which was assumed to be a 6-mm shortening of the strand according to Collins & Mitchell (1997).

a

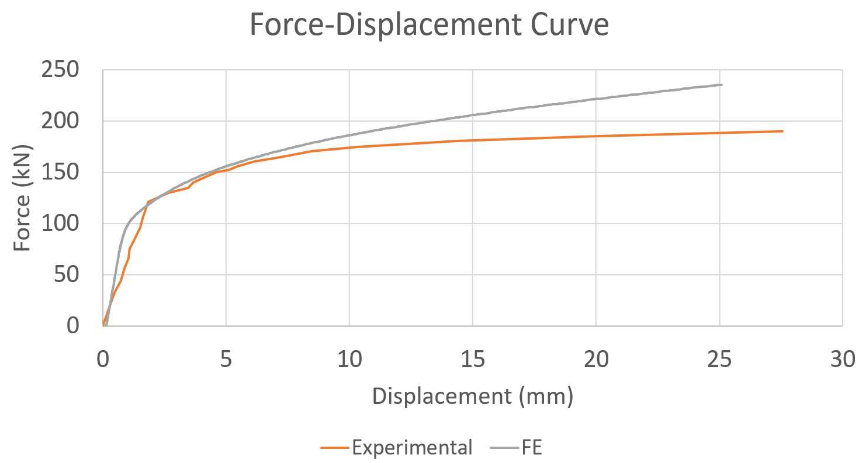


b

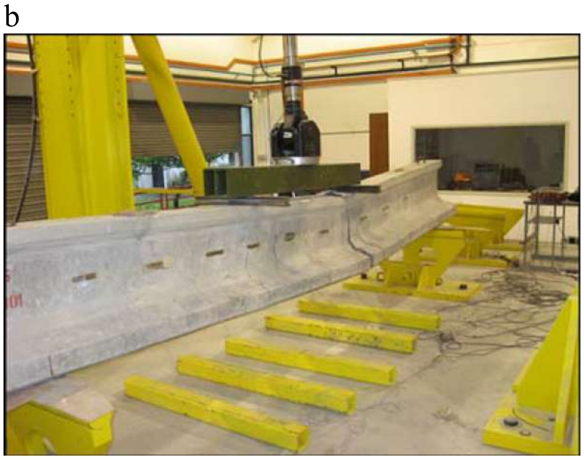

c

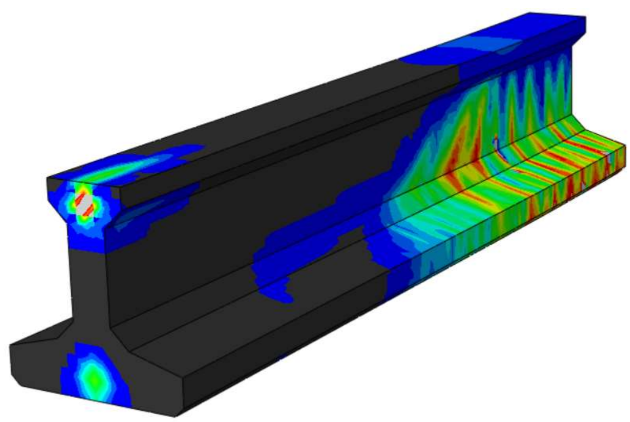

**Figure 4-3. Sound prestressed concrete validation: a. Comparison of experimental and FE results for prestressed concrete validation, b. Cracking pattern recorded in the lab (Cheng, et al., 2015), c. Cracking pattern (plastic strain) predicted by the FE model for half the beam.**

Based on Figure 5-3a, it is clear that the overall behaviour of the prestressed beam was captured. The initial slope of the FE curve was very close to what was observed in the experiment, as well as the point of slope change, which represents when the non-prestressed longitudinal reinforcement yields. The ultimate load presented an overestimation of 24%, and the ultimate deflection at midspan displayed an underestimation of only 8%, both of which are well within an acceptable error margin. It is noted that the ultimate load overestimation is likely related to the perfect bond assumption adopted for the reinforcement, which is not capable of describing the behaviour of the beam as accurately after reinforcement yields. Lastly, the cracking pattern comparison shown in Figure 4-3b-c shows that the FE model results matched well what was observed in the laboratory. In both cases, the beam failed by flexure, with several flexural (vertical) cracks being recorded close to the midspan.

## 4.4 Thermal Analysis Validation

### 4.4.1 Description

The temperature vs. time curves recorded by Lawrence (2009) on mass concrete blocks cast in the laboratory were used in the thermal analysis validation presented next. The author used a total of 4 different typical mass concrete mixes, with the mix entitled “1” being very similar to that used in the Paulo Afonso IV dam. The blocks were 1.07×1.07×1.07 m, and they were insulated on all four sides and at the bottom, while the top was exposed to the environment. The insulation consisted of an internal layer of plywood (19 mm on the sides and 38 mm at the bottom) and an external layer of polystyrene (76 mm on the sides and bottom). Moreover, the temperature was recorded over time at 25 mm, 102 mm and 533 mm below the surface at the center and the corner of the specimens until the temperature within the concrete stabilized. Finally, the heat of hydration (as energy per mass, i.e., W/g) was determined through isothermal calorimetry tests, as presented in Figure 4-4.

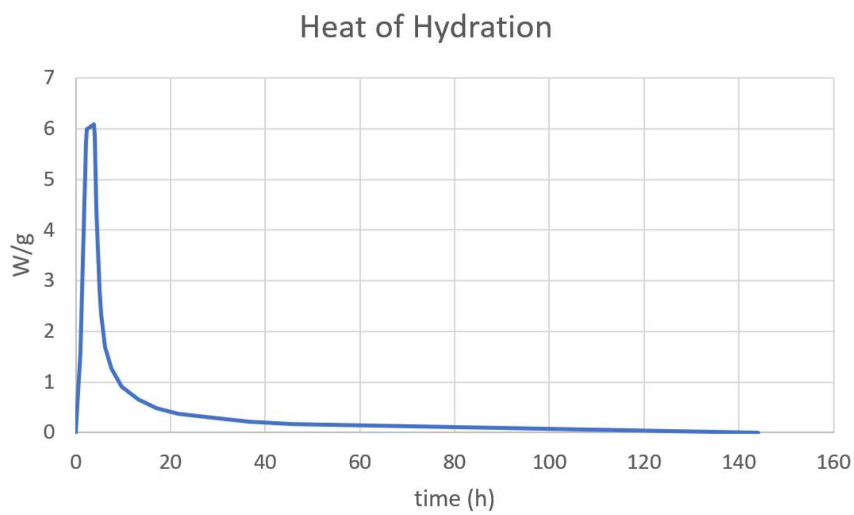


**Figure 4-4. Heat of Hydration over time for "mix 1". Source: Lawrence (2009).**

In order to simulate the thermal boundary conditions, both the concrete and the insulation were modeled. The external insulated surfaces were assumed as adiabatic and the surface exposed to the environment was modeled including both convection and radiation interactions. Perfect bond was assumed at the interfaces between different materials, allowing free heat flow. The mesh of one fourth of the concrete block is presented in Figure 4-5. Moreover, the coefficients presented in Table 4-1 and adopted in the analysis were based on values reported in the literature (Castilho et al., 2015; Lawrence, 2009; Léger et al., 1996; Malm, 2016).

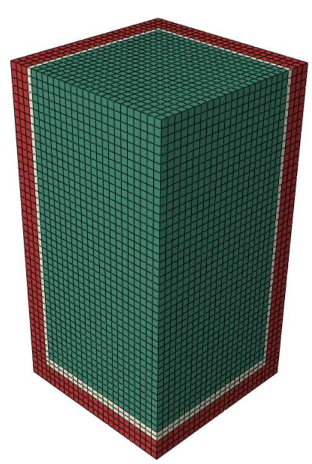

**Figure 4-5. Mesh of one-fourth of the concrete block (polystyrene in red, plywood in white and concrete in green).**

**Table 4-1. Thermal properties used in the sound concrete thermal analysis validation.**

| Property | Concrete | Plywood | Polystyrene | General |
|---|---|---|---|---|
| $E\ (GPa)$ | 44.2 | 8.3 | 2.5 | - |
| $\upsilon$ | 0.2 | 0.2 | 0.4 | - |
| $\rho\ (kg/m^3)$ | 2450 | 620 | 1000 | - |
| $\alpha$ | $1.0 \times 10^{-5}$ | $1.6 \times 10^{-5}$ | $8.5 \times 10^{-5}$ | - |
| Conductivity $(J/hmC)$ | 8532 | 540 | 126 | - |
| Specific Heat $(J/kgC)$ | 940 | 1377 | 27 | - |
| Air-Concrete Convection Coef. $(W/Cm^2)$ | - | - | - | 23 |
| Radiation Emissivity | - | - | - | 0.82 |
| Stefan-Boltzmann Constant $(J/hm^2K^4)$ | - | - | - | $2.04 \times 10^{-4}$ |

where $E$ represents the modulus of elasticity, $\upsilon$ is Poisson's ratio, $\rho$ is the specific density and $\alpha$ is the coefficient of volumetric expansion. It is also important to emphasize that the air temperature was modeled based on a sinusoidal curve (Léger et al., 1996) and that the sun radiation followed the LGJK1997 approach (Castilho et al., 2015). The latter is capable of estimating the heat flux that the structure will be subjected to and is based on several parameters, including latitude, surface orientation and inclination, hour of the day, day of the year, etc.

### 4.4.2 Discussion of Results

The temperature measured in the laboratory was compared to the results obtained through the FE model for the center and the corner of the concrete block, as presented in Figure 4-6.

a

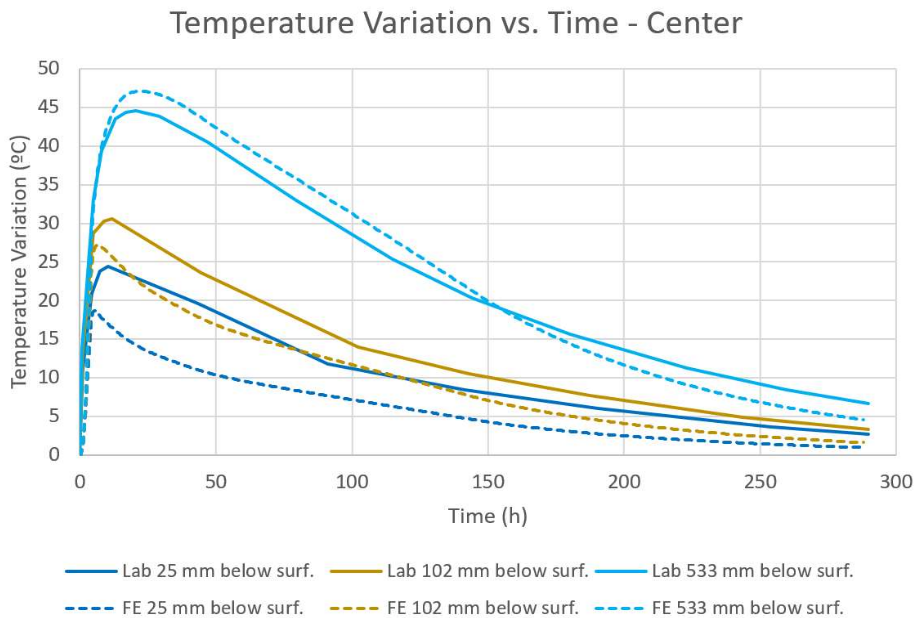


b

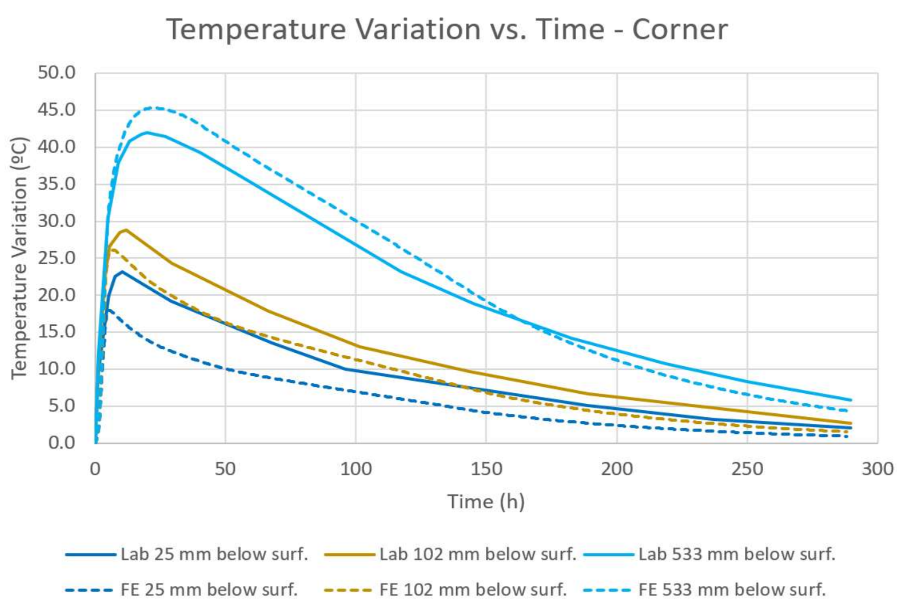


**Figure 4-6. Temperature variation vs. time: a. Blocks center, b. Blocks corner.**

As expected, the temperature closer to the surface reached a lower maximum temperature and stabilized faster than the other points, because the effect of both convection and radiation heat losses were more prominent there. Moreover, the results yielded by the FE model were satisfactorily close to the experimental values recorded. There is a relatively small underestimation of the temperature at 25-mm and 102-mm depths below the surface (with a maximum difference of -5.5ºC and -4.5ºC, respectively). Furthermore, there is a small overestimation of the temperature profile until approximately 50% of the analysis at a depth of 533-mm below the surface (with a maximum difference of 3ºC) and then a slight underestimation of the results until the end of the analysis. Considering that the thermal properties attributed to the materials were average values obtained from the literature and that the precision of the measuring device used was ±2.2ºC, the results presented led to the conclusion that the approach implemented properly simulated the thermal phenomena involved. Finally, the distribution of the temperature variation at different points in time is presented in Figure 4-7 to illustrate the early heat gain and consequent heat loss over the entire section.

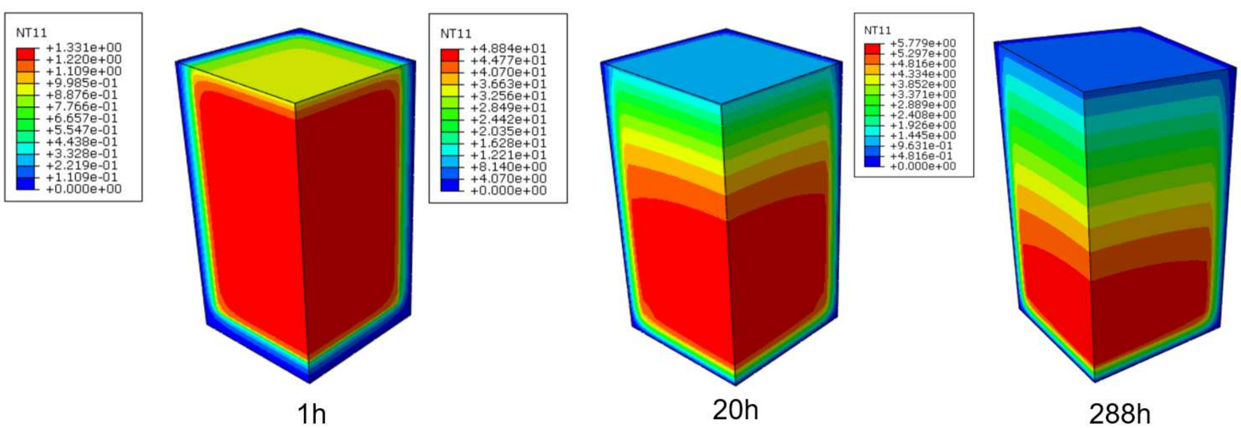


**Figure 4-7. Temperature variation (ºC) of one-fourth of the concrete block 1h, 20h and 288h after casting.**

## 4.5 Paulo Afonso IV Dam Analysis

### 4.5.1 Finite Element Implementation

The analysis of the dam is divided in two parts. First, a linear-elastic thermo-mechanical analysis of the spillway is performed to determine the stress-state due to thermal loads, as well as the variation of the temperature profile of the dam. Then, the residual thermal stresses are imported into a non-linear mechanical ASR model, which includes both the long-term loads, the residual thermal stresses and the reaction's expansion. The principle of superposition had to be assumed (residual thermal stresses are imported directly into the mechanical model) because of limitations of the software when modeling imposed strain and non-linear damage at the same time.

For both analyses, the soil is modeled through spring elements based on the mechanical properties measured by CHESF in the field (Cavalcanti et al., 2006). An alternative strategy to represent the soil-structure interaction would be to include elements to represent the surrounding soil. This would probably be just as accurate (if linear elastic materials had been used) or more accurate (if the soil had been modeled as a non-linear material) than the approach adopted. However, this option was not implemented, because it would be significantly more complex than using spring elements for three main reasons. First, it would be necessary to define several new parameters, which would require further validation analyses and which would introduce new uncertainties. Second, using elements to represent the soil would significantly increase the computational cost of the analysis. Third, meshing would be an even bigger challenge than what it already was, since the dam's geometry is so intricate. Therefore, the simplification of modeling the soil through spring elements was deemed to be the best option for the current analysis.

The mechanical properties of the concrete were determined based on field tests (Cavalcanti et al., 2006), which indicated that the average modulus of elasticity was 22 GPa, the Poisson ratio was 0.20 and the compressive strength was 40.6 MPa (in 2006). These values were used to develop the time and expansion dependent mechanical properties of the concrete based on the mechanical properties deterioration due to ASR (Sanchez et al., 2017), creep (Collins & Mitchell, 1997) and assuming a gain of compressive strength of 30% over time (Sanchez, 2014). In addition, steel relaxation was accounted for by reducing the modulus of elasticity of the prestressing strands over time (Collins & Mitchell, 1997).

The thermal material properties of the linear-elastic thermo-mechanical analysis were based on the values presented in Table 4-2 and assuming only the initial mechanical material properties (based on the premise that ASR would not have had time to develop yet), while the mechanical properties of the non-linear mechanical ASR analysis were assumed to vary over time.

**Table 4-2 Thermal properties used in the PAIV analysis.**

| Thermal Property | Unit | Value | Thermal Property | Unit | Value |
|---|---|---|---|---|---|
| Convection coef. water-conc. | $W/Cm^2$ | 500 | Specific heat reinforcement | $J/kgC$ | 465 |
| Convection coef. air-conc. | $W/Cm^2$ | 23.0 | Conductivity concrete | $W/Cm$ | 2.37 |
| Convection coef. rock-conc. | $W/Cm^2$ | 1000 | Conductivity rock mass | $W/Cm$ | 3.35 |
| Convection coef. rock-air | $W/Cm^2$ | 18.25 | Conductivity reinforcement | $W/Cm$ | 39 |
| Convection coef. rock-water | $W/Cm^2$ | 500 | Density rock mass | $kg/m^3$ | 2300 |
| Radiation absorptivity | - | 0.525 | Thermal exp. conc. | $1/C$ | 9.0E-06 |
| Radiation coefficient | $W/Cm^2$ | 4.72 | Thermal exp. rock mass | $1/C$ | 8.9E-06 |
| Emissivity | - | 0.82 | Ground reflectivity | - | 0.20 |
| Specific heat concrete | $J/kgC$ | 939 | Water reflectivity | - | 0.15 |
| Specific heat rock mass | $J/kgC$ | 874 | | | |

The thermal loads applied to the linear-elastic thermo-mechanical analysis were the following: convection (air-concrete, water-concrete and rock mass-concrete), radiation (air-concrete, water-concrete and rock mass-concrete), sun radiation (vertical surfaces, horizontal surfaces and inclined surfaces) and heat of hydration as energy per mass. The latter was based on mix 1 (Figure 4-4), which is quite similar to the concrete mixture of the spillway. Both air, water and soil were modeled as boundary conditions only. The water temperature was assumed to be equal to 80% of the air temperature (Malm, 2016), and the soil temperature was assumed to be equal to the air temperature. The loads applied to the non-linear mechanical ASR model were: prestressing, hydrostatic (both directly on the structure as a function of the depth and as pressure/surface traction load on the beam due to the water load on the gate), self-weight, residual thermal stresses and ASR expansion (for each isothermal region).

Different reference (input) expansion curves were defined for each region based on their different average temperatures and overall conditions, according to Goshayeshi (2019). However, both the relative humidity and the alkali content were assessed differently based on data reported in the literature. First, the relative humidity of the entire spillway was assumed to be equal to or higher than 96%, because the environmental relative humidity only affects the first few outer centimeters of the structure (Comi et al., 2012). Therefore, since most elements in the model have between 25 and 50 cm, the entire structure was assumed to not be influenced by the external (air) relative humidity. Moreover, massive structures are known to present almost no leaching due to their size in comparison to slender structures and concrete cores (Lindgård et al., 2013). Since the AAR analytical model used to define the ASR-induced expansion curve was based on concrete cores, which presented significant leaching, the amount of alkalis was increased to simulate the effect of the lack of leaching. In general, ASR-affected concrete cores lose between 3 and 20% of alkalis in the first 4 weeks and between 10 and 50% after one year (duration of the test) (Lindgård et al., 2013). Therefore, the alkali content for the entire structure was increased by 50% in order to be conservative and because this phenomenon is only being accounted for indirectly by increasing the alkali content of the mix.

The finite element models (Figure 4-8) consisted of 3D brick (C3D8RT) and triangular prism (C3D6T) elements representing concrete (green), 3D truss elements (T3D2T) for prestressing tendons (red), and 3D shell elements (S4R) representing prestressing anchorage plates (red). The external plates (at the beam region) were assumed to be 5 cm thick, and the internal plates were modeled with a 25-cm thickness. Lastly, both models included symmetry boundary conditions along the XZ plane, and spring elements representing the linear elastic soil along XY and YZ planes.

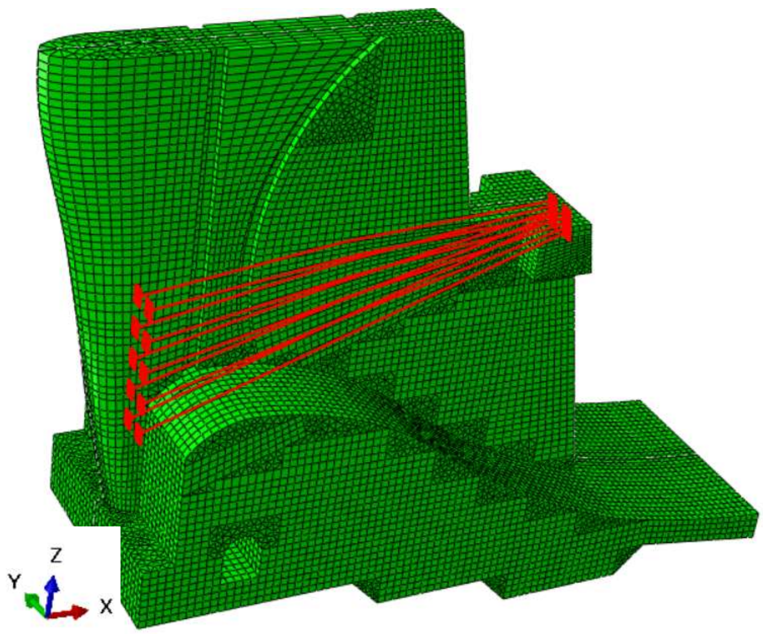


**Figure 4-8. PAIV mesh.**

### 4.5.2 Discussion of Results – Linear-Elastic Thermo-Mechanical Analysis

Two linear-elastic thermo-mechanical analyses were performed, with the first including the simulation of the heat of hydration according to the values from "mix 1" presented in Figure 4-4, while the second did not include it. The main purpose of including the heat of hydration was not to perform an accurate simulation of the temperature variation within the spillway, but rather to evaluate how long the temperature would take to stabilize and be affected only by the external environmental conditions. This holds true specially because the construction in layers was not modeled and because no information regarding that stage of the construction was available, which means that including the heat of hydration as if the entire spillway had been cast at the same time would greatly overestimate the heat generated. The analyses were assumed to begin on January 1st 1975 and they were stopped on January 1st 2025; therefore, simulating a total of 50 years in service.

Results indicated that the effect of the overestimated heat of hydration would have completely dissipated (difference smaller than 3%) after 730 days (2 years) for the core and 405 days for the cover, as shown in Figure 4-9. Therefore, the heat of hydration was deemed not to be a critical parameter affecting the reaction, especially because its effect on the first 2 years is basically negligible when a total of 50 years are simulated in the mechanical analysis and because the approach adopted to represent the heat of hydration is not very accurate, as previously stated.

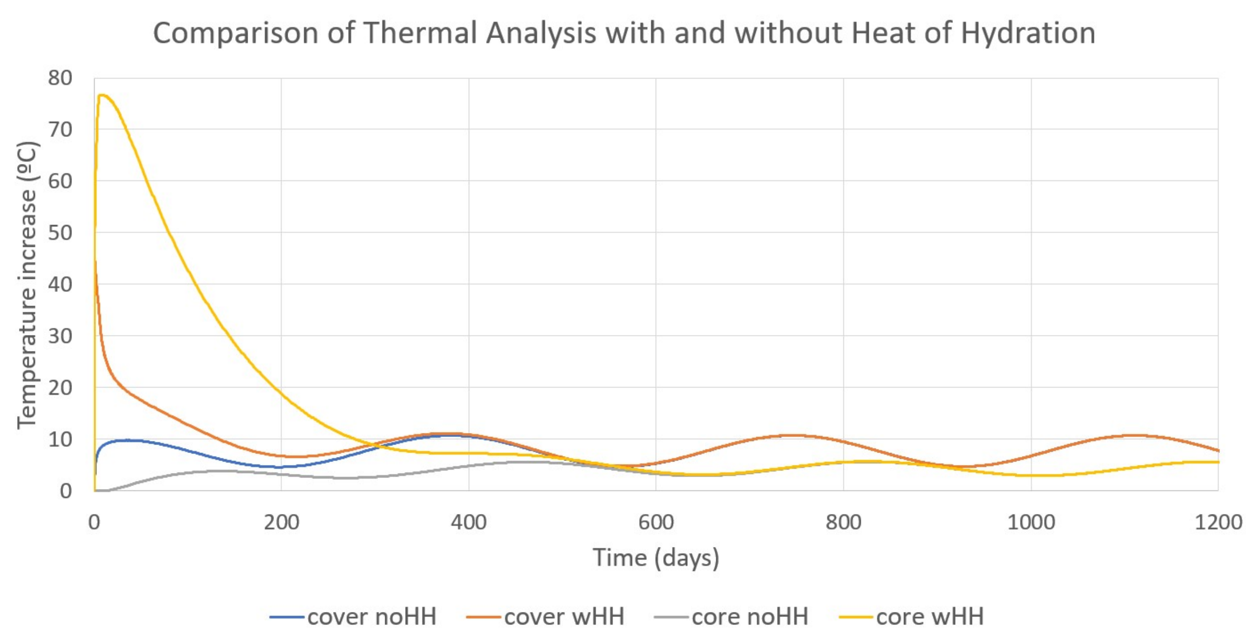


**Figure 4-9. Comparison of thermal analyses with heat of hydration (wHH) and without heat of hydration (noHH) for the concrete cover (approximately 25 cm below the surface) and the dam core.**

The influence that potential microcracking due to thermal stresses could have on the expansion and orientation of ASR cracking was assumed to be negligible at a macro-scale when compared to other phenomena involved in the analysis. Therefore, it was a model simplification to not simulate thermal microcracking.

As expected, the temperature of the dam core takes longer to stabilize than that of the cover, and there is a delay between the two regions, because of the time that the heat gain from (or the loss to) the environment takes to reach deeper regions. The temperature profile for the summer (day 1095 of the thermal analysis, which coincides with January 1st 1978) was used to define the isothermal regions. A total of 6 regions were defined: +6 ºC, +5 ºC, +4 ºC, +3 ºC, +2 ºC and -3 ºC above or below the air temperature. Note that the regions containing the temperatures ranging from +1 ºC to -2 ºC were so insignificantly small that it made more sense to cluster them all together with the -3 ºC region to simplify the implementation of the ASR curves. Also, temperatures above +6 ºC occur only at the surface of the dam, because of the way the sun radiation was implemented; yet, those temperatures quickly dropped after the first few centimeters. Hence, since the element (and not the nodal) average was the desired temperature data to define ASR reference (input) curves, those regions were assumed to be contained within the highest temperature region (+6 ºC). Figure 4-10a illustrates the temperature profile previously described. Figure 4-10b shows the residual thermal stresses.

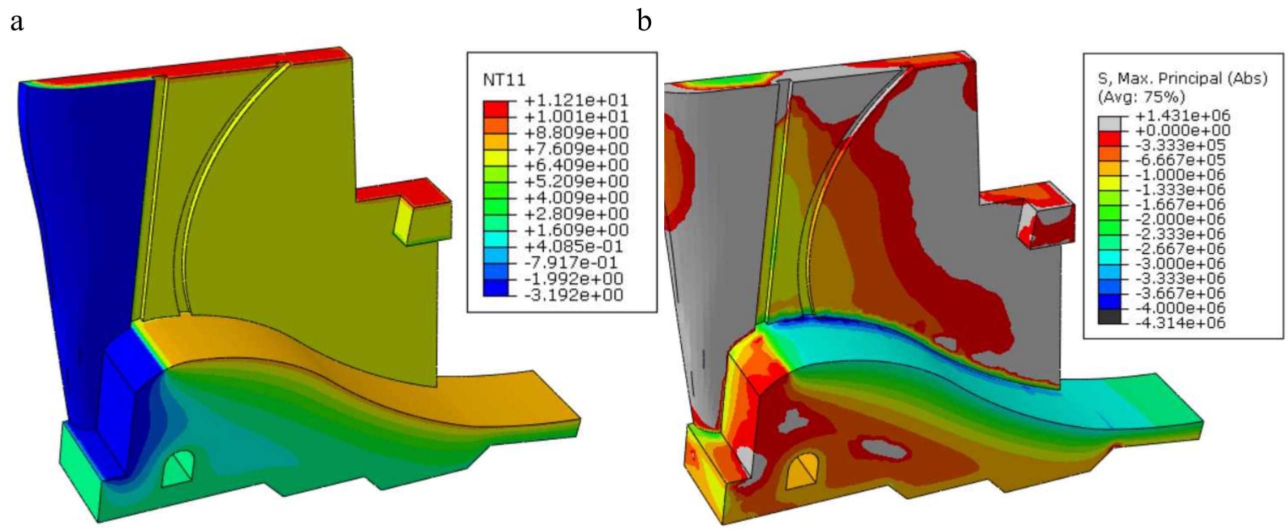


**Figure 4-10. PAIV model for day 1095: a. Temperature above or below air temperature (values in ºC), b. Residual thermal stresses (values in Pa).**

Figure 4-10a clearly shows that the temperature of the horizontal surfaces is higher than the temperature of the inclined surfaces, and both of those are higher than the temperature of the vertical surfaces. This is expected, since vertical surfaces tend to be exposed to sun radiation for shorter periods of time throughout the day. Moreover, it is also clear that the region in contact with water displays a lower temperature, which is due to the high convection coefficient between water and concrete, as well as the fact that the water temperature is lower than the air temperature.

Figure 4-10b shows that several regions were under tensile stresses (grey zones), but these stresses were not high enough to reach the initial tensile strength of the concrete (1.98 MPa). Likewise, the compressive stresses obtained were also far from the initial compressive strength of the concrete (36 MPa). Therefore, the hypothesis of performing a linear-elastic thermo-mechanical analysis to minimize computational effort is reasonable for this specific case.

### 4.5.3 Discussion of Results – Non-Linear Mechanical ASR Analysis

A representative predicted expansion curve for the conditions previously explained is shown in Figure 4-11 (solid blue line). However, if the average ($1.86 \times 10^{-5}/year$) or the maximum ($3.40 \times 10^{-5}/year$) strain rate measured on the dam over a period of three years (from January 2012 to December 2014) are assumed instead of the theoretical stabilization predicted by the analytical model, the following average (solid orange line) and maximum (solid black line) representative expansion curves are obtained. Moreover, curves assuming a constant rate equal to the average rate (dashed orange line) and the maximum rate (dashed black line) are also presented.

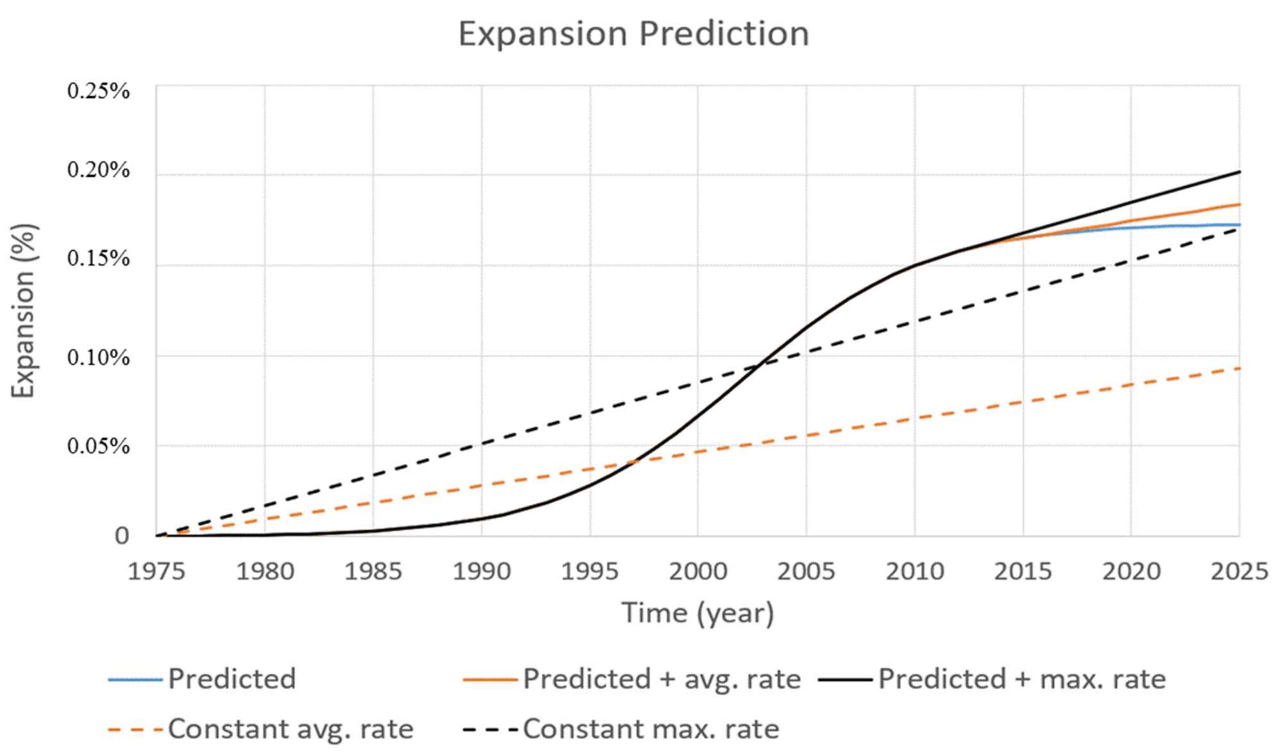


**Figure 4-11. Representative AAR expansion curves.**

These average and maximum rate curves are presented, because several authors, such as Gocevski & Yildiz (2017), have reported that ASR-induced expansion in massive structures can either continue indefinitely and/or be assumed as linear. This is due to the alkali release from aggregates, the important source of reactive silica minerals from large aggregates and the absence (or very little amount) of leaching. Conversely, the expansion in slender structures and lab specimens, which were the basis of the analytical model developed by Goshayeshi (2019), were found to stabilize over time due to leaching (Gorga et al., 2018).

CHESF conducted microscopic analysis (i.e., Damage Rating Index - DRI) on concrete cores extracted from distinct locations (i.e., water intake and spillway) of PAIV in 2007 to evaluate its damage degree and estimate its expansion attained to date. The DRI was initially proposed by Grattan-Bellew & Danay (1992) to evaluate "ASR development" and has recently been modified to appraise "induced expansion and damage" in its broader sense along with reducing the variability between petrographers performing the test (Villeneuve & Fournier, 2012). The DRI consists of assessing the presence of petrographic features of deterioration on polished concrete sections with the use of a stereomicroscope (15-16x magnification). These damage features associated with a given damage mechanism (for instance ASR) are counted through a 1 $cm^2$ grid (i.e., 10 x 10 mm units) drawn on the surface of polished concrete sections under evaluation. The number of counts corresponding to each type of petrographic features is then multiplied by weighing factors, whose purpose is to balance their relative importance towards the mechanism of distress considered. CHESF analyses were performed according to Grattan-Below & Danay method (Grattan-Bellew & Danay, 1992), which means that the weighing factors selected for analysis had the aim of primarily quantifying "ASR development" at the time. In this work, the values obtained by CHESF were converted to the new approach proposed by Villeneuve & Fournier (2012) (i.e., new weighing factors were used), since the new procedure showed to be more reliable and accurate to assess ASR-induced expansion and damage (Sanchez et al., 2015). Figure 4-12 illustrates the DRI results obtained.

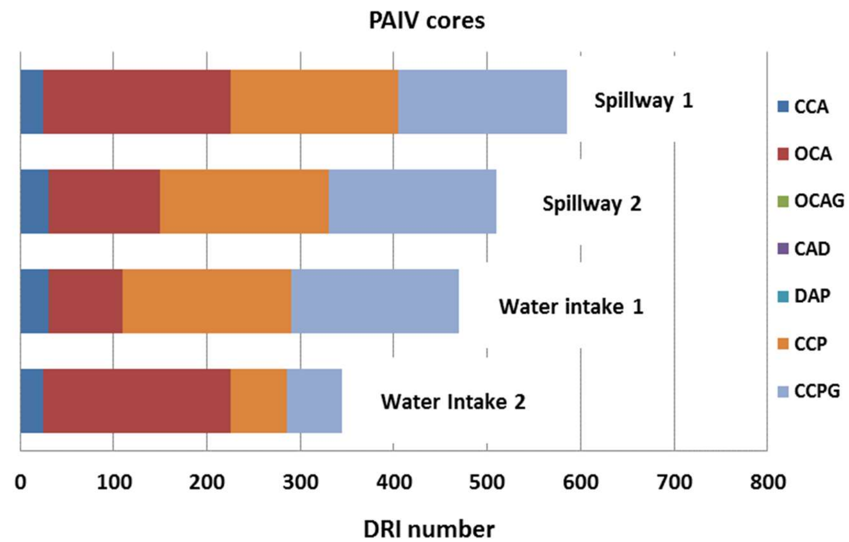


**Figure 4-12. DRI Charts obtained on cores extracted from the water intake and spillway (two samples each).**

Analyzing the data above, one clearly verifies the presence of ASR damage in all samples evaluated, since important amount of cracks was observed within the aggregate particles, especially without gel (OCA). Moreover, non-negligible amount of cracks has also been verified in the cement paste, with and without gel (CCP and CCPG), which besides highlighting once more the presence of ASR on the samples, also indicates that ASR-induced damage probably reached moderate to high distress levels. Adopting the classification proposed by Sanchez et al. (2017), it has been estimated that the expansion level of the water intake would have been moderate (0.12%; DRI numbers ranging from 330 to 500), while the spillway would have likely been between moderate and high (0.12-0.20%; DRI numbers varying from 500 to 765). However, it is important to emphasize that the fairly scattered DRI results observed were likely due to the following reasons: intrinsic anisotropic nature of ASR, small number of extracted cores evaluated by CHESF and, conversion of the DRI results to the new approach. Furthermore, even though the aggregate used in PAIV is considered to be a moderately reactive aggregate (i.e., ± 0.12% at one year according to the concrete prism test - CPT), all the curves based on the analytical model in Figure

4-11 predict that the expansion would be around 0.13% in 2007. This indicates that the analytical model is accurately predicting the expansion according to the DRI results when the specific phenomena affecting ASR-affected in massive structures (i.e., alkali release from aggregates, source of reactive silica minerals from large aggregates and the little amount of leaching) are accounted for indirectly, as described in chapter 4.5. Moreover, note that when a constant rate is assumed, both the average rate and the constant rate underestimate the expansion predicted by the laboratory test (0.06% and 0.11%, respectively).

Another interesting point is that CHESF reported that the first major crack due to ASR was observed in 1985, while the model predicted it would happen only in 1991. Therefore, if the curves based on the analytical model were shifted by 6 years, the damage that would have been achieved in 2007 (0.16%) would be much closer to the expansion predicted through the DRI (0.12-0.20%). Hence, there is a strong indication that the previously described phenomena affecting the reaction in massive structures (i.e., alkalis release from aggregates, absence/little amount of alkalis leaching, etc.) may influence the induced initial expansion and kinetics over time. This assumption should be further investigated and incorporated into the analytical model proposed by Goshayeshi (2019) to improve its accuracy for massive structures.

In summary, the results yielded by the proposed approach were found to be fairly good and to represent the expansion accurately enough, especially considering the lack/uncertainties of the in-situ and microscopic data gathered. Additionally, a comparison between the resulting FE cracking pattern and the observed damage for the current year (2018), based on the predicted expansion curve (solid blue line), is presented in Figure 4-13 and Figure 4-14. Note that the scale of Figure 4-13 was determined by matching plastic strain outputs with field measurements.

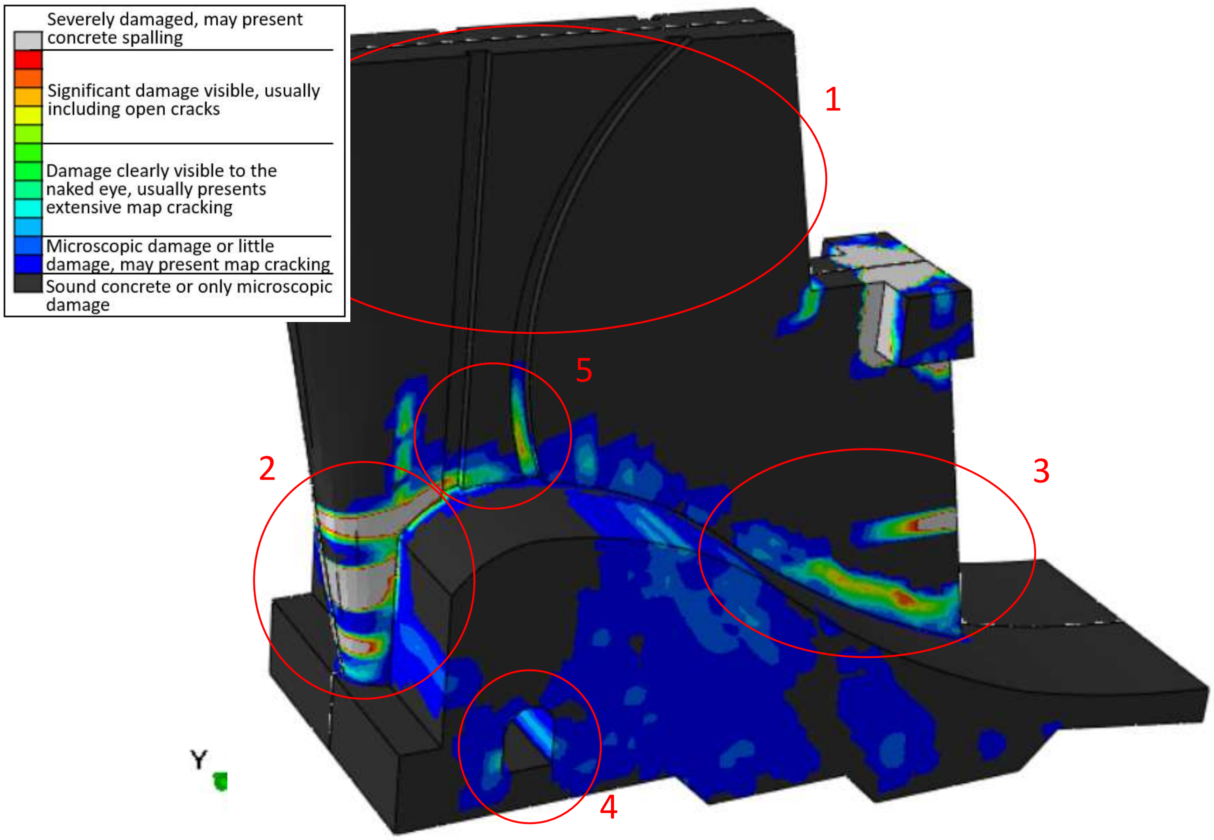


**Figure 4-13. PA-IV FE predicted damage (plastic strain) with emphasis on 5 different regions: 1) Top of the column, 2) Upstream base of the column, 3) Downstream base of the column, 4) Gallery and 5) Main radial gate and emergency gate.**

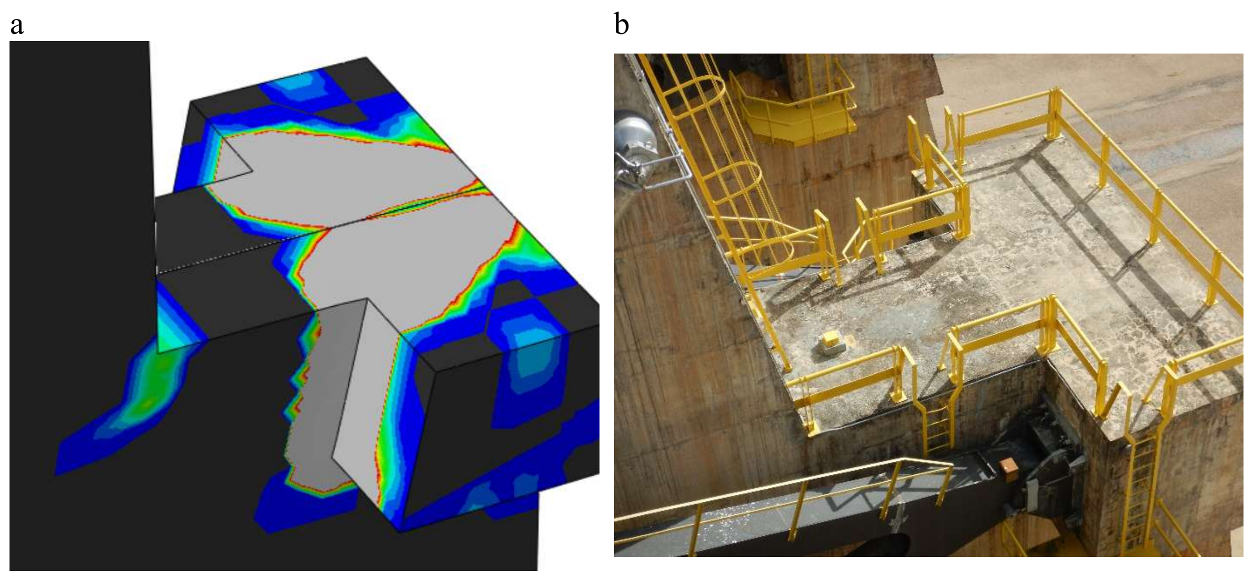

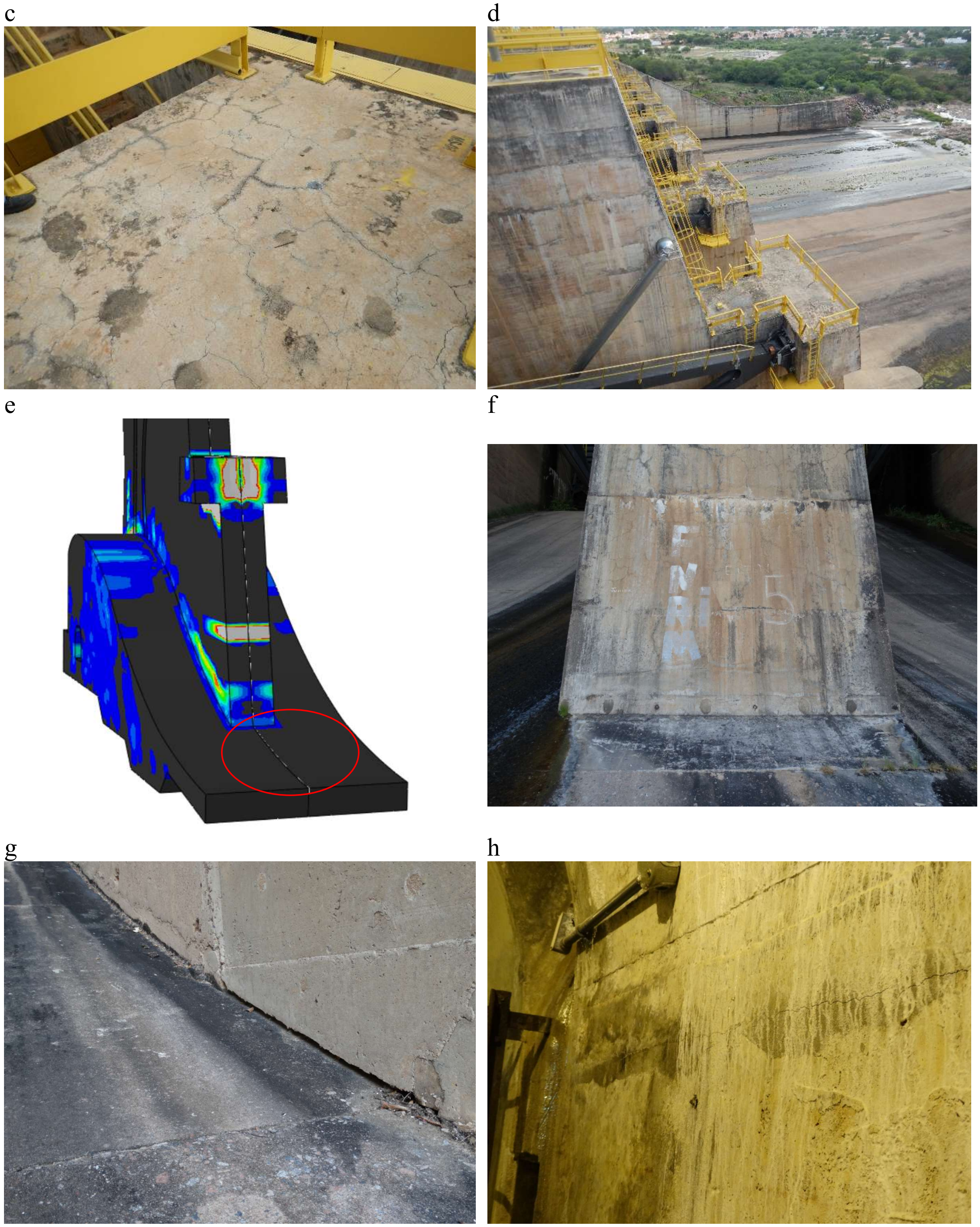


**Figure 4-14. PA-IV: a. FE predicted damage on beam, b. Observed damage on beam, c. Map cracking overview, d. alkali-silica gel leaching in between consecutive concrete layers overview, e. FE predicted damage on the back of the column's base (downstream), f. Observed damage on the back of the column's base (downstream), g. Observed damage on the side of the column's base (downstream), h. Observed damage on gallery.**

Several conclusions can be drawn from the presented figures. First, the damage at the top of the beam (Figure 4-14b and Figure 4-14c) is clearly captured by the model (Figure 4-14a). Some of the damage was initially caused by the long-term loads (gravity, prestressing and water load on the gate); however, the damage in that region significantly increased due to ASR-induced expansion. This is a critical region of the dam, where high loads are applied, which means that careful monitoring is recommended to assess the state of the concrete and the prestressing anchorage.

Second, the FE model predicted that the top of the column (Figure 4-13– region 1) would display almost no damage, which does not match what has been observed in the field (Figure 4-14d). This discrepancy can be explained by two main reasons. First, the interface between concrete layers was not modeled in the simulation; therefore, that discontinuity region and its consequential differential expansions were not captured. Second, the top of the column was unrestrained in both the X and Z direction, while having a 5 mm displacement allowance along the Y direction (i.e., along the axis of the gate). Even so, since the maximum predicted displacement along Y is 2.16 mm for 2018 (Figure 4-15), the entire region is basically unrestrained, which explains the lack of damage in that area of the FE model. Moreover, this damage does not seem to be critical and it most certainly does not compromise the overall accuracy of the FE simulation.

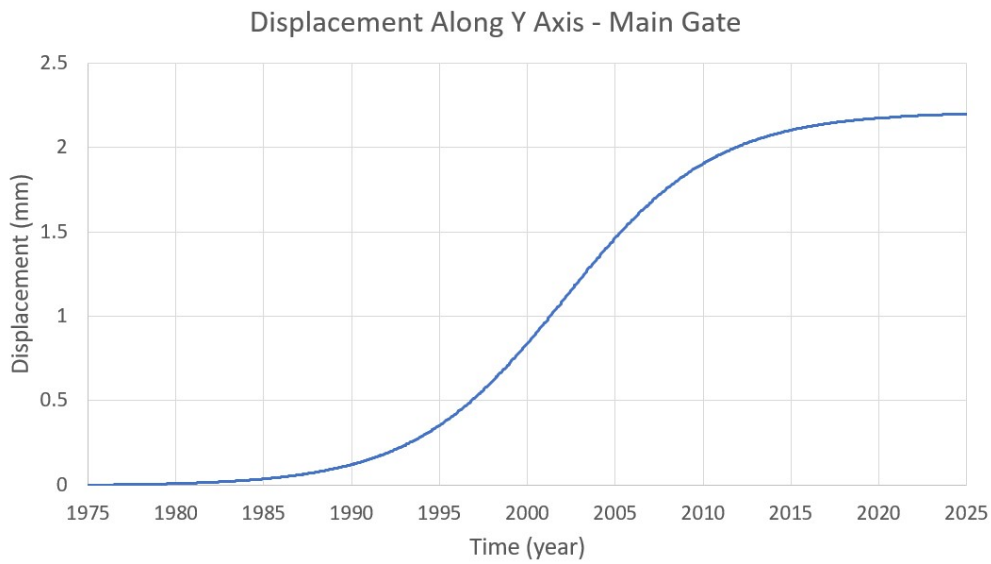


**Figure 4-15. Displacement along Y axis for the main gate**

As presented in Figure 4-15, the maximum displacement predicted along Y was significantly smaller than the displacement allowance of 5 mm, which means that the gate will likely not be affected by the reaction. Even if the reaction does not stabilize, as previously stated, the chance that the 5-mm value would be reached within the service life of the structure is very small.

Another important point in the discussion is that the FE proposed approach forecasts that region 2 (Figure 4-13) would develop severe cracking. Unfortunately, this could not be checked because that region was submerged and no field investigations have been performed to inspect that location. However, it is important to emphasize that this damaged area may just be a numerical inconsistency of the model because that is the region where the prestressing strands are anchored, which could lead to unrealistically high tensile stresses.

It is also clear that the interface between the base of the spillway and the column (Figure 4-13– region 3 and Figure 4-14e) displays significant damage. This is explained by the fact that the reaction at the base is constrained along the Y direction, which leads to a meaningful expansion redistribution, while the column is basically unrestrained in all directions. The resulting differential expansion between the two regions leads to high tensile stresses and, consequently, to the damage observed in Figure 4-14f and Figure 4-14g. Likewise, the gallery (Figure 4-13– region 4) also displays significant damage (Figure 4-14g) due to its geometrical discontinuity. Therefore, there is a risk of water leakage in both the gallery and the base of the column, both of which should be closely monitored.

Lastly, the FE model predicts damage behind the main radial gate, while the emergency gate seems to not be as compromised (Figure 4-13– region 5). As a result of that cracked region, the simulation estimates that the stress in the tendons reaches a maximum value of 1570 MPa in 2018, which is very close to the yielding stress (1580 MPa) and not too far away from the ultimate stress of the prestressing strands (1860 MPa). The average stress variation of the tendon is not critical in all other regions (Figure 4-16); according to the analysis, the critical section only starts diverging from the average section in the year 2000, which is when the cracking first appears. Unfortunately, it was not possible to check if the predicted damage behind the main gate actually exists, but it is highly recommended that eventual inspection should be performed in that region.

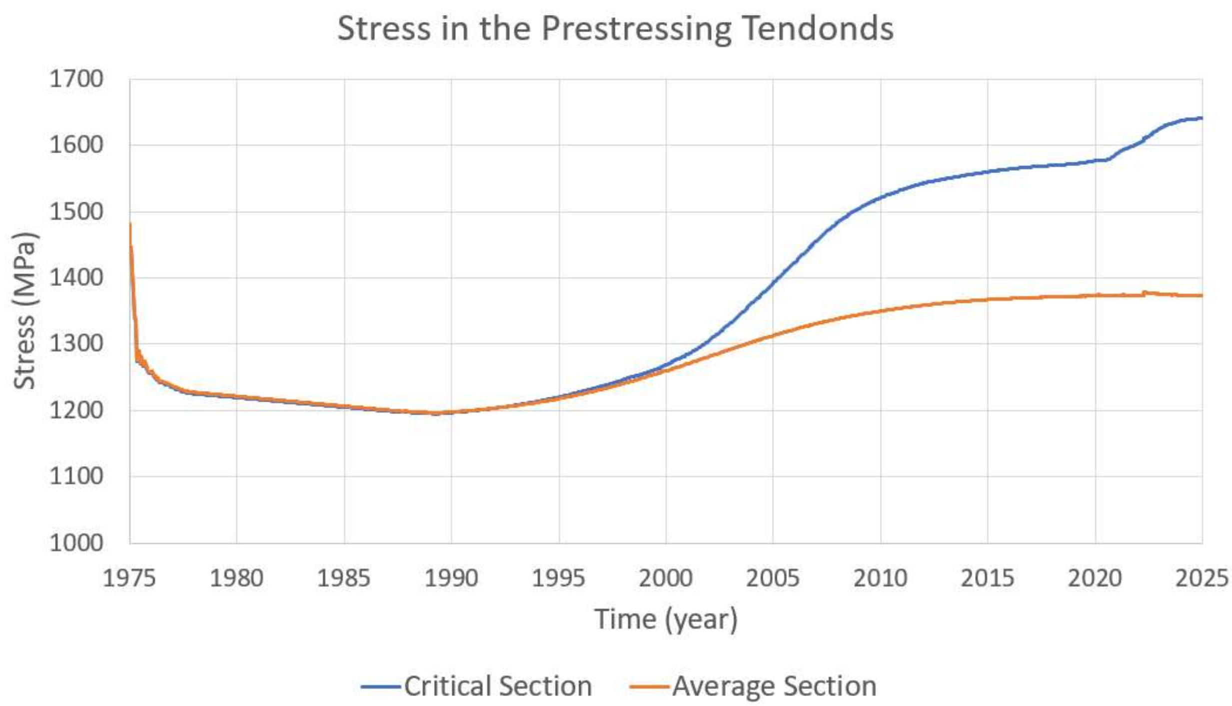


**Figure 4-16. Stress in the prestressing tendons over time**

Concern regarding prestressed tendons and anchor bars is a recurring topic for ASR-affected massive structures. For instance, the unreinforced Val de la Mare gravity dam was built between 1957 and 1961 in the United Kingdom, having been diagnosed with ASR in 1971 (Horswill et al., 1994). Based on the extent of damage and large displacements observed, prestressed anchor bars were installed in 1975 as part of the remedial works aiming to enhance the safety of the structure. They were initially prestressed to 850 kN; however, monitoring indicated that the reaction further increased the prestressing 870 kN by 1980. Concerned about potential future failure of the anchor rods, the prestressing was released to 830 kN and monitoring continued henceforth. Luckly, no further issues were observed, because the reaction stabilized after 1984.

## 4.6 Conclusions

Based on the analyses and results presented, several conclusions can be made:

- The proposed FE model is capable of both simulating prestressing and thermal analyses of sound concrete;
- The linear-elastic thermo-mechanical analysis predicted that the heat of hydration would have dissipated after two years, therefore not being a critical phenomenon affecting ASR reaction. Moreover, the residual thermal stresses observed were found to be lower than the tensile and compressive strengths of the concrete, therefore not leading to damage;
- The non-linear ASR mechanical model seems to be quite promising in evaluating ASR-affected massive structures. The proposed model was able to accurately predict the damage profile observed in the field and the expansion predicted through microscopic (DRI) analyses. This was achieved by indirectly accounting for phenomena exclusively linked to ASR-affected massive structure, i.e., the alkali release from aggregates, the important source of reactive silica minerals from large aggregates and the absence (or very little amount) of leaching. If those are not accounted for, the model underestimates the predicted expansion by more than half. Therefore, further research is still required to properly assess and take the effect of those phenomena into consideration;
- The non-linear mechanical ASR model identified critical areas in the spillway that should be closely monitored: beam, base of the column and behind the main radial gate. Special attention should be given to the latter due to its link to potential prestressing failure, which is a common concern for ASR-affected massive structures. However, the operation of the main radial gate should not be negatively influenced by the reaction over the lifespan of the structure.

## 4.7 Acknowledgements

The authors gratefully acknowledge the financial support received from the Natural Sciences and Engineering Council of Canada (NSERC) and Ontario Centres of Excellence (OCE) in partnership with GHD. Moreover, the authors would like to thank the Companhia Hidro-Elétrica do São Francisco (CHESF), in particular Mr. Alberto Cavalcanti and Mrs Patricia Neves for all the help and data provided throughout the project.

## 4.8 Appendix

Implementation of AAR-induced expansion

Goshayeshi (2019) proposed an analytical/empirical approach to estimate AAR-induced expansion over time. The model, built upon Larive's works, accounts for five of the most important (and measurable) parameters that affect AAR physicochemical reaction (i.e., aggregate's type and reactivity, alkali content, temperature, and relative humidity), thus being able to fully describe AAR-kinetics and unrestrained induced expansion in the laboratory. It has been developed based on a comprehensive experimental campaign and literature data using a wide variety of reactive aggregate types and natures (≈10 distinct reactive aggregate natures), distinct mix-designs and concrete mechanical properties (25, 35 and 45 MPa) according to the Concrete Prism Test (CPT) (ASTM C1293-18a, 2018). Coefficients were obtained and attributed to each of the five parameters previously described according to their influence on AAR-kinetics and ultimate expansion (Goshayeshi, 2019). The coefficients related to the aggregate's type and reactivity were used to attribute base values to the latency time ($\tau_l$), characteristic time ($\tau_c$) and expansion at infinity ($\varepsilon_{AAR}^{\infty}$) on Equation 4-1. Moreover, the other coefficients (i.e., alkali content, temperature and relative humidity) were introduced as new variables, which modify the initial values of $\tau_l$, $\tau_c$ and $\varepsilon_{AAR}^{\infty}$. The proposed model is presented on Equation 4-1 (Goshayeshi, 2019).

$$\varepsilon_{AAR}(t) = \frac{1 - e^{-\frac{t}{\tau_c k_{C,T} k_{C,RH}}}}{1 + e^{-\frac{(t-\tau_l k_{L,T} k_{L,RH})}{\tau_c k_{C,T} k_{C,RH}}}} \times (k_{\infty,T} k_{\infty,RH} k_{\infty,A}) \varepsilon_{AAR}^{\infty} \tag{4-1}$$

where $k_{C,T}$ and $k_{C,RH}$ are the temperature and relative humidity coefficients for $\tau_c$, respectively; $k_{L,T}$ and $k_{L,RH}$ are the temperature and relative humidity coefficients for $\tau_l$, respectively; and $k_{\infty,T}$, $k_{\infty,RH}$ and $k_{\infty,A}$ are the temperature, relative humidity and alkali content coefficients for $\varepsilon_{AAR}^{\infty}$, respectively.

This model has been proven to be quite efficient in describing both CPT laboratory results (despite some issues with laboratory accelerated test procedures such as alkalis leaching) and AAR-affected concrete blocks (400×400×700 mm) stored outdoors and monitored for over 15 years (Goshayeshi, 2019).

The chemical process involved in the reaction is computationally, and indirectly, implemented in the FE model by imposing an equivalent AAR strain based on an unrestrained AAR-induced expansion model (Equation 4-1). The curve obtained from this analytical approach can be understood as the input (reference) expansion curve for the FE model, because it represents the free (i.e., unrestrained and unconfined) expansion that is expected over a period of time. Equation 4-2 presents the total strain of the model $\varepsilon_{tot}$ as a function of the elastic strain $\varepsilon_{el}$, plastic strain $\varepsilon_{pl}$ and equivalent AAR-induced strain $\varepsilon_{AAR}$.

$$\varepsilon_{tot} = \varepsilon_{el} + \varepsilon_{pl} + \varepsilon_{AAR} \tag{4-2}$$

The physical aspects of the reaction are assessed by taking into consideration the triaxial stress-state dependence of the expansion. Gautam et al. (2017) proposed a non-linear mathematical approach stating that ASR-induced expansion is reduced in the compressed direction and redistributed to the less stressed/unstressed directions. The experiment is based on concrete cubes exposed to different constant stress-states over time, with phenomena like creep and Poisson`s effect not being neglected. The experimental results indicate that the expansion may be reduced down to 34% or increased up to 232% of the reference expansion, depending on the tridimensional stress-state. Moreover, the model does not account for the effect of tensile stresses on the reaction; therefore, any regions that are not being compressed have an expansion equal to the reference. The approach proposed by Gautam et al. (2017) was adopted because it is based on triaxial stress-state experiments, with each direction being assessed independently, therefore being able to realistically represent the actual expansion of the reaction.  It is worth noting that, although initially developed for ASR, this stress-dependent model is assumed to be applicable for both ASR and ACR cases.

### 4.9 Data Availability and Statement

All data, models, and code generated or used during the study appear in the submitted article. Yet, if needed, some or all data, models, or code generated or used during the study are available from the corresponding author by request.

### 4.10 References


ASTM C1293-18a. (2018). *Standard Test Method for Determination of Length Change of Concrete Due to Alkali-Silica Reaction*.

Bompa, D. V., & Onet, T. (2010). Identification of concrete damaged plasticity constitutive parameters. *The National Technical-Scientific Conference- Modern Technologies for the 3rd Millenium*, 39–46.

Castilho, E., Leitão, N. S., & Tiago, C. (2015). Thermal analysis of concrete dams during construction phase. *Second International Dam World Conference*.

Cavalcanti, A. J. C. T., Juliani, M. A. C., Becocci, L., & Carrazedo, R. (2006). Avaliação dos Efeitos da Reação Álkali-Agregado no Vertedouro da Usina de Paulo Afonso IV. *II Simpósio Sobre Reação Álkali-Agregado Em Estruturas de Concreto (RAA 2006) - IBRACOM*.

Charlwood, R. (1994). A review of alkali aggregate in hydro-electric plants and dams. *International Journal on Hydropower Dams*, 73–80.

Cheng, H. T., Mohammed, B. S., & Mustapha, K. N. (2009). Experimental and analytical analysis of pretensioned inverted T-beam with circular web openings. *International Journal of Mechanics and Materials in Design*, *5*(2), 203–215.

Collins, M. P., & Mitchell, D. (1997). Stress-strain response of reinforcement. In *Prestressed concrete structures*. Reponse Publications.

Comi, C., Kirchmayr, B., & Pignatelli, R. (2012). Two-phase damage modeling of concrete affected by alkali–silica reaction under variable temperature and humidity conditions. *International Journal of Solids and Structures*, *49*(23–24), 3367–3380.

Esposito, R. (2016). *The Deteriorating Impact of Alkali-Silica Reaction on Concrete: Expansion and Mechanical Properties*. Ipskamp Drukkers.

Fournier, B., & Bérubé, M.-A. (2000). Alkali-aggregate reaction in concrete: a review of basic concepts and engineering implications. *Canadian Journal of Civil Engineering*, *27*(2), 167–191.

Gautam, B. P., Panesar, D. K., Sheikh, S. A., & Vecchio, F. J. (2017). Multiaxial expansion-stress relationship for alkali silica reaction-affected concrete. *ACI Materials Journal*, *114*(1), 171–184.

Gocevski, V., & Yildiz, E. (2017). Macro-modelling of AAR-affected hydraulic structures. *Dam Swelling Concrete (DSC 2017)*.

Gorga, R. V. (2018). *Engineering-Based FE Approach to Appraise Slender Structures Affected by Alkali-Aggregate Reaction (AAR)* [M.A.Sc. Thesis]. University of Ottawa.

Gorga, R. V., Sanchez, L. F. M., & Martín-Pérez, B. (2018). FE approach to perform the condition assessment of a concrete overpass damaged by ASR after 50 years in service. *Engineering Structures*, *177*, 133–146.

Goshayeshi, N. (2019). *Contribution to the Development of Analytical Models to Forecast Alkali-Aggregate Reaction (AAR) Kinetics and Induced Expansion* [M.A.Sc. Thesis, University of Ottawa].

Grattan-Bellew, P. E., & Danay, A. (1992). Comparison of laboratory and field evaluation of alkali- silica reaction in large dams. *International Conference on Concrete Alkali-Aggregate Reactions in Hydroelectric Plants and Dams*.

Grimal, E., Sellier, A., Le Pape, Y., & Bourdarot, E. (2008). Creep, shrinkage, and anisotropic damage in alkali-aggregate reaction swelling Mechanism-Part I: A constitutive model. *ACI Materials Journal*, *105*(3), 227–235.

Horswill, P., Snowden, H. N., & Weeks, R. C. (1994). Val de la Mare Dam, Jersey: Instrumentation, monitoring and stability analysis of an ASR damaged dam. *8th Conference of the British Dam Society*, 119–133.

Lawrence, A. M. (2009). *A finite element model for the prediction of thermal stresses in mass concrete* [PhD Thesis]. University of Florida.

Léger, P., Côté, P., & Tinawi, R. (1996). Finite element analysis of concrete swelling due to alkali-aggregate reactions in dams. *Computers & Structures*, *60*(4), 601–611.

Lindgård, J., Thomas, M. D. A., Sellevold, E. J., Pedersen, B., Andiç-Çakir, Ö., Justnes, H., & Rønning, T. F. (2013). Alkali–silica reaction (ASR)—performance testing: Influence of specimen pre-treatment, exposure conditions and prism size on alkali leaching and prism expansion. *Cement and Concrete Research*, *53*, 68–90.

Malm, R. (2016). *Guideline for FE analyses of concrete dams*.

Pan, J., Feng, Y. T., Jin, F., & Zhang, C. (2013). Numerical prediction of swelling in concrete arch dams affected by alkali-aggregate reaction. *European Journal of Environmental and Civil Engineering*, *17*(4), 231–247.

Sanchez, L. F. M. (2014). *Contribution to the Assessment of Damage in Aging Concrete Infrastructures Affected by Alkali-Aggregate Reaction* [PhD. Thesis]. Université Laval.

Sanchez, L. F. M., Fournier, B., Bastien, J., Mitchell, D., & Noël, M. (2016). Overall assessment of an ASR affected overpass "Robert-Bourassa/Charest" after nearly 50 years in service. *8th International Conference on Bridge Maintenance, Safety and Management - IABMAS*.

Sanchez, L. F. M., Fournier, B., Jolin, M., & Duchesne, J. (2015). Reliable quantification of AAR damage through assessment of the Damage Rating Index (DRI). *Cement and Concrete Research*, *67*, 74–92.

Sanchez, L. F. M., Fournier, B., Jolin, M., Mitchell, D., & Bastien, J. (2017). Overall assessment of Alkali-Aggregate Reaction (AAR) in concretes presenting different strengths and incorporating a wide range of reactive aggregate types and natures. *Cement and Concrete Research*, *93*, 17–31.

Saouma, V., & Perotti, L. (2006). Constitutive Model for Alkali-Aggregate Reactions. *Materials Journal*, *103*(3), 194–202.

Simulia. (2014). *Abaqus/CAE - Complete Abaqus Environment* (6.14). Dassault Systèmes Corporation.

Villeneuve, V., & Fournier, B. (2012). Determination of the damage in concrete affected by ASR—The damage rating index (DRI). *14th International Conference on Alkali-Aggregate Reaction in Concrete - ICAAR*.

Wahalathantri, B. L., Thambiratnam, D. P., Chan, T. H. T., & Fawzia, S. (2011). A material model for flexural cracks simulation in reinforced concrete elements using ABAQUS. *EddBE2011*.

# 5. TECHNICAL PAPER 02/03 – FINITE ELEMENT ASSESSMENT OF ASR-AFFECTED BEMPOSTA DAM USING AN IMPROVED MACRO-SCALE MODELING APPROACH

Gorga, R.V.[a]; Sanchez, L. F. M. [a]; Martín-Pérez, B. [a]; Noël, M. [a], Dias, I.F [b], Batista, A.L. [b]

(a) University of Ottawa, ON, Canada
(b) LNEC, Lisbon, Portugal

## 5.1 Abstract

Modeling damage generated by distress mechanisms such as alkali-silica reaction (ASR) in concrete structures is very complex, yet necessary to correctly assess the current (diagnosis) and future structural response (prognosis) of affected concrete structures. In this context, a macro-scale modeling approach that accounts for the most important parameters affecting ASR through an engineering approach, without the need for non-technical guesses or to "fit" model parameters, was developed by Gorga et al. The proposed approach accounts for material properties deterioration as a function of expansion, takes into consideration anisotropic stress-state-dependent expansion redistribution, and estimates the ASR-induced free expansion based on a physico-chemical semi-empirical equation. Moreover, it has already been used to assess ASR-affected slender and massive structures. Even though promising, there are aspects of the simulation that need to be further enhanced to more accurately assess ASR-affected massive structures. This study aims to present the most recent developments implemented, along with a validation performed by analyzing the ASR-affected Bemposta Dam in Portugal, which has been extensively monitored for almost 50 years. The dam structure is thoroughly described, results of previous analyses performed by Laboratório Nacional de Engenharia Civil (LNEC) are reported, and modeling approaches (proposed and LNEC's) are compared. Results are validated by new laboratory tests and indicate that the structure is not expected to have its serviceability impacted for the period analyzed (up to 2039).

*Keywords: Alkali-aggregate reaction, Finite element modeling, Prognosis, Diagnosis, Dam.*

## 5.2 Introduction

Alkali-silica reaction (ASR), the most common type of alkali aggregate reaction (AAR), is one of the most important deterioration mechanisms that significantly impact the durability and serviceability of concrete infrastructure globally (Sanchez et al., 2015). There have been numerous reports of ASR leading to damage on many structures, ranging from superficial map cracking to severe loss of capacity and the need for demolition (Caron et al., 2001; Charlwood, 1994; Gorga et al., 2018; Saouma & Perotti, 2006). Due to their economic impact and overall importance, massive structures are often even more critical than slender structures when affected by the reaction (Gorga et al., 2020). Over the years, several finite element (FE) method approaches have been developed to assess the current (diagnosis) and predict the future (prognosis) condition of ASR-affected massive structures (Grimal et al., 2008; Léger et al., 1996; Ulm et al., 2000; Winnicki et al., 2014). Those models varied significantly in scope, implementation, variables considered, and level of complexity. However, there is still a lack of consensus within the engineering community regarding the best approach to simulate the structural implications of the reaction, which parameters should be considered, and how to ensure results are reliable. Within this perspective, the model by Gorga et al. (2018, 2020, 2021) has proven to be a very promising alternative, having successfully been adopted to simulate both slender and massive structures. Even so, there are aspects of the simulation that need to be further enhanced to more accurately assess ASR-affected massive structures. This work intends to present the most recent developments implemented, along with a validation performed by analyzing the ASR-affected Bemposta Dam in Portugal. Results from the analysis will be compared with another simulation of the same structure (Dias et al., 2022), highlighting differences and outcomes.

## 5.3 Background

Alkali aggregate reaction (AAR) is a complex concrete distress mechanism that results from a chemical reaction between the alkalis from the concrete pore solution and some mineral reactive phases from the aggregates used to make concrete (Fournier & Bérubé, 2000). AAR is typically classified into two different mechanisms, alkali-silica reaction (ASR) and alkali-carbonate reaction (ACR), with ASR being by far the most common. ASR develops when three components are present: aggregate containing reactive mineral phases, high moisture content (commonly assumed $\geq 85\%$), and high alkali content. The reaction produces an expansive gel that may induce tensile stresses in the concrete and generate cracking, affecting the concrete material properties and potentially leading to structural failure in more extreme cases. There have been several reports of AAR in massive dam structures leading to loss of equipment alignment (such as impairing turbine operation due to opening ovalization), excessive cracking leading to leakage, map cracking, concrete mechanical properties deterioration, inability to operate gates, and closure of expansion joints (Caron et al., 2001; Charlwood et al., 2012; Gorga et al., 2020). Moreover, AAR can lead to significant deterioration of the mechanical properties of concrete (Sanchez et al., 2017). Therefore, performing an adequate assessment of the current state (diagnosis) and prediction of the future behaviour (prognosis) of such structures is important to minimize economic losses and ensure safety.

In field structures, ASR-induced expansion is highly anisotropic, and it is affected by several parameters, including relative humidity, temperature, stress-state, alkali content, aggregate type, aggregate reactivity, etc. (Gautam et al., 2017; Gorga, 2018; Saouma & Perotti, 2006; F. J. Ulm et al., 2002). Additionally, internal gradients in temperature and humidity result in differential expansion within the structure (Comi et al., 2012; Gorga et al., 2018), and the mechanical properties of the affected material progressively degrade as the reaction advances (Sanchez et al., 2017). Given the inherent complexity of the physicochemical phenomena and their macroscopic consequences, traditional analytical calculations are inadequate for accurately capturing the effects of this distress mechanism. Consequently, finite element modeling is one of the most attractive alternatives to assess AAR-affected structures.

Esposito and Hendrix (2012) classify ASR models in different categories, ranging from micromodels (based on ion diffusion/reaction products) to macro-models (based on concrete expansion). The main goal of the proposed model is to assess the implications of ASR on structural components and global systems; therefore, the present work focuses only on macro-models. The first AAR macro-models (based on concrete expansion) were very simple due to the limited knowledge and available computational tools at the time, simulating the expansion as an equivalent isotropic expansion (Charlwood, 1994). Eventually, the influence of other parameters was introduced, increasing the accuracy of the simulations. Several approaches were proposed, mainly differing on how the concrete medium was simulated. On one side, continuous-medium models accounting for a relatively small number of parameters achieved a significant degree of success without explicitly simulating/calculating the chemical aspects of the reaction (Pan, et al., 2013; Saouma & Perotti, 2006; Ulm et al., 2000; Winnicki et al., 2014). Conversely, porous-medium models were also developed, incorporating as many parameters as possible into the calculations to try to simulate the reaction from a micro-meso scale and extrapolating the results to macro-scale structural components (Grimal et al., 2008).

Several of these models have been used to assess AAR-affected massive structures. Ulm et al. (2000) validated their coupled thermo-chemo-mechanical model based on a 2D gravity dam analysis. Even though results were not compared to measured data, the authors observed the formation of an ASR front propagation in the zone described by the heat characteristic length due to the effect of the reaction's chemical kinetics (temperature dependency). Pan et al. (2013) validated their approach by analyzing the Kariba arch dam. Even though no thermal analysis was conducted, the computed radial displacements and most of the vertical displacements matched the measured data well, which was gathered for over 30 years. The same was found when comparing the cracking pattern predicted and the limited information about the actual cracking pattern of the dam. Chulliat et al. (2017) analyzed the Chambon gravity dam, located in the French Alps, based on the model developed by Grimal et al. (2008). The model was calibrated based on measured data, and laboratory tests were performed to define the concrete strength, modulus of elasticity, creep coefficients, ASR kinetics, chemical advancement and damage. The results were in agreement with the measured data regarding stress orientation and intensity, cracking pattern and overall structural behaviour.

Despite significant advancements in the field and insightful analyses being conducted, most existing modeling approaches either neglect or overemphasize the critical physicochemical parameters governing the chemical reaction. Consequently, these approaches often result in models that are either overly simplistic, thus failing to accurately evaluate the underlying distress mechanisms, or too complex, necessitating extensive computational programming and processing. Moreover, such complex models frequently require the fitting of certain variables using literature-derived data or non-empirical approximations, rendering them impractical and potentially unreliable/unrealistic. This diminishes the practical utility and applicability of these models in real-world scenarios. In this context, the comprehensive and intuitive engineering-based finite element approach proposed by Gorga et al. (Gorga, 2018; Gorga et al., 2018, 2020) was developed and proved itself as a very attractive approach due to being capable of:

1- Estimating the free AAR expansion curve through a time-dependent semi-empirical approach based on the most important parameters affecting AAR development, i.e., alkali content, humidity, type and reactivity of the aggregate and temperature.
2- Representing the anisotropic stress-state-dependent AAR expansion through a time-dependent subroutine.
3- Including concrete mechanical properties deterioration (compressive strength, tensile strength and modulus of elasticity) as a function of induced expansion.
4- Simulating concrete damage in both compression and tension, allowing for an accurate representation of damage propagation and accumulation.
5- Not requiring parameter fitting.

This approach has been successfully used to simulate and assess both slender and massive structures, with a good agreement between computational and measured values being observed. Although very promising, there are still aspects of the approach that need further development to improve its accuracy when simulating massive structures. The key required improvements identified are the following:

1- Update the AAR-induced expansion subroutine to allow the thermal and structural analyses to be fully integrated, as before those analyses were performed separately.
2- Improve solar radiation calculations to account for all the parameters affecting the phenomenon.
3- Update the AAR semi-empirical model subroutine to take into consideration the most recent developments in the field (De Grazia et al., 2021; Nguyen et al., 2022).
4- Implement into the subroutine a new time-dependent creep model that accounts for the entire stress history of the structure.

5- Perform a more in-depth analysis of a massive structure with more recorded data in order to validate the approach for such structures.

## 5.4 Research Significance

Existing ASR models are limited either by being overcomplicated, requiring parameter fitting and extensive computational power, or by being oversimplified, failing to capture all critical features of the distress mechanism. Moreover, there is a clear necessity to enhance the approach by Gorga et al. for a more accurate assessment of AAR-affected massive structures. Therefore, an updated model is proposed alongside a new validation. Through a partnership with the Laboratório Nacional de Engenharia Civil (LNEC) – in Lisbon, Portugal – extensive monitoring data from the AAR-affected Bemposta dam in Portugal was acquired and utilized to validate the proposed modeling approach. Complimentarily, the proposed model and its predictions were compared to simulations previously performed by LNEC (Dias et al., 2022), providing further insight into the current and future behaviour of the structure. Ultimately, this work intends to provide the engineering community with an all-encompassing and validated modeling approach to assess AAR-affected structures, able to provide accurate diagnosis and prognosis without the need to fit parameters while still accounting for all the most important aspects affecting both the structure and the reaction.

## 5.5 Modeling Approach by Gorga et al.

### 5.5.1 Existing model description

The model proposed by Gorga et al. (Gorga, 2018; Gorga et al., 2018, 2020) used the concrete damaged plasticity (CDP) model available in the commercial FE software Abaqus Standard by Simulia. This material model describes the elastic and inelastic hydrostatic pressure-dependent behaviour of concrete under both compression and tension. Cracking intensity and orientation in tension and compression were evaluated through the development of plastic strain. Mechanical properties deterioration (i.e., reduction of modulus of elasticity, compressive strength, and tensile strength) was assumed to be a function of the AAR expansion level according to Sanchez et al. (2017), being constantly updated for each element as the reaction progresses.

The unrestrained reaction kinetics and expansion prediction over time were calculated according to the physico-chemical semi-empirical model developed at the University of Ottawa (Goshayeshi, 2019). This approach added modifying parameters to the mathematical S-shaped curve proposed by Larive (1997) to account for the effect of aggregate type and reactivity, temperature, relative humidity, and alkali content. Parameters varied over time to represent real climatic data. At the time, it was assumed that the analytical AAR model was able to approximately capture the in-service expansion potential based on field data experiments by several authors (Gorga et al., 2018). AAR expansion was modeled by imposing an anisotropic and stress-state dependent equivalent AAR strain according to Gautam et al. (2017), which was implemented through an Abaqus user subroutine (USDFLD). When present, steel was modeled as an elasto-plastic material for both reinforcing bars and prestressing strands. Prestressing was imposed as an equivalent negative thermal gradient if applicable. Depending on the simulation, thermo-mechanical structural behaviour over time was modeled using decoupled simulations. Residual thermal stresses were imported as initial conditions (predefined field) onto the non-linear mechanical ASR model, and isothermal regions were defined manually.

### 5.5.2 Previous validations

The authors performed a total of four validations based on laboratory tests before using the proposed approach to simulate real (in-service) structures, including simulations of sound reinforced concrete, sound prestressed concrete, thermal behaviour of sound concrete, and ASR-affected reinforced concrete. Modeling sound reinforced and prestressed concrete proved that the material models and modeling approach were able to accurately represent the structural behaviour of the reinforced concrete members up to (shear or bending) failure. Modeling the thermal behaviour of sound concrete verified that the proposed approach was able to accurately simulate concrete's heat of hydration and temperature stabilization over time. Lastly, the anisotropic stress-state dependent ASR expansion behaviour (Gautam et al., 2017) was validated by simulating ASR-affected push-off specimens with different amounts of reinforcement confinement.

The first real structure used as validation was the Robert-Bourassa Charest (RBC) overpass, an ASR-affected bridge structure located in Quebec City, Canada (Gorga et al., 2018). After nearly 50 years in service, the structure was demolished, and extensive data was collected from the Y-shaped piers, which was used as validation for the FE model. Quantitative microscopic evaluations (e.g., damage rating index tests - DRI) were able to estimate the expansion attained to date on piers, both exposed and not exposed to the environment (protected or not by the deck against solar radiation, splashing, rain, snow, etc.). An excellent match between the calculated expansion and the test results was observed. Moreover, qualitative visual comparison of cracking extent and orientation indicated that the model was able to represent the damage undergone by the real piers. Lastly, a comparison of the strain in the stirrups calculated by the model and measured in the lab showed that the proposed approach was able to match the test results very well, without the need for fitting parameters.

The second real structure appraised was the Paulo Afonso IV (PAIV) dam (spillway). The dam was built between 1975 and 1981, with the first signs of ASR being observed in 1985. Laboratory tests determined the material properties of concrete and the equivalent expansion level through the

DRI test. Additionally, expansion measurements from extensometers were also obtained directly from CHESF ("Companhia Hidro Elétrica do São Francisco"). The analysis of the dam was divided into two parts (Gorga et al., 2020). First, a linear-elastic thermo-mechanical analysis of the spillway was performed to determine the stress-state due to thermal loads, as well as the variation of the temperature profile of the dam. Then, the residual thermal stresses were imported into a non-linear mechanical ASR model, which included both the long-term loads, the residual thermal stresses, and the reaction's expansion. Different reference (input) ASR expansions (Goshayeshi, 2019) were imposed for each isothermal region. The model was able to accurately predict the cracking patterns observed at different locations and expansion measured through laboratory tests, as well as identify high risk regions.

### 5.5.3 Model development

The previous subroutine in Abaqus was a USDFLD subroutine, i.e., a subroutine to define field variables at a material point. It allowed the calculation of the expansion redistribution coefficients per direction, which are a function of the stress state on the element. AAR expansion according to Larive's curve (Larive, 1997) was represented in the model by imposing an equivalent isotropic thermal expansion, which was then recalculated and redistributed along each principal direction separately, emulating anisotropic AAR expansion. Moreover, material properties were incorporated as a function of temperature (used again as a proxy for expansion) and were reduced as analysis time progressed. This analysis was adequate if thermal analysis did not have to be considered at the same time as AAR, as temperature was already being used as a proxy for AAR. Therefore, a new alternative had to be developed to allow the simultaneous calculation of AAR, temperature profiles, and creep strains.

In this context, a combined USDFLD-UEXPAN subroutine was developed. The USDFLD allows the critical calculation values per element to be both carried over to the next time-step and to be used directly in the UEXPAN calculations. The UEXPAN subroutine allows the user to define incremental strains, which can be of any type. This means that the AAR, thermal, and creep strains can be calculated (and stored) separately, and then be imposed together per direction as a total imposed strain. Material properties can also be reduced in each element as a direct function of expansion, which is calculated within the USDFLD subroutine.

It was also deemed necessary to update the calculation of AAR-induced expansion. Previously, the AAR-induced expansion equation was defined as a function of time, following Larive's curve (Equation 5-1) as per Goshayeshi (2019) using Equations 5-1 and 5-2.

$$\varepsilon_{AAR}(t) = \frac{1 - e^{-\frac{t}{\tau_c}}}{1 + e^{-\frac{(t-\tau_L)}{\tau_c}}} \times \varepsilon_{AAR}^{\infty} \tag{5-1}$$

$$\Delta\varepsilon_{AAR}(t_i) = \varepsilon_{AAR}(t_i) - \varepsilon_{AAR}(t_{i-1}) \tag{5-2}$$

where $\varepsilon_{AAR}(t)$ is the AAR strain at time $t$, $\varepsilon_{AAR}^{\infty}$ is the AAR strain at infinity, $\tau_L$ and $\tau_c$ are coefficients, and $\Delta\varepsilon_{AAR}$ is the AAR strain increment. For more details on (omitted) parameters for $\tau_c$ and $\tau_L$, which account for the effect of temperature, relative humidity, alkali content, alkali release, and leaching on AAR-induced expansion, refer to Goshayeshi (2019), De Grazia et al. (2021) and Nguyen et al. (2022). With this approach, it was possible to calculate the AAR strain increment at each time step, given that the values of $\varepsilon_{AAR}^{\infty}$, $\tau_L$ and $\tau_c$ are constant for that step. Therefore, a final free expansion curve could then be determined for each isothermal region. However, a recent study (Nguyen et al., 2022) found that a better representation of the real behaviour of structures affected by AAR can be obtained if the calculation is made as a function of the attained total expansion instead of time. For this reason and to fully automate the calculation within the subroutine, the AAR-induced expansion (strain) calculation approach was updated. For a given expansion level reached ($\varepsilon_{AAR}(t)$) and for the current coefficient values, an equivalent time ($t_{eff}$) can be calculated for the existing curve. This equivalent time corresponds to the time at which $\varepsilon_{AAR}(t)$ would have been reached if the current coefficients were constant for the entire analysis. The AAR strain increment can then be calculated as shown in Equation 5-3 through 5-5, where $\Delta t$ is the time-step increment. Note that the equation for $t_{eff}$ (Equation 5-3) is obtained simply by rearranging Larive's equation (Equation 5-1) as a function of time.

$$t_{eff\_i-1} = -\tau_c \times \ln\left[\frac{1-\frac{\varepsilon_{AAR}}{\varepsilon_{AAR}^{\infty}}}{\frac{\varepsilon_{AAR}}{\varepsilon_{AAR}^{\infty}} \times e^{\frac{\tau_L}{\tau_c}} + 1}\right] \tag{5-3}$$

$$t_{eff\_i} = t_{eff\_i-1} + \Delta t \tag{5-4}$$

$$\Delta\varepsilon_{AAR}(t_i) = \varepsilon_{AAR}\left(t_{eff\_i}\right) - \varepsilon_{AAR}\left(t_{eff\_i-1}\right) \tag{5-5}$$

With these equations, the effect of temperature on AAR-induced expansion is then calculated directly through the new subroutine. Therefore, manually subdividing the model into isothermal regions is no longer necessary. Moreover, the new subroutine is also able to simultaneously impose different expansion curves for different regions by manually specifying different field variable values and associating specific values of $\tau_c$, $\tau_L$ and $\varepsilon_{AAR}^{\infty}$ for each of them.

Lastly, creep strain calculation was added to the subroutine, as there are no built-in material models in Abaqus that allow for both creep and plasticity to be specified simultaneously. A full description of the creep strain calculation can be found in Chapter 2.6.3; however, in summary, the subroutine uses the Dirichlet series to calculate creep strain while accounting for the entire stress-history on each element without having to record the entire set of data (Batista, 1998; Bazant & Wu, 1973; Póvoas, 1991). Dirichlet series use a chain of N Kelvin models assembled in series to represent a creep compliance curve, leading to the following equations based on the rectangular integration curve approximation (Equation 5-6 through 5-8).

$$\Delta\varepsilon_{creep}(t_n) = \sum_{i=1}^{N} \varepsilon_i^*(t_{n-1}) \times \left(1 - \mathrm{e}^{-\Delta t_n/\tau_i}\right) \tag{5-6}$$

$$\varepsilon_i^*(t_{n-1}) = \varepsilon_i^*(t_{n-2}) \times (\mathrm{e}^{-\Delta t_{n-1}/\tau_i}) + \Delta\sigma(t_{n-1})/E_i(t_{n-1}) \tag{5-7}$$

$$\varepsilon_i^*(t_1) = \Delta\sigma(t_1)/E_i(t_1) \tag{5-8}$$

where $\Delta\varepsilon_{creep}(t_n)$ is the creep strain increment at a given time $t_n$; $E_i$ and $\tau_i$ are the individual values for the spring and dashpot coefficients of each Kelvin model; and $\varepsilon_i^*(t_{n-1})$ represents the group of interval variables describing the influence of the entire stress history up to the time increment $t_{n-1}$ that will influence the subsequent time increment.

In summary, the new USDFLD-UEXPAN subroutine in Abaqus (Simulia, 2024) allows the incremental calculation of the thermal, AAR-induced, and creep strains in addition to the elastic and plastic strains calculated through the mechanical model, resulting in Equation 5-9:

$$\begin{aligned} \varepsilon_{tot} &= \varepsilon_{subroutine} + \varepsilon_{mechanical} \\ &= \left(\varepsilon_{thermal} + \varepsilon_{AAR} + \varepsilon_{creep}\right) + (\varepsilon_{elastic} + \varepsilon_{plastic}) \end{aligned} \tag{5-9}$$

where $\varepsilon_{tot}$ is the total strain, $\varepsilon_{subroutine}$ is the strain calculated through the subroutine, which is the sum of the thermal strain ($\varepsilon_{thermal}$), the AAR strain ($\varepsilon_{AAR}$) and the creep strain ($\varepsilon_{creep}$), and $\varepsilon_{mechanical}$ is the mechanical strain calculated directly by the software, which is equal to the sum of the elastic strain ($\varepsilon_{elastic}$) and the plastic strain ($\varepsilon_{plastic}$).

With the updated subroutine, the thermal and mechanical analyses are fully integrated. To optimize computational processing power, a thermal analysis is first conducted, where the temperature for each node is determined for the entire analysis period. The entire temperature history is then imported into the AAR-mechanical analysis.

It is also worth noting that the solar radiation approach was improved compared to the Paulo Afonso IV model (Gorga et al., 2020). Although surfaces still need to be subdivided manually based on tilt and orientation, the new approach (Duffie & Beckman, 2013; Hottel, 1976; Liu & Jordan, 1960) is able to determine the daily total solar radiation for each day of the year for the entire analysis period based on a detailed calculation that accounts for surface orientation, tilt, latitude, longitude, position of sun along the sky, clear sky solar radiation, and intensity of extraterrestrial solar radiation as shown in the Appendix (Chapter 5.9).

## 5.6 Bemposta Dam

### 5.6.1 Bemposta Dam overall description

The Bemposta dam (Figure 5-1) is a hollow arch-gravity dam located in the international section of the Douro River, between Portugal and Spain (Dias et al., 2022). The dam body is 87-meters high and 297-meters long. Construction started in 1960 and was completed in 1964.

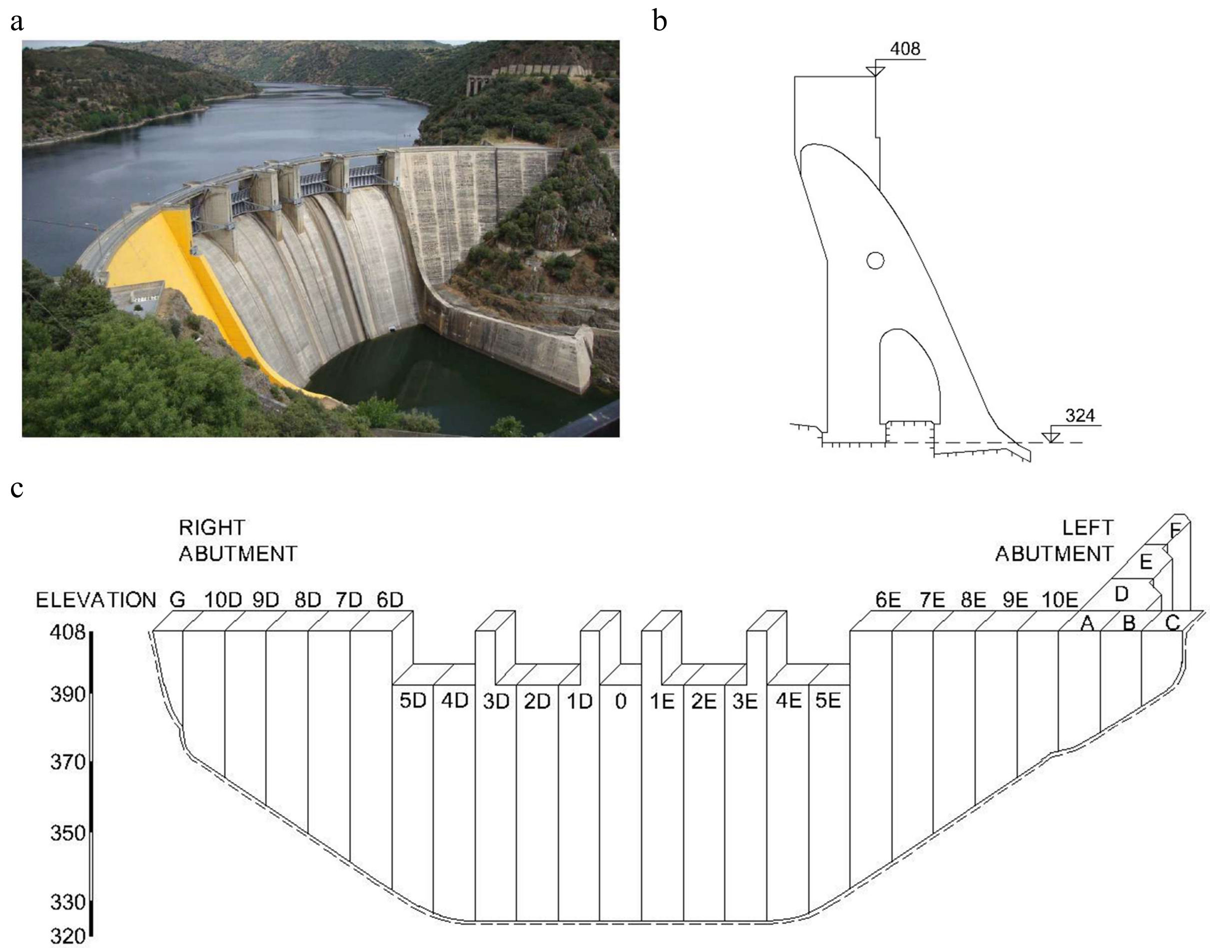


**Figure 5-1. Bemposta dam: a. Overview, b. Section, c. Elevation. Source: Dias et al. (2022).**

The dam has been regularly monitored by LNEC since 1977. The following data has been recorded: air, water and internal concrete temperature, downstream and upstream water levels, horizontal and vertical strains and displacements, joint movements, and piezometric data.

The first signs of expansion due to ASR were observed in the 1990's after approximately 30 years of operation. Over the years, measurements of the dam using inverted pendulums, standard pendulums, extensometers, and topographic campaigns showed permanent radial, vertical, and tangential displacements. Recorded relative tangential displacements (in relation to the lowest measurement point at elevation 330 m) were small on average, not surpassing 13 mm at any given point. Interestingly, the tangential displacements observed at the top of blocks 3D and 3E (see

Figure 5-1) were not the same, even though the structure is almost symmetrical. The former displayed almost no relative tangential displacements, whereas the latter displayed about 11 mm displacement toward the abutment. As expected, relative radial displacement was more pronounced at the center of the dam, reaching relatively high values of up to 35 mm. Vertical displacements were also significant, reaching values of about 35 mm at the top of the central piers. Approximately symmetrical behaviour was observed both radially and vertically, with the maximum observed difference between each side being around 30%. In almost all construction and expansion joints, relative movement was small or negligible. Other observed signs of ASR included map cracking and white efflorescence in several locations, including the galleries. Gate operation has not been impacted, with the total original gap being between 10 and 20 mm per gate.

Extensometers recorded both free and restrained in-situ expansion for the specific temperature and relative humidity exposure conditions present within the structure. The former was performed by drilling cores without extracting them, but rather filling the surrounding gap with flexible material, making the concrete virtually stress-free. Results showed that expansion rates and total expansion values varied significantly between different regions. Fitted curves by LNEC predicted final free expansion values between 0.012% and 0.100%, with the average being about 0.05%.

The water level was mostly constant over the entire time period, usually being at 402 m elevation level. Uplift pressure measured through piezometers was, in general, very low.

Field investigations reported that the bedrock foundation is mostly in good condition. Measured modulus of elasticity varied from 2 to 94 GPa, with the average in each investigated region being between 21 and 29 GPa. Moreover, there is very little information regarding the concrete mix used, with the amount of alkalis in the system and the type of aggregates used being unknown. From recorded mechanical tests around the time of construction, the average compressive strength at one year was between 30.2 and 34.6 MPa, while the compressive strength at 28 days was between 20.7 and 27.1 MPa, and the modulus of elasticity was between 29.7 and 35.8 GPa.

To date, the structure has not undergone any rehabilitation campaigns, as its operation was never compromised.

In this context, Dias et al. (2022) developed a comprehensive FE model to assess the current state and estimate the future behaviour of the Bemposta Dam.

### 5.6.2 LNEC Bemposta Dam model description

The thermo-structural model simulated concrete as a linear visco-elastic material, accounting for creep due to the applied loads and stress relaxation due to prescribed strains (expansions). As the expansive process is of moderate magnitude compared to other Portuguese dams, and limited cracking had been observed, concrete non-linear behaviour/damage was not modeled, and degradation of concrete mechanical properties was not considered. Note that in a recent research paper (Dias & Batista, 2025), the LNEC model was updated, mainly to account for the nonlinear tensile behaviour of concrete through the implementation of a damage model. The enhanced approach was applied to the Covão do Meio dam in Portugal, a structure that exhibits significant superficial cracking.

The rock mass foundation was assumed as linear-elastic (with a modulus of elasticity of 15 GPa) and was included in the model to simulate the elastic support of the dam. Perfect bond between the concrete and the rock mass foundation was adopted. Additionally, the gates were modeled as large hexahedral elements with a very low modulus of elasticity, only to transfer the water load pressure to the surrounding structure.

The main structural loads acting on the dam were considered, namely: upstream hydrostatic pressure, seasonal thermal variations, concrete creep, and ASR expansion. Uplift pressure and downstream hydrostatic pressure were not accounted for based on the assumption that their effects would not be significant.

The thermal component of the model considered air temperature (modeled as convection), water temperature (imposed as a temperature boundary condition), and solar radiation (accounting for the orientation of each surface and time).

A total of three free expansion curves (LNEC Zones A-C in Figure 5-5b), which have a sigmoid shape similar to that proposed by Larive (1997), were estimated from the strains measured in the no-stress strain gauges/extensometers, from the observed vertical and horizontal displacements, and also from the results obtained with the numerical modeling (by means of a fitting procedure). Those were applied to three manually specified zones, which were assumed to have different values of internal relative humidity. In order to estimate the future behaviour of the dam and given the lack of information about the future evolution of the reaction, such as results from residual expansion laboratory tests, the dam behaviour forecast was performed considering two scenarios of ASR expansion. The first was labelled as optimistic and assumed that the expansion would stabilize within a couple of decades. The second scenario was pessimistic and assumed that there would still be significant expansion potential, basically maintaining the same rate. Both scenarios were simulated up to 2039, which corresponds to a service life of 75 years.

The expansion model directly accounted for the effect of temperature and stress-state. The effect of temperature was represented by an $\varepsilon_{AAR}^{\infty}$ multiplier based on the activation energy theory, being determined locally for each Gauss point. Stress-state expansion dependency was simulated locally as a $\varepsilon_{AAR}^{\infty}$ reduction multiplier (as per Larive, 1997). Moreover, expansion redistribution to other directions was not considered. Lastly, humidity was not explicitly accounted for in the expansion model but was considered in a simplified way by considering less free expansions in the downstream leg of the dam, given that the large cavity may break the water flux through the dam body from the upstream face.

### 5.6.3 LNEC Bemposta Dam model description

The computed temperatures estimated by the LNEC model matched very well with the field measurements. Moreover, the computed displacement components (vertical, radial and tangential) were very close to the recorded values, as illustrated in Figure 5-2. Displacements were considered positive in the upstream direction (radially) and towards the right abutment (tangentially). Note that the non-symmetrical tangential behaviour of the dam was not captured, with both blocks 3D and 3E displaying effectively zero relative tangential displacement.

a

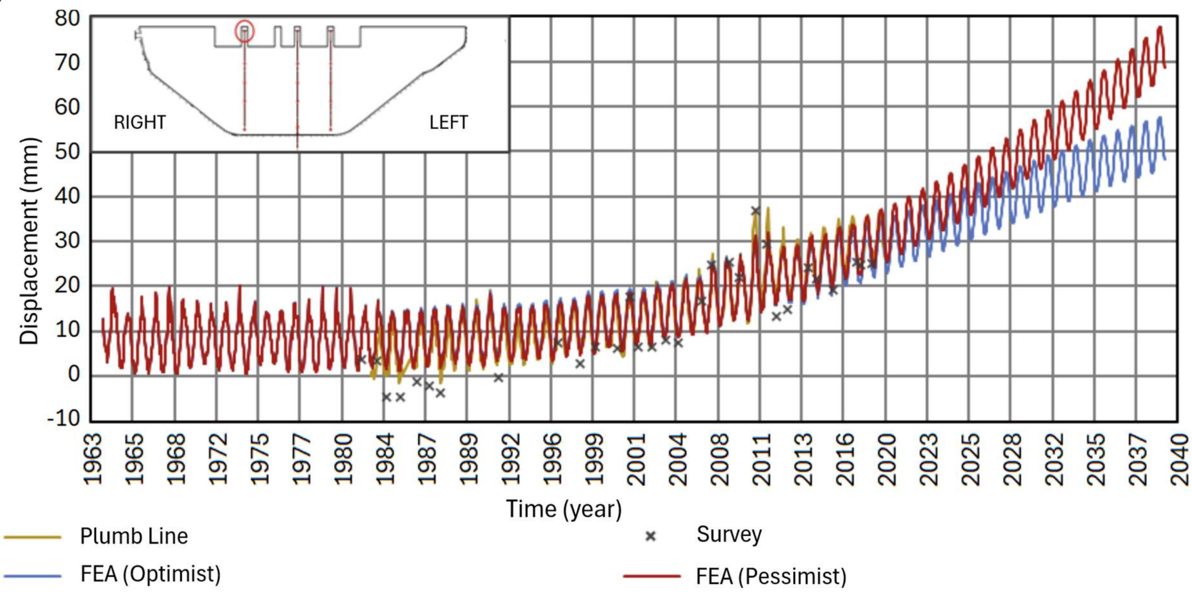

b

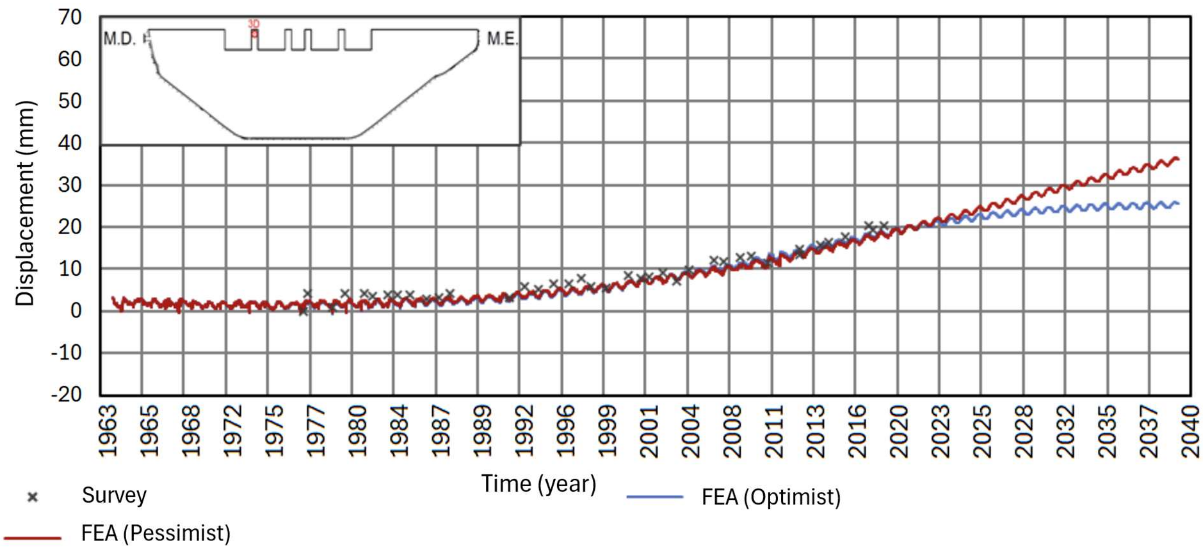


**Figure 5-2. Bemposta Dam LNEC model – Block 3D at 402 m elevation near crest: a. radial displacement, b. vertical displacement. Source: Dias et al. (2022).**

The analysis also showed that the compressive stresses on the dam body in the year 2020 were already relevant in some regions, reaching 10 MPa in the left abutment. The maximum tensile stresses in 2020 were moderate, around 2.7 MPa on the left abutment and 3.6 MPa on the spillway sidewalls, which was consistent with the limited cracking observed on the dam faces. Stresses tended to be highest around the abutments and at the dam-foundation interface, with the latter being a result of the perfect bond formulation adopted. Results predicted for year 2039 showed that the maximum compressive and tensile stresses would respectively reach 18.6 MPa and 6.9 MPa for the pessimistic scenario, and 13.2 MPa and 4.9MPa for the optimistic scenario.

### 5.6.4 New laboratory Tests

In addition to the data reported and published by LNEC (Dias et al., 2022), new concrete cores from five different locations were extracted from the dam and sent to the University of Ottawa for microscopic evaluation, particularly the damage rating index (DRI). The DRI is a semi-quantitative petrographic tool used to assess the cause, but especially the extent of damage in concrete affected by distress mechanisms such as AAR (Sanchez et al., 2017). The extent of damage of affected concrete is identified by counting specific petrographic features associated with a damage mechanism (i.e., AAR in this case), such as cracks in aggregates, cement paste, and the presence of reaction products (e.g., alkali-silica gel). Weighing factors are attributed to each of these petrographic features to balance their specific contribution towards the overall damage evaluated. Finally, a DRI number (i.e., number of counts multiplied by weighing factors) is computed and normalized to 100 $cm^2$. The higher the DRI number, the greater the damage observed. Test results are summarized in Table 5-1.

**Table 5-1 DRI test results for Bemposta dam cores.**

| Block | Elevation (m) | DRI number | Damage degree | Estimated Attained Expansion |
|---|---|---|---|---|
| 6D | 364.7 | 213 | Negligible/Marginal | 0.04%$\pm$0.01% |
| 6E | 364.7 | 318 | Marginal | |
| 0 | 364.7 | 402 | Marginal/Moderate | |
| 2D | 330.0 (Upstream leg) | 269 | Marginal | |
| 2E | 330.0 (Upstream leg) | 565 | High | 0.11%$\pm$0.01% |

### 5.6.5 Gorga et al. Bemposta Dam Model Description

For the thermal analysis, quadratic heat transfer tetrahedral elements (DC3D10) were used, and a standard transient heat transfer analysis step was implemented. Surface film and surface radiation interactions were specified to represent convection and radiation with the surrounding environment. Surface heat flux loads were adopted to simulate incident solar radiation. At the start of the analysis, the dam was specified to be at 16.5ºC throughout the entire thickness, which is the average yearly temperature for the area.

For the mechanical analysis, standard first-order 3D stress tetrahedral elements (C3D4) were adopted, and a non-linear geometry static general analysis step was specified. A gravity load equal to 9.81 $m/s^2$ was imposed, as well as pressure loads on both the dam body and foundation based on the node elevation for the average upstream hydrostatic load. Boundary conditions were specified as fixed along all directions for the foundation bottom surface, and as symmetry along both vertical surfaces. As previously described, nodal temperatures were imported directly from the thermal analysis for the entire analysis period. The interface between the dam body and foundation was simulated using a contact formulation with normal hard contact behaviour, penalty formulation tangential behaviour (with a friction coefficient of 0.5), and automatic contact stabilization. Additionally, the dam was also simulated with tie constraints (perfect bond) to better understand the effect of the interface simulation on the results.

The overall mesh size for the system was the same for both analyses, varying from 2 to 4 m for the dam body, and totaling about 176,000 elements. The foundation mesh size ranged from 2 m near the dam to approximately 50 m closer to the edge boundary condition, adding up to about 11,000 elements. The total analysis time was 75 years (from 1964 to 2039), allowing the behaviour of the structure to be predicted 20 years into the future.

Material properties for the linear-elastic foundation and non-linear concrete, as well as other coefficients adopted, are shown in Table 5-2. The compressive strength and modulus of elasticity of both the foundation and concrete were determined based on laboratory tests performed by LNEC (Dias et al., 2022). Moreover, the non-linear compressive and tensile behaviours were specified as described in Gorga (2018) and Gorga et al. (2018, 2020).

**Table 5-2 Mechanical properties and coefficients.**

| | Unit | Concrete | Foundation | Other |
|---|---|---|---|---|
| Thermal conductivity | $W/mK$ | 3.00 | 3.35 | - |
| Coefficient of thermal expansion | $1/K$ | $0.9 \times 10^{-5}$ | $0.9 \times 10^{-5}$ | - |
| Specific heat | $J/kgC$ | 880 | 874 | - |
| Elastic modulus | $GPa$ | 26.8 | 15.0 | - |
| Compressive strength | $MPa$ | 32.0 | - | - |
| Tensile strength | $MPa$ | 3.02 | - | - |
| Density | $kg/m^3$ | 2450 | | - |
| Convection coefficient water-concrete | $W/Km^2$ | - | - | 500 |
| Convection coefficient rock-water | $W/Km^2$ | - | - | 500 |
| Convection coefficient air-concrete | $W/Km^2$ | - | - | 20 |
| Convection coefficient air-rock | $W/Km^2$ | - | - | 20 |
| Convection coefficient rock-concrete | $W/Km^2$ | - | - | 1000 |
| Radiation coefficient | $W/Km^2$ | - | - | 4.72 |
| Emissivity | - | - | - | 0.82 |
| Stefan-Boltzmann constant | $J/sK^4m^2$ | - | - | $5.67 \times 10^{-8}$ |
| Absorptivity | - | - | - | 0.525 |

Concrete non-linear behaviour was defined according to the concrete damaged plasticity model. Even though the type of aggregate used is unknown, it has been reported that the lithology of the area where the structure was built comprises mainly of granitic-gneiss rocks (Dias et al., 2022; Rebelo, 2020). Therefore, it is estimated that the mechanical properties deterioration due to ASR would be similar to the granites found in Virginia, USA (V+UL35), which presented reduction of modulus of elasticity ($E$), compressive strength ($f`_c$) and tensile strength ($f_t$) as shown in Table

5-3 according to Sanchez et al. (2017). Linear interpolation between these values was implemented.

**Table 5-3 Mechanical properties deterioration.**

| AAR Expansion Level (%) | Reduction $E$ (%) | Reduction $f`_c$ (%) | Reduction $f_t$ (%) |
|---|---|---|---|
| 0.00 | 0.0 | 0.0 | 0.0 |
| 0.05 | 6.5 | 0.0 | 14.7 |
| 0.08 | 12.3 | 2.3 | 28.1 |

Unlike previous studies, creep was calculated directly in the new subroutine based on a creep compliance curve determined by LNEC through both laboratory tests and empirical equations (Dias et al., 2022; Rebelo, 2020). A Dirichlet series with five Kelvin models was used to best fit the reported creep compliance curve shown in Equation 5-10, where t' is the load application time.

$$J(t,t') = \frac{1}{43.26}\left[1 + 4.48\left(t'^{0.40} + 0.05\right) \times (t - t')^{0.12}\right] \tag{5-10}$$

Air and water temperatures adopted by the thermal model were measured/estimated by LNEC (Dias et al., 2022; Rebelo, 2020) and are presented in Figure 5-3. Note that: i) the average external air temperature is 16.5ºC, ii) the water temperature was subdivided into depths from #1 to #7, which corresponds to bands of approximately 10 m and displayed the following average elevations: #1=395 m, #2=385 m, #3=374 m, #4=364 m, #5=353 m, #6=343 m, and #7=330m, and iii) curves #6 and #7 are so close together that they are almost indistinguishable.

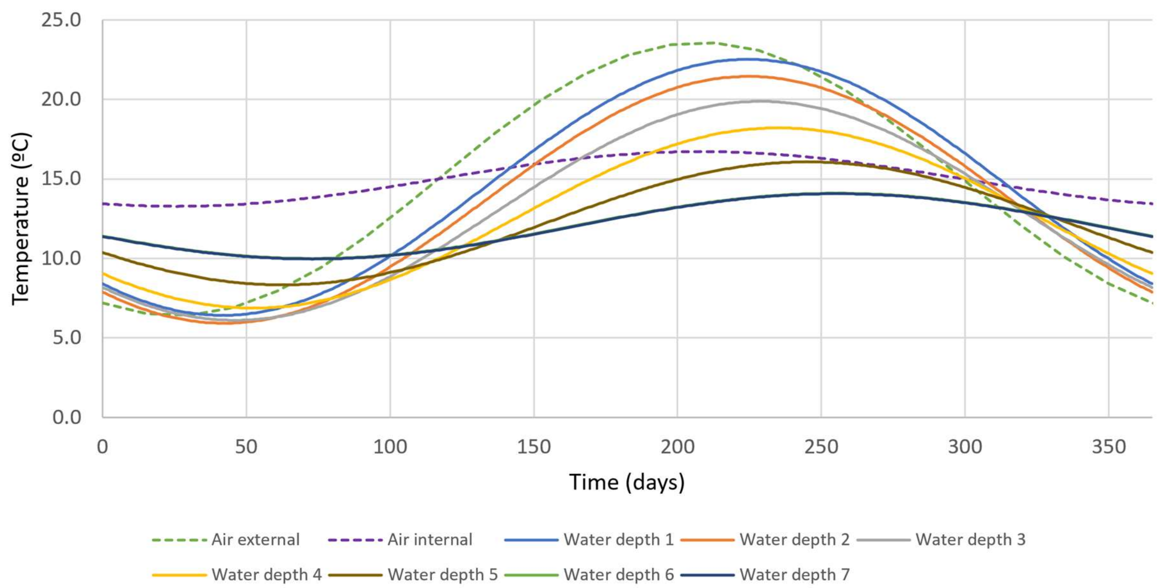


**Figure 5-3. Temperatures adopted by the thermal model**

As there was no information regarding the type of aggregate used, alkali leaching, alkali release, internal relative humidity or alkali content of the mix, the AAR free expansion curve was determined based on the available information: DRI test results, free in-situ expansion rates, lithology of the region, the concrete compressive strength at time of construction, the recorded displacement values, and finite element model results. A detailed explanation covering all the assumptions adopted when determining the free expansion curve is presented in the next section.

Construction and expansion joints were not simulated, and given the fact that they have not undergone significant damage or displayed meaningful displacements, the effect of the reaction on the joints was not assessed in this study.

Lastly, the main differences between the proposed and the LNEC modeling approaches are summarized in Table 5-4.

**Table 5-4 Main differences between LNEC and proposed modeling approaches.**

| Parameter | Proposed approach | LNEC (Dias et al., 2022; Rebelo, 2020) |
|---|---|---|
| Free expansion equation determination | Based on analytical free expansion equation, DRI test results, monitoring data, recorded free expansions and finite element model results | Based on monitoring data, recorded free expansions and finite element model results |
| Number of free expansion equations implemented | One | Three |
| Effect of temperature on AAR expansion | Affecting kinetics only | Affecting expansion at infinity only |
| Effect of humidity on AAR expansion | Accounted for directly (on the free expansion analytical equation) and assumed homogeneous on entire dam | Accounted for indirectly (manual subdivision of expansion zones) and varied between different regions |
| Expansion redistribution | Included | Not included |
| Stress-state dependency | According to Gautam et al. (2017) | According to Larive (1997) |
| Modeling of dam-foundation interface | Contact formulation | Perfect bond formulation |
| Concrete material model | Non-linear visco-plastic | Linear visco-elastic |
| Effect of mechanical properties deterioration | Included | Not included |

## 5.7 Discussion of Results

### 5.7.1 Temperature history

As done by LNEC, the proposed model was also able to closely match the recorded temperature data of the dam at several locations at different depths (Figure 5-4). Thermometers 14, 17 and 20 were located on block 0 at 357 m elevation, and were located upstream, halfway through the dam body, and downstream, respectively (refer to Figure 5-1). Similarly, thermometers 86, 88 and 91 were located on block 6E at 342 m elevation, and were also located upstream, halfway through the dam body, and downstream, respectively. As results are cyclical, short periods of 4 years were chosen to display the accuracy of the simulation.

a

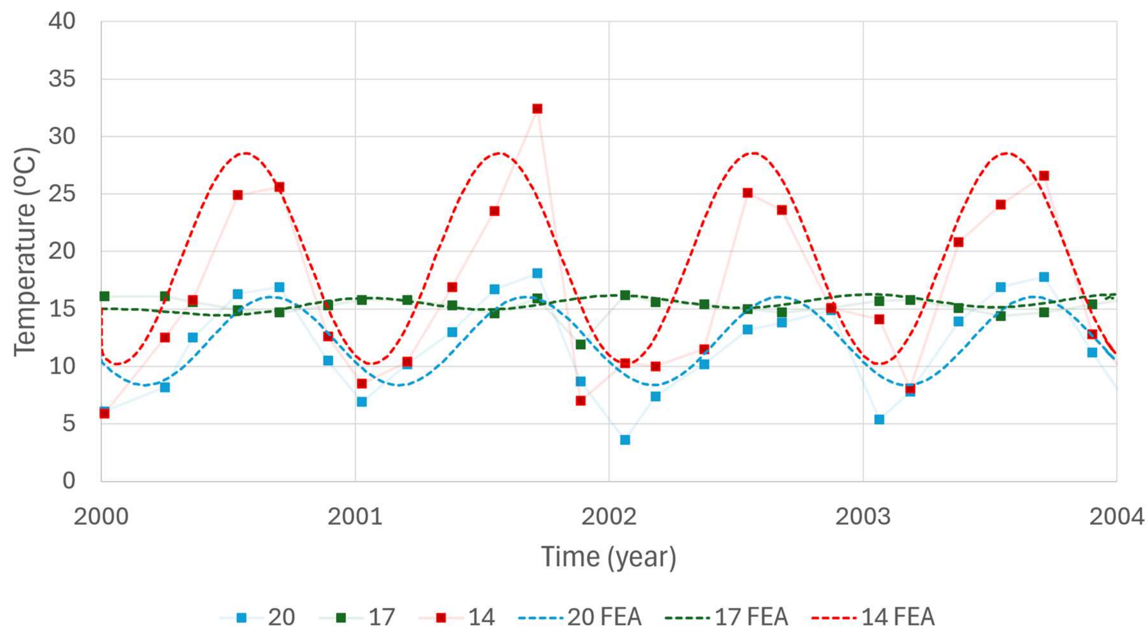


b

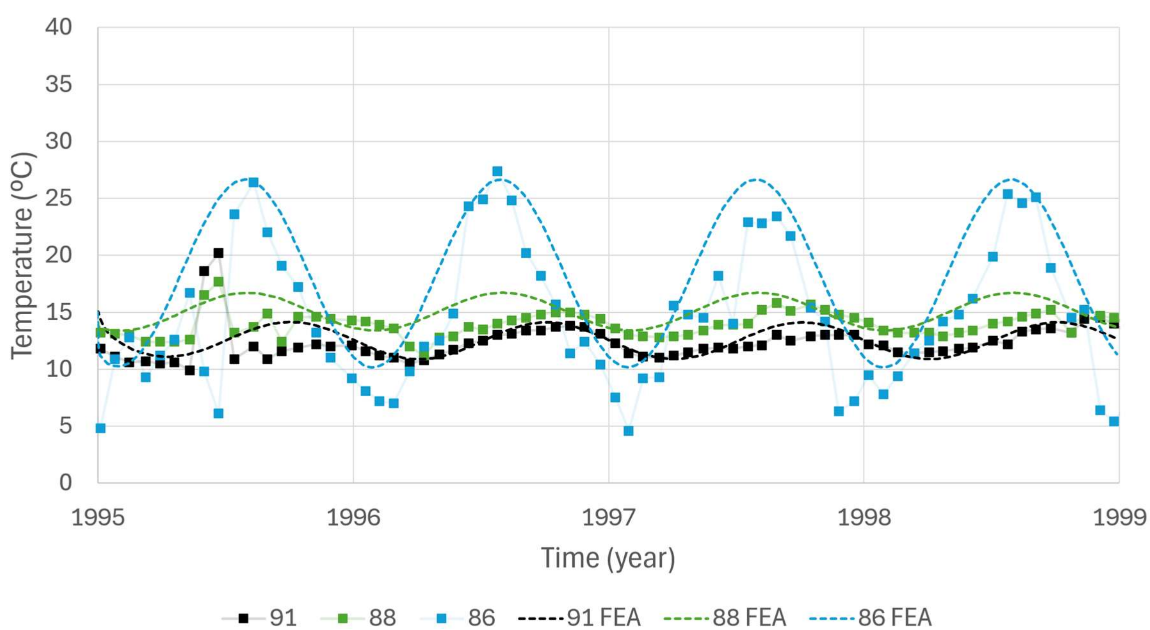


**Figure 5-4. Temperature history comparison between model and monitoring data: a. Block 0 at 357 m, b. Block 6E at 342 m.**

It was observed that the areas below ground presented lower temperatures because of the lack of solar radiation, and the upstream face temperature was approximately 5ºC lower than the downstream face because of the contact with the water. Moreover, core temperatures did not vary drastically because of the insulation effect of the thick concrete layers (core temperature was 13.5ºC during summer and 16ºC during winter, whereas the downstream face temperature was 27.5ºC during summer and 10ºC during winter). Lastly, it was observed that the temperature on the downstream face of the right abutment was 3 to 5ºC higher than on the upstream face of the left abutment because of the orientation of the surfaces relative to the solar exposure.

### 5.7.2 AAR free expansion curve

The University of Ottawa's AAR analytical model (De Grazia et al., 2021; Goshayeshi, 2019; Nguyen et al., 2022) was used to determine the best fit curve between the measured on-site free expansion curves, with results later being checked against available monitoring data and attained expansion estimated through DRI tests. The only known equation variable was the temperature at the locations where the expansions were measured, which is shown in Table 5-5. Assuming that the concrete used was rolled compacted concrete with design compressive strength of approximately 20 MPa at 28 days as tested at the time of construction, it was estimated that the alkali content of the mix was between 2 and 3 $kg/m^3$ (similar to Miranda dam in Portugal - Custódio et al., 2017). Leaching was expected to be minimal due to the size (and thickness) of the structure. The internal relative humidity of the dam was estimated to be between 95 and 85% based on data presented in the literature (Jensen, 2004; Nilsson, 2023; Oxfall et al., 2014). Note that the analyzed structures presented in the literature are all slender structures (bridges and nuclear power plants), but the same general conditions were assumed. External humidity conditions are known to affect only the first few centimeters of the structure (Comi et al., 2012; Gorga et al., 2018), and the dam is not severely cracked or with extensive leakage problems; therefore, the effect of the external humidity conditions is not expected to significantly influence the internal relative humidity.

**Table 5-5 Monthly temperatures at extensometer locations.**

| | Temperature (ºC) | | | | |
|---|---|---|---|---|---|
| month | Ext. #3 | Ext. #5 | Ext. #6 | Ext. #9 | Ext. #12 |
| 1 | 13.1 | 15.3 | 16.8 | 17.7 | 16.2 |
| 2 | 12.7 | 12.7 | 15.8 | 15.9 | 15.9 |
| 3 | 12.4 | 12.5 | 14.9 | 15.3 | 15.5 |
| 4 | 12.2 | 14.6 | 14.3 | 16.1 | 15.1 |
| 5 | 12.3 | 18.5 | 14.3 | 18.0 | 14.8 |
| 6 | 12.5 | 23.2 | 14.8 | 20.7 | 14.7 |
| 7 | 12.9 | 27.3 | 15.7 | 23.3 | 14.8 |
| 8 | 13.3 | 29.9 | 16.7 | 25.1 | 15.1 |
| 9 | 13.6 | 30.1 | 17.6 | 25.8 | 15.6 |
| 10 | 13.8 | 28.0 | 18.2 | 25.0 | 15.9 |
| 11 | 13.7 | 24.1 | 18.2 | 23.0 | 16.2 |
| 12 | 13.5 | 19.4 | 17.7 | 20.3 | 16.3 |
| average | 13.0 | 21.3 | 16.3 | 20.5 | 15.5 |
| maximum | 13.8 | 30.1 | 18.2 | 25.8 | 16.3 |

Based on the assumptions presented, a single free expansion curve with alkali content of 2.5 $kg/m^3$, alkali release of 1.0 $kg/m^3$ (adding up to a total of 3.5 $kg/m^3$), 5% leaching, 85% internal relative humidity, $\varepsilon_{AAR}^{\infty} = 0.08$, $\tau_L = 700\ days$, and $\tau_c = 190\ days$ was used to represent the behaviour of the entire structure. The proposed curve could not be compared directly to the measured expansion curves (Figure 5-5a) because their temperature averages and ranges vary significantly. Therefore, all measured expansion curves were first approximated by determining best fit Larive's coefficients ($\tau_c$ and $\tau_L$), adopting the same assumptions just described for all cases, which might not be true for the real structure, and were then adjusted to the same temperature (16ºC). It was observed that the resulting curves can be categorized as having three different reactivities: more reactive (purple lines), less reactive (orange lines) and non-reactive (green line), with the proposed curve (blue line) being very close to the more reactive curves (Figure 5-5b). This indicates that the variables are not homogeneous within the entire structure, but a single average curve is still able to represent the overall behaviour as shown subsequently. Moreover, the proposed curve was very close to the average of all three curves adopted by LNEC (dashed lines). It is worth noting that there have been records in the literature of very slowly reactive granitic aggregates in Portugal (Silva et al., 2016), which did not present visible reactivity according to the standard CPT - concrete prism test (CSA A23.2-14A, 2014), i.e., 1 year at 38ºC, 100% relative humidity and with 5.25 $kg/m^3$ alkali content. Only when tested under the ACPT - accelerated concrete prism test (RILEM AAR-11 as per Borchers et al., 2021), i.e., half a year at 60ºC, 100% relative humidity and with 5.25 $kg/m^3$ alkali content, any reactivity could be observed. This matches what the model would predict for this aggregate, as it would only present about 0.01% expansion for the standard concrete prism test, but 0.06% for the accelerated concrete prism test (Figure 5-5c). Under the damage degree classification proposed by Sanchez et al. (2016), the aggregate would be considered as having negligible expansion.

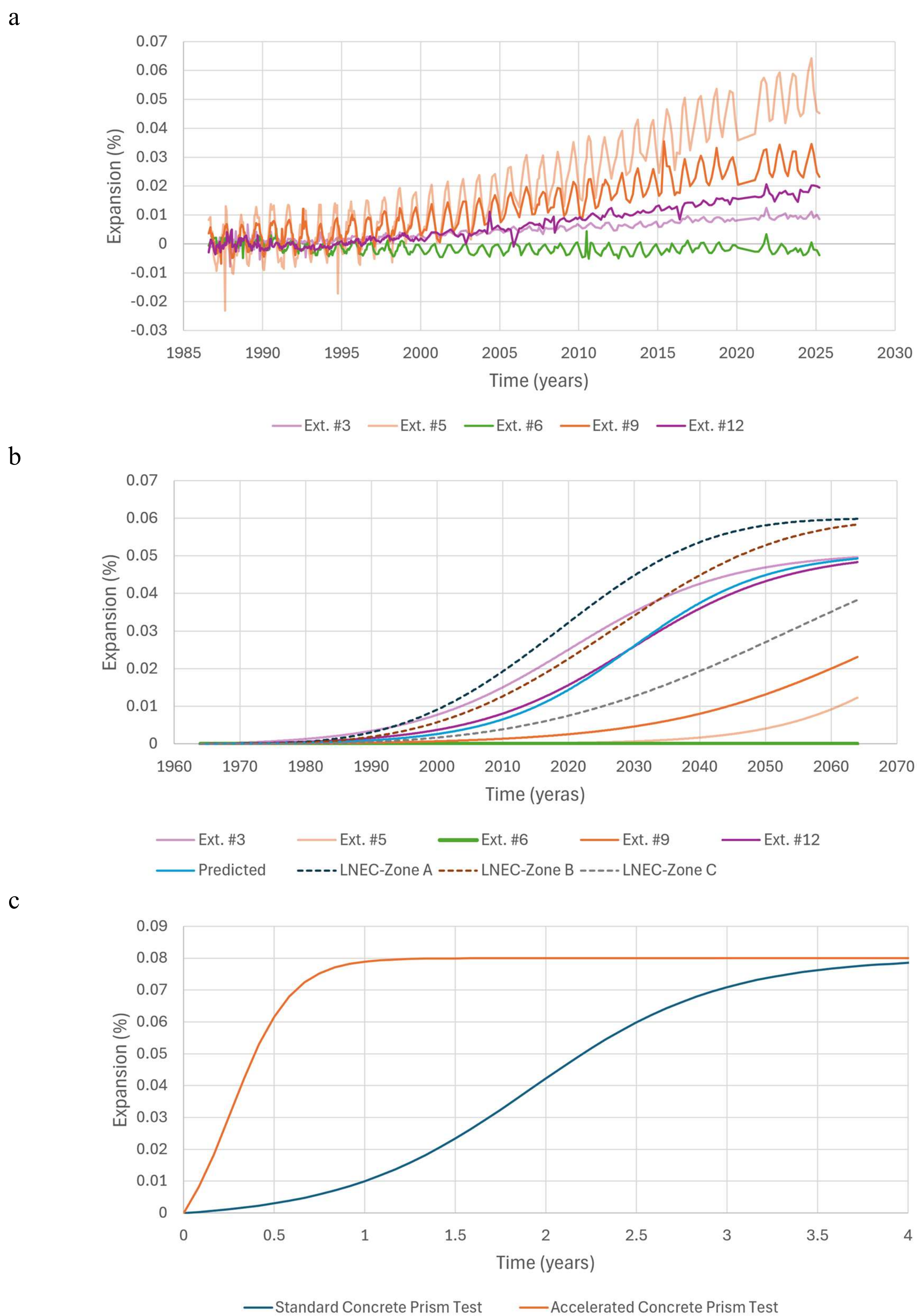


**Figure 5-5. Free AAR-induced expansion curves: a. Recorded extensometer data, b. Comparison of proposed, recorded and LNEC curves, c. Predicted CPT and ACPT.**

As shown by the DRI results and the in-situ free expansion curves, there is significant variation in expansion within the structure. Part of this difference can be attributed to different stress-states and temperatures between the analyzed areas. However, those two factors alone cannot explain the large range reported. Therefore, the most likely cause is variation in concrete mix (alkali content) and types of aggregates used during construction. For massive structures, it is common practice for the aggregates to be sourced locally. As it was not known that the area had reactive aggregates, it is possible that varying amounts of the reactive aggregate ended up in different parts of the structure. Note that according to the most recent developments adopted by the University of Ottawa's AAR analytical model (Olajide et al., 2025), internal humidity is believed to only affect kinetics, not total expansion. Even using older models (De Grazia et al., 2021; Goshayeshi, 2019; Poyet et al., 2006), the reduction in expansion would likely not surpass 30% when internal relative humidity is reduced from 100 to 85%. Therefore, the variation in internal relative humidity in a structure that displays a small amount of cracking and no leakage problems is not expected to be the main cause for the variation in expansion observed.

It is also important to highlight that for the same values of alkali content, alkali release, leaching and internal humidity assumed along with other combinations of values for $\varepsilon_{AAR}^{\infty}$, $\tau_L$ and $\tau_c$ could also generate a curve that would reasonably fit the same data points. However, without knowing the aggregate, a better estimation of the free expansion curve is currently not possible.

### 5.7.3 Diagnosis, prognosis and recommendations

When comparing the modeling approaches for the interface between dam body and foundation, it was observed that perfect bond (tie) and contact formulations yielded similar overall stresses and basically the same displacements. The maximum difference in displacement observed between the two models was 15% for radial displacement and less than 2% for vertical and tangential displacements. The impact of varying the coefficient of friction in the contact simulation was negligible. The only noticeable differences between the two alternatives were the following: i) Tie simulations are faster to compute as there are fewer conversion conditions to be satisfied for each time step and the overall formulation is simpler; ii) Contact simulation resulted in a more homogeneous stress distribution at the interface between the surfaces; and iii) Tie simulation led to a small amount of stress concentration at the interface between the dam body and the foundation, with compressive stresses being larger (around 30 to 40% on average) at the edges of the dam. As the contact simulation is overall considered to be more accurate, reduces stress concentration and provides more homogeneous interface stresses, it was adopted henceforth. Even so, adopting perfect bond (as performed by LNEC) is not expected to significantly affect the results of the model.

It has been reported that DRI test results are influenced by the stress-state of the structure (Zahedi et al., 2021), with the direction of restraint displaying lower attained expansion compared to those unrestrained/less restrained due to expansion redistribution. Therefore, to estimate the expansion attained to date, the total redistributed expansion per direction, including temperature effects (calculated within the finite element model), was adopted. Results of expansion for the locations and direction of coring (y-axis) predicted expansions between 0.039 and 0.017% in 2025, which are similar to the predicted values of 0.030 to 0.050% determined through the DRI test. Accordingly, this suggests that the proposed AAR free expansion curve can estimate the current expansion attained by the dam up to the current date with reasonable accuracy.

When comparing the field-recorded displacements and the finite element model results, a good match was observed for the radial (Figure 5-6), tangential (Figure 5-7) and vertical (Figure 5-8) displacements, as was the case for the LNEC model. As shown, the same overall movement trend is expected to be maintained for many years in most cases. Note that zero displacement is assumed as the first survey data point, and the other curves are adjusted up to match that.

a

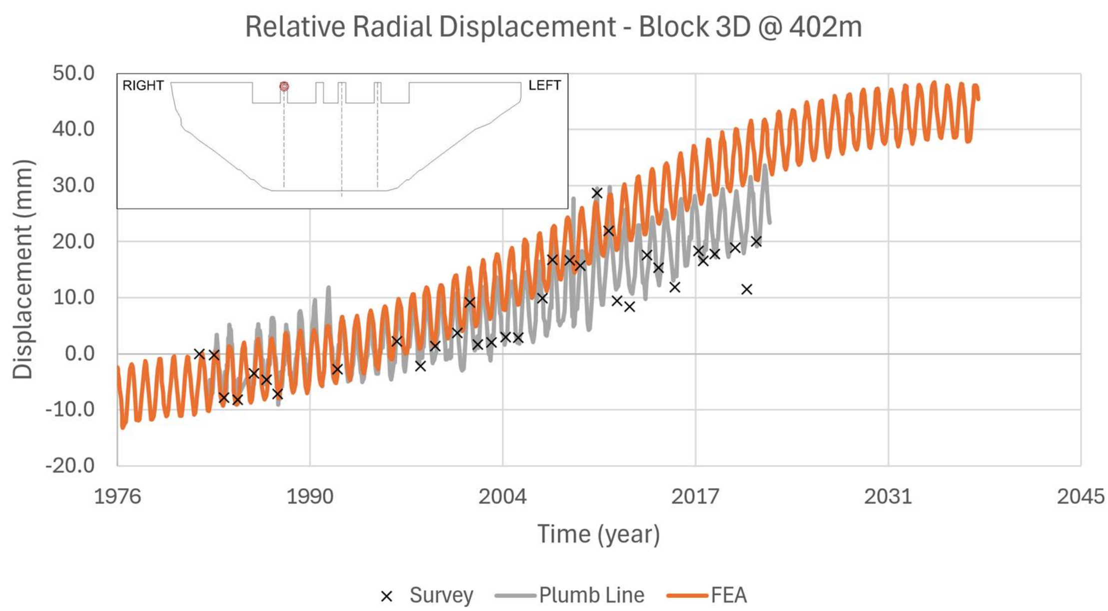


b

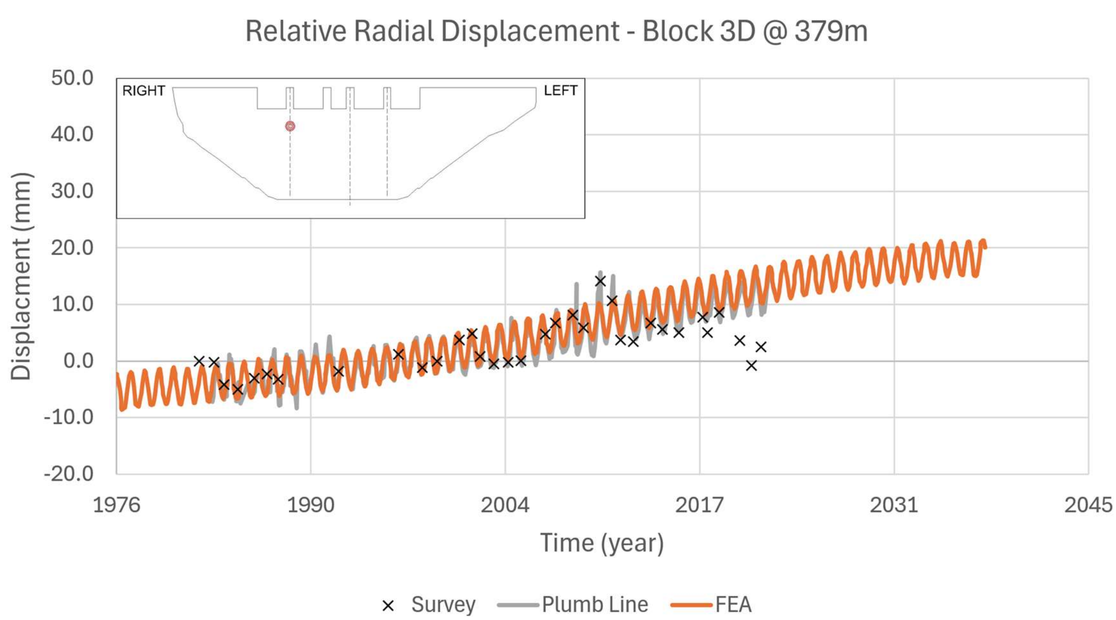


**Figure 5-6. Predicted (FEA) vs recorded relative radial displacements for block 3D: a. at 402 m elevation, b. at 379 m elevation.**

a

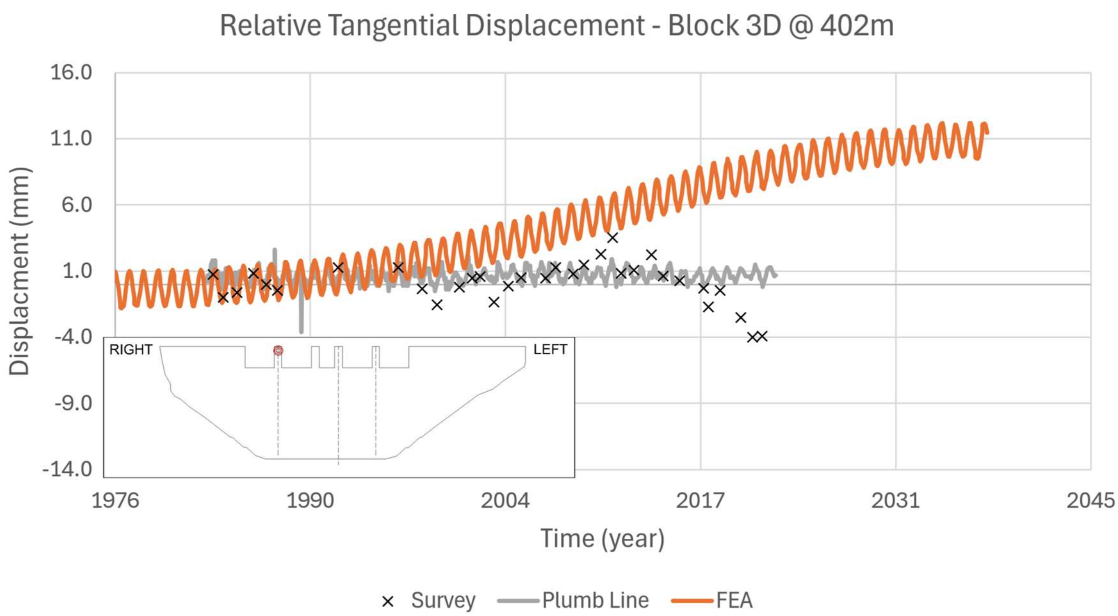


b

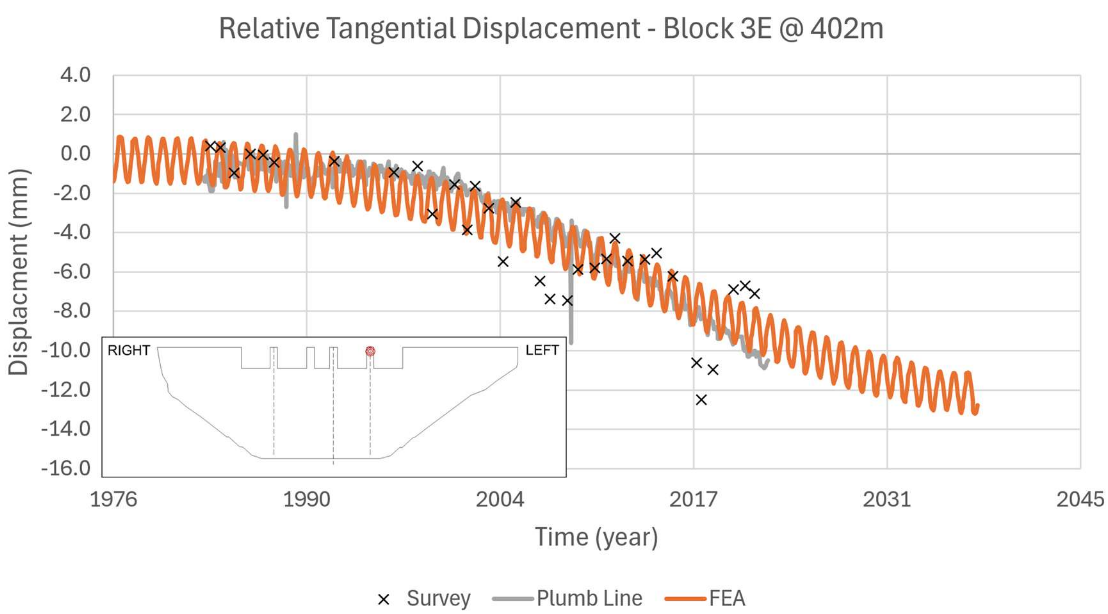


**Figure 5-7. Predicted (FEA) vs recorded relative tangential displacements at 402m elevation: a) for block 3D; b) for block 3E.**

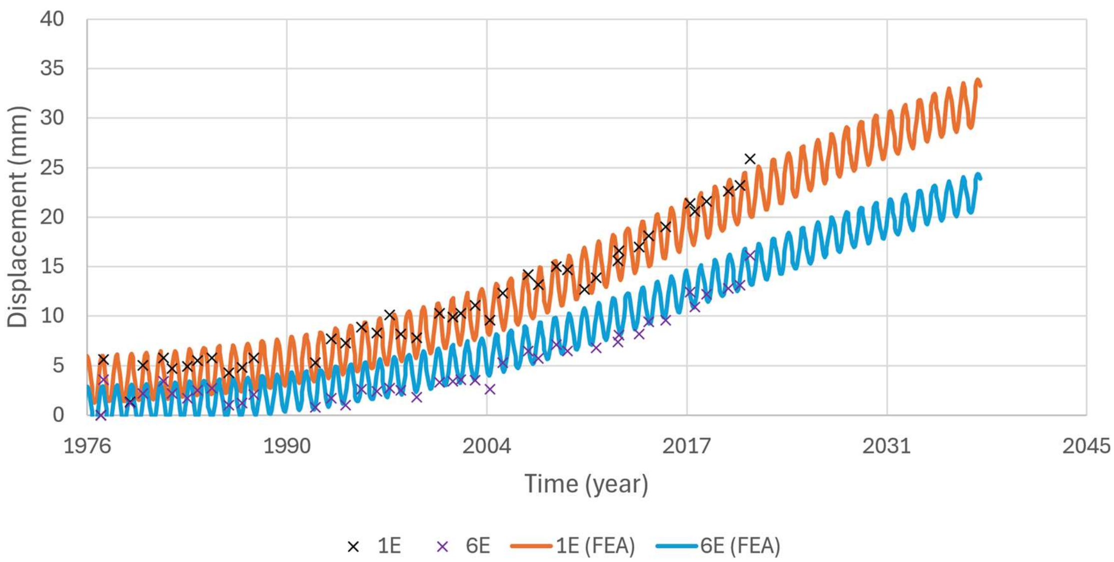


**Figure 5-8. Predicted (FEA) vs recorded absolute vertical displacements for block 1E and 6E at 402 m elevation.**

It is interesting to note that neither the proposed approach nor the LNEC model were able to correctly capture the different tangential behaviour of the top of blocks 3E and 3D. Block 3E displayed permanent tangential displacements, whereas block 3D showed almost no permanent movement. Note that the same lack of symmetry was not observed when comparing radial and vertical displacements. The proposed model predicted permanent tangential displacement on both blocks, whereas the LNEC model predicted no tangential movement on either block. There are two possible explanations for this non-symmetrical behaviour: i) pocket(s) of low or high expansion on one of the sides, and ii) different foundation stiffness between the two abutments. Investigating both of those further is beyond the scope of this work and would require extensive result fitting, which is contrary to the basis of the proposed approach. Nevertheless, permanent tangential displacement values were very small, less than 10 mm over 60 years. Therefore, the overall accuracy of either one of the models is not expected to be compromised by not capturing this behaviour.

Gate opening variation over time was also estimated, as shown in Figure 5-9. It was observed that the total gap was not reducing but rather increasing over time. This occurred because of the curved shape of the dam, which tends to "open" (i.e., increase the curvature's diameter) at the top as expansion develops. Based on what was presented, gate operation is not expected to be affected due to AAR expansion.

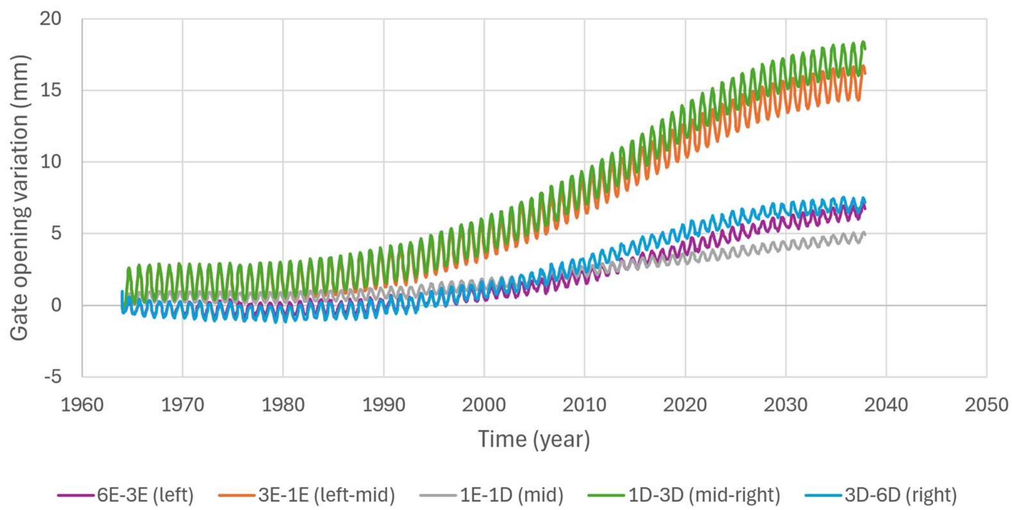


**Figure 5-9. Gate opening variation over time.**

As expected, overall stresses on the dam body were not exceedingly large and did not lead to severe damage, matching what has been observed in the field. When only loads were applied (without AAR), stresses on the dam body were low, with the maximum compressive stress value being around 4.5 MPa (along Z-axis). In 2020, AAR-induced expansion caused the maximum compressive stress to be 9.5 MPa (along X-axis in the winter just above the downstream leg of the spillway). A small amount of stress concentration was also observed at the top of the edges of the dam. However, disregarding those, the maximum overall compressive stress was around 5.5 MPa on the right abutment and 6.5 MPa on the left abutment, with the latter also displaying around 10.5 MPa in compression at the transition zone to the leg. As contact formulation was adopted instead of perfect bond, the elements at the dam-foundation interface did not display high stresses. The compressive stresses observed are of the same order of magnitude as those reported by LNEC for 2020. Tensile stresses cannot be directly compared to the LNEC model, as their model was linear (visco-) elastic.

In 2039, the same overall stress distribution was observed (Figure 5-10), with stresses not changing significantly. Maximum compressive stresses previously described increased by approximately 1 MPa, and the areas under higher stress also increased by about 20%. Note that the increase in maximum compressive stress was small because the expansion rate had started to decrease after 2020 for the outer layer of the downstream face, as those elements displayed the warmest temperatures. Most of the dam was still far from reaching the same behaviour.

a

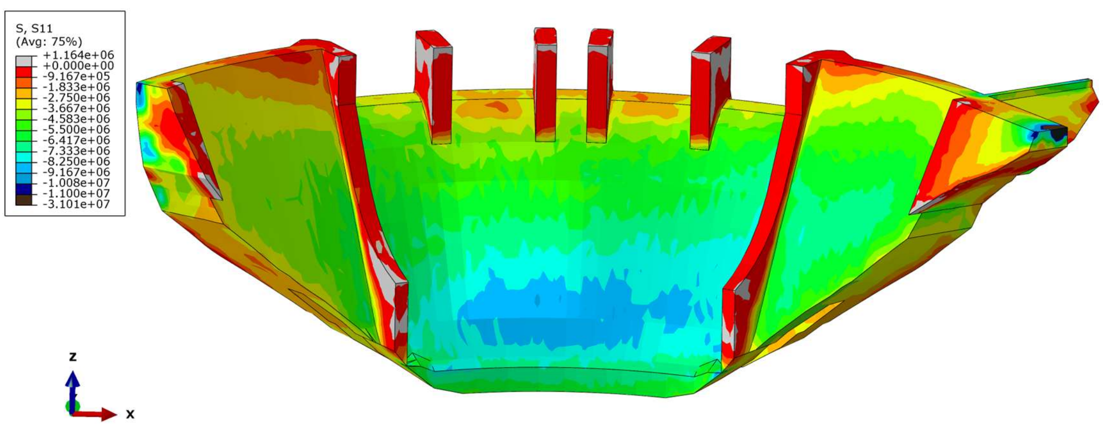


b

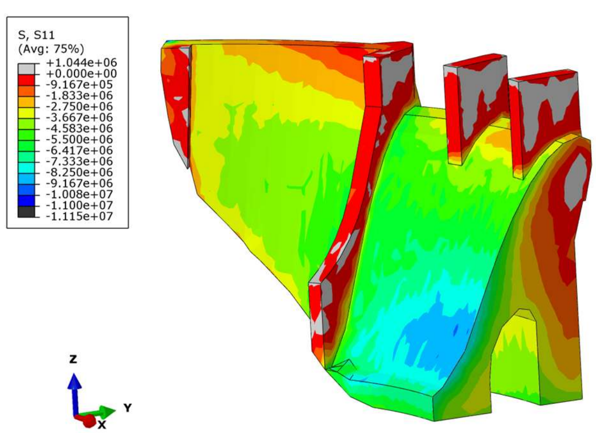


**Figure 5-10. Stresses (in Pa) along X-axis predicted in 2039: a) downstream face; b) through the section.**

The first signs of damage due to AAR – determined by development of plastic strain – in above ground areas predicted by the model started around 1996, matching when they were first observed in the field (around the mid 1990's). In 2025, predicted tensile damage tended to be mostly concentrated around geometry transition areas (i.e., around the leg on the left abutment, around pier bases and edges of the spillway), at the top of both abutments, and at the top of the spillway between piers 1E-3E and 1D-3D. Map cracking along the surface was observed only in very limited areas. Note that fine superficial map cracking was not captured due to the large size of the elements used to model the dam, as larger elements tend to average out expansion gradients. In 2039 (Figure 5-11), the previously described areas showed more intense cracking, maximum plastic strain increased by 25%, and the downstream face displayed extensive map cracking. Even so, overall damage was limited and not expected to affect the performance of the structure.

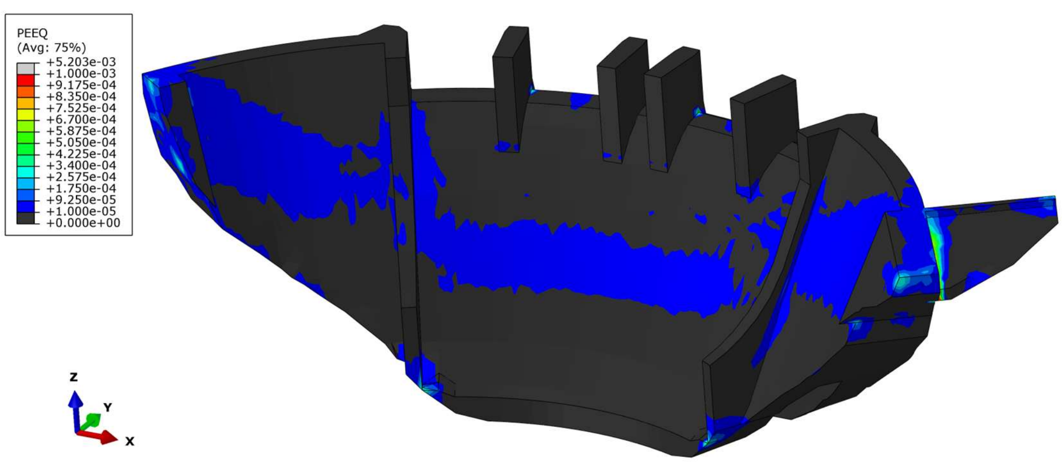


**Figure 5-11. Plastic strain (damage) predicted in 2039 on the downstream face.**

Lastly, it was also observed that creep played an important role in the overall behaviour of the structure. Along the X-axis, compressive stresses were largest, and so was the (negative) induced creep strain. In some areas, creep strain magnitude was up to 50% that of AAR, effectively reducing the net-imposed strain along the X-axis by half. In most locations, the degree of the described phenomenon (along the X-axis) was smaller, but still significant, ranging from 10 to 40%. Along the other directions, stresses were smaller, and so were the creep-induced strains. Therefore, the effect of creep was significantly smaller, usually not surpassing 20% of the AAR-induced strain.

After 2039, the predicted free expansion AAR curve tends to level off. However, it is currently not possible to know if the future predictions are correct for two main reasons. First, alkali release from the aggregates may play an important role in continuously supplying alkalis to the system, preventing the expansion from stabilizing. Second, the expansion curve was estimated from the recorded in-situ expansion values, not from a specific known aggregate expansion curve. Without knowing the aggregate (and concrete mix), it is not possible to determine with any degree of certainty what the final expansion may be. Therefore, it is highly recommended to 1) determine what the (reactive) aggregate of the dam is through petrographic analysis, and 2) perform residual expansion tests on cores extracted from the dam. Both test results will contribute to a better understanding and further validate the AAR-induced expansion taking place in the structure and its consequences.

Overall, the Bemposta dam is expected to remain fully operational for the period analyzed. Stresses are expected to remain within acceptable ranges, gate operation will not be affected, and cracking (damage) extent is predicted to be limited, not leading to leakage or any other significant distress signs. Nevertheless, it is also recommended that monitoring, surveys and inspections continue, periodically comparing measured and finite element model results to ensure no significant unexpected change in behaviour is taking place.

## 5.8 Conclusions

AAR is a very complex mechanism, and the economic impact it can have on the operation/safety of massive structures is very significant. Given the addition of ongoing monitoring data from the Bemposta dam and laboratory testing, such as DRI, revisiting the results previously described by LNEC is evidently worth the effort. Through a thorough assessment of the Bemposta dam using the proposed modeling approach, and after comparing the results presented with the model by LNEC, the following was observed:

- A new subroutine that calculates creep, thermal and AAR-induced strain simultaneously with the non-linear mechanical model was successfully implemented. With this development, the proposed approach was able to accurately simulate the behaviour of the Bemposta dam, matching monitoring data well.

- The analytical AAR free expansion equation adopted was able to represent the free in-situ expansion curves measured by LNEC, confirming it can realistically describe AAR-induced expansion in massive structures.

- DRI test results and monitoring data confirmed that the assumptions adopted and the results obtained are accurate and realistic. It is also important to highlight that all results presented were achieved with minimal parameter fitting.

- There are some advantages in using the proposed approach: (i) it provides a more comprehensive description of the effect of temperature and humidity on AAR-induced expansion, (ii) it simulates dam body-foundation interaction using contact formulation, (iii) it estimates the AAR-induced free expansion curve(s) through a semi-empirical equation validated for both laboratory and field-exposed specimens, (iv) it redistributes AAR-induced expansion based on the triaxial state of stress, (v) it considers the non-linear material behaviour of concrete, and (vi) it degrades the concrete mechanical properties according to the level of expansion attained. However, both LNEC's model and the proposed FE model were able to represent the massive structure well, and both approaches concluded that the serviceability of the structure should not be affected in the near future.

- Even though the Bemposta dam is expected to remain fully operational for the time period analyzed, constant monitoring and additional laboratory tests are still recommended.

### 5.9 Appendix – Solar Radiation Calculation

The following procedure describes how to calculate the solar radiation incident on an opaque inclined surface (Duffie & Beckman, 2013; Hottel, 1976; Liu & Jordan, 1960). First, the zenith angle $z$ (angle between sun rays and the vertical), incidence angle $\theta$ (angle between the solar rays and a line normal to the surface) and surface solar azimuth angle $\gamma$ (angle between projection of the sun rays and the normal to the surface on the horizontal plane) are determined according to Equations 5-11 through 5-17.

$$\delta = 23.45º \times \sin\left(360\left(284 + \frac{n}{365}\right)\right) \tag{5-11}$$

$$h = 0.25 \times (number\ of\ minutes\ from\ local\ solar\ noon) \tag{5-12}$$

$$\alpha = \mathrm{asin}(cos(L) \times cos(\delta) \times cos(h) + sin(L) \times sin(\delta)) \tag{5-13}$$

$$\phi = \mathrm{acos}\left(\frac{sin(\alpha) \times sin(L) - sin(\delta)}{cos(\alpha) \times cos(L)}\right) \times \left(\frac{h}{|h|}\right) \tag{5-14}$$

$$z = 90º - \alpha \tag{5-15}$$

$$\gamma = \phi - \psi \tag{5-16}$$

$$\theta = \begin{cases} 0 \rightarrow if\ \gamma < 270º\ or\ \gamma > 90º \\ \mathrm{acos}(cos(\alpha) \times cos(|\gamma|) \times sin(\beta) + sin(\alpha) \times cos(\beta)) \rightarrow otherwise \end{cases} \quad (5\text{-}17)$$

where $\delta$ is the declination angle (angular position of the sun at solar noon with respect to the equatorial plan, varying from -23.45º to 23.45º), $n$ is the day of the year (from 1 to 365), $\alpha$ is the solar altitude (angle between the sun rays and the horizontal), $\phi$ is the solar azimuth angle (angle between the projection of the sun rays and due south - positive in the afternoon), $L$ is the latitude (in degrees with north being positive), $\psi$ is the surface azimuth (angle between the projection of the normal to the surface on a horizontal plane and due south - east is negative), $\beta$ is the tilt/slope between surface and horizontal (between 0º and 180º), $h$ is the hour angle (positive in the afternoon) and solar noon is the time that the sun crosses the meridian of the observer.

Next, it is necessary to determine the clear sky radiation ($\tau_b$) and the correction factor for clear sky atmospheric diffuse transmittance ($\tau_d$) as shown in Equations 5-18 through 5-22 and Table 5-6, where $a_0$, $a_1$, $k$, $r_0$, $r_1$ and $r_k$ are semi-empirical coefficients and $A$ is the altitude (in km).

$$\tau_b = a_0 + a_1 e^{\left(-\frac{k}{\cos(z)}\right)} \delta = 23.45º \times \sin\left(360\left(284 + \frac{n}{365}\right)\right) \quad (5\text{-}18)$$

$$a_0 = r_0(0.4237 - 0.00821(6 - A)^2) \quad (5\text{-}19)$$

$$a_1 = r_1(0.5055 + 0.00595(6.5 - A)^2) \quad (5\text{-}20)$$

$$k = r_k(0.2711 + 0.01858(2.5 - A)^2) \quad (5\text{-}21)$$

$$\tau_d = 0.2710 - 0.2939\tau_b \quad (5\text{-}22)$$

**Table 5-6 Clear sky radiation coefficients.**

| Climate | $r_0$ | $r_1$ | $r_k$ |
|---|---|---|---|
| Tropical | 0.95 | 0.98 | 1.02 |
| Mid-latitudes (summer) | 0.97 | 0.99 | 1.02 |
| Mid-latitudes (winter) | 1.03 | 1.01 | 1.00 |
| Subarctic | 0.99 | 0.99 | 1.01 |

Then, the extraterrestrial normal solar radiation $I_{on_n}$ (just outside the atmosphere for a day $n$) and the total instantaneous solar radiation incident on an inclined surface ($I_t$) can be estimated according to Equations 5-23 through 5-27, where $I_{sc}$=1353$W/m^2$ is a solar constant, $I_b$ is the direct solar radiation beam component, $I_{ds}$ is the diffuse solar radiation sky component, $I_{dg}$ is the diffuse solar radiation reflected from the ground component and $\rho$ is the solar reflectance of the ground surface (assumed as 0.32 for new concrete, 0.14 for bitumen and gravel roof, 0.10 for bituminous parking lot, 0.25 for bright green grass and 0.20 for crushed rock).

$$I_{on_n} = I_{sc}\left(1 + 0.033 \times \cos\left(\frac{360n}{365}\right)\right) \tag{5-23}$$

$$I_t = \begin{cases} 0 \rightarrow if\ \alpha < 0º\ or\ \theta < -90º\ or\ \theta > 90º \\ I_b + I_{ds} + I_{dg} \rightarrow otherwise \end{cases} \tag{5-24}$$

$$I_b = I_{on_n} \times \tau_b \times \cos(\theta) \tag{5-25}$$

$$I_{ds} = I_{on_n} \times \sin(\alpha) \times \tau_d \times \left(\frac{1 + \cos(\beta)}{2}\right) \tag{5-26}$$

$$I_{dg} = \left(I_{on_n} \times \sin(\alpha) \times (\tau_b + \tau_d)\right) \times \rho \times \left(\frac{1 - \cos(\beta)}{2}\right) \tag{5-27}$$

Lastly, the total absorbed instantaneous solar radiation incident on an inclined surface ($I_{t-abs}$) is determined as shown in Equation 5-28, where $a_{abs}$ is the material absorptivity.

$$I_{t-abs} = I_t \times a_{abs} \tag{5-28}$$

## 5.10 References


Batista, A. L. (1998). Análise do comportamento ao longo do tempo de barragens abóbada [Ph.D. Thesis]. Universidade Técnica de Lisboa and Laboratório Nacional de Engenharia Civil (LNEC).

Bazant, Z. P., & Wu, S. T. (1973). Dirichlet Series Creep Function for Aging Concrete. Journal of the Engineering Mechanics Division, 99(2), 367–387.

Borchers, I., Lindgård, J., Rønning, T. F., & Wigum, B. J. (2021). Recommendation of RILEM TC 258-AAA: RILEM AAR-11: determination of binder combinations for non-reactive mix design or the resistance to alkali-silica reaction of concrete mixes using concrete prisms − 60 °C test method. Materials and Structures, 54(6), 203.

Caron, P., Tinawi, R., & Léger, P. (2001). Slot cutting response of compressed concrete structures. 4th International Conference on Fracture Mechanics in Concrete and Concrete Structures, 879–886.

Charlwood, R. (1994). A review of alkali aggregate in hydro-electric plants and dams. International Journal on Hydropower Dams, 73–80.

Charlwood, R., Scrivener, K., & Sims, I. (2012). Recent developments in the management of chemical expansion of concrete in dams and hydro projects—Part 1: Existing structures. Hydro 2012 - Innovative Approaches to Global Challenges.

Chulliat, O., Grimal, E., & Bourdarot, E. (2017). Chambom Dam - A Struggle Against AAR. Dam Swelling Concrete (DSC 2017).

Comi, C., Kirchmayr, B., & Pignatelli, R. (2012). Two-phase damage modeling of concrete affected by alkali–silica reaction under variable temperature and humidity conditions. International Journal of Solids and Structures, 49(23–24), 3367–3380.

CSA A23.2-14A. (2014). Potential Expansivity of Aggregates - Procedure for Length Change Due to Alkali-Aggregate Reaction in Concrete Prisms.

Custódio, J., Ferreira, J. I., Silva, A. S., Ribeiro, A. B., & Batista, A. L. (2017). The diagnosis and prognosis of ASR and ISR in Miranda dam, Portugal. In A. Sellier, É. Grimal, S. Multon, & É. Bourdarot (Eds.), Swelling Concrete in Dams and Hydraulic Structures: DSC 2017 (1st Ed., pp. 321–337). John Wiley & Sons, Inc.

De Grazia, M. T., Goshayeshi, N., Gorga, R., Sanchez, L. F. M., Santos, A. C., & Souza, D. J. (2021). Comprehensive semi-empirical approach to describe alkali aggregate reaction (AAR) induced expansion in the laboratory. Journal of Building Engineering, 40.

Dias, I. F., & Batista, A. L. (2025). Modelling of concrete swelling effects in dams, considering the influence of temperature, humidity, stress field, viscoelasticity and cracking. Magazine of Concrete Research, 1–18.

Dias, I. F., Batista, A. L., & Rebelo, R. (2022, May). Prediction of the structural behaviour of Bemposta dam (Portugal), affected by concrete swelling. 16th International Conference on Alkali-Aggregate Reaction in Concrete (ICAAR).

Duffie, J. A., & Beckman, W. A. (2013). Solar engineering of thermal processes (Fourth Edition). John Wiley & Sons, Inc.

Esposito, R., & Hendriks, M. A. N. (2012). Degradation of the mechanical properties in ASR-affected concrete: Overview and modeling. Numerical Modeling Strategies for Sustainable Concrete Structures - SSCS 2012.

Fournier, B., & Bérubé, M.A. (2000). Alkali-aggregate reaction in concrete: a review of basic concepts and engineering implications. Canadian Journal of Civil Engineering, 27(2), 167–191.

Gautam, B. P., Panesar, D. K., Sheikh, S. A., & Vecchio, F. J. (2017). Multiaxial expansion-stress relationship for alkali silica reaction-affected concrete. ACI Materials Journal, 114(1), 171–184.

Gorga, R. V. (2018). Engineering-Based FE Approach to Appraise Slender Structures Affected by Alkali-Aggregate Reaction (AAR) [M.A.Sc. Thesis]. University of Ottawa.

Gorga, R. V., Sanchez, L. F. M., & Martín-Pérez, B. (2018). FE approach to perform the condition assessment of a concrete overpass damaged by ASR after 50 years in service. Engineering Structures, 177, 133–146.

Gorga, R. V., Sanchez, L. F. M., Martín-Pérez, B., Fecteau, P. L., Cavalcanti, A. J. C. T., & Silva, P. N. (2020). Finite Element Assessment of the ASR-Affected Paulo Afonso IV Dam. Journal of Performance of Constructed Facilities, 34(4).

Gorga, R. V., Sanchez, L. F. M., Martín-Pérez, B., & Noël, M. (2021). Engineering-based finite-element approach to appraise reinforced concrete structures affected by alkali–aggregate reaction. Magazine of Concrete Research, 74(8), 379–391.

Goshayeshi, N. (2019). Contribution to the Development of Analytical Models to Forecast Alkali-Aggregate Reaction (AAR) Kinetics and Induced Expansion [M.A.Sc. Thesis, University of Ottawa].

Grimal, E., Sellier, A., Le Pape, Y., & Bourdarot, E. (2008). Creep, shrinkage, and anisotropic damage in alkali-aggregate reaction swelling Mechanism-Part I: A constitutive model. ACI Materials Journal, 105(3), 227–235.

Hottel, H. C. (1976). A Simple Model for Estimating the Transmittance of direct solar radiation through clear atmospheres. Solar Energy, 18(2), 129–134.

Jensen, V. (2004). Alkali–silica reaction damage to Elgeseter Bridge, Trondheim, Norway: a review of construction, research and repair up to 2003. Materials Characterization, 53(2–4), 155–170.

Larive, C. (1997). Apports combinés de l'éxpérimentation et de la modélisation à la compréhension de l'alcali-réaction et de ses effets mécaniques.

Léger, P., Côté, P., & Tinawi, R. (1996). Finite element analysis of concrete swelling due to alkali-aggregate reactions in dams. Computers & Structures, 60(4), 601–611.

Liu, B., & Jordan, R. (1960). The Interrelationship and characteristic distribution of direct, diffuse, and total solar radiation. Solar Energy, 4(3), 1–19.

Nguyen, T. N., Sanchez, L. F. M., Li, J., Fournier, B., & Sirivivatnanon, V. (2022). Correlating alkali-silica reaction (ASR) induced expansion from short-term laboratory testings to long-term field performance: A semi-empirical model. Cement and Concrete Composites, 134(2).

Nilsson, L.O. (2023). Predicting moisture in field concrete - decisive parameters. CEMENT, 11, 100052.

Olajide, O. D., Nokken, M. R., & Sanchez, L. F. M. (2025). Moisture dynamics and influence on alkali-silica reaction induced expansion: A comprehensive laboratory study. CEMENT, 20, 100146.

Oxfall, M., Johansson, P., & Hassanzadeh, M. (2014). Moisture profiles in concrete walls of a nuclear reactor containment after 30 years of operation . Nordic Concrete Research - Proceedings of XXII Nordic Concrete Symposium, 479–482.

Pan, J., Feng, Y. T., Jin, F., & Zhang, C. (2013). Numerical prediction of swelling in concrete arch dams affected by alkali-aggregate reaction. European Journal of Environmental and Civil Engineering, 17(4), 231–247.

Pan, J., Feng, Y., Xu, Y., Jin, F., Zhang, C., & Zhang, B. (2013). Chemo-damage modeling and cracking analysis of AAR-affected concrete dams. Science China Technological Sciences, 56(6), 1449–1457.

Póvoas, R. H. C. F. (1991). Modelos não-lineares de análise e dimensionamento de estruturas laminares de betão incluindo efeitos diferidos [Ph.D. Thesis]. University of Porto.

Poyet, S., Sellier, A., Capra, B., Thèvenin-Foray, G., Torrenti, J.M., Tournier-Cognon, H., & Bourdarot, E. (2006). Influence of Water on Alkali-Silica Reaction: Experimental Study and Numerical Simulations. Journal of Materials in Civil Engineering, 18(4), 588–596.

Rebelo, R. P. B. T. (2020). Estudo do comportamento estrutural de barragens arco-gravidade afetadas por expansões do betão. Aplicação à barragem da Bemposta [M.A.Sc. Thesis]. Universidade Nova de Lisboa.

Sanchez, L. F. M., Fournier, B., Bastien, J., Mitchell, D., & Noël, M. (2016). Overall assessment of an ASR affected overpass "Robert-Bourassa/Charest" after nearly 50 years in service. 8th International Conference on Bridge Maintenance, Safety and Management - IABMAS.

Sanchez, L. F. M., Fournier, B., Jolin, M., & Duchesne, J. (2015). Reliable quantification of AAR damage through assessment of the Damage Rating Index (DRI). Cement and Concrete Research, 67, 74–92.

Sanchez, L. F. M., Fournier, B., Jolin, M., Mitchell, D., & Bastien, J. (2017). Overall assessment of Alkali-Aggregate Reaction (AAR) in concretes presenting different strengths and incorporating a wide range of reactive aggregate types and natures. Cement and Concrete Research, 93, 17–31.

Saouma, V., & Perotti, L. (2006). Constitutive Model for Alkali-Aggregate Reactions. Materials Journal, 103(3), 194–202.

Silva, A. S., Fernandes, I., Soares, D., Custódio, J., Ribeiro, A. B., Ramos, V., & Medeiros, S. (2016, July). Portuguese experience in ASR aggregate assessment. Proceedings of the 13th International Conference on Alkali-Aggregate Reactivity in Concrete (ICAAR).

Simulia. (2024). Abaqus/CAE - Complete Abaqus Environment (2024). Dassault Systèmes Corporation.

Ulm, F. J., Petrson, M., & Lemarchand, E. (2002). Is ASR-expansion caused by chemoporoplastic dilatation? Concrete Science and Engineering, 4(13), 47–55.

Ulm, F.J., Coussy, O., Kefei, L., & Larive, C. (2000). Thermo-Chemo-Mechanics of ASR Expansion in Concrete Structures. Journal of Engineering Mechanics, 126(3), 233–242.

Winnicki, A., Seręga, S., & Norys, F. (2014). Chemoplastic modelling of Alkali-Silica Reaction (ASR). Computational Modelling of Concrete Structures - Proceedings of EURO-C 2014, 2, 765–774.

Zahedi, A., Trottier, C., Sanchez, L. F. M., & Noël, M. (2021). Microscopic assessment of ASR-affected concrete under confinement conditions. Cement and Concrete Research, 145, 106456.

# 6. TECHNICAL PAPER 03/03 – EFFECTIVENESS OF SLOT CUTTING AS A REHABILITATION TECHNIQUE ON AAR-AFFECTED MASSIVE STRUCTURES

Gorga, R.V.[a]; Sanchez, L. F. M.[a]; Martín-Pérez, B. [a]; Noël, M. [a]

(a) University of Ottawa, Ottawa, ON, Canada

## 6.1 Abstract

Damage caused by alkali-aggregate reaction (AAR) can lead to economic losses and negatively impact the structural safety of hydroelectric power generation structures. Rehabilitation options for AAR-affected massive structures are limited, with slot cutting being one of the few viable alternatives. Although several reports are available in the literature describing successful implementation of this technique, its efficacy remains the subject of ongoing debate among researchers. In this context, the macro-scale finite element model developed by Gorga et al. is a very attractive approach to assess slot cutting as a rehabilitation technique, as it accounts for the most important parameters affecting the reaction through an engineering approach, without the need for non-technical guesses or to "fit" model parameters. In order to further improve its accuracy, the initial model's subroutine developed in 2018 is enhanced by incorporating a more detailed concrete creep modeling approach, and then it is used to perform a slot cutting parametric analysis. A generic gravity dam is used as a case study to assess the effect of several parameters affecting damage progression after slot cutting. Results indicate that while slot cutting does not significantly reduce overall stresses or cracking, it may be successful in improving local structural performance of components sensitive to deflection or distortion such as gates or turbine openings.

## 6.2 Introduction

Alkali-silica reaction (ASR), the most common type of alkali aggregate reaction (AAR), is a distress mechanism known to cause damage in hydroelectric power generation structures that can lead to economic losses and negatively impact their structural safety (Veilleux, 1995). One of the few rehabilitation alternatives for such massive concrete structures is the slot cutting technique, which consists of cutting vertical slots on the dam body to release the built-up compressive stresses and reduce permanent displacements (Caron et al., 2001). Several reports are available in the literature describing successful implementation and computer simulations of this technique Charlwood, 1994 in Amberg et al., 2009, Grimal et al., 2008, Grimal et al., 2008, Curtis et al., 2005, Curtis et al., 2016, Li & Coussy, 2002, 2004, Metalssi et al., 2014); however, its efficacy remains the subject of ongoing debate among researchers (Caron et al., 2001; Gocevski & Yildiz, 2017; Veilleux, 1995). Moreover, most of them still heavily rely on parameter fitting to match field measurements or do not account for the critical parameters affecting AAR. While incorporating empirical coefficients or adjusting parameters to fit measured data may replicate the structure's current state, the reliability of prognostic outcomes cannot be ensured unless the parameters possess physical meaning and their effects have been thoroughly assessed. In this context, a thorough assessment of slot cutting as a rehabilitation technique is necessary, with the model proposed by Gorga et al. (2018, 2020) being a very attractive simulation approach. The proposed approach accounts for the most important parameters affecting the reaction through an engineering approach, without the need for non-technical guesses or to "fit" model parameters. Moreover, it has already been validated for both slender and massive structures. This work aims to present the most recent developments of the proposed model, including validating an enhanced creep simulation approach and slot cutting modeling implementation, followed by a thorough assessment of slot cutting as a rehabilitation technique through parametric analyses.

## 6.3 Background

AAR is defined as a chemical reaction between "unstable" silica mineral forms within the aggregates and the alkali hydroxides (Na, K – OH) dissolved in the concrete pore solution. This reaction generates a secondary product (i.e., alkali-silica gel) that induces expansive pressures within the reacting aggregate material(s) and the adjacent cement paste upon moisture uptake from its surrounding environment. Common effects of the induced expansion include microcracking, reduction of the material's properties (mechanical/durability) and, in some cases, compromising functionality/safety (Fournier & Bérubé, 2000). AAR is usually divided into two different categories: alkali-silica reaction (ASR) and alkali-carbonate reaction (ACR), ASR being by far the most commonly found around the world.

There have been several reports of AAR in massive structures leading to loss of equipment alignment (such as impairing turbine operation due to opening ovalization), excessive cracking leading to leakage, map cracking, concrete mechanical properties deterioration, introduction of excessive stresses on prestressing strands, inability to operate gates and closure of expansion joints (Caron et al., 2001; Charlwood et al., 2012; Gorga et al., 2020). Therefore, performing an adequate assessment of the current state (diagnosis) and prediction of the future behaviour (prognosis) of such structures is important to minimize economic losses and ensure both their functionality and safety.

One of the few alternatives with reported beneficial effects on AAR-affected dams is the slot cutting technique. This approach involves cutting vertical slots on the dam with diamond wire saws to release (some) of the built-up compressive stresses that developed within the dam body due to AAR expansion and reduce permanent displacements that may be impairing gates and turbine functionality (Caron et al., 2001). Additionally, it can also reduce detrimental effects of cyclic seasonal temperature loadings in cold climates, reduce leakage and close cracks/joints. Some of the dams where this technique was implemented and positive outcomes were observed include the Fontana gravity dam - USA (Abraham & Sloan, 1978), Pian Telessio arch-gravity dam - Italy (Amberg et al., 2009; Stucchi & Catalano, 2023), Chambon gravity dam - France (Chulliat et al., 2017), Hiwasse gravity dam - USA (Curtis et al., 2005), Mactaquac gravity dam - Canada (Curtis et al., 2016), and Salanfe gravity dam - Switzerland (Droz et al., 2013).

Even though beneficial effects have been observed in most cases reported in the literature, there are reports of instances where slot cutting led to further damage (increase in expansion rate and cracking) when compared to a “no intervention” scenario (Gocevski & Yildiz, 2017). The authors suggest that slot cuts on gravity dams and their components should not be performed if the expansion rate is categorized as mild (less than 15 micro-strain per year) or if the aggregate is moderately reactive according to CSA A23.2-14A (expansion between 0.040 and 0.120 % per year in the concrete prism test - CPT) with a concrete mix containing alkali content lower than 1.8 kg/m3. Moreover, possible detrimental effects/implications of slot cutting include resumption of high swelling rate due to release of beneficial restraints, formation of high stress concentration zones near the cut tip, potential occurrence of secondary deformations detrimental to the functionality of mechanical equipment, introduction of new thermal boundaries by allowing penetration of cold/warm air and requirement of sealing/waterproofing, monitoring and maintenance (Caron et al., 2001; Veilleux, 1995).

In numerical simulations using the finite element method, slot cuts have been modeled using three different approaches: as a contact interface without element removal (Droz et al., 2013; Metalssi et al., 2014), by simple element removal of one layer at a time (Saati & Mortazavi, 2009), or by implementing an artificial “slot cutting material”, which has its stiffness reduced before it is deleted in an explicit (quasi-static) analysis (Gocevski & Yildiz, 2017). Moreover, concrete creep also becomes an important part of the analysis, as stresses vary significantly before and after the cutting procedure (Caron et al., 2001). However, as previously described, existing models that have been used to simulate slot cutting still heavily rely on parameter fitting to match field measurements or do not account for the critical parameters affecting AAR. In this context, the model proposed by Gorga et al. (2018, 2020) is a very promising alternative. The model is able to predict the expansion based on the most important (and measurable) parameters affecting the reaction from a materials perspective. Those include aggregate type and reactivity, temperature, alkali content, relative humidity and exposure conditions. All these parameters are measurable and can be accurately determined for any case evaluated. Moreover, based on the local analytical AAR free expansion equation (De Grazia et al., 2021; Goshayeshi, 2019; Nguyen et al., 2022), the anisotropic (stress-state-dependent) expansion relationship (Gautam et al., 2017) and the mechanical properties deterioration as a function of the expansion level (Sanchez et al., 2017), the static implicit approach was able to accurately perform the diagnosis and prognosis of both slender Gorga et al., 2018) and massive (Gorga et al., 2020) real AAR-affected concrete structures without overcomplicating or oversimplifying the reaction.

Even so, the model does have some limitations. In previous studies, creep was only accounted for in a simplified manner, by reducing the modulus of elasticity through a creep coefficient. Furthermore, slot cutting modeling had not been implemented in the model up to this point. Therefore, in order to accurately simulate slot cutting, the model by Gorga et al. is enhanced with a new updated subroutine that accounts for creep explicitly through an iterative process and a new approach to simulate slot cutting. These newly-implemented features allow to conduct a parametric study, highlighting both the positive and negative impacts of slot cutting, the effect of the most important variables affecting the rehabilitation technique and providing general guidelines for intervention.

## 6.4 Research Significance

Overall, slot cutting is a major (expensive) intervention, often considered the only alternative to rehabilitate massive concrete structures affected by AAR. It creates new joints that need to be assessed, monitored and maintained, while still significantly affecting the stress profile and (potentially) the displacements of the dam body (Veilleux, 1995). Studies in the literature have reported conflicting results regarding its effectiveness. There are currently no specific guidelines or conclusive evidence demonstrating that slot cutting has a net benefit to the structural performance of these structures. Moreover, previous models used to simulate slot cutting either rely on "fitting" parameters or do not account for the most important parameters affecting AAR. Therefore, there is a significant gap in the literature that warrants further investigation.

## 6.5 Creep Theoretical Background

Concrete creep (including creep recovery) has an important effect on the long-term performance of mass concrete structures after slot cutting due to the significant change in stress-state. Therefore, before describing the validation analysis, a brief discussion of the creep phenomenon is presented.

Creep can be understood as an increase in strain when concrete is subjected to a constant stress, which may be generated from mechanical loading, thermal loading, chemical expansion, etc. (Collins & Mitchell, 1997; Mehta & Monteiro, 2014). This strain can be positive or negative, depending on the stress history applied to the member. For example, if a load is sustained for an extended period of time and then removed, the section will experience creep followed by partial creep recovery.

Creep is a complex phenomenon and is a function of several parameters, including stress-state, temperature, relative humidity, curing conditions, volume-to-surface ratio, concrete mechanical properties, strain-softening, concrete mix parameters and time of loading (Bazant, 1988; Collins & Mitchell, 1997).

Applying the superposition principle, uniaxial creep can be mathematically represented as a generic function if a stress history is assumed as a succession of infinitesimal stresses ($d\sigma$) applied at time $t'$ (Batista, 1998). This function is often called the creep compliance function $J(t, t')$, and it represents the strain ε at time t caused by a constant unit stress acting since the loading time t'. If the strain is assumed to be composed only of the elastic and creep components, this function can be determined as shown in Equation 6-1.

$$\varepsilon(t) = \int_{t'}^{t} J(t, t') d\sigma(t') \tag{6-1}$$

In general, superposition is valid within the service stress range of structures as strains produced in the concrete body at any time t by a stress increment at any time t' are independent of the effects of any stress applied either earlier or later than t' as long as the stress-strain behaviour is linear (Bazant, 1988; Collins & Mitchell, 1997). This creep stage is known as primary creep and is usually valid when stresses are below the linear creep threshold, i.e., below 40% of the concrete compressive strength (Yu et al., 2021). Secondary and tertiary stages, where the stress-strain behaviour is not linear, are not captured by Equation 6-1.

Creep can be modeled either as a reduction in the modulus of elasticity over time (simplified approach) or as a strain that considers the effect of the entire stress history, with the latter being more accurate and realistic. When calculating creep as a strain, the stress history can be approximated as a sum of stress increments, but this requires the entire stress history to be computationally stored to properly calculate the effect of all the stress increments (Batista, 1998). As the analysis time progresses, the amount of stored data keeps increasing, which is not feasible for large-scale simulations.

An alternative to storing all this data is to approximate the calculation of creep strain through a series of exponential equations known as Dirichlet series (Batista, 1998; Bazant & Wu, 1973, 1974; Póvoas, 1991). These series make use of Kelvin or Maxwell chain rheological models to represent the visco-elastic behaviour of concrete (Mehta & Monteiro, 2014). In essence, both models comprise several dashpot-spring assemblies that capture the variation of strain over time.

When a number $N$ of Kelvin models are assembled in series in a chain (Figure 6-1) to represent a creep compliance curve, the Dirichlet series equation (Equation 6-2) is obtained (Póvoas, 1991).

$$\varepsilon(t,t') = \sum_{i=1}^{N} \frac{1}{E_i(t')} \times \left( 1 - \mathrm{e}^{-\frac{(t-t')}{\eta_i / E_i}} \right) \tag{6-2}$$

where $E_i$ is the spring stiffness for the i-th Kelvin model and $\eta_i$ is the viscosity coefficient of the i-th Kelvin model. Figure 1 illustrates the physical meaning of this equation, where the gradual contribution of each Kelvin series adds up to a total approximated creep compliance curve. Note that creep compliance curves represent the value for a given value of stress, meaning that the strain calculated through Equation 6-2 is per stress value used to generate the creep compliance curve.

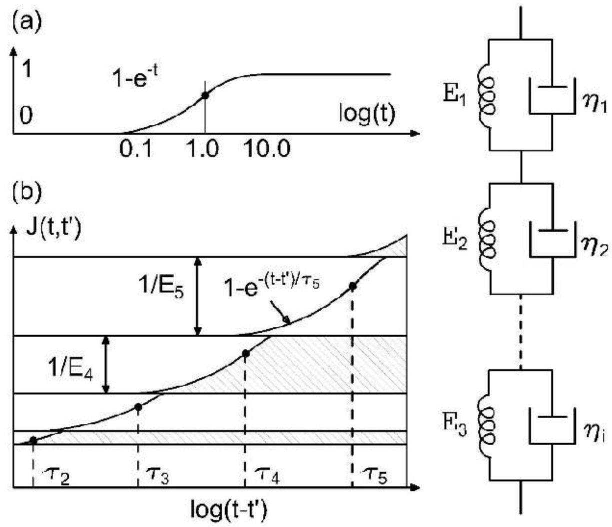


**Figure 6-1. Dirichlet series graphical representation of creep compliance function: a. Curve for a single term, b, Complete curve, c. Kelvin model in series. Source: Mehta & Monteiro (2014) and Póvoas (1991).**

If one or more creep compliance curves are known (either from laboratory tests or equations proposed in the literature), the individual values of $E_i$ and $\tau_i$ for the Kelvin models can be selected. A comprehensive approach is described in Bazant (1988) (as well as Póvoas, 1991 and Batista, 1998). Based on the (integral) rectangular approximation and the Dirichlet series approximation, it can be shown that the creep strain increment ($\Delta\varepsilon_{creep}$) at a given time $t_n$ can be given by Equations 6-3 through 6-5 (Batista, 1998; Bazant & Wu, 1973; Póvoas, 1991):

$$\Delta\varepsilon_{creep}(t_n) = \sum_{i=1}^{N} \varepsilon_i^*(t_{n-1}) \times \left(1 - \mathrm{e}^{-\Delta t_n/\tau_i}\right) \tag{6-3}$$

$$\varepsilon_i^*(t_{n-1}) = \varepsilon_i^*(t_{n-2}) \times (\mathrm{e}^{-\Delta t_{n-1}/\tau_i}) + \Delta\sigma(t_{n-1})/E_i(t_{n-1}) \tag{6-4}$$

$$\varepsilon_i^*(t_1) = \Delta\sigma(t_1)/E_i(t_1) \tag{6-5}$$

where variable $\varepsilon_i^*(t_{n-1})$ represents the group of interval variables describing the influence of the entire stress history up to the time increment $t_{n-1}$ that will influence the subsequent time increment. With this approach, it is then possible to calculate the creep strain taking into consideration the entire stress history by only storing the $\varepsilon_i^*(t_{n-1})$ variable. This is significantly more computationally efficient than storing the entire stress history, and allows for much more optimized simulations. This is valid as long as the material properties are maintained constant between time increments and the stress variation over the stress history is constant (i.e., without jumps, which is common for uncracked concrete).

## 6.6 Creep and Slot Cutting Simulation Validation

### 6.6.1 Validation test description

In order to ensure that slot cutting can be accurately simulated, the experiment conducted by Caron et al. (2001) was used as a validation analysis. The laboratory test comprised slot cutting of externally prestressed plain concrete beams. The overall arrangement, cutting procedure and dimensions are shown in Figure 6-2. The concrete was not affected by AAR.

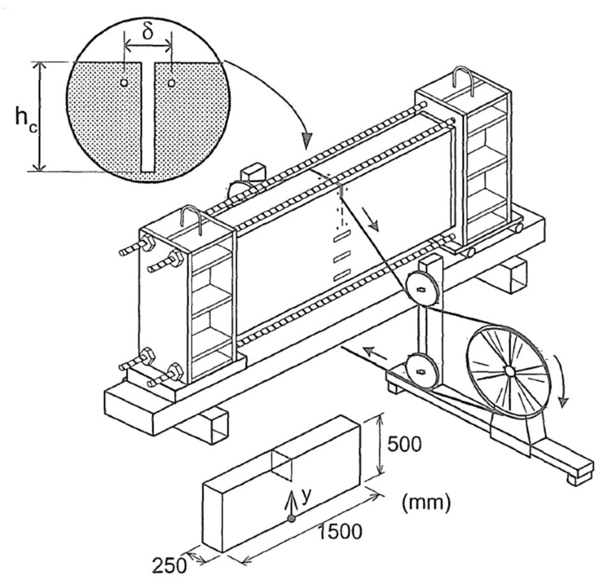


**Figure 6-2. Slot cutting laboratory test arrangement, cutting procedure and geometry. Source:** Caron et al. (2001)**.**

Two identical beams were tested, both subjected to 5 MPa compressive stress and having a 10 mm-wide and 167 mm-deep cut. Specimens 1 and 2 were 71 and 114 days old, respectively, at the time they were tested. Short and long-term slot closure (deflection) values were monitored by three pairs of gages for 28 days. Stresses were also estimated from strain measurements from three strain gages below the cut.

Tests on concrete cylinders were performed to determine the material properties of the concrete immediately prior to cutting. It was measured that the moduli of elasticity ($E$) were equal to 32.7 and 33.6 GPa, and the compressive strengths were 34.4 and 34.1 MPa for specimens 1 and 2, respectively . Moreover, it was observed that Equation 6-6 was able to accurately predict results from the performed creep test, where $\varepsilon_{creep}$ is the creep strain, $t$ is time and $\sigma_0$ is the constant stress magnitude.

$$\varepsilon_{creep} = \frac{\sigma_0}{E} + \frac{\sigma_0}{52350MPa}(1 - e^{-t/9.056}) \tag{6-6}$$

### 6.6.2 Model description

A finite element model was then generated in Abaqus Standard 2024 (Simulia, 2024). All elements were first-order 6-node wedge elements with size of approximately 30 mm, adding up to about 15,000 elements. A mesh sensitivity analysis with elements of approximately 15 mm showed that refining the mesh was not altering the results; therefore, the coarser mesh was considered adequate. The concrete was assumed linear elastic, as stresses were not expected to reach non-linear behaviour in tension nor compression. Contact formulation with automatic stabilization at the slot cut assumed hard contact for normal and rough friction formulation for tangential behaviour.

Regarding creep, the Dirichlet series approach previously described with five Kelvin models was implemented into a combined USDFLD-UEXPAN subroutine in Abaqus, which allows the incremental calculation of the thermal, AAR-induced, and creep strains. In this formulation, the

AAR strain was calculated based on Larive's equation (Larive, 1997) and thermal strain was calculated as an isotropic strain based on the temperature gradient ($\Delta T$) and the coefficient of thermal expansion ($\alpha$) as shown in Equations 6-7 and 6-8, respectively.

$$\varepsilon_{AAR}(t) = \frac{1 - e^{-\frac{t}{\tau_c}}}{1 + e^{-\frac{(t-\tau_L)}{\tau_c}}} \times \varepsilon_{AAR}^{\infty} \tag{6-7}$$

$$\varepsilon_{thermal} = \Delta T \alpha \tag{6-8}$$

where $\varepsilon_{AAR}(t)$ is the AAR-induced strain at time $t$, $\varepsilon_{AAR}^{\infty}$ is the AAR strain at infinity, $\tau_L$ and $\tau_c$ are coefficients and $\Delta\varepsilon_{AAR}$ is the AAR strain increment. These strains are added to the elastic and plastic strains calculated through the mechanical model, resulting in Equation 6-9.

$$\begin{aligned} \varepsilon_{tot} &= \varepsilon_{subroutine} + \varepsilon_{mechanical} \\ &= \left(\varepsilon_{thermal} + \varepsilon_{AAR} + \varepsilon_{creep}\right) + \left(\varepsilon_{elastic} + \varepsilon_{plastic}\right) \end{aligned} \tag{6-9}$$

where $\varepsilon_{tot}$ is the total strain, $\varepsilon_{subroutine}$ is the strain calculated through the subroutine, which is the sum of the thermal strain ($\varepsilon_{thermal}$), the AAR strain ($\varepsilon_{AAR}$) and the creep strain ($\varepsilon_{creep}$), and $\varepsilon_{mechanica}$ is the mechanical strain calculated directly by the software, which is equal to the sum of the elastic strain ($\varepsilon_{elastic}$) and the plastic strain ($\varepsilon_{plastic}$).

Shrinkage strain was not included in the simulation because shrinkage associated with moisture loss (i.e., drying shrinkage) is significantly less important than other types of applied strain (e.g., thermal volumetric variations) for structures with 1 m or more in thickness (Mehta & Monteiro, 2014).

It is important to emphasize that the creep approach has limitations. Some of the underlying assumptions of the creep model are not strictly valid, but their effects are considered negligible. First, the approach assumes that a single combination of $E_i$ values for the Kelvin model chain can represent creep for any loading time. This is deemed reasonable as values tend to vary very little for times in the order of magnitude of years (see creep equations for Serra et al., 2012, Rebelo, 2020 and Dias et al., 2022) and the goal of the analysis is to evaluate the long-term behaviour of the structure, not the early age performance. Second, the model is not able to capture irreversible creep recovery or the secondary or tertiary creep stages. Moreover, uniaxial creep theory is assumed as valid for all three directions independently, without accounting for the effect that creep along one direction would have on the other two orthogonal directions. All of these are considered secondary effects, with the most relevant creep component still being captured by the primary uniaxial creep model. Third, the approach is assumed to be reasonably accurate even though the superposition and Dirichlet series theory base assumptions are not necessarily met, i.e., linear stress-strain relationship, constant material properties between time increments and constant stress variation over time. Other authors have been able to successfully implement creep using this approach, even for AAR-affected structures (Dias et al., 2022; Rebelo, 2020), meaning that the error caused by not meeting the requirements previously listed is not expected to be significant.

Regarding slot cutting simulation, none of the previously listed approaches from the literature were found to be ideal. Element removal as performed by Saati & Mortazavi (2009) was not viable in static implicit analyses, as the principle of energy conservation used to determine when equilibrium is reached would be violated. Implementing an artificial "slot cutting material" as performed by Gocevski & Yildiz (2017) has the same issue, as the artificial material has to be deleted after its stiffness is reduced to accurately simulate the surface-to-surface interaction. Simulating slot cutting through contact without element removal (Droz et al., 2013; Metalssi et al., 2014) was determined to be the most promising alternative, as it does not run into the same issues. This approach requires the slot cut to be left open from the beginning of the analysis. Before the cut is performed, a surface-to-surface contact (including tangential and normal behaviour) with zero initial clearance between the surfaces is specified. This allows the analysis to be conducted as if there was no opening because the contact emulates the solid mass of concrete. Then a "cut step" is defined, where the first contact surface is deactivated, and a second contact is activated. The latter has the same formulation, but without specifying initial clearance equal to zero. This allows the concrete to displace and close the gap until it reaches a stable position. In this step, contact is only activated once the surfaces touch each other. Lastly, a new step can be specified and the post-cut simulation starts. This approach was able to simulate the cut of the validation analysis, but the contact formulation was not behaving as well as expected at the base of the opening, leading to stress concentration before the cut (±15% when compared to a solid model). It is believed that the reasons for this were that some nodes were shared between the two surfaces while the gap was still open and because the contact was not able to perfectly represent the desired stiffness along all directions. Note that the base was simulated with a "V" shape instead of a square to avoid excessive stress concentration and improve mesh quality (avoid very narrow elements).

To address the limitations of previous methods, a new modeling approach is proposed herein. Contact is specified in a similar manner as described above, including activation and deactivation. However, a "dummy" independent concrete part in the shape of the gap is included. The first contact (before slot cutting) is enforced between the faces of the opening on the main structure and the faces of the dummy part. A second contact (post-cutting) is then specified between the two surfaces of the cut, as previously done. In the second stage, the dummy material is ignored as it has no interaction with the main structure anymore.

### 6.6.3 Discussion of results

Results from the simulation are presented in Table 6-1 and Figure 6-3. It was observed that the accuracy of the analysis was improved by adopting the modulus of elasticity $E_c$ calculated from the compressive strength $f_c'$ (as per CSA A23.3-24 and shown in Equation 6-10), which was equal to 27 GPa instead of the measured 33 GPa. This reduced the average analysis error for short-term deflection from -11% to +7% and the long-term deflection from +27% to +11%, while the stress remained constant at +17% when compared to recorded values.

$$E_c = 4730\sqrt{f_c'} \tag{6-10}$$

**Table 6-1 Laboratory and FEA stresses for slot cutting validation analysis.**

| Beam Height (mm) | Lab Test 1 Predicted Stress (MPa) | Lab Test 2 Predicted Stress (MPa) | FEA Longitudinal Stress (MPa) |
|---|---|---|---|
| 300 | -11.4 | -11.2 | -10.5 |
| 200 | -5.2 | -7.0 | -6.1 |
| 100 | -2.7 | -3.4 | -4.9 |

a

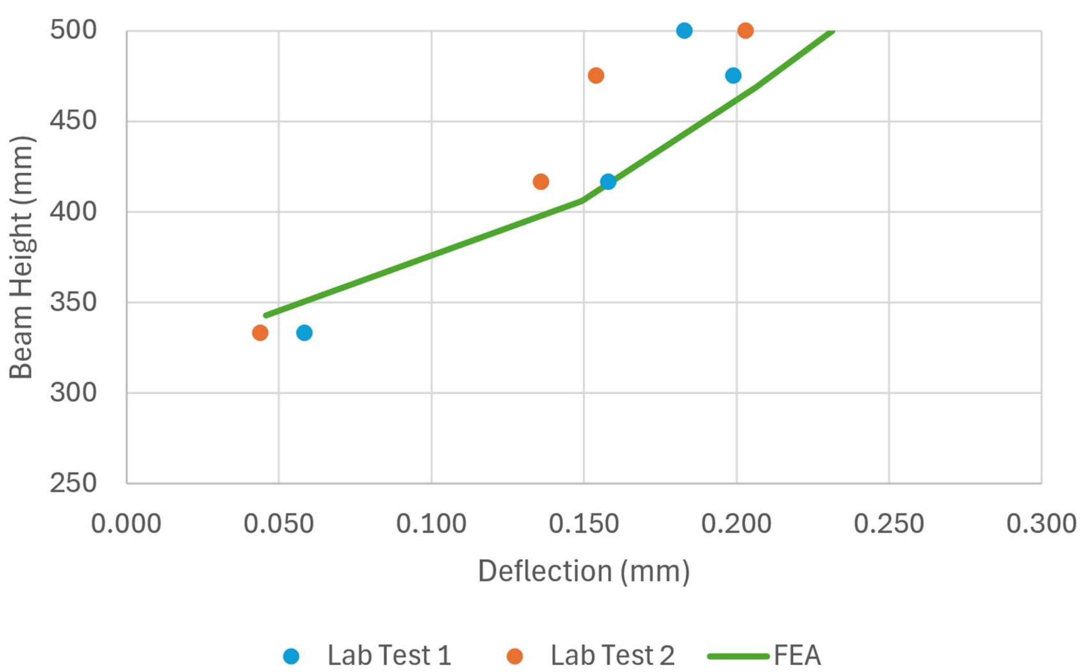

b

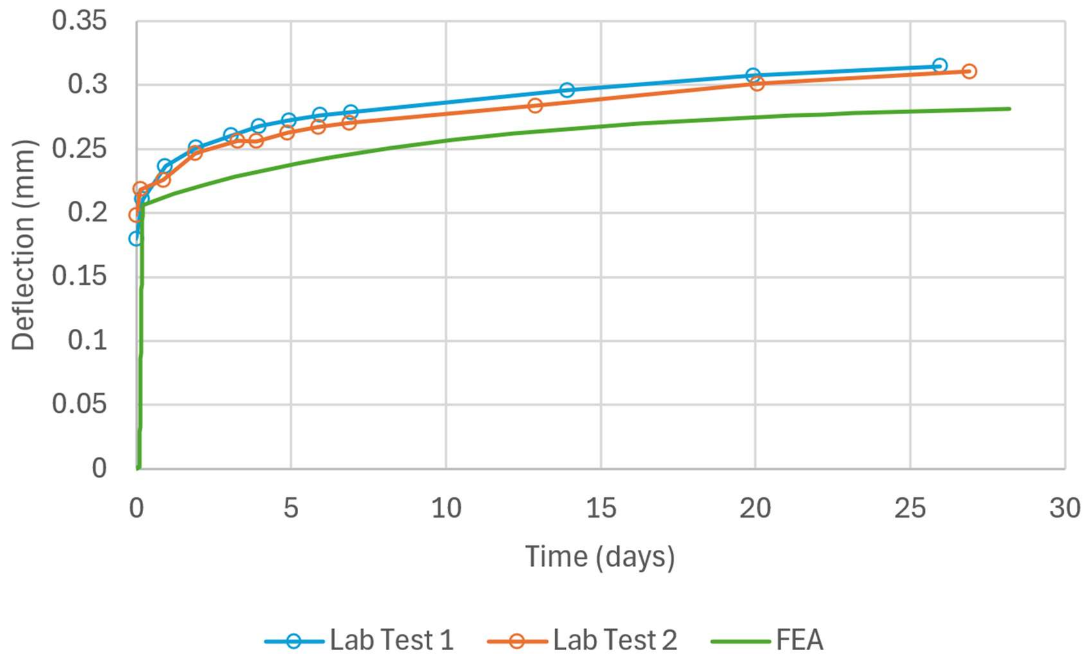


**Figure 6-3. Laboratory and FEA slot closure for slot cutting validation analysis: a. short-term, b. long-term.**

Results matched the reported data very well, especially considering the intrinsic high variability related to slot cutting, as reported by Droz et al. (2013) and Caron et al. (2001). Short-term slot closure values were very close to the laboratory data, only being 20% larger than the average of the test specimens at the very top of the beam. Similarly, long-term slot closure closely matched the experiment. The reported final deflection (+11%) was closer than what had been reported for the finite element model by Caron et al. (2001), who obtained errors of -11% and -26% for tests 1 and 2, respectively. Also, the observed deflection was significantly smaller than the slot cut width (10 mm), meaning the cut remained open throughout the entire test period. Lastly, stresses from the FE model were very close to the values predicted by the authors, although the compressive stress at a height of 100 mm was slightly larger than what was reported. The observed differences between test and model may have been caused by inaccuracies when determining mechanical properties and stresses in the lab, or limitations of the modeling approach; however, the overall behaviour was clearly captured, and the model is considered adequate. Note that, except for the immediate vicinity around the crack tip, all stresses are well below 50% of the compressive strength, and tensile stresses are below 0.5 MPa; therefore, the assumption of linear elasticity is reasonable.

The FE model (Figure 6-4a,b) also captured the overall stress distribution described by the authors (Figure 6-4c). In general, the following regions can be identified after slot cutting (Caron et al., 2001): 1) decompression zone – where compressive stresses are significantly relieved, sometimes even turning into tensile stresses; 2) additional compression zone – due to stress concentration around the tip of the cut and the flexural components introduced in the system (forces are still applied to the entire original area but they have to pass through the remaining concrete area, generating flexure and, consequently, compression above the new neutral axis); 3) additional tension zone – due to the flexural component introduced in the system; and 4) unaffected zone – areas too far from the cut to be affected by the rehabilitation technique. It is important to emphasize that the asymmetry observed was due to how the boundary conditions were specified, i.e., being fixed along Y only on one side.

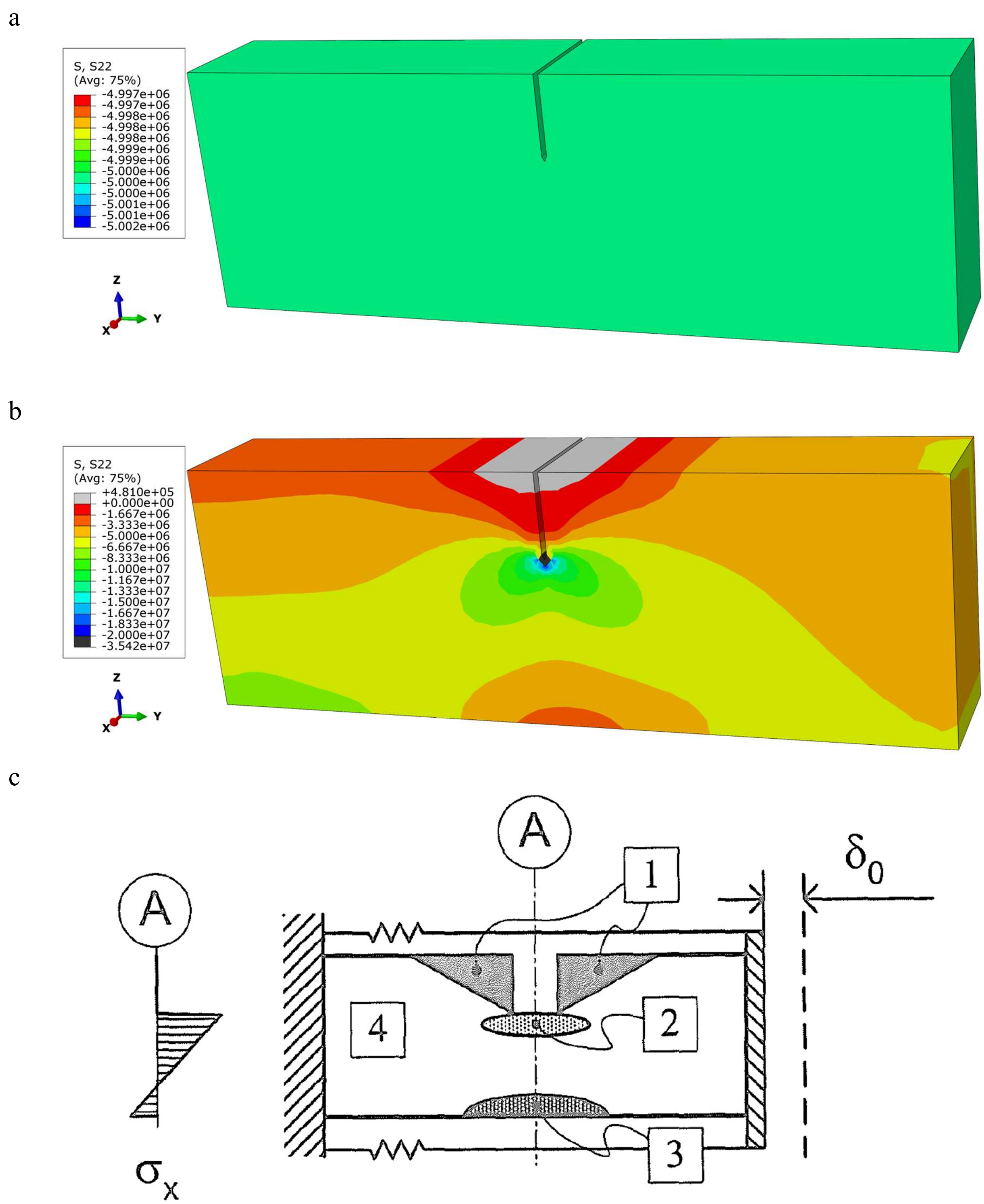


**Figure 6-4. Slot cutting experiment stress profile (units in Pa): a. FEA before cut, b. FEA after cut, c. Predicted by** Caron et al. (2001)**.**

It was observed that the new proposed modeling approach was able to accurately simulate the pre- and post-cut stresses, with negligible amounts of stress concentration (less than 1%). Therefore, making it more suitable than the other previously listed alternatives.

## 6.7 Slot Cutting Parametric Study

### 6.7.1 Description

Once the modelling procedure was validated, a parametric study was conducted to evaluate the overall impact of slot cutting on AAR-affected dams, as well as to determine general good practice guidelines when performing this rehabilitation technique. The first step was to determine a detailed program based on the slot cutting variables expected to have the most significant effects on the structure.

An extensive literature review of previous case studies allowed the identification of the following critical slot cutting parameters: location of the cut(s) (i.e., proximity to discontinuities such as vertical joints, gates, changes in geometry, etc.), number of cuts, and cut geometry (slot width and depth) (Amberg et al., 2009; Caron et al., 2001; Chulliat et al., 2017; Curtis et al., 2005, 2016; Metalssi et al., 2014; Stucchi & Catalano, 2023; Veilleux, 1995). Most authors recommended avoiding making cuts near discontinuity areas (such as changes in geometry), favored several smaller cuts instead of fewer larger cuts to allow stresses to be more evenly distributed, and reported cuts spaced between 25 and 100 meters. Moreover, cuts reported in the literature were generally between 10 and 20 mm-wide and had a depth between 15 and 55% of the dam height. The total number of slot cuts reported varied from 4 to 22 for each dam, with the cuts introduced in single or multiple campaigns.

Even though not addressed by any of the authors previously mentioned, the time at which the slot cut is performed is another parameter worth evaluating. Theoretically, the structure will be under lower stresses if the cut is performed earlier. Altering the stresses may significantly affect the stress-state-dependent AAR expansion, meaning that an earlier cut may diminish the potentially positive effect of reducing the expansion along a highly compressed direction. Lastly, the impact of creep will also be assessed when compared to AAR expansion and thermal expansion.

Based on the information provided and with the goal of individually assessing the impact of each variable, a series of parametric analyses were conducted. The analyses included varying slot cut widths (15 and 5 mm), slot cut depths (15, 32.5, and 50% of the dam height), time at which the cut is performed (9,000 and 2,000 days), number of cuts (1 or 2 slot cuts), and presence of discontinuities (dam with and without gates). Width of 15 mm was selected as it is the average of the values reported in the literature, and 5mm is an extrapolation to see how a very thin cut would behave. Moreover, 9,000 days (roughly 25 years) was selected because a reasonable amount of expansion will have been reached at that time, while still allowing a significant (and almost equal) amount of expansion to take place after the cut. The early cut at 2,000 days (roughly 5 years) was selected because it would take place before most of the specified expansion had time to develop, representing a preemptive or early intervention remedial action. Lastly, 1 and 2 cuts were used instead of the larger number reported in the literature (4 to 22) because a smaller number of cuts allows for a better visualization of the slot cutting mechanism and to more easily isolate the effect of the variables being evaluated.

A generic geometry inspired by the Fontana (USA) and Furnas (Brazil) gravity dams (Fairbairn et al., 2004; Pan et al., 2013; Winnicki et al., 2014) was specified for the parametric analysis, as shown in Figure 6-5. The proposed dam is 150 m-long, has vertical ends on both sides and has two basic versions: standard (constant cross-section with varying cut properties) and with two gates (each gate is 10 by 10 m with a central column with dimensions of 3 by 10 m, and a single cut that is 15 mm-wide, has a depth of 50% of the dam height, and located 10 m away from the opening).

a

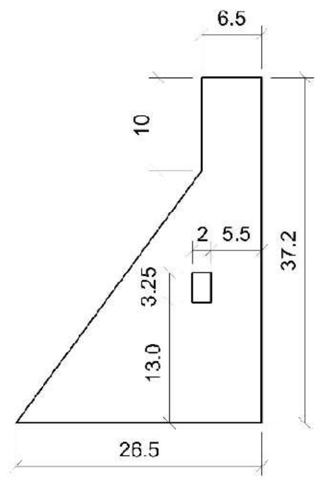


b

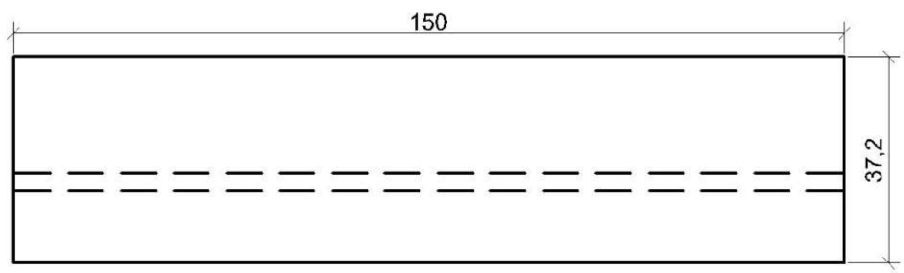


c

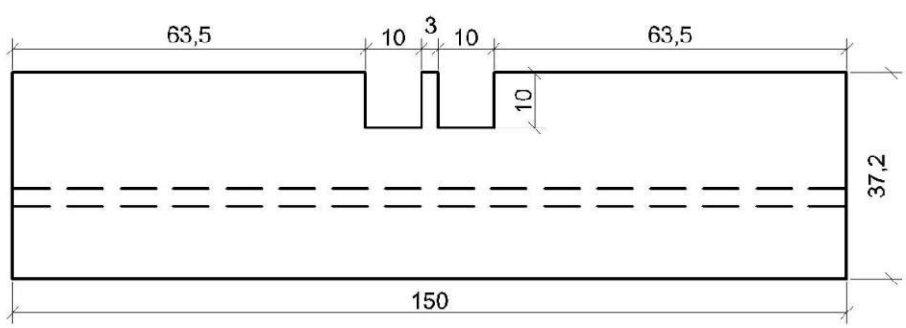


**Figure 6-5. Generic gravity dam geometry (units in meters): a. Section, b. Standard dam elevation, c. Dam with gates elevation.**

Concrete was assumed as non-linear according to the concrete damaged plasticity model for the dam body and linear-elastic for the dummy slot cut part. The mechanical properties of the concrete were determined assuming compressive strength of 20 MPa, density of 2,450 kg/m3 and all other mechanical parameters were defined as previously described by Gorga et al. (2018). Mechanical properties deterioration was assumed as 15.0, 39.5 and 46.6% reduction of modulus of elasticity; 3.4, 3.5 and 16.5% reduction of compressive strength and 28.2, 62.2 and 74.3% reduction of tensile strength at 0.05, 0.12 and 0.20% expansion levels, respectively, following Sanchez et al. (2017). Linear interpolation between the values was implemented. Unlike previous studies, creep was calculated directly in the new subroutine based on the Bemposta Dam creep compliance curve determined by LNEC through both laboratory tests and empirical equations (Dias et al., 2022; Rebelo, 2020) as shown in Equation 6-11.

$$J(t,t') = \frac{1}{43.26}\left[1 + 4.48\left({t'}^{0.40} + 0.05\right) \times (t - t')^{0.12}\right] \tag{6-11}$$

The finite element model used first-order 6-node wedge and first-order 8-node brick reduced integration elements, with dimensions varying between 1 and 1.75 m. The finite element models had close to 100,000 elements, which provided a good balance between level of detail and computational processing time. Mechanical boundary conditions were represented using spring elements, whose stiffness was calculated based on an elastic foundation assumption, with a modulus of elasticity equal to 15 GPa. The modulus of elasticity value was based on values reported for the Bemposta dam (Dias et al., 2022; Rebelo, 2020). The bottom surface was simulated with spring elements along all three principal directions, while the vertical ends had spring elements only normal to the surface. This simplification was assumed sufficient as the main goal of the model was simply to assess the effect of slot cutting under one given boundary condition. Applied loads included only water pressure load on the entire vertical surface and gravity, both of which were applied instantly to the structure, i.e., in less than a day. Other loads were assumed as not critical for the parametric analysis. Contact formulation with automatic stabilization assumed hard contact for normal behaviour and penalty friction formulation with 0.8 friction coefficient for tangential behaviour.

The models were simulated both with varying and constant temperatures, with the latter being adopted whenever it was desired to single out the effect of one variable. Thermal boundary conditions were assumed to be equal to those for the Bemposta Dam (Dias et al., 2022; Rebelo, 2020) when varying temperature was considered, and equal to 20ºC when it was assumed constant, as the latter is roughly the average value calculated using a heat transfer finite element analysis of the dam.

The thermal and mechanical models were considered as fully coupled, even though they were calculated separately. First, a transient thermal model was calculated to determine the full temperature history of each element. Then, the entire temperature history was imported into the AAR mechanical model, which used the new version of the AAR expansion subroutine, as given by Equation 6-7, to calculate the total strain applied to the model.

AAR expansion was defined from trial and error to both provide an almost linear expansion rate and to have a total free expansion (i.e., before redistribution based on stress-state) of about 0.20% at 50 years (18,250 days). It was determined that a reasonable value could be obtained for $\tau_c$=12,410, $\tau_L$=10,950 and $\varepsilon^{\infty}$=4%, as the total free expansion would be between 0.25 and 0.10% at 50 years when temperature and stress-state expansion redistribution are considered within the model. It is important to emphasize that these variable values are not representative of a specific aggregate type as the goal of the analysis is not to evaluate the effect of real aggregates, but rather to understand the overall behaviour of the structure when subjected to AAR expansion and slot cuts.

All models had a total analysis time of 50 years, with the slot cut happening at the 9,000-day mark (25 years). This means that the total free expansion (including temperature effects) at the time of the cut would be between 0.11 and 0.04%, with the compressive stress along the length (x-axis) being around 5 MPa. The only exception was for the early slot cut analysis, which assumed the slot cut would be introduced at 2,000 days (5.5 years). For that case, the total expansion was between 0.02 and 0.01%. The slot cut was modeled as if it had been completed in a single day.

### 6.7.2 Discussion of results

Mechanism description: AAR expansion generates a complex stress-state on the dam, being severely affected by any boundary conditions, geometric discontinuities and non-uniform loads. Every case is unique, but some of the most common potential sources of discontinuity include gates, expansion joints, galleries, water loads, structure-foundation interaction, thermal profile, changes of geometry, etc. Moreover, AAR will generally lead to compression along the length of the dam (x-axis) (Figure 6-6a,b) and cracking anywhere where there is an expansion gradient (near any of the listed sources of discontinuities). The high compressive stresses along the length of the dam may lead to ovalization of turbine openings (i.e., guide vanes) and loss of equipment alignment, inability to operate gates, and closing of expansion joints, which are significant problems on top of the intrinsic structural effects of AAR like cracking (possibly leading to leakage) and concrete mechanical properties deterioration. In this scenario, slot cutting may be chosen as a rehabilitation technique to try to minimize the negative consequences of AAR expansion.

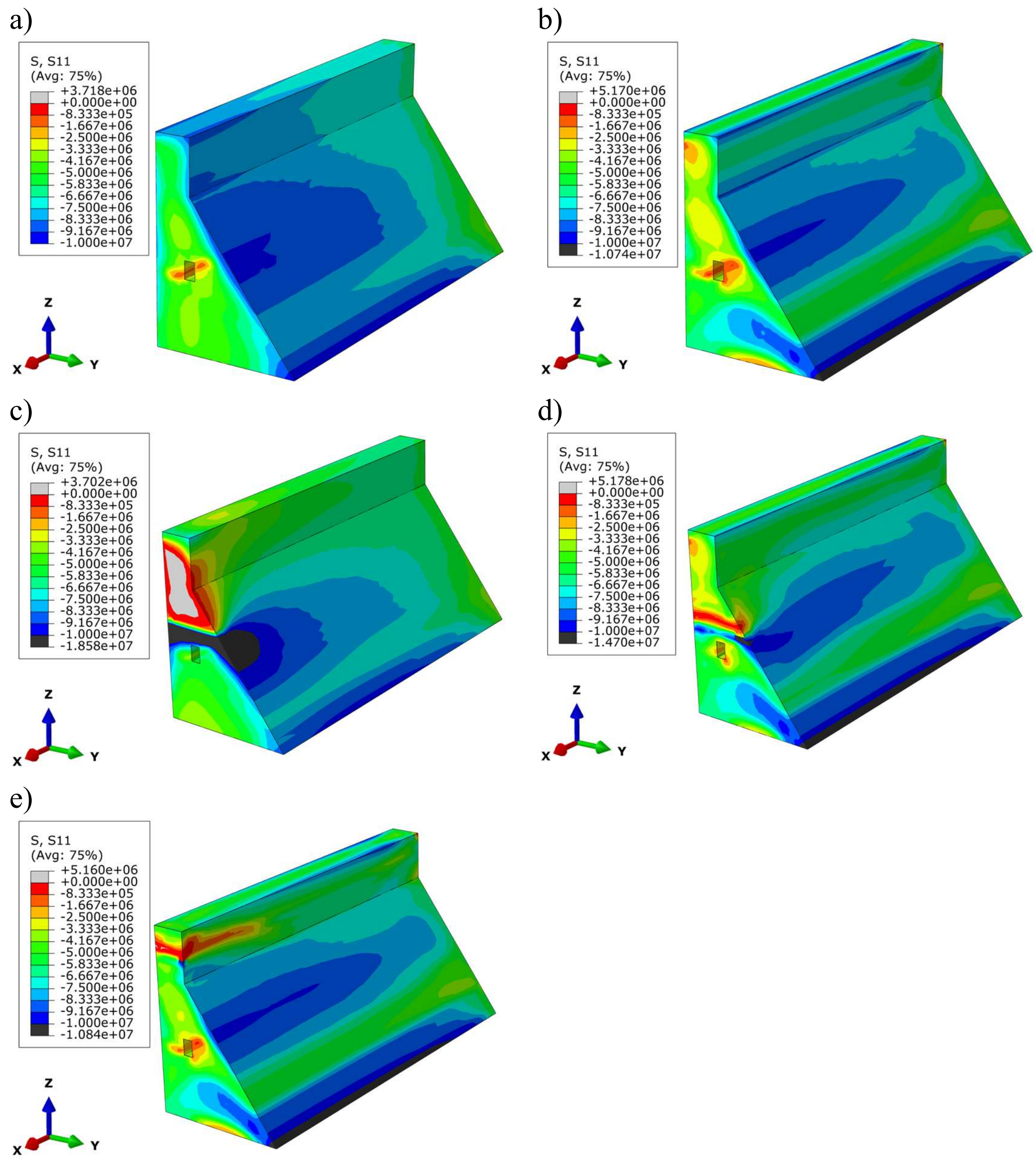


**Figure 6-6. Dam stresses (section half-way through length @ slot cut) along X-axis at: a) Base model at time=9,000 days w/o cut, b) Base model at time=18,250 days w/o cut, c) Slot cut model at time=9,000 days immediately after cut (50%h cut), d) Slot cut model at time=18,250 days w/ cut (50%h cut), e) Slot cut model at time=18,250 days (15%h cut) - (units in Pa).**

As soon as slot cutting is performed (Figure 6-6c), the two surfaces start moving toward one another due to the internal compression stress-state generated by the AAR expansion. Before the surfaces are in contact with each other, the overall behaviour described previously for the laboratory test by Caron et al. (2001) and shown in Figure 6-4c is observed. The decompression and the unaffected zones are delimited by a spread angle, which will be a function of many parameters, including concrete linear and non-linear mechanical properties, cracking pattern, orientation and intensity, aggregate interlocking, etc. Immediately below the cut, a stress concentration zone is formed, where very high compressive stresses develop due to the new internal load path introduced. This region is of special importance, as excessive stresses may lead to concrete crushing when the concrete compressive strength may already have been reduced due to AAR. Lastly, the additional tension zone develops at the bottom of the dam. However, due to the high compressive stresses along that direction and the restraint provided by the foundation, the effect of this additional tension is basically negligible.

If the two surfaces of the cut never touch, stress concentration at the additional compression zone will increase as the reaction develops, but the overall stress-state will remain roughly the same. However, if the surfaces of the cut come in contact after a period of time, there are important changes to the local stress profile. A new load path is formed, allowing compressive stresses to start being transferred due to normal contact (Figure 6-6d). In this scenario, the following was observed: 1) compressive stresses in the stress concentration zone start reducing; 2) compressive stresses in the decompression zone start increasing; 3) as the reaction progresses, the tendency is for the slot cut to keep closing off, i.e., for the contact area to keep increasing over time. However, the last 10 to 25% of the cut depth requires significantly more total expansion in order to close off, as a very large amount of stress is already being transferred through contact and the structure reaches a temporary equilibrium at that point; 4) a larger contact area leads to a more homogeneous load path and final stress-state; 5) naturally, the top of the cut will be in contact first, as that is where the maximum deflection will take place; 6) slip between the surfaces tends to be small due to high friction forces.

Whether or not the two surfaces of a single cut will be in contact, as well as how large the contact area will be, is primarily a function of the cut width, cut depth, dam geometry, compressive stress magnitude and mechanical properties of both the foundation and the concrete. Secondary effects may include temperature gradient, creep, etc. In general, deeper cuts, larger compression stresses and narrower cuts tend to display larger contact areas.

Cut width: To check the effect of cut widths, the same model was subjected to a single slot cut of 15 or 5 mm width. As expected, the decompression experienced by the dam was significantly smaller for the narrowest slot cut, and the amount of stress concentration in the additional compression zone was also lower. The 5 mm-wide cut completely closed off in about 7 years, which did not happen for the wider cut case even after 25 years. This led to a final stress-state that was very similar to the base model, i.e., without slot cutting. Therefore, properly evaluating the ideal width of the cut is essential to make sure the effects of the cut are not negligible.

Cut depth: A total of three cut depths were assessed: 15%, 32.5% and 50% of the dam height. The simulations showed that deeper cuts have a larger decompression area, but that also led to larger compressive stresses immediately below the cut (Figure 6-6b, d and e). It was also interesting to notice that for the deepest cut, the additional compression zone ended up reducing the amount of cracking around the gallery immediately around the cut tip, which was the area with the most intense (and potentially dangerous) cracking. However, this beneficial effect was not observed further away from the cut. Even though deeper cuts affect a larger overall area, determining the ideal cut depth must consider the allowable compression in the additional compression zone, whether the cut will go through galleries or other critical areas, equipment access and capacity to cut through wider portions of the dam, etc.

Number of cuts: The dam model was simulated with two equally spaced cuts of 7.5 mm width each and an equivalent single cut of 15 mm width to assess the effect of the number of cuts. Results showed that a smaller amount of decompression was spread over a larger total area and the compressive stresses in the additional compression zone were lower immediately after the cut when two cuts were modeled. However, there was basically no difference between the two after most of the cut had closed off. Total cracking (Figure 6-7) and total expansion were also basically the same throughout the entire analysis for the two cases.

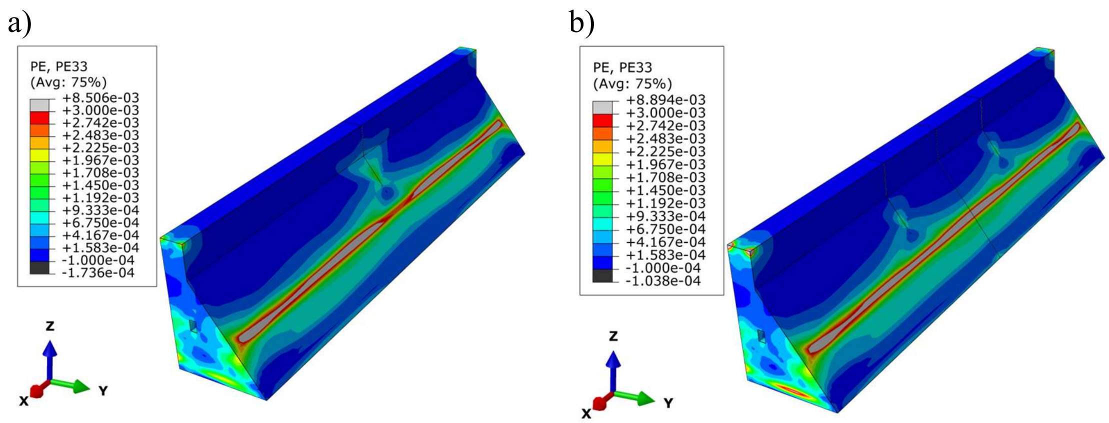


**Figure 6-7. Dam plastic strain along Z-axis (vertical cracking) at time =18,250 days: a. Single cut, b. Two cuts.**

Time at cut: When the same 15 mm-wide 50% dam height cut was performed at 9,000 and 2,000 days, a few interesting observations are made. First, only very subtle differences could be observed regarding cracking at the end of the analysis, with the early cut displaying slightly more cracking around the cut tip due to that area being in tension longer and slightly less damage around the gallery immediately below the crack tip. Second, stresses were also almost the same, with the early cut displaying marginally higher compressive stresses in the decompression zone. Lastly, the total AAR expansion (including stress-state redistribution and temperature) was not the same for both cases. As shown in Figure 6-8a, the total expansion along the length of the dam (x-axis) for points adjacent to the cut at 90, 75, 60, 40 and 20% of the height of the dam was always higher above the cut for the early cut. After the cut, the strain rate increased up to 266%, but after both the cut surfaces were in contact and reached an equilibrium state, the rates were the same and the maximum measured difference in total expansion between the two cases was only 7%. Below the cut, the two total expansions were basically the same. Moreover, the difference along the height of the dam (z-axis) between the two cases was negligible in most cases (Figure 6-8b). The only exception was for the point at 40% height, which displayed a total expansion difference of 6%. It was also observed that the AAR expansion along the width of the dam (y-axis) displayed basically the same behaviour as that for the z-axis. These differences in total expansion occurred because the stresses at the time of the earlier cut have a lower magnitude, meaning that immediately after the early cut, the x-axis stresses in both the decompression zone and the additional compression zone are lower. Lower compressive stresses lead to less expansion reduction along that direction (with consequential increase in long-term expansion). In addition, it was observed that the total AAR expansion along all directions away from the decompression zone was basically the same for both cases at the end of the analysis. Note that on Figure 6-8, “E” stands for early cut and “%H” means the percentage height of the dam where the data is taken from.

a)

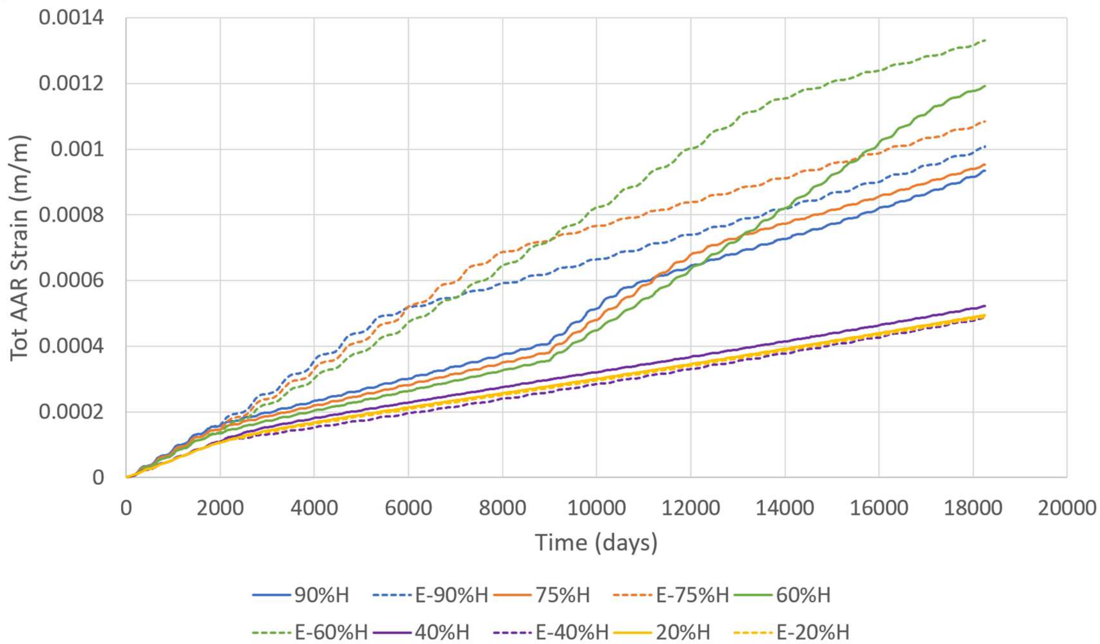


b)

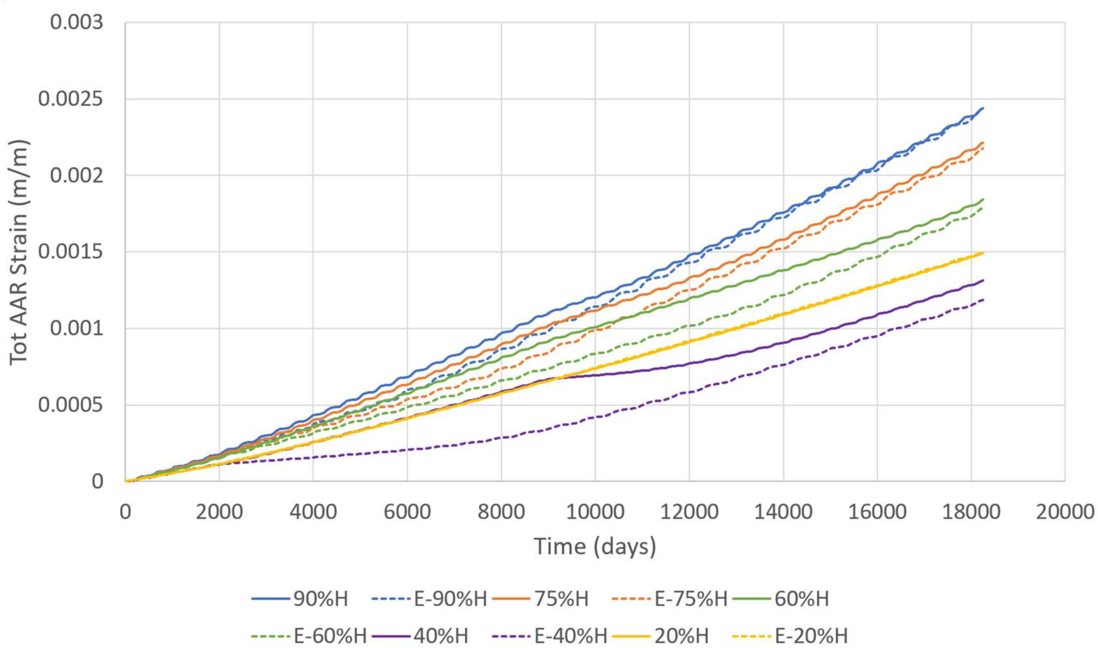


**Figure 6-8. Effect of cut timing (15mm-wide, 50% dam height slot cut) on total AAR expansion (strain) along: a. length (x-axis), b. height (z-axis).**

In summary, it was observed that the slot cut timing has an impact on the total expansion experienced by the structure immediately adjacent to the cut. However, in general the difference in expansion is only on the order of a few percentage points in the decompression zone and is not sufficient to change the overall outcome of the rehabilitation technique for the dam as a whole. The one exception may be for cuts adjacent to discontinuities/areas of non-uniform geometry such as turbine openings/water intakes, where a temporary higher expansion rate might result in more damage due to the expansion gradients around the non-uniform geometry of that area (as reported by Gocevski & Yildiz, 2017). Situations like that are so unique that they must be assessed on a case-by-case basis.

Presence of discontinuities: The effect of slot cutting on a dam with gates was assessed assuming that the gate operation would be compromised at some point due to the displacement caused by AAR expansion. As a result of the highly non-linear stresses around the gates, it was observed that those regions displayed significant cracking even without the slot cut. Moreover, when comparing the cracking pattern of the cases with and without slot cutting, very little difference was observed (Figure 6-9a,b). As for all other simulations, stresses were reduced in the decompression zone and increased in the additional compression zone. Even though no major effect regarding cracking or stresses was observed, the gate opening adjacent to the cut did get reduced. Immediately after the cut, the gap increased by 8.5 mm (just over half the cut width) as shown in Figure 6-9c. Note that the cut was 10 m away from the edge of the gate, and the depth of the cut was 18.6 m, meaning that the edge of the gate was well within the decompression zone. As the reaction progressed, the gap started decreasing again. The difference between the two cases did not remain constant though, starting at 8.5 mm as previously stated and being equal to 4.25 mm at the end of the analysis.

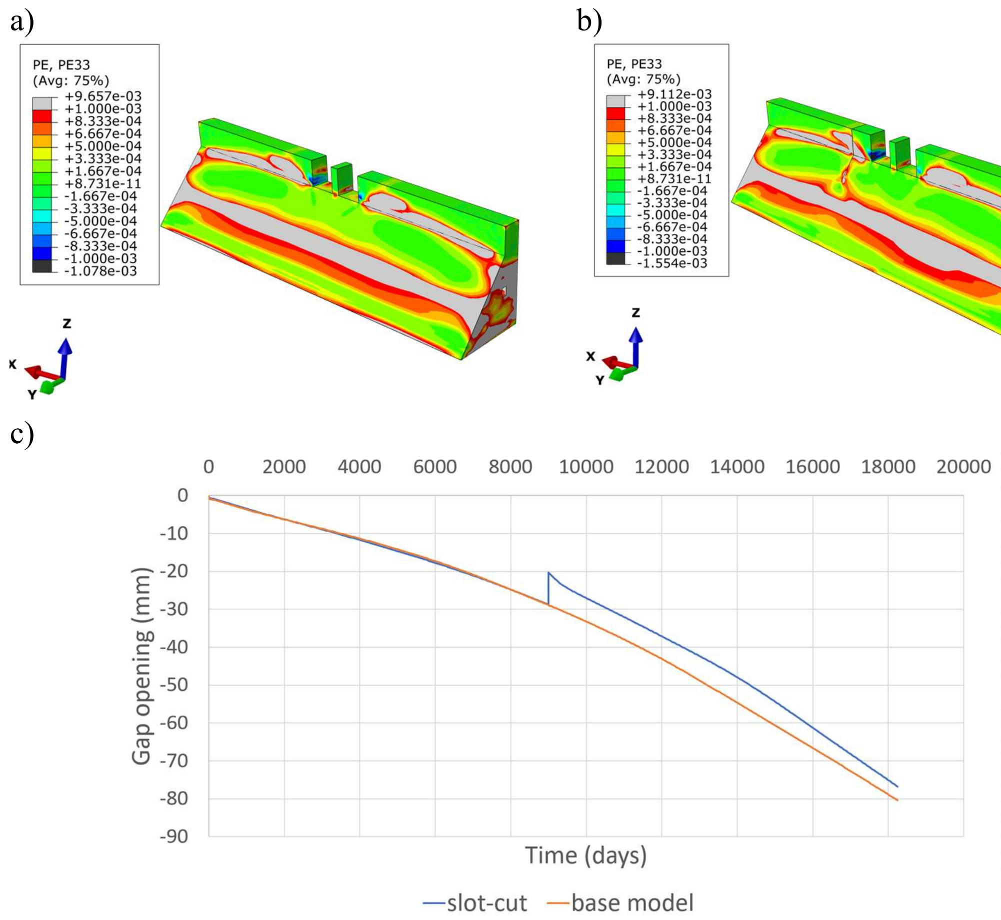


**Figure 6-9. a. Dam plastic strain along Z-axis (vertical cracking) at time =18,250 days for base model (no slot cutting), b. Dam plastic strain along Z-axis (vertical cracking) at time =18,250 days for single slot cut, c. Gate opening vs. time.**

It can be concluded that slot cutting was able to increase the gate opening and could potentially restore its functionality, even if only temporary. Whether or not the increase in gap opening would be sufficient would be a function of the type of gate, available gap, and expansion attained to date. Therefore, if gate operation, ovalization of turbine openings, loss of equipment alignment or closing of expansion joints are of concern, a properly located slot cut can (temporarily) restore adequate performance. However, a proper assessment of the expansion rate is essential to understand the performance of the rehabilitation technique over time and to optimize the possible (multiple) slot cutting campaigns. As previously mentioned, it is also essential to properly model those areas to ensure that releasing stresses will not have a negative effect on the expansion and generate more damage over time.

The effect of proximity to other sources of discontinuity (such as sudden geometric changes) was not directly modeled, as the number of variations and potential outcomes is very large and it is difficult to establish representative cases. Even so, the analyses presented clearly show how complex the structural interactions of slot cutting may be. In this context, secondary deformations may even be potentially detrimental to the functionality of mechanical equipment. Therefore, it is easy to justify recommending to perform slot cuts as far away as possible from discontinuities that are not intended to be rehabilitated, in order to minimize stress gradients, differential displacement and consequential concrete cracking.

<u>Temperature</u>: Temperature gradients also lead to AAR expansion gradients, as both variables are directly related to each other. After the heat of hydration had dissipated for the cases analyzed, the heel of the dam was the point with the coldest average temperature, and the external face in contact with the air and exposed to sun radiation was the warmest. Therefore, the expansion gradient roughly followed that as well. Regarding slot cutting, there are two important consequences of temperature. First, the expansion gradient caused contact between the two surfaces to be more non-linear, with the point closer to the exposed surface displaying higher normal forces. Second, the seasonal temperature changes made the cut open and close cyclically. Obviously, the thermal gradient affected the overall behaviour of the dam, the total amount of expansion, and the expansion gradient. However, besides what was previously described, there were no further significant effects related to slot cutting. The newly introduced thermal boundary condition (new surfaces in contact with air) did not meaningfully affect the thermal profile of the dam, nor the AAR expansion.

It is important to note that the thermal and mechanical effects of water on cracks were not simulated, as these was considered significantly less important than all the other parameters assessed.

Creep: For all cases simulated, creep was significantly less important than AAR expansion and temperature, but its effect was also far from negligible. In general, creep strain was one to two orders of magnitude lower than AAR strain along the height (z-axis) and width (y-axis) of the dam (Figure 6-10b). However, the creep strain values were up to 35% of the AAR strain along the length of the dam (x-axis), even though they were lower than that in average (Figure 6-10a). Similarly, creep recovery along y and z axes was negligible, but reduced the total imposed creep strain along x-axis by more than 50% in some instances. This larger effect along the x-axis can be explained by the fact that AAR-induced strain there was lower as it was reduced by the large compressive stresses, while the same larger compressive stresses increased the amount of creep as it is directly proportional to the stress magnitude. Moreover, it is interesting to notice that creep along the x-axis reduced the total imposed strain as it is negative, compared to the positive AAR strain. Therefore, neglecting creep is not recommended, but it is a conservative approach regarding total imposed strain.

a)

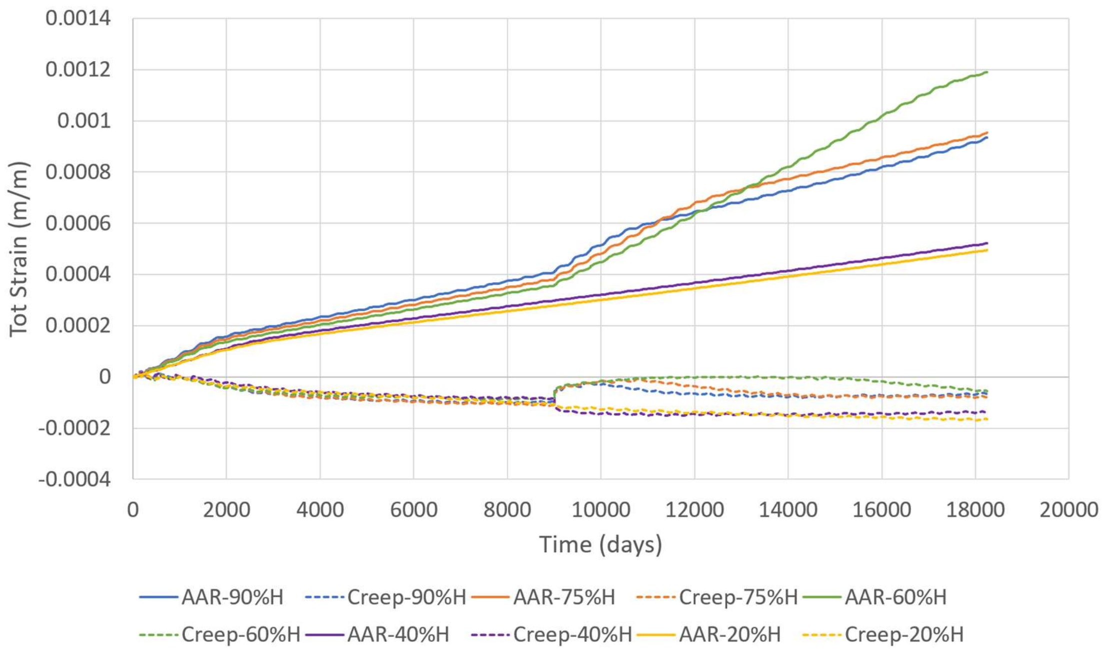


b)

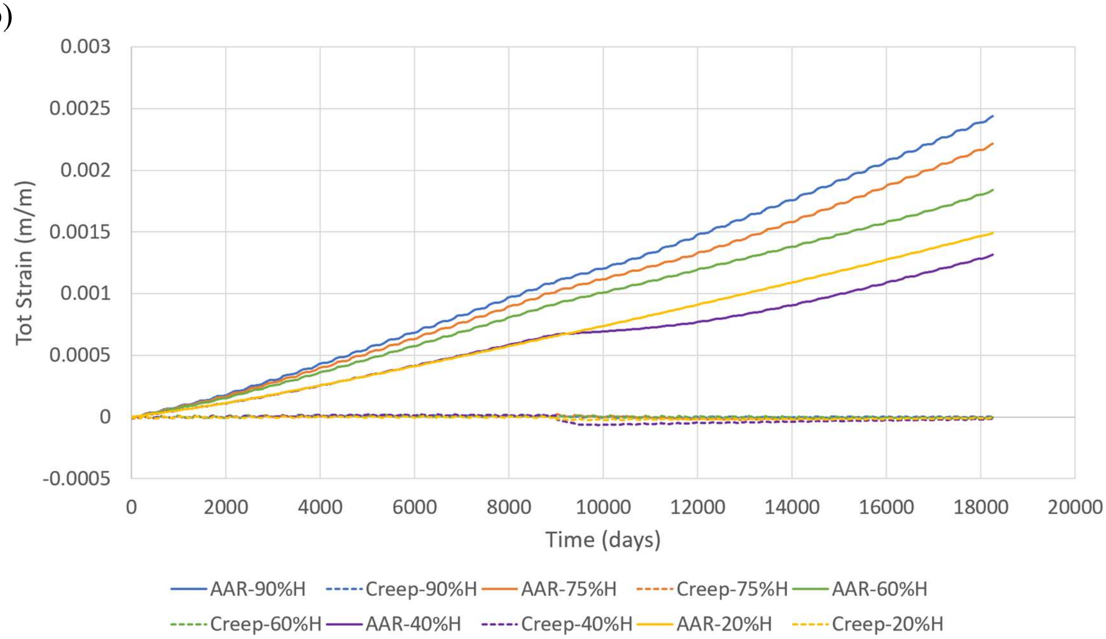


**Figure 6-10. Creep and AAR imposed strain (with 15mm-wide, 50% dam height slot cut @ 9,000 days) along: a. length (x-axis), b. height (z-axis).**

<u>Overall effectiveness</u>: Finally, to evaluate the overall effectiveness of slot cutting as a rehabilitation technique, a few topics need to be discussed. First, the overall effect on cracking (pattern, location, intensity, etc.) is very hard to gauge, as it depends on a large number of variables.

Some of those include geometry, linear and non-linear material behaviour, stress-state, AAR expansion level, temperature, etc. Even so, for the cases studied, it was observed that slot cutting was not able to reduce cracking. In general, a significant amount of cracking was observed around the tip of the cut due to the non-uniform stress-state and consequential expansion gradient. Moreover, cracking elsewhere was not significantly affected unless they were in the additional compression zone. Second, stresses were also not significantly improved by introducing cuts. Stresses in the decompression zone were indeed lowered, but this phenomenon was limited to that area. Elsewhere, either there was no effect (unaffected zone) or the situation was worsened (larger stresses in the additional compression zone). Therefore, slot cutting does not seem to improve the overall performance of the structure or improve its safety margin.

However, the one situation where slot cutting displayed very promising results was in improving the local performance of specific components, for example, by increasing gate openings, reopening expansion joints, or even reducing ovalization of turbine openings and restoring equipment alignment. In all situations, careful assessment of the effects of slot cutting is still essential to ensure the stress release and subsequent increase in AAR expansion rate will not cause additional damage. In general, slot cutting might not be a permanent solution depending on the AAR expansion rate and magnitude, but well-planned campaigns with properly located cuts may be able to improve the performance of those specific components.

Even though not structural, one last consideration that should not be neglected is that the slot cut will need to be waterproofed to prevent water leakage. This has an associated cost, and periodic monitoring and maintenance will be required.

## 6.8 Conclusions

First, theoretical background on creep and slot cutting modeling were described in detail and approaches are proposed. Creep was modeled using Dirichlet (exponential) series, which allowed the analysis to take into consideration the entire stress history without having to store all the data for the entire analysis period. Slot cutting was simulated through contact modeling with activation and deactivation, along with a “dummy” concrete part. Both creep and slot cutting approaches were then validated by simulating slot cutting laboratory tests reported in the literature (Caron et al., 2001). Results matched the recorded data well regarding short-term deflection, long-term deflection and stress profile, proving that the approaches were able to accurately represent both creep (including recovery) and slot cutting over time.

Then, the previously described approaches were used in a parametric analysis of a generic gravity dam with the goal of better understanding the structural implications of slot cutting on massive structures and the individual effect of several parameters. The most important conclusions are presented below:

- The slot cutting structural mechanism is complex. After the cut and before the surfaces are in contact, decompression, additional compression and unaffected zones are formed and usually clearly defined. As the cut closes off due to the compressive stresses generated by current and future AAR expansion, stresses become more uniform.

- Wider and deeper cuts lead to larger decompression zones, but also to larger compressive stresses in the additional compression zone. Properly determining the optimal values of width and depth is essential to obtain the best outcome for the rehabilitation technique.

- More cuts lead to less decompression spread over a larger area and less stress concentration at the crack tip immediately after the cut. However, basically no difference between the two models could be observed after the cut surfaces came into contact, including stresses, total cracking and total expansion.

- Altering when the cut is performed slightly changed the total expansion and expansion rate adjacent to the cut, but it had basically no effect on the overall final stress-state and cracking profile of the dam. The one exception may be for cuts adjacent to discontinuities/areas of non-uniform geometry such as turbine openings/water intakes, where a temporary higher expansion rate might result in more damage due to the expansion gradients around the non-uniform geometry of that area. Situations like that are so unique that they must be assessed on a case-by-case basis.

- The complex structural interactions of slot cutting and potential secondary deformations may be detrimental to the performance of the structure and to the functionality of mechanical equipment. Therefore, cuts should be as far away as possible from discontinuities that are not intended to be rehabilitated, such as changes in geometry.

- Creep strain is usually substantially lower than AAR-induced strain, but its effect is large enough that it should not be neglected. Moreover, properly capturing creep recovery is significant enough in slot cutting analysis that it should be modeled. Even so, analyses that do not incorporate creep tend to overestimate the expansion and be conservative.

- The analyses conducted indicate that slot cutting is not able to improve the overall performance of the structure or improve its safety margin, as no significant beneficial global effects were observed regarding cracking and stress-state. However, properly positioned slot cutting can (temporarily) restore adequate local structural performance of specific components such as gates, turbine openings misaligned equipment, and expansion joints.

Although each case is unique and requires its own technical evaluation, general guidelines and good practices for slot cutting can be derived from the previously presented literature and the discussed results. In general, slot cutting is not recommended as a rehabilitation technique to improve the overall performance of the dam, including reducing stresses in the dam body or minimizing cracking over large areas. However, slot cutting may be a well-suited alternative for specific components with compromised serviceability, such as gates, turbine openings, expansion joints and or sensitive mechanical equipment. For that purpose, cuts should be adequately located, wide enough (usually between 10 and 20mm) and deep enough (15 to 55% of the dam height) to allow the target area to be within the decompression zone. As few cuts as necessary are recommended, ideally with one on each side of the selected region to allow a more uniform stress-state to develop. Special care shall be taken regarding 1) stresses in the additional compression zone, especially given the reduction of mechanical properties caused by AAR, 2) changes in expansion rate and potential additional damage in non-uniform geometry areas, 3) waterproofing, maintenance and monitoring of the cut, 4) properly assessing the current (diagnosis) and future condition (prognosis) of the structure, which shall be done with laboratory tests and computer modeling. The latter shall ideally be performed as described in previous sections, including creep, temperature, AAR stress-state redistribution, reduction of mechanical properties, including all relevant loads and properly defining boundary conditions, as those may have a large effect on the stress-state and consequential AAR expansion.

### 6.9 Future Work

Even though many aspects of slot cutting have been thoroughly assessed, further parametric analysis of turbine openings (i.e., guide vanes), water intakes or other non-uniform geometry regions would provide a better understanding of the feasibility of the rehabilitation technique and the consequences of the temporary additional expansion rate in those areas.

### 6.10 References


Abraham, T. J., & Sloan, R. C. (1978). TVA cuts deep slot in dam, ends cracking problem. Civil Engineering—ASCE, 48(1), 66–70.

Amberg, F., Bremen, R., & Brizzo, N. (2009). Rehabilitation of the Pian Telessio dam (IT) affected by AAR-reaction. Commission Internationale Des Grands Barrages.

Batista, A. L. (1998). Análise do comportamento ao longo do tempo de barragens abóbada [Ph.D. Thesis]. Universidade Técnica de Lisboa and Laboratório Nacional de Engenharia Civil (LNEC).

Bazant, Z. P. (1988). Mathematical modeling of creep and shrinkage of concrete (1st ed.). John Wiley and Sons.

Bazant, Z. P., & Wu, S. T. (1973). Dirichlet Series Creep Function for Aging Concrete. Journal of the Engineering Mechanics Division, 99(2), 367–387.

Bazant, Z. P., & Wu, S. T. (1974). Rate-type creep law of aging concrete based on maxwell chain. Materials and Structures, 7, 45–60.

Caron, P., Tinawi, R., & Léger, P. (2001). Slot cutting response of compressed concrete structures. 4th International Conference on Fracture Mechanics in Concrete and Concrete Structures, 879–886.

Charlwood, R. (1994). A review of alkali aggregate in hydro-electric plants and dams. International Journal on Hydropower Dams, 73–80.

Charlwood, R., Scrivener, K., & Sims, I. (2012). Recent developments in the management of chemical expansion of concrete in dams and hydro projects—Part 1: Existing structures. Hydro 2012 - Innovative Approaches to Global Challenges.

Chulliat, O., Grimal, E., & Bourdarot, E. (2017). Chambom Dam - A Struggle Against AAR. Dam Swelling Concrete (DSC 2017).

Collins, M. P., & Mitchell, D. (1997). Stress-strain response of reinforcement. In Prestressed concrete structures. Reponse Publications.

CSA A23.2-14A. (2014). Potential Expansivity of Aggregates - Procedure for Length Change Due to Alkali-Aggregate Reaction in Concrete Prisms.

CSA A23.3-24. (2024). Design of concrete structures.

Curtis, D. D., Davis, B. J., Rahman, S., & Powell, R. C. (2005). Updated Assessment of Concrete Growth Effects on Hiwassee Dam. 25th Annual USSD Conference.

Curtis, D. D., Feng, L., Sooch, G. S., Zheng, J., & Fletcher, J. (2016). Practical Analysis and Assessment of AAR Affected Dams and Hydroelectric Plants. United States Society of Dams, 36th Annual USSD Conference.

De Grazia, M. T., Goshayeshi, N., Gorga, R., Sanchez, L. F. M., Santos, A. C., & Souza, D. J. (2021). Comprehensive semi-empirical approach to describe alkali aggregate reaction (AAR) induced expansion in the laboratory. Journal of Building Engineering, 40.

Dias, I., Batista, A. L., & Rebelo, R. (2022, May). Prediction of the structural behaviour of Bemposta dam (Portugal), affected by concrete swelling. 16th International Conference on Alkali-Aggregate Reaction in Concrete (ICAAR).

Droz, P., Menouillard, T., Vallotton, O., & Leroy, R. (2013). Slot cutting an AAR-affected dam: case study of the Salanfe dam. International Journal on Hydropower and Dams, 20(5).

Fairbairn, E., Ribero, F., Toledo-Filho, R., Lopes, L., & Silvoso, M. (2004). Smeared cracking FEM simulation of alkali silica expansion using a new macroscopic coupled model. 12th International Conference on Alkali-Aggregate Reaction - ICAAR.

Fournier, B., & Bérubé, M.A. (2000). Alkali-aggregate reaction in concrete: a review of basic concepts and engineering implications. Canadian Journal of Civil Engineering, 27(2), 167–191.

Gautam, B. P., Panesar, D. K., Sheikh, S. A., & Vecchio, F. J. (2017). Multiaxial expansion-stress relationship for alkali silica reaction-affected concrete. ACI Materials Journal, 114(1), 171–184.

Gocevski, V., & Yildiz, E. (2017). Macro-modelling of AAR-affected hydraulic structures. Dam Swelling Concrete (DSC 2017).

Gorga, R. V. (2018). Engineering-Based FE Approach to Appraise Slender Structures Affected by Alkali-Aggregate Reaction (AAR) [M.A.Sc. Thesis]. University of Ottawa.

Gorga, R. V., Sanchez, L. F. M., & Martín-Pérez, B. (2018). FE approach to perform the condition assessment of a concrete overpass damaged by ASR after 50 years in service. Engineering Structures, 177, 133–146.

Gorga, R. V., Sanchez, L. F. M., Martín-Pérez, B., Fecteau, P. L., Cavalcanti, A. J. C. T., & Silva, P. N. (2020). Finite Element Assessment of the ASR-Affected Paulo Afonso IV Dam. Journal of Performance of Constructed Facilities, 34(4).

Goshayeshi, N. (2019). Contribution to the Development of Analytical Models to Forecast Alkali-Aggregate Reaction (AAR) Kinetics and Induced Expansion [M.A.Sc. Thesis, University of Ottawa].

Grimal, E., Sellier, A., Le Pape, Y., & Bourdarot, E. (2008). Creep, shrinkage, and anisotropic damage in alkali-aggregate reaction swelling Mechanism-Part I: A constitutive model. ACI Materials Journal, 105(3), 227–235.

Larive, C. (1997). Apports combinés de l'éxpérimentation et de la modélisation à la compréhension de l'alcali-réaction et de ses effets mécaniques.

Li, K., & Coussy, O. (2002). Concrete ASR degradation: from material modeling to structure assessment. Concrete Science and Engineering, 4(13), 35–46.

Li, K., & Coussy, O. (2004). Numerical assessment and prediction method for the chemico-mechanical deterioration of ASR-affected concrete structures. Canadian Journal of Civil Engineering, 31(3), 432–439.

Mehta, P. K., & Monteiro, P. J. M. (2014). Concrete: Microstructure, Properties, and Materials (4th ed.). McGraw-Hill Education.

Metalssi, O. O., Seignol, J. F., Rigobert, S., & Toutlemonde, F. (2014). Modeling the cracks opening-closing and possible remedial sawing operation of AAR-affected dams. Engineering Failure Analysis, 36, 199–214.

Nguyen, T. N., Sanchez, L. F. M., Li, J., Fournier, B., & Sirivivatnanon, V. (2022). Correlating alkali-silica reaction (ASR) induced expansion from short-term laboratory testings to long-term field performance: A semi-empirical model. Cement and Concrete Composites, 134(2).

Pan, J., Feng, Y., Xu, Y., Jin, F., Zhang, C., & Zhang, B. (2013). Chemo-damage modeling and cracking analysis of AAR-affected concrete dams. Science China Technological Sci-ences, 56(6), 1449–1457.

Póvoas, R. H. C. F. (1991). Modelos não-lineares de análise e dimensionamento de estruturas laminares de betão incluindo efeitos diferidos [Ph.D. Thesis]. University of Porto.

Rebelo, R. P. B. T. (2020). Estudo do comportamento estrutural de barragens arco-gravidade afetadas por expansões do betão. Aplicação à barragem da Bemposta [M.A.Sc. Thesis]. Universidade Nova de Lisboa.

Saati, V., & Mortazavi, A. (2009, May 19). Numerical Modeling of In-situ Stress Calculation Using Borehole Slotter Test. International Symposium on Rock Mechanics (ISRM) - SI-NOROCK 2009.

Sanchez, L. F. M., Fournier, B., Jolin, M., Mitchell, D., & Bastien, J. (2017). Overall assessment of Alkali-Aggregate Reaction (AAR) in concretes presenting different strengths and incorporating a wide range of reactive aggregate types and natures. Cement and Concrete Research, 93, 17–31.

Serra, C., Batista, A. L., & Tavares de Castro, A. (2012). Creep of Dam Concrete Evaluated from Laboratory and In Situ Tests. Strain, 48, 241–255.

Simulia. (2024). Abaqus/CAE - Complete Abaqus Environment (2024). Dassault Systèmes Corporation.

Stucchi, R., & Catalano, E. (2023). The numerical modelling of the Pian Telessio dam affected by AAR. In R. Boes, P. Droz, & R. Leroy (Eds.), Proceedings of the 12th ICOLD European Club Symposium. CRC Press.

Veilleux, M. (1995). Hyrdo-Quebec`s experience using deep slot cutting to rehabilitate concrete gravity dams affected by alkali-aggregate reaction. 2nd International Conference on Alkali-Aggregate Reactions in Hydroelectric Plants and Dams.

Winnicki, A., Seręga, S., & Norys, F. (2014). Chemoplastic modelling of Alkali-Silica Reaction (ASR). Computational Modelling of Concrete Structures - Proceedings of EURO-C 2014, 2, 765–774.

Yu, P., Li, R. Q., Bie, D. P., Liu, X. C., Yao, X. M., & Duan, Y. H. (2021). A coupled creep and damage model of concrete considering rate effect. Journal of Building Engineering, 45(15).

# 7. CLOSURE

## 7.1 Conclusions

The assessment and management of AAR in massive concrete structures, such as dams, require advanced modeling techniques to capture the complex interplay of mechanical, thermal, and chemical phenomena. In this context, the work presented (Papers 01 through 03) provides critical insights into finite element modeling of AAR-affected massive structures and the efficacy of slot cutting as a rehabilitation technique.

<u>Finite Element Modeling of AAR</u>: The finite element model proposed in Paper 01 successfully simulates prestressing and thermal analyses for sound concrete from laboratory experiments. Moreover, (decoupled) thermal analysis of the PAIV dam shows that the heat of hydration dissipates within a few years (two in the case analyzed) and does not significantly influence AAR kinetics. Residual thermal stresses are also found to be below the concrete's tensile and compressive strengths, indicating no contribution to damage. The non-linear mechanical model for AAR demonstrates promise in evaluating massive structures even though it was just a first attempt at modeling such structures. Predictions of field-observed damage profiles are accurate and estimated expansion level matched results from DRI tests. The analysis relies on indirectly accounting for phenomena unique to massive structures, such as alkali release from aggregates, the presence of reactive silica in large aggregates, and minimal alkali leaching. Neglecting these factors results in underestimating expansion by over 50%, highlighting the need for further research to better integrate and incorporate these phenomena. The model was also able to identify critical areas that require monitoring in the spillways, including beams, column bases, and regions behind radial gates, with the latter requiring special attention due to its link to potential prestressing

failure. Moreover, the model predicts that the operation of radial gates is unlikely to be compromised over the structure's lifespan.

Paper 2 advances this framework by incorporating a subroutine that simultaneously incorporates creep, thermal, and AAR-induced strains within a non-linear mechanical model, along with new more refined solar radiation calculations and new implementation of the free expansion equation based on more recent research. This approach accurately simulates the behaviour of the Bemposta dam, aligning well with in-situ monitoring data from LNEC and DRI test results with minimal parameter fitting. The adopted analytical AAR free-expansion equation effectively represents in-situ expansion curves, confirming its suitability for massive structures. Despite differences in assumptions regarding temperature, humidity, dam body-foundation interactions, expansion redistribution, stress-state dependency, material models, and property deterioration, both the proposed model and LNEC's approach predict that the dam's serviceability will remain unaffected in the near future, though ongoing monitoring and laboratory testing are recommended.

Slot Cutting as a Rehabilitation Technique: Paper 3 provides a detailed theoretical framework for modeling creep and slot cutting. Creep is modeled using Dirichlet (exponential) series, enabling efficient consideration of the entire stress history without storing extensive data. Slot cutting is simulated through a novel simulation approach comprising contact modeling with activation and deactivation, along with a "dummy" concrete part. Validation against laboratory tests confirms the accuracy of the proposed approaches in capturing short-term and long-term deflections and stress profiles, including creep recovery. A parametric analysis of slot cutting on a generic gravity dam further elucidates the structural implications, mechanisms involved and influence of several parameters on the rehabilitation technique. Key findings include:

- Mechanisms: Slot cutting generates complex interactions and distinct zones of decompression, additional compression, and unaffected areas post-cutting. As cuts close due to ongoing AAR expansion, stresses become more uniform.
- Cut dimensions: Wider and deeper cuts (typically 10–20 mm wide and 15–55% of dam height) create larger decompression zones but increase compressive stresses in adjacent areas, evidencing that care is necessary to properly optimize these variables.
- Number of cuts: Multiple cuts distribute decompression over a larger area with reduced stress concentration at crack tips initially, but post-closure behaviour shows negligible differences in stresses, cracking, or expansion.
- Timing and location: The timing of cuts has minimal impact on overall stress states and cracking profiles, except near discontinuities (e.g., turbine openings), where temporary increases in expansion rates may exacerbate damage due to non-uniform geometry. Those areas are so unique that they must be assessed on a case-by-case basis.
- Structural interactions with discontinuities: Slot cutting near discontinuities can induce secondary deformations detrimental to structural performance or mechanical equipment functionality; therefore, cuts should be placed away from such areas.
- Creep effects: While the creep strain magnitude is lower than the AAR-induced strain, it is significant enough to warrant inclusion in models, particularly when the stress-state changes significantly as a result of slot cutting.
- Effectiveness: Slot cutting does not enhance overall structural performance or safety margins, as it yields no significant global benefits in terms of cracking or stress reduction. However, strategically placed cuts can temporarily restore local serviceability for specific components, such as gates, turbine openings, expansion joints, or sensitive equipment.

Adequate assessment and evaluation of each case is necessary to optimize the outcomes of the rehabilitation technique.

- Additional considerations: Stresses in compression zones must be estimated and managed, potential damage in non-uniform geometry areas must be closely evaluated, ensuring waterproofing and maintenance of cuts is necessary, and conducting thorough diagnostic and prognostic assessments using laboratory tests and advanced computational models is always recommended.

In summary, the proposed approach to model massive AAR-affected structures demonstrates significant progress in simulating the reaction, with validations against monitoring data and DRI results confirming their accuracy. While modeling massive structures, the model still successfully maintains its original intent, requiring no (or minimal) fitting, while still accounting for the most important aspects affecting both the reaction and the structure. Slot cutting, while not a universal solution, can be effective for localized rehabilitation when carefully designed, but its implementation requires meticulous planning and ongoing monitoring to ensure structural integrity.

## 7.2 Recommendations for Future Work

Even though the major aspects of modeling AAR-affected massive structures and slot cutting as a rehabilitation technique have been thoroughly assessed, the proposed approach can be further refined. In this context, the following recommendations for future work are presented:

- Regarding mechanical properties deterioration, it is recommended that the effect of reducing the material properties as a function of the expansion per direction (instead of based on the average attained value before expansion redistribution) be assessed.

- Regarding the proposed creep modeling approach, it would be recommended to further develop the subroutine by extending the uniaxial creep formulation to a more general three-dimensional case, accounting for the effect that creep along one direction would have on the other two orthogonal orientations. Moreover, accouting for age-related effects on the creep variables would also improve its accuracy for early age structure simulations.
- Regarding overall applicability of the proposed approach, the model would be greatly enhanced if the combined effect of other distress mechanisms (e.g., delayed ettringite formation – DEF, corrosion, etc.) alongside AAR were coded, simulated and validated.
- Regarding model validation, it is recommended to simulate and verify the impact of performing coupled hygroscopic analysis along with the thermo-mechanical-AAR model already presented. Moreover, comparing different expansion redistribution equations (proposed by different authors) might also be beneficial.
- Regarding slot cutting, it would be helpful to perform a parametric analysis of turbine openings (i.e., guide vanes), water intakes or other non-uniform geometry regions to provide a better understanding of the feasibility of the rehabilitation technique and the consequences of the temporary additional expansion rate in those areas.